Technische Universität Berlin – Institute of Fluid Mechanics and Technical Acoustics
Deutsches Zentrum für Luft- und Raumfahrt – Institute of Aerodynamics and Flow Technology

Master's Thesis

Assessment and recalibration of transition criteria for laminar-turbulent transition driven by crossflow instabilities

by

Maximilian Höchel

A thesis submitted in partial fulfillment for the degree of

M. Sc. Mechanical Engineering – Computation

Supervisors: Dr.-Ing. Daniela G. François (DLR)
Prof. Dr. rer. nat. Julius Reiss (TU Berlin)

Berlin/Göttingen, January 26, 2022

Declaration of Originality

Hiermit erkläre ich, dass ich die vorliegende Arbeit selbständig und eigenhändig sowie ohne unerlaubte fremde Hilfe und ausschließlich unter Verwendung der aufgeführten Quellen und Hilfsmittel angefertigt habe.

Hereby I declare that I have written this thesis autonomously and on my own, without any unauthorized external help, and exclusively using the resources and tools listed.

Göttingen, January 26, 2022

Abstract

The major task of laminar-turbulent transition modeling for the boundary layer is to predict the transition line on solid surfaces in order to accurately compute the skin friction. A correct computation of the skin friction is important for the design of the surface geometry of new aircrafts, especially for the wing. One method of transition prediction is the local correlation-based transition modeling, which strongly relies on the use of *transition criteria*. There are separate transition criteria for different transition mechanisms. In this thesis, three different transition criteria for *crossflow instability dominated transition* (CFT) are analyzed: The C1 criterion of Arnal et al. (1984), the helicity criterion of Grabe et al. (2018), and the criterion of Langtry et al. (2015). They are assessed with regard to their accuracy, judged by means of simulations of several wind tunnel experiments reported in the literature. The transition in the simulations is either set manually (fixed transition) or computed by the γ-$\tilde{\mathrm{Re}}_{\theta \mathrm{t}}$ transition model with CFT extension using the C1 criterion (free transition).

The present analysis is motivated by the following facts: For certain test cases the prediction of the transition line based on the C1 and the helicity criteria is inaccurate in comparison to other test cases. In addition, the transition prediction using Langtry's criterion is not implemented in the used fluid dynamics solver *TAU*, yet. But evaluating the accuracy of Langtry's criterion with respect to transition prediction by means of fixed transition simulations is possible nevertheless. The analysis shows whether the implementation of approach of Langtry et al. (2015)would be worth the effort.

These are the findings for the C1 criterion: For shape factors $H_{12} > 2.43$ the crosswise displacement thickness Reynolds number $\mathrm{Re}_{\delta 2}$ at the transition location can be correlated well with the shape factor for many test cases. For lower shape factors the original correlation equation is suited good for the flow around a prolate spheroid and an infinite swept cylinder but not for the flow around two wing-like geometries. Therefore, for low shape factors a reformulation of the C1 criterion is proposed, which is implemented into the fluid dynamics solver. It is presented that computations with the γ-$\tilde{\mathrm{Re}}_{\theta \mathrm{t}}$ transition model with CFT extension using the adapted C1 criterion yield almost no improvement of the transition lines compared to computations with the original C1 criterion. Explanations for that fact are suggested which show general deficiencies of the transition prediction model.

The helicity Reynolds number $\mathrm{Re}_{\mathrm{He}}$ relevant for the helicity criterion cannot be well-correlated with the shape factor H_{12} at the transition location among the several test cases. It is concluded that the parameters of the helicity criterion are less appropriate for CFT prediction than the ones of the C1 and Langtry's criteria.

The momentum thickness Reynolds number Re_{θ} of Langtry's criterion can be correlated very well with the non-dimensional crossflow strength H_{cf} at the transition location. As the original equation of Langtry's criterion does not cover the test cases optimally, an improved formulation is proposed. The implementation of Langtry's approach into the fluid dynamics solver *TAU* is recommended. However, the sensitivity of the transition line prediction to an inaccurately computed momentum thickness Reynolds number is high, as the transition momentum thickness Reynolds number $\mathrm{Re}_{\theta \mathrm{t}}$ may have a streamwise slope similar to the one of the computed momentum thickness Reynolds number Re_{θ}.

Generally, the parameters for the CFT-criteria are approximated locally in the frame of the γ-$\tilde{\mathrm{Re}}_{\theta \mathrm{t}}$ transition model with CFT extension. For the C1 approach, the accuracy of this approximation

is improved by recalibration of a certain model parameter, called *critical-to-transition ratio* C. In the formulation of Grabe et al. (2018) it is a constant, but in present work a dependency of the optimal value on the Reynolds number based on the streamwise chord length of the surface geometry and the boundary layer edge state is found. The new C-correlation is implemented into the fluid dynamics solver. Preliminary results for one test case are shown and discussed. Next steps for a continuation of the work are suggested.

Danksagung (Acknowledgements)

Ich danke der Abteilung *$C^2A^2S^2E$ Göttingen* des *Instituts für Aerodynamik und Strömungstechnik* des *Deutschen Zentrums für Luft- und Raumfahrt* für die Möglichkeit der Erstellung diese Arbeit. Insbesondere muss ich mich bei Dr. Daniela François für die großartige Betreuung bedanken: You helped me a lot in our numerous discussions, so thank you very much!
Auch ihrem Kollegen Dr. Normann Krimmelbein gilt mein Dank dafür, dass ich an seinem reichen Erfahrungsschatz zur Transitionsmodellierung, insbesondere der linearen Stabilitätstheorie, teilhaben konnte. Ich möchte mich auch beim Gruppenleiter Dr. Andreas Krumbein für die wertvollen Anmerkungen zu meiner Arbeit bedanken.
Ebenso danke ich Prof. Dr. Julius Reiss vom Fachgebiet *Numerische Fluiddynamik* der *Technischen Universität Berlin* für die Begutachtung dieser Arbeit. Seinem Kollegen Dr. Mathias Lemke danke ich dafür, dass er bei organisatorischen Fragen immer nur ein Telefonat entfernt war.

Contents

List of Figures

List of Tables

Nomenclature

Symbol name	Unit	Description
A	m^2	surfaace area
$\boldsymbol{A}_\mathrm{c}$	-	convective flux Jacobian matrix
N	1	amplification factor
$\mathcal{B}$	-	boundary layer
C	1	critical-to-transition ratio
$C_D^{(\omega)}$	$\frac{1}{\mathrm{s}^2}$	cross diffusion of specific turbulent dissipation rate
CFL	1	Courant-Friedrichs-Lewy number
$C_{\mathrm{He,max}}$	1	model coefficient
D	N	drag force
$D^{\text{art. diss.}}$	-	artificial dissipation
$D^{(\gamma)}$	$\frac{\mathrm{kg}}{\mathrm{s\ m}^3}$	intermittency destruction
$\mathcal{E}$	-	boundary layer edge
F_2	1	model function
F_onset	1	model function
$F_{\mathrm{onset},1}$	1	model function
$F_{\mathrm{onset},2}$	1	model function
$F_{\mathrm{onset},3}$	1	model function
$F_{\theta\mathrm{t}}$	1	model function
$F_{\theta\mathrm{t}2}$	1	model function
H_{12}	1	boundary layer shape factor
H_CF	1	non-dimensional crossflow strength
He	$\frac{\mathrm{m}}{\mathrm{s}^2}$	helicity
K_general	1	general cut-off value for preconditioning
K_spatial	1	spatial cut-off value for preconditioning
K_v	1	scale factor for viscous time step size
L	N	lift force
$L(\cdot)$	-	Laplace-like operator
N_c	1	number of cells
$N_{c,f}$	1	Number of faces for cell c
N_crit	1	critical amplification factor
$P_\mathrm{CF}^{(\theta\mathrm{t})}$	$\frac{\mathrm{kg}}{\mathrm{s\ m}^3}$	source term of transported momentum thickness Reynolds number due to crossflow instability dominated transition
$\boldsymbol{P}$	-	preconditioning matrix
$P^{(\gamma)}$	$\frac{\mathrm{kg}}{\mathrm{s\ m}^3}$	intermittency production
$P^{(k)}$	$\frac{\mathrm{m}^2}{\mathrm{s}^3}$	model coefficient
$P^{(\omega)}$	$\frac{1}{\mathrm{s}^2}$	specific turbulent dissipation rate production
Pr	1	Prandlt-number
$P^{(\theta\mathrm{t})}$	$\frac{\mathrm{kg}}{\mathrm{s\ m}^3}$	production of transported transition momentum thickness Reynolds number

Continued on next page

Symbol name	Unit	Description
R	N	force magnitude
R^2	1	regression determination coefficient
$\boldsymbol{R}$	-	vector of residuals due to spatial and temporal discretization
$\boldsymbol{R}_\Omega$	-	vector of residuals due to spatial discretization
Re	1	Reynolds number
$\mathrm{Re}_{\mathrm{He}}$	1	helicity Reynolds number
Re_{c}	1	critical Reynolds number
$\mathrm{Re}_{c,\mathrm{e}}$	1	Reynolds number based on chord length and boundary layer edge state
$\mathrm{Re}_{\delta 2}$	1	crosswise displacement thickness Reynolds number
Re_{θ}	1	momentum thickness Reynolds number
$\tilde{\mathrm{Re}}_{\theta\mathrm{t}}$	1	transported transition momentum thickness Reynolds number
Re_{v}	1	vorticity Reynolds number
$\mathbb{R}$	-	bet of real numbers
$\tilde{R}$	$\frac{\mathrm{J}}{\mathrm{kg\ K}}$	specific ideal gas constant
R^{turb}	1	viscosity ratio
$\vec{R}$	N	aerodynamic force
S	$\frac{1}{\mathrm{s}}$	strain rate magnitude
$\underline{\underline{S}}$	$\frac{1}{\mathrm{s}}$	shear rate
$\mathcal{S}$	-	streamline
$\underline{\underline{S}}^*$	$\frac{1}{\mathrm{s}}$	deviatoric shear rate
T	K	fluid temperature
$\mathcal{T}$	-	transition line
$\boldsymbol{T}$	-	matrix of eigenvectors of convective flux Jacobian
T_{ref}	K	Sutherland reference temperature
Tu	1	turbulence intensity
a	$\frac{\mathrm{m}}{\mathrm{s}}$	speed of sound
a_1	1	model coefficient
c	m	chord length
c_{CF}	1	model coefficient
c_R	1	force coefficient
$c^{\text{art. diss.}}$	-	coefficient of artificial dissipation
c_{e1}	1	model coefficient
c_{f}	1	skin friction coefficient
c_p	1	pressure coefficient
$\tilde{c}_p$	$\frac{\mathrm{J}}{\mathrm{kg\ K}}$	heat capacity at constant pressure
$c_{\theta\mathrm{t}}$	1	model coefficient
$\tilde{c}_v$	$\frac{\mathrm{J}}{\mathrm{kg\ K}}$	heat capacity at constant volume
d_1	m	wall distance of first point
d_{ref}	m	reference wall distance
$\vec{d}$	-	(general) diffusive flux
e	1	Euler's number

Continued on next page

Symbol name	Unit	Description
e_{in}	J	internal energy
$\vec{e}$	1	unit vector
f	-	(generic) function
f	Hz	frequency
$f_{\text{criterion, C1}}$	1	function of the C1 criterion
$f_{\text{criterion, He}}$	1	function of the helicity criterion
$f_{\text{roughness}}$	1	roughness function of Langtry's approach
h_{ma}	m	arithmetic mean roughness
h_{p2p}	m	peak-to-peak roughness
h_{rms}	1	root-mean-square roughness
k	$\frac{\text{m}^2}{\text{s}^2}$	specific turbulent kinetic energy
$k_{1,2}$	1	user-chosen coefficients for artificial dissipation
l	m	length scale for local helicity approach
l_γ	m	length of the intermittency development region
$\vec{n}$	m	unit normal vector
p	Pa	fluid pressure
q	Pa	dynamic pressure
$\vec{q}$	$\frac{\text{W}}{\text{m}^2}$	heat flux
r	m	radius
$\boldsymbol{r}$	-	vector of Riemann invariants of Euler equations
s	-	(general) source term
t	s	time
t^*	s	pseudo-time
$\tilde{t}$	s	time scale parameter
u	$\frac{\text{m}}{\text{s}}$	Velocity magnitude
u_{e}	$\frac{\text{m}}{\text{s}}$	boundary layer edge velocity magnitude
$\tilde{u}_{\text{e}}$	$\frac{\text{m}}{\text{s}}$	approximated boundary layer edge velocity
$\vec{u}_{\text{e}}$	$\frac{\text{m}}{\text{s}}$	boundary layer edge velocity
$\vec{u}$	$\frac{\text{m}}{\text{s}}$	Velocity
$\vec{x}_{P^{(\gamma)}}$	m	intermittency production onset location
$\vec{x}_{\text{c}}$	m	critical location
$\vec{x}_{\text{t},c_{\text{f}}}$	m	transition location depicted by the skin friction distribution
$\vec{x}$	m	position vector
$\vec{x}_\Gamma$	m	position vector on the surface Γ
$\vec{x}_\Omega$	m	position vector in the domain Ω
y_n	m	wall normal coordinate
y_n	m	wall normal coordinate
y^+	1	non-dimensional wall normal coordinate
Δ	-	(general) difference
Λ	$^\circ$	sweep angle
Ω	-	flow domain
α	$\frac{1}{\text{m}}$	amplification rate

Continued on next page

Symbol name	Unit	Description
α	$^\circ$	angle of attack
$\beta^{(k)}$	1	model coefficient
$\beta^{(\omega)}$	1	model coefficient
$\gamma_\int$	1	boundary layer integral intermittency
$\gamma_{c,f}$	-	face f of cell c
γ_{eff}	1	effective intermittency
$\tilde{\gamma}$	1	isentropic exponent
δ	-	boundary layer thickness
δ_1	m	boundary layer displacement thickness
$\boldsymbol{\delta}$	-	(general) vector-valued difference
θ	m	boundary layer momentum thickness
$\theta^{*\text{Langtry}}$	m	local approximated momentum thickness according to Langtry
λ	$\frac{\text{W}}{\text{m K}}$	thermal conductivity
λ_2	1	boundary layer pressure gradient parameter
$\boldsymbol{\lambda}_\text{c}$	-	vector of eigenvalues of convective flux Jacobian
λ^{turb}	$\frac{\text{W}}{\text{m K}}$	eddy thermal conductivity
μ	Pa s	dynamic viscosity
μ_{ref}	Pa s	Sutherland reference viscosity
μ^{turb}	Pa s	eddy viscosity
ν	$\frac{\text{m}^2}{\text{s}}$	kinematic viscosity
ρ	$\frac{\text{kg}}{\text{m}^3}$	fluid density
$\underline{\underline{\sigma}}$	$\frac{\text{N}}{\text{m}^2}$	stress tensor
$\sigma^{(\gamma)}$	1	model coefficient
$\sigma^{(k)}$	1	model coefficient
$\sigma^{(\omega)}$	1	model coefficient
$\sigma^{(\theta\text{t})}$	1	model coefficient
$\underline{\underline{\tau}}_\text{v}$	$\frac{\text{N}}{\text{m}^2}$	viscous shear stress tensor
τ_w	$\frac{\text{N}}{\text{m}^2}$	wall shear stress
ϕ	-	(general) placeholder
φ	$^\circ$	azimuth angle
ω	$\frac{1}{\text{s}}$	specific turbulent dissipation rate
ω_c	-	cell c
$\vec{\omega}$	$\frac{1}{\text{s}}$	vorticity
Γ	-	solid surface
Ma	1	Mach number
Su	K	Sutherland constant
ε	-	(general) small deviation
$\varepsilon_{2,4}$	1	second/forth order dissipation coefficient
y_n	m	wall normal coordinate

Subscripts

$(\cdot)_{\mathcal{B}}$	quantity evaluated at $(\vec{x}_{\Gamma}, y_n) \in \Gamma \times \mathbb{R}^+$
$(\cdot)_{\mathrm{CF}}$	crossflow quantity
$(\cdot)_{\mathrm{FF}}$	farfield quantity
$(\cdot)_{\mathrm{L}}$	left quantity
$(\cdot)_{\mathrm{LE}}$	leading edge quantity
$(\cdot)_{\mathrm{R}}$	right quantity
$(\cdot)_{\mathrm{corr}}$	corrected quantity
$(\cdot)_{\mathrm{cw}}$	crosswise quantity
$(\cdot)_{\mathrm{e}}$	boundary layer edge quantity
$(\cdot)_{\mathrm{exp}}$	experimental quantity
$(\cdot)_{\mathrm{inv}}$	inviscid quantity
$(\cdot)_{\mathrm{lam}}$	laminar quantity
$(\cdot)_{\mathrm{max}}$	maximum quantity
$(\cdot)_{n}$	normal quantity
$(\cdot)_{\mathrm{opt}}$	optimal quantity
$(\cdot)_{\mathrm{sw}}$	streamwise quantity
$(\cdot)_{\mathrm{sym}}$	symmetry quantity
$(\cdot)_{\mathrm{t}}$	transition
$(\cdot)_{\mathrm{turb}}$	turbulent quantity
$(\cdot)_{\mathrm{v}}$	viscous quantity
$(\cdot)_{\Lambda=0^\circ}$	zero sweep angle quantity
$(\cdot)_{0}$	total (thermodynamic) quantity
$(\cdot)_{\infty}$	freestream quantity
$(\cdot)^*$	local approximated quantity
$\overline{(\cdot)}$	mean quantity
$\tilde{(\cdot)}$	modified quantity
$(\cdot)'$	fluctuation quantity

Abbreviations

CCD	charge-coupled devices
CFT	crossflow instability dominated transition
DLR	Deutsches Zentrum für Luft- und Raumfahrt
FSC	Falkner-Skan and Cooke
LCTM	local correlation-based transition modeling
LUSGS	lower-upper symmetric Gauss-Seidel
NN	nearest neighbor
RMS	root-mean-square
SST	shear stress transport
TST	Tollmien-Schlichting instability dominated transition
TU	technical university

1 Introduction

1.1 Motivation

Transport aircrafts shall operate as cost-efficient as possible, what saves fuel and thus reduces exhaust gas. In addition, the flight time should be reduced, in order to increase the transport performance. These aims are influenced mainly by the drag of the airplane, which, for steady state flight, splits into the pressure and the viscous drag. On the one hand, as aircrafts fly with high speed (transonic Mach number), compressibility effects invoke the generation of shocks in the flow around the wing surface. These shocks strongly increase the *pressure drag*, and therefore the shock strength should be kept low. This is achieved mainly by sweeping the wing, i.e. rotating it around the vertical axis. On the other hand, the thin boundary layer on the body surface is responsible for the *viscous drag*. This force can be influenced by an appropriate surface shaping. The most obvious way for that is to keep the boundary layer state *laminar* (in contrast to *turbulent*). By doing so, the apparent increase of the local fluid viscosity, characteristic for turbulent flow, is avoided. Indeed, starting from the leading edge of the wing the boundary layer is usually laminar. But along the streamlines, it tends to transition to the turbulent state. There are different transition types. This work focuses on a specific type of *natural transition*. Along the streamlines in the boundary layer, flow instability waves/vortices grow under many circumstances. When grown enough, the instability waves trigger the laminar-turbulent transition of the boundary layer. An important task of the engineering of the wing is to move that transition as downstream as possible by reducing the instabilities' growth rates.

One of the main engineering tools for assessing wing design alternatives with regard to laminar-turbulent transition is *computer simulation*. There are multiple ways for transition prediction in simulations. The methods should require minimal computational power, give accurate results, and be easy to use by engineers or researchers. Especially the last aspect motivates the use of *local correlation-based transition modeling* (LCTM). In this context, a model is a mathematical description of simplified physical phenomena, based on certain assumptions. LCTM is less physics-based than other transition prediction methods, for example the e^N-method, but simpler. Often, *transition tranport models* (TTM) are used that are formulated locally and correlation-based. These TTM rely strongly on the use of *transition criteria*. These are correlations between boundary layer parameters. They are expressed by locally formulated mathematical equations that hold for points on the transition line. The accuracy of the transition criteria has a strong impact on the accuracy of the whole transition prediction.

The thesis focuses on crossflow instability dominated transition (CFT). Crossflow instabilities arise due to the spanwise flow (crossflow) inside the boundary layer, which is caused by the wing sweep. The stronger the crossflow and the higher the surface roughness is compared to the boundary layer thickness, the more crossflow instabilities are amplified. So if CFT takes place, it takes place near to the leading edge of the wing. Then the majority of the wing surface is covered by a turbulent boundary layer with high skin friction. This is why CFT should be avoided with high importance. The present work is using the γ-$\tilde{\mathrm{Re}}_{\theta\mathrm{t}}$ transition transport model with different extensions for CFT. Contrary to the aim of high accuracy, it is known that for certain test case configurations this model gives poor results. For example for some configurations of the *TELFONA Pathfinder wing* the CFT is predicted too upstream with respect to the measurements. The reasons for that are

violated model assumptions of the LCTM and inappropriate calibrations of parameters/functions within the correlation-based transition model. This thesis focuses on the latter, in particular the CFT criterion and a certain model parameter called *critical-to-transition ratio* C. This parameter is multiplied to the transition Reynolds number coming from the transition criterion.

1.2 General Approach

There are multiple CFT criteria proposed in the literature. In this work, the *C1 criterion* [3], the *helicity criterion* [19] and *Langtry's criterion* [31] are assessed. This is done by means of several wind tunnel experiments reported in the literature. The test cases are simulated with fixed transition. The transition is set downstream of the measured transition location or transition location predicted by the e^N-method, if such data is available. From now on, the transition location given by the experiment or the e^N-method is called reference transition location. The laminar boundary layer parameters are evaluated at the reference transition locations. It is tried to correlate these parameters with each other. It is checked whether the correlations coindide with the C1, the helicity, and Langtry's criterion. It turns out that an improvement of the correlation is possible for the C1 criterion. Therefore, the adapted C1 criterion is implemented into the used fluid dynamics solver and used for the free transition prediction, in order to judge the improvements of the transition location prediction in comparison to the one by the original C1 criterion.
The *TAU* code of the German Aerospace Center (DLR) is used for the computations. In it the *local C1 approach* using the C1 criterion and the *local helicity approach* using the helicity criterion are implemented. *Langtry's approach* [31] is not implemented, but Langtry's corresponding criterion can be analyzed nevertheless by means of fixed transition simulations. It will be identified whether the implementation of Langtry's approach for the CFT extension of the γ-$\tilde{\mathrm{Re}}_{\theta\mathrm{t}}$ would be worth the effort.
Even if a CFT criterion was very accurate, the use of it by the LCTM might result in inaccurately computed transition lines with respect to measurements. This is because the variables correlated in a transition criterion are defined on the surface Γ of the body. In order to make the model local, the variables of the transition criterion are replaced by appropriate local approximations that are defined locally in the whole flow domain Ω. Therefore a specific model parameter, the *critical-to-transition ratio* C of the local C1 approach, is recalibrated. In the original local C1 approach, it is a constant $C = 0.75$. It turns out in the fixed transition analysis that the C1 criterion yields a better correlation than the helicity criterion. Therefore, the recalibration of the critical-to-transition ratio is only done for the local C1 approach. The new C-correlation is implemented into the fluid dynamics solver and used for free transition prediction to evaluate the improvements of the transition prediction compared to the one with the constant critical-to-transition ratio $C = 0.75$.

1.3 Structure of the Thesis

The thesis is structured as follows: Firstly, the theoretical background is given that is needed for understanding the present work. This part is divided into the fundamentals of general aerodynamics, turbulence phenomena and their modeling, and the transition phenomena and their modeling. Secondly, the numerical methods for the solution of the equations of the physical model are described by the statement of the partial differential equation problem, the spatial discretization, the temporal discretization, and considerations about the numerical accuracy relevant for transition modeling. Thirdly, the test cases for the analysis are presented by the list of test cases and general rules for the

selection of appropriate configurations within the test cases, the general proceeding in case of missing wind tunnel reference conditions, as well as the principle way of determining the simulation domain Ω. Then the individual test cases are described by the corresponding experimental and numerical setups, the comparison of measured and computed pressure distributions, and the concrete choice of CFT configurations that will be taken into account for the analysis. Forthly, the transition criteria are assessed/recalibrated by a detailed description of the fixed transition analysis of the test cases, a show and interpretation of the results for the individual test cases as well as for a synopsis of the test cases, and a check of the improvements of the computed transition lines in comparison to the experiments. Fifthly, the recalibration of the critical-to-transition ratio C for the local C1 approach is presented. The methodology, derivation of a new correlation, and check of the accuracy of the transition prediction with the new C-correlation by applying it to free transition prediction is given. The final chapter consists of a summary of this work and an outlook to future work.
The softwares used are the fluid dynamics solver *DLR TAU code* for the numerical solution of the model, *Tecplot 360* of Tecplot Inc. for some visualizations, and *Python* with the *PyTecplot* library of Tecplot Inc. for postprocessing.

2 Theoretical Fundamentals and State of the Art

This chapter provides the theoretical foundation needed for understanding the present work. In addition, many notions are introduced which are used in the later chapters. Fluid flow in general, boundary layer theory and flows around swept wings are explained. Turbulence is described both from a phenomenological perspective and by the Menter SST k-ω turbulence model. Afterwards, theory for laminar-turbulent transition of boundary layers on swept wings along with modeling approaches are given. The latter is focused on the γ-$\tilde{\mathrm{Re}}_{\theta\mathrm{t}}$ transition transport model with extensions for crossflow instability dominated transition.

2.1 Mean Flow Aerodynamics

2.1.1 Mathematical Description and Non-Dimensional Parameters

The *fluid flow* is characterized in each point $\vec{x}_\Omega$ of the *flow domain* $\Omega \subset \mathbb{R}^3$ and for each *time* $t \in [0, t_{\max}]$ ($t_{\max}$ is the *end time*) by the *thermodynamical state* and *fluid motion*. In the following, the time dependency is dropped for brevity.
Thermodynamic state (static) variables are for example the *density* ρ, *pressure* p, *temperature* T or *internal energy* e_{in}. The thermodynamic state is uniquely defined by any two thermodynamic variables and the other can be derived from them by material models. In this work, the fluid is air and it is assumed to be an ideal gas, what means

$$\frac{p}{\rho} = \tilde{R}\,T, \tag{2.1}$$

where $\tilde{R} = 287.0\,\frac{\mathrm{J}}{\mathrm{kg\,K}}$ is the *specific ideal gas constant* of air at a chosen reference state. In addition, the gas is assumed to be calorically perfect, which means

$$e_{\mathrm{in}} = \frac{\tilde{R}}{\tilde{\gamma} - 1}\,T, \tag{2.2}$$

where $\tilde{\gamma} = 1.4$ is the *isentropic exponent*, $\tilde{c}_v = \frac{R}{\tilde{\gamma}-1}$ the *isochoric heat capacity* and $\tilde{c}_p = \tilde{\gamma}\,\tilde{c}_v$ the *isobaric heat capacity*.
For the equations of motion, further constitutive laws are needed. The *dynamic viscosity* is assumed to follow the *Sutherland law* [20]

$$\mu = \mu_{\mathrm{ref}} \left(\frac{T}{T_{\mathrm{ref}}}\right)^{\frac{2}{3}} \frac{T_{\mathrm{ref}} + \mathrm{Su}}{T + \mathrm{Su}} \tag{2.3}$$

with the *Sutherland reference viscosity* $\mu_{\mathrm{ref}} = 17.16\,\mu$ Pa s, the *Sutherland reference temperature* $T_{\mathrm{ref}} = 273.0\,\mathrm{K}$, and the *Sutherland constant* $\mathrm{Su} = 110.0\,\mathrm{K}$. In the equations of motion, often the fraction $\nu = \frac{\mu}{\rho}$ appears, and the name *kinematic viscosity* is given to it. Another material property is the *speed of sound* a. Based on the relations for an isentropic change of state, for example

$$\frac{p}{\rho^{\tilde{\gamma}}} = \text{const.}, \tag{2.4}$$

and the ideal gas law (equation 2.1) it is

$$a = \sqrt{\tilde{\gamma}\tilde{R}T}. \tag{2.5}$$

Fluids conduct heat in the presence of temperature gradients. The *thermal conductivity* λ is the corresponding proportionality constant. It is needed for the *Prandtl number* $\mathrm{Pr} = \frac{\mu\tilde{c}_p}{\lambda}$, which is the ratio of the speed of momentum diffusion to heat diffusion. It is assumend to be $Pr = 0.72$ [20]. The fluid motion is defined by the change in position of the particles with time, i.e. the *velocity* vector $\vec{u} = \frac{\mathrm{d}\vec{x}}{\mathrm{d}t}$. By combining it with thermodynamic state variables, the *Mach number*

$$\mathrm{Ma} := \frac{u}{a} \tag{2.6}$$

can be derived, where $u \equiv \|\vec{u}\|$. By using the isentropic relation 2.4, the *total state* can be defined, which is denoted by the subscript $(\cdot)_0$. It is the thermodynamic state of the flow if it was isentropically decellerated to $\vec{u} = \vec{0}$. By combining the isenthalpic relation for a calorically perfect gas

$$\tilde{c}_p T + \frac{u^2}{2} = \text{const.} \tag{2.7}$$

with the isentropic relation 2.4, the isentropic relations of gas dynamics can be derived:

$$\frac{p_0}{p} = \left(1 + \frac{\tilde{\gamma}-1}{2}\mathrm{Ma}^2\right)^{\frac{\tilde{\gamma}}{\tilde{\gamma}-1}}. \tag{2.8}$$

The flow is present in the flow domain Ω with the boundary $\partial\Omega$ which contains the solid surfaces $\Gamma \subset \partial\Omega$, for example a wing surface. In many engineering applications, the interesting effect of a flow is the aerodynamic *force* $\vec{R}$ onto the surface Γ:

$$\vec{R} = \int_\Gamma \underbrace{\underline{\underline{\sigma}}(\vec{x}_\Gamma)}_{-p\underline{\underline{I}}+\underline{\underline{\tau}}_\mathrm{v}} \cdot \vec{n}(\vec{x}_\Gamma)\,\mathrm{d}^2\vec{x}_\Gamma = \underbrace{\int_\Gamma -p(\vec{x}_\Gamma)\,\vec{n}(\vec{x}_\Gamma)\,\mathrm{d}^2\vec{x}_\Gamma}_{\vec{R}_p} + \underbrace{\int_\Gamma \underline{\underline{\tau}}_\mathrm{v}(\vec{x}_\Gamma)\cdot\vec{n}(\vec{x}_\Gamma)\,\mathrm{d}^2\vec{x}_\Gamma}_{\vec{R}_\mathrm{v}} \tag{2.9}$$

Hereby, $\underline{\underline{\sigma}}$ is the stress tensor acting on the surface, $\underline{\underline{\tau}}_\mathrm{v}$ is its viscous part, and $\vec{n}$ denotes the unit normal vector of the surface Γ, pointing into Ω. $\underline{\underline{I}}$ denotes the second order unit tensor. As it is known empirically [23], the force $R := |\vec{R}|$ is determined by the *freestream* velocity $\vec{u}$, density ρ, dynamic viscosity μ, body size/shape, and fluid compressibility. The freestream is the undisturbed flow in absence of a body, denoted by the index $(\cdot)_\infty$. Combining the named influences and applying the *Buckingham-Π theorem* leads to a relation of non-dimensional terms, what can be written as [23]

$$c_R = f(\mathrm{Ma}_\infty, \mathrm{Re}_\infty). \tag{2.10}$$

f denotes some function, $c_R = \frac{R}{A\,q_\infty}$ is the *force coefficient*, A is a characteristic *surface area* of the body, and $q = \rho\frac{u^2}{2}$ is the (incompressible) *dynamic pressure*. The freestream Reynolds number is $\mathrm{Re}_\infty = \frac{u_\infty\, c}{\nu_\infty}$. c is a characteristic *length* of the body (often the chord length). Equation 2.10 expresses that the force coefficient c_R is mainly influenced by the freestream Mach number Ma_∞ and freestream Reynolds number Re_∞. If for R in c_R only the component in flight direction is inserted (drag force D), the *drag coefficient* c_D is obtained. Analogously, the component of the force $\vec{R}$ perpendicular to the flight direction (pointing up, lift force L) leads to the *lift coefficient* c_L.

The force R onto the body surface Γ can be separated into an *inviscid* $\vec{R}_p$ and a *viscid* part $\vec{R}_\mathrm{v}$.

The inviscid part $\vec{R}_p$ comes from the pressure p acting onto the surface Γ. The pressure difference $p-p_\infty$ is commonly non-dimensionalized by the freestream dynamic pressure q_∞, giving the *pressure coefficient*

$$c_p(\vec{x}_\Omega) := \frac{p(\vec{x}_\Omega) - p_\infty}{q_\infty} \; \forall \vec{x}_\Omega \in \Omega. \tag{2.11}$$

The viscid force onto the body Γ comes from the shear stress tensor $\underline{\underline{\tau}}_\mathrm{v}$. In the integral for the viscid force $\vec{R}_\mathrm{v}$ in equation 2.9 the wall normal part is usually small. This motivates the definition of the *wall shear stress*

$$\vec{\tau}_\mathrm{w}(\vec{x}_\Gamma) = \underline{\underline{\tau}}_\mathrm{v}(\vec{x}_\Gamma) \cdot \vec{n}(\vec{x}_\Gamma) - (\vec{n} \cdot \underline{\underline{\tau}}_\mathrm{v} \cdot \vec{n})(\vec{x}_\Gamma)\, \vec{n}(\vec{x}_\Gamma) \; \forall \vec{x}_\Gamma \in \Gamma, \tag{2.12}$$

which is the wall tangential component of the vector $\underline{\underline{\tau}}_\mathrm{v} \cdot \vec{n}$. Also non-dimensionized by the freestream dynamic pressure q_∞, that yields the skin friction coeffient

$$c_\mathrm{f}(\vec{x}_\Gamma) := \frac{|\vec{\tau}_\mathrm{w}(\vec{x}_\Gamma)|}{q_\infty} \; \forall \vec{x}_\Gamma \in \Gamma. \tag{2.13}$$

The convention that its sign is flipped if the shear stress at the wall $\vec{\tau}_\mathrm{w}$ is directed upstream, i.e. $\vec{u}_\infty \cdot \vec{\tau}_\mathrm{w} < 0$, is applied.

The Mach number Ma describes the compressibiliy of the flow, as it compares the flow velocity u to the speed of sound a, which determines the propagation speed of disturbances in the fluid. Albeit obeying the same equations of motion, the fluid behaves phenomenologically different for different Mach number regimes. If $\mathrm{Ma}(\vec{x}_\Omega) < 1 \, \forall \vec{x}_\Omega \in \Omega$, the flow is globally *subsonic*. For $\mathrm{Ma} < 0.3$ the flow almost behaves like incompressible flow ($\frac{\partial \rho}{\partial p} \approx 0$) and the influence of the Mach number Ma in equation 2.10 is weak. If $\mathrm{Ma}(\vec{x}_\Omega) > 1 \, \forall \vec{x}_\Omega \in \Omega \setminus \mathcal{B}$ everywhere except in the boundary layer $\mathcal{B}$, the flow is globally *supersonic*. If the Mach number Ma is somewhere in the domain Ω above and somewhere else (excluding the boundary layer $\mathcal{B}$) below 1, the flow is *transonic*. Both in transonic and supersonic flow, *shocks* occur in the presence of a solid surface Γ. This means that sudden spatial changes of the flow state with high dissipation of kinetic energy into internal energy exist.

The Reynolds number Re describes the ratio of inertia to viscous forces. By that, it determines the influence of friction shear stresses $\underline{\underline{\tau}}$ onto the mean flow. It also is a measure of how likely the flow becomes turbulent, as viscous stress $\underline{\underline{\tau}}$ dampens (inviscid) flow instabilities. Thus, the Reynolds number Re is an important quantity for transition.

2.1.2 Boundary Layer Theory

First, a mathematical convention is introduced:

$$(\cdot)_\mathcal{B}(\vec{x}_\Gamma, y_n) \equiv (\cdot)(\vec{x}_\Gamma + y_n \, \vec{n}(\vec{x}_\Gamma)) \; \forall (\vec{x}_\Gamma, y_n) \in \Gamma \times \mathbb{R}^+ \tag{2.14}$$

Verbally expressed, when any variable, that is defined in whole Ω, gets the index $\mathcal{B}$ appended, the spatial arguments are passed in a different way: The surface position $\vec{x}_\Gamma \in \Gamma$ and the wall normal coordinate y_n are given instead of the volumetric position $\vec{x}_\Omega \in \Omega$.

In contrast to the freestream flow state, at solid walls Γ the flow velocity vector $\vec{u}$ must be zero (no slip condition). Therefore, a so-called boundary layer $\mathcal{B} \subset \Omega$ evolves, which is a thin shear-dominated layer of flow next to the wall Γ in which the velocity $\vec{u}(\vec{x}_\Omega)$ increases rapidly from zero at the wall Γ to the boundary layer edge value at $\mathcal{E} = \partial\mathcal{B} \setminus \Gamma$. The flow outside the boundary layer $\mathcal{B}$ is called the *external* flow $\Omega \setminus \mathcal{B}$.

According to Prandtl [48], for sufficiently high freestream Reynolds numbers Re_∞, the external flow can be seen as approximately inviscid. The external flow is what determines the flow behaviour in general, as many fluid dynamic phenomena can be described by inviscid models. On eof the main effects of the presence of a boundary layer is the *non-zero wall shear stress* $\tau_\mathrm{w} > 0$ due to the finite velocity gradient $\partial_n \vec{u}$ at the wall, what imposes a drag force onto the body. In addition the boundary layer has a *displacement effect* of the inviscid flow outside the boundary layer, which can be considered as a offset of the wall in wall normal direction $\vec{n}$, what lets the body appear thicker to the inviscid flow.
In the boundary layer $\mathcal{B}$ certain terms are negligibly small, for example the wall normal derivative of the pressure $\partial_n p(\vec{x}_\Omega) \approx 0 \, \forall \vec{x}_\Omega \in \mathcal{B}$. The boundary layer velocity profile $\vec{u}(\vec{x}_\Omega) \, \forall \vec{x}_\Omega \in \mathcal{B}$ is the main characteristic of the boundary layer and is influenced by the whole flow field Ω. In case of certain idealized flow cases with laminar boundary layer the velocity profile $\vec{u}(\vec{x}_\Omega) \, \forall \vec{x}_\Omega \in \mathcal{B}$ can be calculated analytically by solving the boundary layer equations [56].
The *approximated boundary layer edge velocity* is

$$\tilde{u}_\mathrm{e}(\vec{x}_\Gamma) = \sqrt{u_\infty^2 + \frac{2\tilde{\gamma}}{\tilde{\gamma}-1}\left[1 - \left(\frac{p_\mathrm{e}(\vec{x}_\Gamma)}{p_\infty}\right)^{1-\frac{1}{\tilde{\gamma}}}\right]\frac{p_\infty}{\rho_\infty}} \; \forall \vec{x}_\Gamma \in \Gamma, \tag{2.15}$$

coming from the compressible Bernoulli equation. In this work, the *boundary layer thickness* is defined as the minimum wall normal coordinate at which the local velocity u reaches the 99% of the approximated boundary layer edge velocity $\tilde{u}_\mathrm{e}$:

$$\delta(\vec{x}_\Gamma) := \underset{y_n \in \mathbb{R}^+}{\arg} \left(u_\mathcal{B}(\vec{x}_\Gamma, y_n) = 0.99 \, \tilde{u}_\mathrm{e}(\vec{x}_\Gamma)\right) \; \forall \vec{x}_\Gamma \in \Gamma. \tag{2.16}$$

The exact *boundary layer edge velocity* is

$$u_\mathrm{e}(\vec{x}_\Gamma) := u_\mathcal{B}(\vec{x}_\Gamma, \delta(\vec{x}_\Gamma)). \tag{2.17}$$

From now on, the index "e" is used as a shorthand for the evaluation of a field quantity in wall normal direction at the boundary layer edge $\mathcal{E}$, i.e. $(\cdot)_\mathrm{e}(\vec{x}_\Gamma) \equiv (\cdot)_\mathcal{B}(\vec{x}_\Gamma, \delta(\vec{x}_\Gamma)) \; \forall \vec{x}_\Gamma \in \Gamma$.
Many properties of the boundary layer can be described by *integral boundary layer parameters*. An integral boundary layer parameter has the form

$$\phi_\int(\vec{x}_\Gamma) = \int_{y_n = 0 \in \mathbb{R}^+} f(\phi_\mathcal{B}(\vec{x}_\Gamma, y_n)) \mathrm{d}y_n \; \forall \vec{x}_\Gamma \in \Gamma. \tag{2.18}$$

According to that definition, integral boundary layer parameters are defined on the surface Γ. Integral boundary layer parameters are less affected by numerical errors than the boundary layer velocity profile $u(\vec{x}_\Omega) \, \forall \vec{x}_\Omega \in \Omega$ [27]. Boundary layer edge variables can be seen as a special type of integral boundary layer parameter (the integrand f in equation 2.18 then contains a mathematical delta distribution).
The *streamwise displacement thickness* is

$$\delta_1(\vec{x}_\Gamma) := \int_0^{\delta(\vec{x}_\Gamma)} \left(1 - \frac{\rho_\mathcal{B} u_{\mathrm{sw},\mathcal{B}}(\vec{x}_\Gamma, y_n)}{\rho_\mathrm{e} u_\mathrm{e}(\vec{x}_\Gamma)}\right) \mathrm{d}y_n \; \forall \vec{x}_\Gamma \in \Gamma. \tag{2.19}$$

It describes the offset/displacement effect mentioned above. The *streamwise velocity* $\vec{u}_{\mathrm{sw}}$ is the velocity component into the streamwise direction

$$\vec{e}_{\mathrm{sw},\mathcal{B}}(\vec{x}_\Gamma, y_n) := \frac{\vec{u}_{\mathrm{e}}}{u_e}(\vec{x}_\Gamma)\ \forall(\vec{x}_\Gamma, y_n) \in \Gamma \times \mathbb{R}^+. \tag{2.20}$$

The *crosswise displacement thickness* is

$$\delta_2(\vec{x}_\Gamma) := -\int_0^{\delta(\vec{x}_\Gamma)} \frac{u_{\mathrm{cw},\mathcal{B}}(\vec{x}_\Gamma, y_n)}{u_{\mathrm{e}}(\vec{x}_\Gamma)} \mathrm{d}y_n\ \forall \vec{x}_\Gamma \in \Gamma. \tag{2.21}$$

The *crosswise velocity* $\vec{u}_{\mathrm{sw}}$ is the velocity component into the crosswise direction

$$\vec{e}_{\mathrm{cw},\mathcal{B}}(\vec{x}_\Gamma, y_n) := \vec{e}_{\mathrm{sw},\mathcal{B}}(\vec{x}_\Gamma, y_n) \times \vec{n}(\vec{x}_\Gamma)\ \forall(\vec{x}_\Gamma, y_n) \in \Gamma \times \mathbb{R}^+. \tag{2.22}$$

A third thickness parameter is the *streamwise momentum thickness*

$$\theta(\vec{x}_\Gamma) := \int_0^{\delta(\vec{x}_\Gamma)} \frac{\rho_{\mathcal{B}} u_{\mathrm{sw},\mathcal{B}}(\vec{x}_\Gamma, y_n)}{\rho_{\mathrm{e}} u_{\mathrm{e}}(\vec{x}_\Gamma)} \left(1 - \frac{u_{\mathcal{B},\mathrm{sw}}(\vec{x}_\Gamma, y_n)}{u_{\mathrm{e}}(\vec{x}_\Gamma)}\right) \mathrm{d}y_n,\ \forall \vec{x}_\Gamma \in \Gamma. \tag{2.23}$$

It characterizes the momentum loss due to viscous friction inside the boundary layer.
The ratio of the displacement thickness to the momentum thickness is the *shape factor*

$$H_{12}(\vec{x}_\Gamma) := \frac{\delta_1}{\theta}(\vec{x}_\Gamma),\ \forall \vec{x}_\Gamma \in \Gamma, \tag{2.24}$$

which describes how "bellied" the boundary layer velocity profile $\vec{u}(\vec{x}_\Omega)\, \forall \vec{x}_\Omega \in \mathcal{B}$ is, as can be seen by the momentum integral theorem of boundary layer theory. Thus, it can be correlated with the streamwise pressure gradient $\partial_{\mathrm{sw}} p(\vec{x}_\Omega)$ inside the boundary layer (or at the boundary layer edge $\vec{x}_\Omega \in \mathcal{E}$). The higher the shape factor H_{12}, the less bellied the boundary layer velocity profile $\vec{u}(\vec{x}_\Omega)$ and the higher the streamwise pressure gradient $\partial_{\mathrm{sw}} p(\vec{x}_\Omega)$. Since a positive, so-called *adverse* pressure gradient leads to a stronger flow decelleration inside the boundary layer $\mathcal{B}$ than at the boundary layer edge $\mathcal{E}$, the flow can even be reversed inside the boundary layer $\mathcal{B}$ (flow separation). This is why the typical maximum shape factor before laminar flow separation occurs is $H_{12,\max} \approx 2.7$.
The streamwise pressure gradient at the boundary layer edge can also be expressed non-dimensional. The *pressure gradient parameter* is

$$\lambda_2(\vec{x}_\Gamma) := \frac{\theta^2}{\nu_{\mathrm{e}}} (\partial_{\mathrm{sw}} u)_{\mathrm{e}}(\vec{x}_\Gamma) \approx -\frac{\theta^2}{\mu_{\mathrm{e}} u_{\mathrm{e}}} (\partial_{\mathrm{sw}} p)_{\mathrm{e}}(\vec{x}_\Gamma). \tag{2.25}$$

A positive pressure gradient parameter $\lambda_2 > 0$ means that streamwise pressure gradient at the boundary layer edge is negative (favorable pressure gradient) or equivalently by energy conservation that the flow is accelerated.
There is a fundamental difference between the laminar $\mathcal{B}_{\mathrm{lam}}$ and the turbulent boundary layer $\mathcal{B}_{\mathrm{turb}}$. In turbulent flow in general, the momentum and energy exchange perpendicular to the mean flow streamlines is much stronger than in laminar flow, which lets flow shear regions grow quicker by diffusion. As a result of that, for the turbulent boundary layer $\mathcal{B}_{\mathrm{turb}}$ the boundary layer thickness δ is higher and the shape factor H_{12} is smaller than for the laminar boundary layer. The more bellied the velocity profile is, the larger the wall normal derivative of the wall tangential velocity and hence the wall shear stress τ_{w}. Thus the turbulent part of the boundary layer should be kept

small, in order to keep the integrand of the integral for the viscid force $\vec{R}_\mathrm{v}$ (see equation 2.9) and thus the drag D low.
It is noted that between the surface Γ and the turbulent part of the boundary layer $\mathcal{B}_\mathrm{turb}$ a *viscous sublayer* is existing. It is present for non-dimensional wall normal coordinates $y^+ < 5$, where

$$y^+_\mathcal{B}(\vec{x}_\Gamma, y_n) := \frac{y_n \sqrt{\frac{\tau_\mathrm{w}(\vec{x}_\Gamma)}{\rho_\mathcal{B}(\vec{x}_\Gamma, y_n)}}}{\nu_\mathcal{B}(\vec{x}_\Gamma, y_n)}. \tag{2.26}$$

2.1.3 Flow Around a Swept Wing Flow

Aircrafts often operate in the transonic flow regime in order to save time. In the transonic flow regime, somewhere in the external flow $\Omega \setminus \mathcal{B}$ around the surface Γ the local Mach number $\mathrm{Ma}(\vec{x}_\Omega) \forall \vec{x}_\Omega \in \Omega \setminus \mathcal{B}$ becomes larger than unity. Along the respective streamlines respective supersonic flow region ends with a shock that reduces the local Mach number Ma to below one. Thas is because over convex surfaces it is impossible for locally supersonic flow to decellerate. Over the shock, the pressure p increases, what reduces the lift L and increases its drag D (called wave drag) of the wing. As the height of the pressure jump across the shock is determined by the component of the velocity $\vec{u}$ normal to the shock front, the shock strength can be reduced by making it oblique to the flow by sweeping the wing. Sweeping the wing means rotating it around the vertical axis by the *sweep angle* Λ. The higher the sweep angle Λ, the higher the critical freestream Mach number $\mathrm{Ma}_{\infty,\mathrm{crit}}$, which is the lowest freestream Mach number Ma_∞ at which the flow is transonic.
For inviscid flow over infinitely long swept rectangular wings (constant chord c), the pressure coefficient c_p on the wing can be related to the *pressure coefficient of the corresponding unswept wing* $c_{p,\Lambda=0}$ by

$$c_p = c_{p,\Lambda=0} \cos^2 \Lambda. \tag{2.27}$$

The consequence is that the pressure coefficient $c_{p,\Lambda=0}$ of the unswept wing gets reduced by the wing sweep. Put differently, the stronger the wing is swept, the lower is the streamwise curvature and the lower the pressure change, i.e. the lower the pressure coefficient c_p. One could also think of it as an effective reduction of the streamwise angle of attack α_sw, as

$$\alpha_\mathrm{sw} = \arctan(\tan \alpha_n \cos \Lambda) \approx \alpha_n \cos \Lambda \tag{2.28}$$

with the angle of attack α_n in the plane normal to the leading edge.
The combination of the wing sweep and streamwise pressure gradient causes a spanwise pressure gradient. This develops a three-dimensional boundary layer profile $\vec{u}_\mathcal{B}(\cdot, y_n)$, which may be regarded as a two-dimensional boundary layer profile with a superimposed secondary flow $\vec{u}_\mathrm{cw}$ in crosswise direction (crossflow). The crosswise component $\vec{u}_\mathrm{cw}$ is zero both at the wall Γ and the boundary layer edge $\mathcal{E}$ (see figure 2.1). The crossflow $\vec{u}_\mathrm{cw}$ exists, whenever the boundary layer edge streamline is curved in a plane parallel to the wall. This can be motivated by the incompressible boundary layer equation in the radial, i.e. crosswise direction [56, 15]:

$$\underbrace{u_\mathrm{cw}\, \partial_\mathrm{cw} u_\mathrm{cw}(\vec{x}_\Omega)}_{\text{crossflow term}} - \underbrace{\frac{u^2_\mathrm{sw}}{r}(\vec{x}_\Omega)}_{\text{centrifugal force}} = -\underbrace{\frac{1}{\rho}\partial_\mathrm{cw} p(\vec{x}_\Omega)}_{\text{pressure force}} + \underbrace{\nu\, \partial_n^2 u_\mathrm{cw}(\vec{x}_\Omega)}_{\text{viscous force}} \ \forall \vec{x}_\Omega \in \mathcal{B}. \tag{2.29}$$

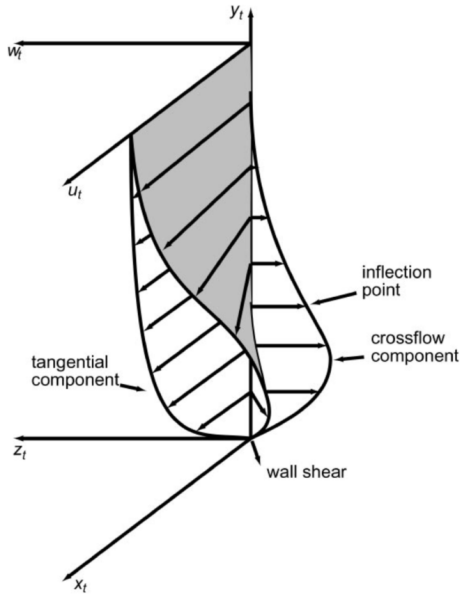

Figure 2.1: Velocity profile of a three-dimensional boundary layer

r denotes the curvature radius of the streamline. Note that in equation 2.29 the radial direction was replaced by the "cw" and the azimuthal direction by "sw" for an easier understanding. The radial direction is not necessarily the one of equation 2.22, but can be the opposite direction, depending on the sign of the streamline curvature. Because the velocity components are zero at the surface Γ, equation 2.29 reduces to

$$0 = -\frac{1}{\rho}\partial_{\mathrm{cw}} p(\vec{x}_\Gamma) + \nu \partial_n^2 \, u_{\mathrm{cw}}(\vec{x}_\Gamma) \; \forall \vec{x}_\Gamma \in \Gamma. \tag{2.30}$$

Per definition the crosswise velocity u_{cw} vanishes at the boundary layer edge $\mathcal{E}$. And the boundary layer edge $\mathcal{E}$ is characterized by vanishing second derivatives of the velocity components. The equation reduces to

$$-\frac{u_{\mathrm{sw}}^2}{r}(\vec{x}_\Omega) = -\frac{1}{\rho}\partial_{\mathrm{cw}} p(\vec{x}_\Omega) \; \forall \vec{x}_\Omega \in \mathcal{E}. \tag{2.31}$$

As $\partial_n p(\vec{x}_\Omega) \approx 0 \, \forall \vec{x}_\Omega \in \mathcal{B}$, it is $\partial_{\mathrm{cw}} \partial_n p(\vec{x}_\Omega) = \partial_n \partial_{\mathrm{cw}} p(\vec{x}_\Omega) \approx 0 \, \forall \vec{x}_\Omega \in \mathcal{B}$ and equation 2.31 can be inserted into equation 2.30. It follows

$$\frac{u_{\mathrm{e}}^2}{r}(\vec{x}_\Gamma) = \nu \, \partial_n^2 u_{\mathrm{cw}}(\vec{x}_\Gamma) \; \forall \vec{x}_\Gamma \in \Gamma. \tag{2.32}$$

The only way to fulfill this is $u_{\mathrm{cw}}(\vec{x}_\Omega) < 0 \, \forall \vec{x}_\Omega \in \mathcal{B} \setminus \partial\mathcal{B}$. The sign can be inferred from equation 2.29. In other words, a radially inwards directed crossflow must take place. The pressure gradient at the boundary layer edge $\mathcal{E}$ is the same inside the boundary layer $\mathcal{B}$, but the streamwise velocity u_{sw} is becoming smaller towards the wall. Therefore, the pressure gradient invokes crossflow. Note that the pressure gradient $\partial_{\mathrm{cw}} p$ may flip the direction along the streamlines. This is the case when the boundary layer edge streamline has an inflection point. The radial direction flips the sign. Therefore the crosswise acceleration inside the boundary layer $\mathcal{B}$ flips the direction. Due to the convection of the crossflow from upstream of the inflection point, an "S"-shaped crosswise velocity profile u_{cw} develops as a transition towards a fully radially inwards directed crossflow u_{cw}. This is why the streamwise distribution of the crosswise displacement thickness δ_2 may have a sign flip.
The size of the crossflow component is dependent on the magnitude of the pressure gradient $\partial_{\mathrm{cw}} p$,

the extend of the favorable pressure gradient region, and the boundary layer thickness δ [11].
The notion of the flow around an *infinite swept wing* is introduced. For this type of flow in spanwise direction (tangential to the leading edge) the spatial derivatives of all flow variables are zero. Hence, the flow is two-dimensional in the sense that the local flow state only depends on the chordwise and a vertical coordinate perpendicular to the chordwise and spanwise direction. However, the flow is still three-dimensional in the sense that vectorial quantities have three components (otherwise no crossflow u_{cw} would exist).

2.2 Turbulence Phenomena

The flow is either laminar, turbulent, or in a transition between both states. In laminar flow the streamlines are smooth and well-ordered. In contrast, in the turbulent case all flow variables can be regarded approximately as a superposition, the so-called *Reynolds decomposition*, of the *mean flow* (denoted by an overbar $\overline{(\cdot)}$) and the spatiotemporal *turbulent fluctuations* (denoted by a dash $(\cdot)'$). For compressible flow there is a difference between the simple and the density-weighted Reynolds decomposition, but this is neglected in this section. Figure 2.2 shows such a time dependent unordered oscillation for the velocity u. The fluctuations are multiple orders of magnitude smaller

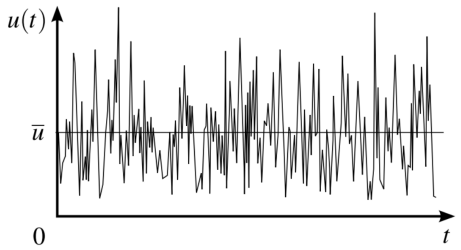

Figure 2.2: Reynolds decomposition of a fluctuating variable

than the corresponding mean flow variable. They are unordered and chaotic. In many engineering applications only the effect of the turbulent vortices onto the mean flow rather than the details of the turbulent fluctuations themselves is important [23]. This is why most often the turbulence is analyzed statistically.
In turbulent flows, on the one hand, kinetic energy $\frac{\overline{u}^2}{2}$ of the mean flow is transformed into *turbulent kinetic energy*

$$k(\vec{x}_\Omega) := \frac{u'^2(\vec{x}_\Omega)}{2} \quad \forall \vec{x}_\Omega \in \Omega, \tag{2.33}$$

which characterizes the size of the turbulent velocity fluctuations. This transformation process is called *turbulence production* and it is known that it is high whereever the mean flow velocity gradient $\nabla\bar{\vec{u}}$ is large [70]. On the other hand, turbulent kinetic energy k get dissipated into internal energy e_{in} of the mean flow. This *turbulence dissipation* is large whereever the gradient of the velocity fluctuations is large, which corresponds to small vertices. This fact can be quantified by the *specific turbulent dissipation rate*

$$\omega(\vec{x}_\Omega) := \frac{\overline{\nu}\,\overline{(\partial_i u_j')^2}}{k}(\vec{x}_\Omega), \ \forall \vec{x}_\Omega \in \Omega, \tag{2.34}$$

which is the ratio of the dissipation rate $\overline{\nu}\,\overline{(\partial_i u_j')^2}$ to the turbulent kinetic energy k.
The turbulent fluctuations strongly increase the diffusion of momentum $\rho\vec{u}$ (apparent increase of the fluid viscosity μ, denoted as the *eddy viscosity* μ^{turb}) and internal energy e_{in} (apparent increase

of the fluid thermal conductivity λ, denoted as the *eddy thermal conductivity* λ^{turb}) as well as of any other diffused quantity in turbulent flows compared to laminar flows. As already mentioned in the section about boundary layers, this increases the viscous drag force of the flow onto the body surface Γ. Therefore, in case of the flow around airplanes, it is mostly seeked for laminar boundary layers.
In this work only *isotropic* turbulence is considered, which means that the *Reynolds stress tensor* $\overline{\rho u_i' u_j'}$ is isotropic. This is a simplification of the reality that allows less complex turbulence modeling. The *turbulence intensity*

$$\text{Tu}(\vec{x}_\Omega) := \frac{\sqrt{\frac{2}{3}k}}{\overline{u}}(\vec{x}_\Omega),\ \forall \vec{x}_\Omega \in \Omega. \tag{2.35}$$

measures the relative size of the turbulent velocity fluctuations u' to the mean flow velocity $\overline{u}$. As aircrafts are moving through resting air, the freestream turbulence intensity can have a value of $\text{Tu}_\infty \ll 0.1\%$.

2.3 Turbulence Modeling with the Menter Shear Stress Transport k-ω Model

The flow is modeled with *convection-diffusion equations*

$$\underbrace{\partial_t \phi(t,\vec{x}_\Omega)}_{\text{transient term}} + \underbrace{\partial_j (u_j \phi)(t,\vec{x}_\Omega)}_{\text{convective term}} = \underbrace{\partial_j d_{\phi,j}(t,\vec{x}_\Omega)}_{\text{diffusion term}} + \underbrace{s_\phi(t,\vec{x}_\Omega)}_{\text{source term}} \forall (t,\vec{x}_\Omega) \in [0,T] \times \Omega \tag{2.36}$$

along with case-dependent boundary and initial conditions. ϕ is a placeholder for the transported quantity and $d_{\phi,j}$ is the diffusive flux. For brevity of the equations, the time and space dependence is dropped for most of the equations from now on. In equation 2.36 in the underbraces the meaning of the terms is given.
Convection-diffusion equations proved useful for the modeling of fluid flow, for example in case of the *Navier-Stokes*-equations [23]. If ϕ is the mass density ρ, the momentum ρu_i or the total energy ρe_t, respectively, one can formulate these (in the absence of source terms) as

$$\partial_t \begin{pmatrix} \rho \\ \rho u_i \\ \rho e_\text{t} \end{pmatrix} + \partial_j \begin{pmatrix} \rho u_j \\ \rho u_i u_j + p\delta_{ij} \\ (\rho e_\text{t} + p) u_j \end{pmatrix} = \partial_j \begin{pmatrix} 0 \\ \tau_{\text{v},ij} \\ \tau_{\text{v},ij} u_i - q_j \end{pmatrix} \tag{2.37}$$

with the *viscous shear stress tensor*

$$\tau_{\text{v},ij} := 2\,\mu\, S_{ij}^*, \tag{2.38}$$

the *deviatoric shear rate*

$$S_{ij}^* := S_{ij} - \frac{1}{3} S_{kk} \delta_{ij}, \tag{2.39}$$

the *shear rate*

$$S_{ij} := \frac{1}{2}(\partial_i u_j + \partial_j u_i), \tag{2.40}$$

and the *heat flux*

$$q_j := \lambda\, \partial_j T. \tag{2.41}$$

In principle, equation 2.37 can be solved numerically in order to accurately predict the flow. But to achieve a discretization-independent solution (*direct numerical simulation*), the spatiotemporal

resolution has to be very fine for turbulent flows. Since the very small turbulent fluctuations are not important for most engineering applications, the Reynolds decomposition for the primitive variables (ρ, p, T, u_i) may be inserted. Then the temporal average of the Navier-Stokes equation over a certain time interval, that separates the mean flow from the turbulent fluctuations, gives the *Reynolds averaged Navier Stokes* (*RANS*) equations (first three line in equation 2.43).
In the RANS equations, the *Reynoldsstress tensor* $\overline{\rho u_i' u_j'}$ comes up, which describes the effect of the turbulent fluctuations on the mean flow. It has to be modeled by a turbulence model (*closure problem*). This also applies for the turbulent heat flux and a term related to the turbulence kinetic energy diffusion in the total energy e_t equation. The *Menter SST k-ω* turbulence model [39] (abbreviated as "SST model") is used for it. It is robustly numerically solvable, has only a weak dependency on the farfield boundary Γ_FF conditions for the turbulence quantities, predicts adverse pressure gradient flows (including separation) relatively well. In addition, it is a good compromise for simulation of anisotropic turbulence phenomena, despite being a model for isotropic turbulence [39]. It is a linear eddy viscosity model, meaning that it is based on the observation that for certain flows, the turbulence acts isotropically like an increase in dynamic viscosity μ (*Boussinesq hypothesis*). Thus, the turbulent diffusion is assumed to be directed into the same direction as the momentum diffusion, i.e. the deviatoric shear rate S_{ij}^* (*gradient diffusion hypothesis*). The same holds true for the thermal conductivity λ with the temperature gradient $\partial_i T$, which is made dependend on the eddy viscosity μ^turb. Under these assumptions, the overall effect of the turbulence on the mean flow may be quantified by the *viscosity ratio*

$$R^\mathrm{turb}(\vec{x}_\Omega) := \frac{\mu^\mathrm{turb}}{\mu}(\vec{x}_\Omega) \; \forall \vec{x}_\Omega \in \Omega. \tag{2.42}$$

It has a similar meaning as the turbulence intensity Tu, but also considers the turbulence dissipating effect of the fluid viscosity μ.
By transformation of the Navier-Stokes equations via the Reynolds decomposition and dot multiplication with the velocity fluctuation $\vec{u}'$, a convection-diffusion equation for the turbulent kinetic energy k can be derived (forth line in equation 2.43). Similarly, a convection-diffusion equation for the specific turbulent dissipation rate ω could be derived, but it is very complicated and hard to interprete. This is why the equation for the specific turbulent dissipation rate ω is formulated by replacing k in the turbulent kinetic energy equation by the specific turbulent dissipation rate ω and adapting the model coefficients for correct dimensions (last line in equation 2.43). The model coefficients are formulated in terms of empirical correlations/model functions. The RANS equation system along with the k and ω equations of the SST model is, where the overbars $\overline{(\cdot)}$ are dropped for simplicity

$$\begin{aligned}
\partial_t \begin{pmatrix} \rho \\ \rho u_i \\ \rho e_\mathrm{t} \\ \rho k \\ \rho \omega \end{pmatrix} + \partial_j \begin{pmatrix} \rho u_j \\ \rho u_i u_j + p\delta_{ij} \\ (\rho e_\mathrm{t} + p) u_j \\ \rho k u_j \\ \rho \omega u_j \end{pmatrix} &= \partial_j \begin{pmatrix} 0 \\ (\mu + \mu^\mathrm{turb}) S_{ij}^* \\ (\mu + \mu^\mathrm{turb}) S_{ij}^* u_i - (\lambda + \lambda^\mathrm{turb}) \partial_j T + \rho D^{(k)} \\ (\mu + \sigma^{(k)} \mu^\mathrm{turb}) \, \partial_j k \\ (\mu + \sigma^{(\omega)} \mu^\mathrm{turb}) \, \partial_j \omega \end{pmatrix} \\
&+ \begin{pmatrix} 0 \\ 0 \\ 0 \\ \rho P^{(k)} - \rho \beta^{(k)} k \omega \\ \rho P^{(\omega)} + \rho C_D^{(\omega)} - \beta^{(\omega)} \rho \omega^2 \end{pmatrix}.
\end{aligned} \tag{2.43}$$

The eddy viscosity is

$$\mu^{\text{turb}}(\vec{x}_\Omega) = \frac{\rho a_1 k}{\max\{a_1\omega,\, \|\vec{\omega}\| F_2\}}(\vec{x}_\Omega)\ \forall \vec{x}_\Omega \in \Omega. \tag{2.44}$$

Hereby, $\vec{\omega} = \operatorname{rot} \vec{u}$ is the vorticity and $F_2(\vec{x}_\Omega)$ is a switch function that is one approximately in the boundary layer $\mathcal{B}$ and zero in the external flow $\Omega \setminus \mathcal{B}$. The *eddy thermal conductivity* is

$$\lambda^{\text{turb}}(\vec{x}_\Omega) = \frac{\mu^{\text{turb}}(\vec{x}_\Omega)\, \tilde{c}_p}{\text{Pr}^{\text{turb}}}\ \forall \vec{x}_\Omega \in \Omega \tag{2.45}$$

with the *turbulent Prandtl number* set to $\text{Pr}^{\text{turb}} = 0.9$.
The source $\rho D^{(k)}$ for the ρe_{t} equation due to turbulent kinetic energy dissipation, the k-production term $\rho P^{(k)}$, the ω-production term $\rho P^{(\omega)}$, the ω-cross-diffusion term $\rho C_D^{(\omega)}$, and the F_2-function are functions of the flow variables and its derivatives and can be found in the literature [39] together with the model constants $\sigma^{(k)}$, $\sigma^{(\omega)}$, $\beta^{(k)}$, and a_1.
When solving the turbulence model numerically, the turbulent kinetic energy k and the specific turbulent dissipation rate ω may become negative in the presence of large transient terms and in stagnation points, what may let the numerical solution diverge [13]. Thus, a lower limit of these values is set. It is derived by reasoning that the eigenvalues of the Reynoldsstress tensor $\overline{\rho u_i' u_j'}$ must be positive, which implies a condition on the specific turbulent dissipation rate ω. It is

$$\begin{aligned} k(\vec{x}_\Omega) &\geq 10^{-5} k_\infty \\ \omega(\vec{x}_\Omega) &\geq \sqrt{\frac{3}{2} S_{ij}^* S_{ij}^*(\vec{x}_\Omega)}\ \forall \vec{x}_\Omega \in \Omega. \end{aligned} \tag{2.46}$$

The turbulence model is also valid in the external (approximately inviscid, i.e. laminar) flow, as the deviatoric flow shear S_{ij}^* and thus the production $P^{(k)}$ of turbulent kinetic energy k are small there. This introduces the issue of the so-called *freestream decay* of turbulent kinetic energy k and related turbulence quantities. Importantly, the freestream turbulence intensity Tu_∞ and viscosity ratio R_∞^{turb} can only be precribed at inflow/farfield boundary Γ_{FF} of the domain Ω. The variable values decrease from there along the streamlines towards the body because the turbulent production terms $P^{(k)}$ and $p^{(\omega)}$ are inactive while the sinks $\rho\beta^{(k)} k\omega$ and $\Phi^{(\omega)} + C_D^{(\omega)}$ are active. It is important to have a physically reasonable turbulence intensity $\text{Tu}(\vec{x}_\Omega)\, \forall \vec{x}_\Omega \in \mathcal{B}$ because there the modeled transition takes place, which may depend strongly on the turbulence intensity $\text{Tu}(\vec{x}_\Omega)\, \forall \vec{x}_\Omega \in \mathcal{B}$. A possible solution to this is to set a higher value for the freestream turbulence intensity Tu_∞ and viscosity ratio R_∞^{turb} at the farfield Γ_{FF} to counteract the decay [65]. This is not useful, as it is very grid-dependent due to the often very coarse spatial discretization in the vicinity of the farfield boundary Γ_{FF} what leads to additional numerical diffusion. In this work a *sustaining turbulence technique* is used, instead. Production terms are added to the turbulence equations:

$$\begin{aligned} k\text{-equation:}&\ + \beta^{(k)} \rho k_\infty \omega_\infty \\ \omega\text{-equation:}&\ + \beta^{(\omega)} \rho \omega_\infty^2 \end{aligned} \tag{2.47}$$

The additional source terms counteract the turbulence freestream decay. Note that equation 2.47 is only used for fully turbulent flow.

2.4 Transition Phenomena

2.4.1 General Description

As in this work the focus is on the laminar-turbulent transition of boundary layers, only this type of laminar-turbulent transition is considered in the following.
For low enough Reynolds numbers the flow is laminar. If the laminar flow is slightly disturbed by freestream fluctuations or sound, these disturbances excite waves, e.g. two-dimensional *Tollmien-Schlichting instability* waves or three-dimensional *crossflow instability* waves over a large range of frequencies/wavelenghts. These waves are called *primary instabilities*. If the laminar flow has a sufficiently large freestream Reynolds number (larger than the so-called *indifference Reynolds number*), it is *linear unstable*. In this case the waves are frequency-selectively amplified and, when sufficiently grown, invoke *secondary instabilities*. The secondary instabilities interact with the primary ones to form complex three-dimensional waves, whose vortices break down, form *turbulence spots*, and finally lead to a fully turbulent flow state. This transition mechanism is called *natural* transition, as it is driven by the growth of flow instability waves. Other types are *bypass* and *separation-induced* transition. [58]
As described in the introduction, for the boundary layer on aircraft surfaces Γ a large area of laminar boundary layer is preferred in order to reduce the skin friction part of the drag force D. This can be achieved by enforcing a high indifference Reynolds number. A way for that is to avoid inflection points in the boundary layer velocity profile. This is because (if the assumptions of the Rayleigh equation of flow instability hold) an inflection point is at least a necessary condition for inviscid instability waves [43].
The state of whether or not a flow is laminar or turbulent can be described by the space- and timedependent *intermittency* $\gamma(\vec{x}_\Omega)\,\forall\vec{x} \in \Omega$. For a fixed point, it is defined as the ratio of times of the presence of turbulent flow to the total time in some moving time interval. So an intermittency of $\gamma \approx 0$ means the flow is fully laminar and an intermittency of $\gamma \approx 1$ means the flow is fully turbulent. The intermittency γ is distributed continuously in space and time, in other words, the change from laminar to turbulent flow is continuous process that takes some time/space.
Some mathematical notations are introduced. The *streamline* through the point $\vec{x}_\Omega \in \Omega$ is denoted by $\mathcal{S}(\vec{x}_\Omega)$. The *turbulent part* of that streamline is

$$\mathcal{S}^{\mathrm{turb}}(\vec{x}_\Omega) = \{\tilde{\vec{x}}_\Omega \in \mathcal{S}(\vec{x}_\Omega) : \gamma(\tilde{\vec{x}}_\Omega) \approx 1\}\ \forall\vec{x}_\Omega \in \Omega. \tag{2.48}$$

The *transition location* of the streamline through $\vec{x}_\Omega \in \Omega$ is

$$\vec{x}_{\mathrm{t}}(\vec{x}_\Omega) := \underset{\tilde{\vec{x}}_\Omega \in \mathcal{S}^{\mathrm{turb}}(\vec{x}_\Omega)}{\operatorname{argmin}} \tilde{\vec{x}}_\Omega \cdot \frac{\vec{u}}{u}(\tilde{\vec{x}}_\Omega). \tag{2.49}$$

Expressed verbally, the transition location of a streamline is the first point along the streamline at which the intermittency γ reaches approximately one or is at least significantly larger than zero.
In the context of boundary layers, commonly the whole boundary layer *at once* is called laminar/-turbulent, even if the streamlines inside the boundary layer transition at different points $\vec{x}_{\mathrm{t}}$. For engineering purposes usually the higher wall shear stress τ_{w} is the most important difference of a turbulent boundary layer to a laminar one. Therefore, the transition of the whole boundary layer is determined by the transition of the streamlines in the close vicinity to the wall, as the increasing turbulence there leads to an apparent increase the fluid viscosity and hence the wall shear stress τ_{w}.

Therefore, the *integral boundary layer intermittency* is introduced as

$$\gamma_{\int}(\vec{x}_{\Gamma}) := \lim_{y_n>0, y_n\to 0} \gamma_{\mathcal{B}}(\vec{x}_{\Gamma}, y_n) \ \forall \vec{x}_{\Gamma} \in \Gamma, \tag{2.50}$$

which characterizes the laminar/turbulent state of the whole boundary layer at once. The *boundary layer edge streamline* $S_{\mathcal{E}}(\vec{x}_{\Gamma}) \subset \mathcal{E}$ is introduced, which is the "streamline" calculated by the wall tangential part of the boundary layer edge velocity $\vec{u}_{\mathrm{e}}(\vec{x}_{\Gamma})$.[1] For boundary layers, the notions "upstream" and "downstream" are defined based on the boundary layer edge streamlines $S_{\mathcal{E}}$. Also defined is the *wall normal projection of the boundary layer edge streamline*

$$\mathcal{S}_{\mathcal{E}\to\Gamma}(\vec{x}_{\Gamma}) = \{\tilde{\vec{x}}_{\Gamma} \in \Gamma : \tilde{\vec{x}}_{\Gamma} + \delta(\tilde{\vec{x}}_{\Gamma})\, \vec{n}(\tilde{\vec{x}}_{\Gamma}) \in \mathcal{S}_{\mathcal{E}}(\vec{x}_{\Gamma})\} \ \forall \vec{x}_{\Gamma} \in \Gamma. \tag{2.51}$$

Similarly to equation 2.49, the transition location $\vec{x}_{\mathrm{t}}(\vec{x}_{\Gamma})$ *of the boundary layer* is the most upstream wall point on the wall normal projection of the boundary layer edge streamline $\mathcal{S}_{\mathcal{E}\to\Gamma}(\vec{x}_{\Gamma})$ at which the integral boundary layer intermittency $\gamma_{\int}(\vec{x}_{\mathrm{t}}) \approx 1$. The set of all boundary layer transition locations is the *transition line* $\mathcal{T} \subset \Gamma$. In wind tunnel experiments the transition line is found by visualization of the wall shear stress τ_{w} or heat transfer q, which are significantly higher in case of a turbulent boundary layer. These visualitations show a relatively sharp distinction between the laminar and the turbulent boundary layer. However, in simulations the skin friction coefficient c_{f} is used to define the computed transition line, as the main goal of transition prediction is to predict the viscid part $\vec{R}_{\mathrm{v}}$ of aerodynamic force $\vec{R}$. In this work the transition line is defined by means of the maximum curvature of the skin friction coefficient c_{f} as

$$\mathcal{T}^{(\mathrm{CFD})} = \{\vec{x}_{\Gamma} \in \Gamma : \operatorname*{argmax}_{\tilde{\vec{x}}_{\Gamma} \in \mathcal{S}_{\mathcal{E}\to\Gamma}(\vec{x}_{\Gamma})} \partial_{\mathrm{sw}}^2\, c_f(\tilde{\vec{x}}_{\Gamma})\}. \tag{2.52}$$

Here, ∂_{sw} means the streamwise derivative along the wall normal projected boundary layer edge streamline $\mathcal{S}_{\mathcal{E}\to\Gamma}(\vec{x}_{\Gamma})$.

2.4.2 Transition Types in Swept Wing Flows

Tollmien-Schlichting Instabilities

For boundary layers on wings, the most common transition phenomenon is the one driven by Tollmien-Schlichting instabilities (called *TST* in the following). They are the driving instability waves for boundary layers without crossflow. They develop as two-dimensional, streamwise traveling harmonic waves with a phase speed less than the boundary layer edge velocity. In figure 2.3 Tollmien-Schlichting-waves are depicted. If the waves become large, they get distorted and interact with each other, forming three-dimensional waves and so-called lambda-vortices. These disaggregate to form turbulent spots, which grow until the whole boundary layer flow is turbulent, see figure 2.4. The transition line of TST is relatively smooth and straight, as the Tollmien-Schlichting-instability mechanism is two-dimensional.

Tollmien-Schlichting instability amplification rates are very sensitive to the turbulence intensity Tu in the boundary layer. If the environment has a large turbulence intensity Tu, Tollmien-Schlichting instabilities may even be bypassed to directly trigger the so-called bypass-transition. Typically,

[1] Note that the boundary layer edge streamline is no real streamline, as the real streamline necessarily cross the boundary layer edge $\mathcal{E}$. This can intuitively be understood by the fact that the boundary layer thickness δ is zero at the leading edge of the surface Γ. If no streamlines crossed the boundary layer edge $\mathcal{E}$, the flow inside the boundary layer would have to develop from nowhere [27].

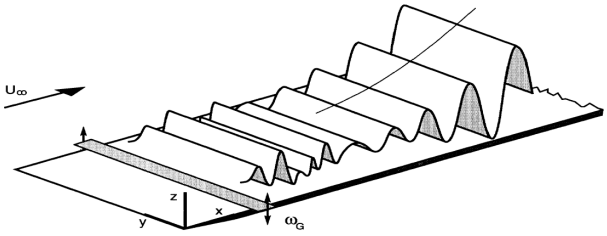

Figure 2.3: Tollmien-Schlichting waves (here created by a forced excitation of the boundary layer) [43]

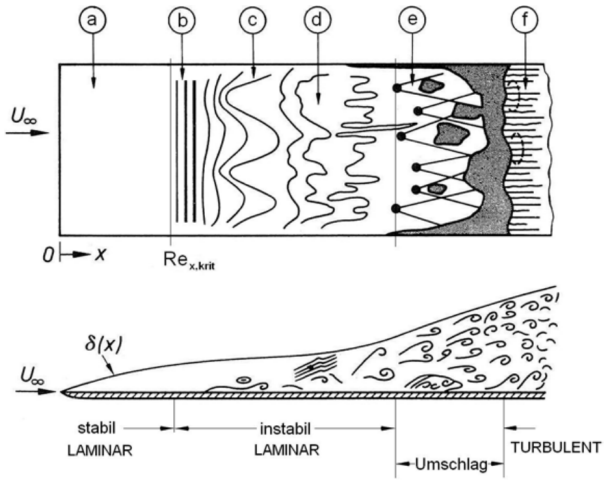

Figure 2.4: Tollmien-Schlichting instability dominated transition of a boundary layer [56]

this is the case in turbomachinery where the flow is highly disturbed due to the unsteady flow around the moving blades, but not in the flow around airplanes, which is mostly steady state and with a resting freestream. Another major influence on the amplification of the Tollmien-Schlichting waves is the pressure gradient parameter λ_2. The lower its value/the stronger the adverse pressure gradient, the higher the amplification.

Crossflow Instabilities

As figure 2.1 already shows, the three-dimensional boundary layer has additional inflection points in the crosswise velocity profile, which act destabilizing onto flow stability. Thus, the crossflow is connected to a new instability mechanism, that may cause transition (called CFT in the following). In contrast to Tollmien-Schlichting instability waves, crossflow instability waves come in two types: stationary and traveling [55].
In environments of low turbulence intensities characteristic of flight, *stationary* waves dominate and are responsible for the transition, if it is a CFT. These waves look like vortices and can be seen in figure 2.5. The wavenumber vector of the stationary waves is almost perpendicular to the boundary layer edge streamline. Thus, the convection of the crosswise velocity fluctuation due to the instability waves leads to a large streamwise velocity fluctuation [55], which is also stationary. This modification of the mean flow in streamwise direction leads to an alternating pattern of acceleration and decelleration of the streamwise flow and strong wave amplification, that rapidly leads to transition. The alternation pattern can be seen in visualizations of the transition line $\mathcal{T}$, that show a "saw-tooth" shape of the transition line. Contrary to the TST, the stationary

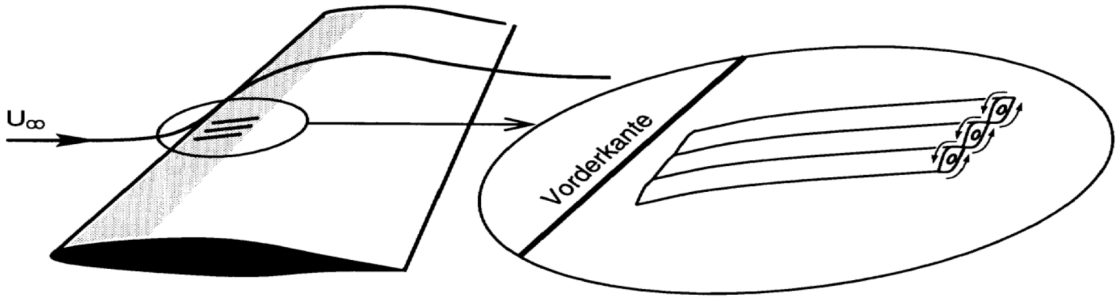

Figure 2.5: Sketch of the stationary crossflow instability vortices on a swept wing [43]

CFT is relatively insensible to the turbulence intensity Tu. (Nevertheless, in the literature [3] the so-called C2-criterion is formulated, which includes the influence of the turbulence intensity Tu, but is based on very little information.)
On the other hand, *traveling* crossflow instability waves dominate the CFT if the turbulence intensity is high enough ($\mathrm{Tu} > 0.15\,\%$, except through sound, which does not have an influence [55]). The transition line is more straight then.
Another major influence onto both stationary and traveling crossflow instability wave amplification is the *surface roughness* (coming from the manufacturing process, for example). This was proven by translating a wind tunnel model of a swept wing with the result that the stationary saw-tooth transition line pattern of the stationary CFT stays fixed to the model [41]. This is especially important as the roughness height is large relative to the small boundary layer thickness δ in the vicinity of the leading edge of the wing. It is important to note that the surface profile along some test distance must be considered with its complete spectrum of wavelengths. The different wavelengths contributions interact differently with the crossflow transition vortices [55]. Hereby, it is noted that convex surface curvatures increases and the non-parallelism of the inviscid streamlines decreases the receptivity, i.e. the sensitivity, to surface roughness.
It is known that concave surface curvature stabilizes stationary crossflow instability vortices and convex surface curvature destabilizes stationary crossflow instability vortices [66].
It is noted that the crossflow instability waves may interact with the Tollmien-Schlichting instabiliy waves, if both are relatively large. In this case the transition takes place more upstream than when only one of the two types of flow instability is present.

Other Transition Types in Swept Wing Flow

Separation-Induced Transition: If the laminar boundary layer detaches from the surface, i.e. an adverse streamwise pressure gradient $\partial_{\mathrm{sw}} p > 0$ forces a backwards directed flow inside the boundary layer, the flow is strongly sheared at the boundary layer edge, what generates turbulent fluctuations. These are traveling into the laminar separation region and force it to become turbulent. As turbulent boundary layers are less sensitive to adverse pressure gradients (lower shape factor H_{12}), the separated flow may attach shortly downstream of the laminar separation. The small region of backwards directed flow is called a *laminar separation bubble*. Laminar separation bubbles are identified by a negative skin friction coefficient c_{f}, as the flow is directed backwards inside the boundary layer.
Shock-Induced Transition: In transonic or supersonic flow, shocks appear which are characterized by a sudden change of the fluid state across it. These shocks touch the surface Γ somewhere and hence are also present in (the supersonic part of) the laminar boundary layer. The strong adverse pressure

gradient due to the jump of the static pressure p across the shock causes a laminar separation bubble and hence a separation induced transition.
Attachment Line Instability: The attachment line is the three-dimensional analogon to a stagnation point in two dimensions. On the attachment line, a spanwise boundary layer develops, and the three-dimensional flow features another type of instability, called attachment line instability wave. These instabilities may be bypassed in case of the so-called leading edge contamination: The turbulent boundary layer on the fuselage can interact with the laminar boundary layer at the wing's leading edge in the vicinity of the wing root. Then the laminar boundary layer directly becomes turbulent there.
Görtler Instability: If the boundary layer edge velocity u_e is high enough and the wing surface is concave, periodically distributed counter-rotating vortices may appear, whose axes are directed streamwise. These come together with a rotatory momentum gradient towards the wall, which acts as a source of instability. [43]
Streamline-Curvature Instability: Near the stagnation point at the leading edge, streamlines are strongly curved by large pressure gradients. A model example of this is the flow along a swept cylinder flow [55]. The streamline-curvature instability is similar to the crossflow instability, but for highly curved streamlines, it leads to a transition more upstream. The cause for it is a centrifugal term in the equations of linear stability analysis [33].

2.5 Transition Modeling

2.5.1 Relationship to the Turbulence Model

The RANS equations together with a turbulence model (equation 2.43) are only useful for simulating fully turbulent flow, in particular a fully turbulent boundary layer. To take into account that the boundary layer may be laminar, the turbulence model must be "switched off", depending on the local intermittency $\gamma(\vec{x}_\Omega) \forall \vec{x}_\Omega \in \mathcal{B}$. In case of the SST turbulence model with the γ-$\tilde{\mathrm{R}}\mathrm{e}_{\theta\mathrm{t}}$ model used for this thesis, the destruction $D^{(k)}$ of total energy e_t and the corresponding production $P^{(k)}$ of turbulent kinetic energy k are modified [32]:

$$\begin{aligned} \tilde{D}^{(k)}(\vec{x}_\Omega) &= \min\{\, \max\{\gamma_\mathrm{eff}(\vec{x}_\Omega), 0.1\}, 1.0 \,\}\, D^{(k)}(\vec{x}_\Omega) \\ \tilde{P}^{(k)}(\vec{x}_\Omega) &= \gamma_\mathrm{eff}(\vec{x}_\Omega)\, P^{(k)}(\vec{x}_\Omega)\ \forall \vec{x}_\Omega \in \Omega. \end{aligned} \tag{2.53}$$

The effective intermittency γ_eff combines the influences of different transition mechanisms. It is similar to the intermittency γ ($\gamma = 0$ is laminar, $\gamma = 1$ is turbulent), but is only a model parameter used to scale the destruction $D^{(k)}$ and production $P^{(k)}$. The reason for the min/max limiters can be found in [32].
The SST turbulence model is calibrated to be fully active in the external flow. Therefore, the effective intermittency is $\gamma_\mathrm{eff}(\vec{x}_\Omega) \approx 1 \forall \vec{x}_\Omega \in \Omega \setminus \mathcal{B}$, even if the external flow is laminar in reality.
A trivial way for determining the effective intermittency γ_eff is to set the transition manually (*fixed transition*). To be precise, the integral intermittency $\gamma_\int(\vec{x_\Gamma})$ is set. This has an effect between the wall and a user-chosen maximum wall distance d_ref, which is set slightly larger than the maximum expected boundary layer thickness $\max_{\vec{x}_\Gamma \in \Gamma} \delta(\vec{x}_\Gamma)$. So for points in the external flow $\Omega \setminus \mathcal{B}$ above the laminar boundary layer that are closer to the wall than d_ref, the destruction $\tilde{D}^{(k)}$ and production $\tilde{P}^{(k)}$ terms are incorrectly disactivated. As the external flow is inviscid, the influence of this disactivation is negligible.

However, in most of the cases the transition location $\vec{x}_\mathrm{t}$ is unknown and must be calculated by means of a prediction method (*free transition*), i.e. a transition model.
When a transition model is applied, the sustaining turbulence terms (equation 2.47) are modified:

$$\begin{aligned} k\text{-equation:} &\quad + \delta_{\Omega\setminus\mathcal{B}}\beta^{(k)}\rho k_\infty\omega_\infty \\ \omega\text{-equation:} &\quad + \delta_{\Omega\setminus\mathcal{B}}\beta^{(\omega)}\rho\omega_\infty^2\gamma_\mathrm{eff} \\ \delta_{\Omega\setminus\mathcal{B}}(\vec{x}_\Omega) &= \begin{cases} 0 & \text{if } \vec{x}_\Omega \in \Omega \\ 1 & \text{otherwise} \end{cases} \end{aligned} \tag{2.54}$$

In order to let the transition modeling be unaffected, equation 2.54 shall only be applied outside the boundary layer $\mathcal{B}$. That is approximately achieved by switching off the source terms for points that are located closer to the surface Γ than d_ref.
Note that the equations given in this subsection already incorporate the use of a specific transition model. Nevertheless, the general idea of switching the destruction $D^{(k)}$ and production $P^{(k)}$ dependent on the laminar/turbulent state of the boundary layer is the same for all transition models that can be coupled to the SST turbulence model.

2.5.2 The e^N-Method

The e^N-method is a transition prediction method. The sufficient condition for secondary instabilities and thus natural transition to occur is that the primary instability waves (e.g. Tollmien-Schlichting waves) have grown enough, which can be computed by the spatial *linear stability analysis* of the boundary layer $\mathcal{B}$. In the linear stability analysis, simplified forms of the Navier-Stokes *disturbance differential equation* are solved with a modal ansatz, yielding a wave form and a complex-valued wave number for a given wave frequency f. The negative imaginary part of the wave number is the *amplification rate* α. The *amplification factor* N can then be computed by the path integral of the amplification rate along the streamline:

$$N(f, \vec{x}_\Omega) = \int_{\vec{x}_0}^{\vec{x}} \alpha(f, \tilde{\vec{x}})\,\mathrm{d}\tilde{\vec{x}} \tag{2.55}$$

$\vec{x}_0$ is the *indifference point*, i.e. the most upstream point where the amplification rate α is larger than zero. For each position $\vec{x}_\Omega$, the maximum amplification factor $N_\mathrm{max}(\vec{x}_\Omega)$ over has frequencies to be found. This can be achieved by computing only a finite number of frequencies and drawing an envelope around the maxima of the amplification factors, see figure 2.6. The N-factor of the

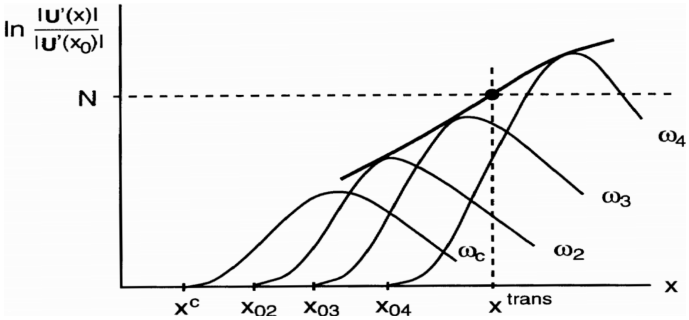

Figure 2.6: Amplification factor N for different wave frequencies (here denoted by ω_i, $i = 1, ...$) [43]

envelope at the transition location $\vec{x}_\mathrm{t}$ is called *critical N-factor* N_crit. It is assumed that the

critical amplification factor N_{crit} is independent of the flow in Ω and thus more or less universally valid for different flows. The critical amplification factor N_{crit} gets calibrated for each instability type individually (Tollmien-Schlichting instability, stationary or travelling crossflow instability, attachment line instability, and others) by means of measurements of the transition location. For example for flat plate often $N_{\mathrm{crit}}^{\mathrm{TS}} \approx 13.5$ for Tollmien-Schlichting instabilities is found [43]. The transition location of the streamline through $\vec{x}_\Omega$ is then computed as

$$\vec{x}_{\mathrm{t}}(\vec{x}_\Omega) = \underset{\tilde{\vec{x}}_\Omega \in \mathcal{S}(\vec{x}_\Omega)}{\arg} \left(\max_{f \in \mathbb{R}_0^+} N(f, \tilde{\vec{x}}_\Omega) = N_{\mathrm{crit}}\right) \forall \vec{x}_\Omega \in \Omega, \tag{2.56}$$

i.e. the location of the (first) intersection of the computed maximum amplification factor N over all frequencies with the critical amplification factor N_{crit}. The procedure is done for all instability types with the individual critical amplification factors N_{crit}. The most upstream transition location of the natural transition types is taken as the actual transition location $\vec{x}_{\mathrm{t}}$.
The advantage of the e^N-method over the local correlation-based transition modeling is that it uses linear stability analysis for the determination of the transition location $\vec{x}_{\mathrm{t}}$. Therefore, if the critical amplification factor N_{crit} is well-calibrated, the transition location $\vec{x}_{\mathrm{t}}$ due to natural transition can be predicted with high accuracy. But in some cases it is difficult to find good calibrations for the critical amplification factors N_{crit} [28]. A further disadvantage is that the e^N-method only works for natural transition. In addition, for the solution of the Navier-Stokes disturbance differential equation simplifications are introduced, for example the assumption of two-dimensionality of the external flow [43]. In case of the flow over complex three-dimensional bodies, the results of the transition location prediction may be inaccurate [28]. Furthermore, to extract boundary layer edge streamlines with the flow variables on it in order to compute the amplification factors N complicates the algorithmic parallelization of the fluid dynamics solver [18].

2.5.3 Local Correlation-Based Transition Modeling with Transition Criteria

Instead of solving instability problems, correlations for variables meaningful to transition may be used. A correlation is an equation that links certain variables and that must be calibrated by means of measurements and/or simulations. The correlations for the transition model are defined locally $\forall \vec{x}_\Omega \in \Omega$ and depend on the flow state in the domain Ω. Correlation-based transition modeling is less physics-based than the e^N-method and therefore less universally valid [32]. On the other hand, it is easier to implement into a fluid dynamics solver. In addition, it requires less expert knowledge for the practical application of the transition model [27]. In the *local correlation-based transition modeling* (LCTM) the used correlations, evaluated for a given point $\vec{x}_\Omega \in \Omega$, only depend on the local flow state in $\vec{x}_\Omega$. This implies that no integral parameters and no track of certain variables along the streamlines are used in the correlation. This is an approximation of the reality, as transition is a non-local phenomenon [43]. The LCTM has the advantage over non-local approaches that the algorithmic parallelization of the fluid dynamics solver is easier [32].
The term *transition transport modeling* (TTM) refers to the use of transport equations (convection-diffusion equations of the type of equation 2.36) for the transition model. The transient, convection and diffusion terms in the transport equations depend on the local state only (by definition of a partial differential equation). The non-local "part" of transition may be contained in the source terms of the transport equations. The source terms are often formulated correlation-based. An important part of that is the *transition criterion*. A transition criterion is a correlation between certain surface variables that holds at the transition line $\mathcal{T}$. Often the surface variables are integral

boundary layer parameters. In the context of the LCTM, these are approximated locally. Then the transition criterion is used to calculate the source term of the TTM. Note that transition criteria are independent of the concrete type of LCTM/TTM, such that it can be used for different types of LCTM/TTM. Therefore, the transition criterion is calibrated separately from the rest of the correlations involved into the transition model.
The γ-$\tilde{\mathrm{Re}}_{\theta \mathrm{t}}$ model [32] is a common instance of TTM which belongs to the LCTM. The used transition criterion is

$$\mathrm{Re}_\theta(\vec{x}_\Gamma) = f_{\mathrm{criterion},\gamma\text{-}\tilde{\mathrm{Re}}_{\theta \mathrm{t}}}(\,\mathrm{Tu}_\mathrm{e}(\vec{x}_\Gamma), \lambda_2(\vec{x}_\Gamma)\,)\ \forall \vec{x}_\Gamma \in \mathcal{T}, \tag{2.57}$$

which is a correlation of the *momentum thickness Reynolds number*

$$\mathrm{Re}_\theta(\vec{x}_\Gamma) := \frac{u_e\,\theta}{\nu_e}(\vec{x}_\Gamma) \tag{2.58}$$

to the boundary layer edge turbulence intensity $\mathrm{Tu}_\mathrm{e}(\vec{x}_\Gamma)$ and the pressure gradient parameter $\lambda_2(\vec{x}_\Gamma)$, that holds on the transition line $\mathcal{T}$. The criterion function $f_{\mathrm{criterion},\gamma\text{-}\tilde{\mathrm{Re}}_{\theta \mathrm{t}}}$ can be found in [32].
The *transition momentum thickness Reynolds number*

$$\mathrm{Re}_{\theta \mathrm{t}}(\vec{x}_\Gamma) := f_{\mathrm{criterion},\gamma\text{-}\tilde{\mathrm{Re}}_{\theta \mathrm{t}}}(\mathrm{Tu}_\mathrm{e}(\vec{x}_\Gamma), \lambda_2(\vec{x}_\Gamma))\ \forall \vec{x}_\Gamma \in \Gamma \tag{2.59}$$

is defined, which is the criterion function $f_{\mathrm{criterion},\gamma\text{-}\tilde{\mathrm{Re}}_{\theta \mathrm{t}}}$ evaluated with the *local* integral boundary layer parameters. Furthermore, the assumption

$$\mathrm{Re}_\theta(\vec{x}_\Gamma) < \mathrm{Re}_{\theta \mathrm{t}}(\vec{x}_\Gamma)\ \forall \vec{x}_\Gamma \text{ upstream of } \mathcal{T} \tag{2.60}$$

is introduced.[2] Then the integral intermittency of the boundary layer is determined by

$$\gamma_\int(\vec{x}_\Gamma) := \begin{cases} 0 & \text{if } \frac{\mathrm{Re}_\theta}{\mathrm{Re}_{\theta \mathrm{t}}}(\vec{x}_\Gamma) < 1 \\ 1 & \text{otherwise} \end{cases} \quad \forall \vec{x}_\Gamma \in \Gamma. \tag{2.61}$$

Expressed verbally: For every point $\vec{x}_\Gamma \in \Gamma$ the computed Reynolds number $\mathrm{Re}_\theta(\vec{x}_\Gamma)$ is compared to the transition Reynolds number $\mathrm{Re}_{\theta \mathrm{t}}(\vec{x}_\Gamma)$, in order to determine the integral intermittency $\gamma_\int(\vec{x}_\Gamma)$.

2.5.4 The γ-$\tilde{\mathrm{Re}}_{\theta \mathrm{t}}$ Transition Transport Model

In the LCTM, the intermittency $\gamma(\vec{x}_\Omega)$ must be defined locally $\forall \vec{x}_\Omega \in \Omega$. This is achieved by the transport equation for the intermittency γ [32]:

$$\partial_t(\rho\gamma) + \partial_j(\rho\gamma u_j) = \partial_j\left[\left(\mu + \frac{\mu^{\mathrm{turb}}}{\sigma^{(\gamma)}}\right)\partial_j\gamma\right] + P^{(\gamma)} - D^{(\gamma)} \tag{2.62}$$

The destruction $D^{(\gamma)}$ is needed to provide a relaminarization ability to the model in case of strongly accelerated flow. The equation for it as well as the model parameter $\sigma^{(\gamma)}$ can be found in the

[2] Assumption 2.60 may be justified by the fact that the computed Reynolds number $\mathrm{Re}_\theta(\vec{x}_\Gamma)$ is zero at the leading edge and usually monotonically increasing streamwise. In addition $\partial_{\mathrm{sw}}\mathrm{Re}_{\theta \mathrm{t}}(\vec{x}_\Gamma) < \partial_{\mathrm{sw}}\mathrm{Re}_\theta(\vec{x}_\Gamma)\,\forall \vec{x}_\Gamma \in \Gamma$ is usually fulfilled. Then, there is only one intersection of the streamwise distribution of the computed Reynolds number $\mathrm{Re}_\theta(\vec{x}_\Gamma)$ with the streamwise distribution of the transition Reynolds number $\mathrm{Re}_{\theta \mathrm{t}}(\vec{x}_\Gamma)$. The intersection location is claimed to be equal to the transition location $\vec{x}_\mathrm{t}$.

literature [32].
Note that the modeled intermittency γ is not a model for the real intermittency γ_{physical} but just a model variable used to find the correct modification of the k-production and k-destruction (equation 2.53). It is [32]

$$\gamma_{\text{eff}} = \max\{\gamma, \gamma_{\text{sep}}\} \tag{2.63}$$

with γ_{sep} being the intermittency in case of separation-induced transition. Its definition can be found in [32]. The modeled intermittency γ is one in the external flow, even if the external flow is laminar. And the modeled intermittency γ may be significantly larger than zero in the (physically) laminar boundary layer $\mathcal{B}_{\text{lam}}$ in order to compute the correct transition location $\vec{x}_{\text{t}}$.
In order to compute the intermittency production $P^{(\gamma)}$, equation 2.61 must be approximated locally in $\vec{x}_\Omega$. From now on, locally approximated quantities are denoted by a superscript $(\cdot)^*$. The local approximated momentum thickness Reynolds number $\text{Re}^*_\theta(\vec{x}_\Omega)$ and the local approximated transition momentum thickness Reynolds number $\text{Re}^*_{\theta\text{t}}(\vec{x}_\Omega)$ are derived in appendix D.1. Re^*_θ and $\text{Re}^*_{\theta\text{t}}$ are then used to compute the intermittency production term

$$P^{(\gamma)} = F_{\text{length}}\sqrt{\gamma F_{\text{onset}}}c_{a1}\rho S(1-\gamma c_{e1}) \tag{2.64}$$

with

$$F_{\text{onset}} = \max\{F_{\text{onset},2} - F_{\text{onset},3}, 0.0\}, \tag{2.65}$$

$$F_{\text{onset},1} = \frac{\text{Re}^*_\theta}{\text{Re}_{\text{c}}(\tilde{\text{Re}}_{\theta\text{t}})}, \tag{2.66}$$

$$F_{\text{onset},2} = \min\{\max\{F_{\text{onset},1}, F^4_{\text{onset},1}\}, 2.0\}, \tag{2.67}$$

and

$$F_{\text{onset},3} = \max\left\{1 - \left(\frac{2}{5}R^{\text{turb}}\right)^3, 0.0\right\}. \tag{2.68}$$

The definitions of the function F_{length} and the parameters c_{a1} and c_{e1} can be found in [32]. The F_{onset} function serves as a switch for the intermittency production $P^{(\gamma)}$. The switching is mainly controlled by equation 2.66, which is similar to the Reynolds number ratio $\frac{\text{Re}^*_\theta}{\text{Re}^*_{\theta\text{t}}}$ with two differences: Firstly, the *critical Reynolds number* $\text{Re}_{\text{c}}(\tilde{\text{Re}}_{\theta\text{t}})$ rather than the local approximated transition Reynolds number $\text{Re}^*_{\theta\text{t}}$ is used. The critical Reynolds number $\text{Re}_{\text{c}}(\tilde{\text{Re}}_{\theta\text{t}})$ is a function of the *transported transition momentum thickness Reynolds number* $\tilde{\text{Re}}_{\theta\text{t}}$, given in [32]. For the explanation in this paragraph it is presupposed that $\tilde{\text{Re}}_{\theta\text{t}} = \text{Re}^*_{\theta\text{t}}$. By definition of Re_{c} it is $\text{Re}_{\text{c}}(\text{Re}^*_{\theta\text{t}}) < \text{Re}^*_{\theta\text{t}}$. Thus, according to equation 2.66, the intermittency production $P^{(\gamma)}$ is triggered at a lower local approximated momentum thickness Reynolds number Re^*_θ than without the critical-to-transition ratio C. This is done because the intermittency production $P^{(\gamma)}$ must start upstream of the transition location $\vec{x}_{\text{t}}$ due to a step in the derivation of the local approximated momentum thickness Reynolds number Re^*_θ:

$$\text{Re}_\theta(\vec{x}_\Gamma) \approx \max_{y_n \in [0, \delta(\vec{x}_\Gamma)]} \text{Re}^*_{\theta,\mathcal{B}}(\vec{x}_\Gamma, y_n) \,\forall \vec{x}_\Gamma \in \Gamma \tag{2.69}$$

For all wall positions $\vec{x}_\Gamma \in \Gamma$, the local approximated transition momentum thickness Reynolds number $\text{Re}^*_{\theta,\mathcal{B}}(\vec{x}_\Gamma, y_n)$ is approximately equal to the real momentum thickness Reynolds number $\text{Re}_\theta(\vec{x}_\Gamma)$ at a certain wall normal coordinate y_n. The intermittency production $P^{(\gamma)}$ will therefore start at a point between the wall Γ and the boundary layer edge $\mathcal{E}$. The corresponding wall position

is called *critical location* $\vec{x}_\mathrm{c}$, which is upstream of the transition location $\vec{x}_\mathrm{t}$.[3] The intermittency γ increases at the location $\vec{x}_\mathrm{c} + \vec{n}(\vec{x}_\mathrm{c}) \underset{y_n \in [0, \delta(\vec{x}_\mathrm{c})]}{\operatorname{argmax}} \mathrm{Re}^*_{\theta,\mathcal{B}}(\vec{x}_\mathrm{c}, y_n)$ and gets convected downstream as well as diffused towards the wall.[4] Where the intermittency in the direct vicinity to the wall increases, the production of turbulent kinetic energy $P^{(k)}$, the eddy viscosity μ^turb, the wall shear stress τ_w, and hence the skin friction coefficient c_f increases. This defines the computed transition location according to the skin friction coefficient $\vec{x}_{\mathrm{t},c_\mathrm{f}}$.
Secondly, the transported transition momentum thickness Reynolds number $\tilde{\mathrm{Re}}_{\theta\mathrm{t}}$ rather than the local approximated transition Reynolds number $\mathrm{Re}^*_{\theta\mathrm{t}}$ is used. In the external flow this makes only a very small difference for the solution of the equations, as by construction it is

$$\tilde{\mathrm{Re}}_{\theta\mathrm{t}}(\vec{x}_\Omega) \approx \mathrm{Re}^*_{\theta\mathrm{t}}(\vec{x}_\Omega), \ \forall \vec{x}_\Omega \in \Omega \setminus \mathcal{B}. \tag{2.70}$$

Inside the boundary layer $\mathcal{B}$ equation 2.70 is false because the pressure gradient parameter λ_2 needed for equation 2.57 cannot be approximated well by using the local streamwise velocity derivative $\partial_\mathrm{sw} u(\vec{x}_\Omega) \, \forall \vec{x}_\Omega \in \Omega$. Therefore, the value from the boundary layer edge $\tilde{\mathrm{Re}}_{\theta\mathrm{t}}(\vec{x}_\Omega) \, \forall \vec{x}_\Omega \in \mathcal{E}$ shall be transported into the boundary layer $\mathcal{B}$ by convection and diffusion. This is achieved by introducing a transport equation for the transported transition momentum thickness Reynolds number $\tilde{\mathrm{Re}}_{\theta\mathrm{t}}$ [32]:

$$\partial_t(\rho \tilde{\mathrm{Re}}_{\theta\mathrm{t}}) + \partial_j(\rho \tilde{\mathrm{Re}}_{\theta\mathrm{t}} u_j) = \partial_j \left[\sigma^{(\theta\mathrm{t})} (\mu + \mu^\mathrm{turb}) \, \partial_j \tilde{\mathrm{Re}}_{\theta\mathrm{t}} \right] + P^{(\theta\mathrm{t})} \tag{2.71}$$

The $\tilde{\mathrm{Re}}_{\theta\mathrm{t}}$-production term is

$$P^{(\theta\mathrm{t})}(\vec{x}_\Omega) = c_{\theta\mathrm{t}} \frac{\rho}{\tilde{t}} (\mathrm{Re}^*_{\theta\mathrm{t}} - \tilde{\mathrm{Re}}_{\theta\mathrm{t}})(1 - F_{\theta\mathrm{t}}(\vec{x}_\Omega))(\vec{x}_\Omega), \ \forall \vec{x}_\Omega \in \Omega. \tag{2.72}$$

The model parameters $\sigma^{(\theta\mathrm{t})}$, c_θ, $\tilde{t}$ and $F_{\theta\mathrm{t}}$ can be found in the literature [32]. $F_{\theta\mathrm{t}}$ is a *blending function* that is zero approximately outside the boundary layer $\mathcal{B}$ ($P^{(\theta\mathrm{t})}$ is active) and one approximately inside it ($P^{(\theta\mathrm{t})}$ is inactive). The source term $P^{(\theta\mathrm{t})}$ acts similar to a *volume penalization*, as outside the boundary layer $\mathcal{B}$ the transported transition momentum thickness Reynolds number $\tilde{\mathrm{Re}}_{\theta\mathrm{t}}$ is forced to the value of the local approximated transition momentum thickness Reynolds number $\mathrm{Re}^*_{\theta\mathrm{t}}$. In the boundary layer $\mathcal{B}$, the forcing is switched off due to the $F_{\theta\mathrm{t}}$-function. Therefore, the transported transition momentum thickness Reynolds number $\tilde{\mathrm{Re}}_{\theta\mathrm{t}}$ is convected and diffused from the boundary layer edge $\mathcal{E}$ into the boundary layer $\mathcal{B}$.

2.5.5 Extension of the γ-$\tilde{\mathrm{Re}}_{\theta\mathrm{t}}$ Model to Transition due to Crossflow Instabilities

In the original γ-$\tilde{\mathrm{Re}}_{\theta\mathrm{t}}$ model only the following transition mechanisms were taken into account, which are two-dimensional in its nature:

- TST
- Bypass transition
- Separation-induced transition

[3] The critical location $\vec{x}_\mathrm{c}$ does not have any physical meaning but is only workaround for the γ-$\tilde{\mathrm{Re}}_{\theta\mathrm{t}}$ model to overcome the transition delay between the start of intermittency production $P^{(\gamma)}$ and the transition location $\vec{x}_\mathrm{t}$. In particular, $\vec{x}_\mathrm{c}$ is *not* the location of where the indifference Reynolds number is reached first. Also, the critical location $\vec{x}_\mathrm{c}$ has nothing to do with the length of the transition region that can be measured in experiments.

[4] Note that downstream of the critical location $\vec{x}_\mathrm{c}$ the intermittency production $P^{(\gamma)}$ is still active. In addition, it will also be activated for other wall normal coordinates than $\underset{y_n \in [0, \delta(\vec{x}_\Gamma)]}{\operatorname{argmax}} \mathrm{Re}^*_{\theta,\mathcal{B}}(\vec{x}_\mathrm{c}, y_n)$ there, as the local approximated momentum thickness Reynolds number Re^*_θ increases streamwise. This accelerates the increase of the intermittency γ in the vicinity to the wall Γ.

If CFT shall be included, a so-called *crossflow extension* of the γ-$\tilde{\mathrm{Re}}_{\theta\mathrm{t}}$ model is possible by adding a term to the intermittency production $P^{(\gamma)}$ [19]

$$P^{(\gamma)} = \left(\underbrace{F_{\mathrm{length}}\sqrt{\gamma F_{\mathrm{onset}}}}_{\text{two-dimensional transition}} + \underbrace{F_{\mathrm{length,cw}}\sqrt{\gamma F_{\mathrm{onset,cw}}}}_{\mathrm{CFT}} \right) c_{a1}\rho S(1-\gamma c_{e1}). \tag{2.73}$$

The function $F_{\mathrm{length,cw}} = 5.0$ is responsible for scaling the intermittency production $P^{(\gamma)}$ relative to the convection/diffusion intermittency transport.
$F_{\mathrm{onset,cw}}$ is formulated analogous to the corresponding term of the original model:

$$F_{\mathrm{onset,cw}} = \max\{F_{\mathrm{onset,cw},2} - F_{\mathrm{onset,cw},3}, 0.0\}, \tag{2.74}$$

$$F_{\mathrm{onset,cw},1} = \frac{\mathrm{Re}^*_\phi}{C\,\mathrm{Re}^*_{\phi,\mathrm{t}}}, \tag{2.75}$$

$$F_{\mathrm{onset,cw},2} = \min\{\max\{F_{\mathrm{onset,cw},1}, F^4_{\mathrm{onset,cw},1}\}, 2.0\}, \tag{2.76}$$

and

$$F_{\mathrm{onset,cw},3} = \max\left\{1 - \left(\frac{2}{3}R^{\mathrm{turb}}\right)^3, 0.0\right\}. \tag{2.77}$$

The concrete definitions of the Reynolds number Re^*_ϕ (placeholder ϕ) and the corresponding transition Reynolds number $\mathrm{Re}^*_{\phi,\mathrm{t}}$ depend on the used transition criterion. The *critical-to-transition ratio* $C < 1$ leads to an activation of the intermittency production $P^{(\gamma)}$ upstream of the transition location $\vec{x}_\mathrm{t}$, in the same manner as in the original model the critical Reynolds number $\mathrm{Re_c} < \mathrm{Re}^*_{\theta\mathrm{t}}$ did.

Local C1 Approach for the Crossflow Extension

The *local C1 approach* [19] is the approach of using the *C1 criterion* for CFT [3] in the γ-$\tilde{\mathrm{Re}}_{\theta\mathrm{t}}$ model. According to the C1 criterion for CFT, the relevant Reynolds number is the *crosswise displacement thickness Reynolds number*[5]

$$\mathrm{Re}_{\delta 2}(\vec{x}_\Gamma) = \frac{|\delta_2| u_\mathrm{e}}{\nu_\mathrm{e}}(\vec{x}_\Gamma),\ \forall \vec{x}_\Gamma \in \Gamma. \tag{2.78}$$

For the local C1 approach the critical-to-transition is $C = 0.75$. The C1 criterion of Arnal et al. [3] reads

$$\mathrm{Re}_{\delta 2}(\vec{x}_\Gamma) = f_{\text{criterion, C1}}(H_{12}(\vec{x}_\Gamma))\ \forall \vec{x}_\Gamma \in \mathcal{T} \tag{2.79}$$

with the criterion function

$$f_{\text{criterion, C1}}(H_{12}(\vec{x}_\Gamma)) = \begin{cases} 150.0 & \text{if } H_{12}(\vec{x}_\Gamma) \le 2.3 \\ \frac{300}{\pi}\arctan\frac{0.106}{(H_{12}(\vec{x}_\Gamma)-2.3)^{2.052}} & \text{otherwise} \end{cases} \forall \vec{x}_\Gamma \in \Gamma. \tag{2.80}$$

The C1 criterion does not take into account the effect of surface roughness. The test cases considered by Arnal et al. [3] were:

[5] Note that the crosswise displacement thickness Reynolds number $\mathrm{Re}_{\delta 2}$ is zero if the crosswise displacement thickness δ_2 is zero, even if a zero displacement thickness δ_2 does not mean that no crossflow exists. CFT can occur nevertheless [43, 27]. Thus, the crosswise displacement thickness Reynolds number $\mathrm{Re}_{\delta 2}$ may be ill-suited for the prediction of CFT in case of an S-shape of the crosswise velocity profile $u_{\mathrm{cw}}(\vec{x}_\Omega)\,\forall \vec{x}_\Omega \in \mathcal{B}$.

- a swept cylinder by Poll [47]
- ONERA D infinite swept wing by DERAT [4] and by Manie et al. [36]
- NACA 64_2A015 infinite swept wing by Boltz et al. [7]

The C1 criterion was found by evaluating the shape factor H_{12} as well as the crosswise displacement thickness Reynolds number $\mathrm{Re}_{\delta 2}$ in numerical computations of the boundary layer equations [3]. The variables were evaluated at the measured transition location $\vec{x}_\mathrm{t} \in \mathit{\Gamma}$ and subsequently a regression curve from the point cloud $\mathrm{Re}_{\delta 2,m}(H_{12,m}), m = 1, \dots, N_m$ (number of points N_m) was determined.
For the local C1 approach the Reynolds numbers and the shape factor H_{12} must be approximated locally, which is derived in appendix D.2.

Local Helicity Approach for the Crossflow Extension

A disadvatage of the local C1 approach is that it makes use of the *Falkner-Skan & Cooke* (FCS) [16, 10]equations which are good approximations of the boundary layer velocity profile $u(\vec{x}_\Omega) \forall \vec{x}_\Omega \in \mathcal{B}$ only on wing-like surfaces and swept cylinders. The *local helicity approach* [19] is applicable more generally to three-dimensional flow. It can be derived from the local C1 approach by neglection of certain terms [19]. The Reynolds number relevant for the CFT criterion is the *helicity Reynolds number*

$$\mathrm{Re}_{\mathrm{He},\mathcal{B}}(\vec{x}_\mathit{\Gamma}, y_n) = \frac{y_n^2}{\nu_\mathcal{B}(\vec{x}_\mathit{\Gamma}, y_n)} \frac{|\mathrm{He}_\mathcal{B}|}{u_\mathcal{B}}(\vec{x}_\mathit{\Gamma}, y_n) \ \forall (\vec{x}_\mathit{\Gamma}, y_n) \in \mathit{\Gamma} \times [0, \delta(\vec{x}_\mathit{\Gamma})] \tag{2.81}$$

$\mathrm{He} = \vec{u} \cdot \vec{\omega}$ is the *helicity*. Note that in general a high vorticitiy $\|\vec{\omega}\|$ is an indicator for the boundary layer $\mathcal{B}$ in contrast to the approximately inviscid external flow, which often can be well-described by potential theory, which assumes irrotational flow (vorticitiy $\vec{\omega} = \vec{0}$). In boundary layers $\mathcal{B}$ without crossflow, the vorticity vector $\vec{\omega}$ is directed perpendicular to the flow direction, i.e. the dot product $\vec{\omega}(\vec{x}_\Omega) \cdot \vec{u}(\vec{x}_\Omega) = \mathrm{He}(\vec{x}_\Omega) = 0 \ \forall \vec{x}_\Omega \in \mathcal{B}$. In contrast, the helicity He is large if and almost only if a crossflow component exists inside the boundary layer $\mathcal{B}$.
For the helicity approach the critical-to-transition ratio is $C = 0.7$.
The transition criterion reads [19]

$$\max_{y_n \in [0, \delta(\vec{x}_\mathit{\Gamma})]} \mathrm{Re}_{\mathrm{He},\mathcal{B}}(\vec{x}_\mathit{\Gamma}, y_n) = f_{\mathrm{criterion,He}}(H_{12}(\vec{x}_\mathit{\Gamma})) \ \forall \vec{x}_\mathit{\Gamma} \in \mathcal{T} \tag{2.82}$$

with the criterion function

$$f_{\mathrm{criterion,He}}(H_{12}(\vec{x}_\mathit{\Gamma})) = \max(-456.83 H_{12}(\vec{x}_\mathit{\Gamma}) + 1332.7,\ 150.0) \ \forall \vec{x}_\mathit{\Gamma} \in \mathit{\Gamma}. \tag{2.83}$$

It does not take into account the surface roughness. It was developed by taking into account simulations of the following wind tunnel experiments:

- ONERA D infinite swept wing by DERAT [4] and by Manie et al. [36]
- NLF(2)-0415 infinite swept wing by Dagenhart and Saric [11]
- 6:1 prolate spheroid by Kreplin et al. [26]

Similarly to before, the equation for the criterion was formulated by evaluating computed laminar boundary layer parameters at the transition line $\mathcal{T}$ of the experiments and then drawing a regression curve through the data points $\mathrm{Re}_{\mathrm{He,t},m} = f_{\mathrm{criterion,He}}(H_{12,m})$, $m = 1, \dots, N_m$. Again, the integral boundary layer parameters used in the transition criterion must be aproximated locally. This is derived in appendix D.3. Note that the helicity Reynolds number Re_He is already defined locally.

Therefore one approximation less has to be introduced, which is an advantage of the local helicity approach over the local C1 approach.

Langtry's Approach for the Crossflow Extension

Langtry et al. [31] model the CFT in a different manner than the local C1 or helicity approach. Instead of modifying the intermittency production term $P^{(\gamma)}$ by adding the CFT term in equation 2.73, a second source term is added to the convection-diffusion equation of the transported transition momentum thickness Reynolds number $\tilde{\mathrm{Re}}_{\theta\mathrm{t}}$:

$$P_{\mathrm{CF}}^{(\theta\mathrm{t})} = c_{\theta\mathrm{t}} \frac{\rho}{t} c_{\mathrm{CF}} \min\left\{\mathrm{Re}_{\theta\mathrm{t,CF}}^{*} - \tilde{\mathrm{Re}}_{\theta\mathrm{t}}, 0\right\} F_{\theta\mathrm{t}2} \tag{2.84}$$

The model constant is $c_{\mathrm{CF}} = 0.6$, $\mathrm{Re}_{\theta\mathrm{t,CF}}^{*}$ is the *local approximated CFT momentum thickness Reynolds number* coming from the CFT criterion given in equation 2.87, and $F_{\theta\mathrm{t}2}$ is a switch for activating the source term inside the boundary layer $\mathcal{B}$ and deactivating it outside. So the switching of $P_{\mathrm{CF}}^{(\theta\mathrm{t})}$ is reverse to the one of $P^{(\theta\mathrm{t})}$: The new production term $P_{\mathrm{CF}}^{(\theta\mathrm{t})}$ forces the transported transition momentum thickness Reynolds number $\tilde{\mathrm{Re}}_{\theta\mathrm{t}}$ to be equal to the local approximated CFT momentum thickness Reynolds number $\mathrm{Re}_{\theta\mathrm{t,CF}}^{*}$ *inside* the boundary layer $\mathcal{B}$. By doing so, according to equations 2.64 and 2.66, the intermittency production term $P^{(\gamma)}$ is triggered at lower local approximated momentum thickness Reynolds numbers Re_{θ}^{*} than without the the modification. hus the transition is moved upstream.
The CFT criterion is defined using the *non-dimensional crossflow strength*

$$H_{\mathrm{CF},\mathcal{B}}(\vec{x}_{\Gamma}, y_n) = \frac{y_n \left|\mathrm{He}_{\mathcal{B}}(\vec{x}_{\Gamma}, y_n)\right|}{u_{\mathcal{B}}^{2}(\vec{x}_{\Gamma}, y_n)}, \tag{2.85}$$

which is based on the helicity He. The non-dimensional crossflow strength H_{CF} is similar to the helicity Reynolds number $\mathrm{Re}_{\mathrm{He}}$, except the latter includes the kinematic viscosity ν and other exponents for the velocity u and the wall normal coordinate y_n in order to non-dimensionalize the helicity He.
The Reynolds number used to characterize the CFT is the momentum thickness Reynolds number Re_{θ} (equation 2.58). It is the same as for the original γ-$\tilde{\mathrm{Re}}_{\theta\mathrm{t}}$ model. Thus, it is possible to formulate the CF extension differently than in the local C1 and the local helicity approach.
Langtry's criterion [31] is[6]

$$\mathrm{Re}_{\theta\mathrm{t,CF}}(\vec{x}_{\Gamma}) = \max_{y_n \in [0, \delta(\vec{x}_{\Gamma})]} f_{\mathrm{criterion,Langtry}}\left(H_{\mathrm{CF},\mathcal{B}}(\vec{x}_{\Gamma}, y_n), \frac{h_{\mathrm{rms}}}{\theta(\vec{x}_{\Gamma})}, R_{\mathcal{B}}^{\mathrm{turb}}(\vec{x}_{\Gamma}, y_n)\right) \;\forall \vec{x}_{\Gamma} \in \mathcal{T} \tag{2.86}$$

with the criterion function

$$\begin{aligned} f_{\mathrm{criterion,Langtry}}\left(H_{\mathrm{CF},\mathcal{B}}(\vec{x}_{\Gamma}, y_n), \frac{h_{\mathrm{rms}}}{\theta(\vec{x}_{\Gamma})}, R_{\mathcal{B}}^{\mathrm{turb}}(\vec{x}_{\Gamma}, y_n)\right) &= f_{\mathrm{roughness}}\left(\frac{h_{\mathrm{rms}}}{\theta(\vec{x}_{\Gamma})}\right) + 319.51 \\ &+ f_{+}(\Delta H_{\mathrm{CF},+}(H_{\mathrm{CF},\mathcal{B}}(\vec{x}_{\Gamma}, y_n), R_{\mathcal{B}}^{\mathrm{turb}}(\vec{x}_{\Gamma}, y_n))) \\ &- f_{-}(\Delta H_{\mathrm{CF},-}(H_{\mathrm{CF},\mathcal{B}}(\vec{x}_{\Gamma}, y_n), R_{\mathcal{B}}^{\mathrm{turb}}(\vec{x}_{\Gamma}, y_n))) \\ &\forall (\vec{x}_{\Gamma}, y_n) \in \Gamma \times \mathbb{R}^{+} \end{aligned} \tag{2.87}$$

[6] For Langtry's approach [31] the local approximated CFT momentum thickness Reynolds number is $\mathrm{Re}_{\theta}^{*\mathrm{Langtry}} := \frac{\theta^{*\mathrm{Langtry}} \frac{u}{0.82}}{\nu)}(\vec{x}_{\Omega}) \forall \vec{x}_{\Omega} \in \Omega$ with the local approximated momentum thickness for Langtry's approach $\theta^{*\mathrm{Langtry}}$. This is why the factor 0.82 appears in [31]. The division of the local velocity u by 0.82 approximates the boundary layer edge velocity u_{e}, which is used in the definition of the standard momentum thickness Reynolds number Re_{θ}.

and

$$\begin{aligned}
f_{\text{roughness}}\left(\frac{h_{\text{rms}}}{\theta}\right) &= -35.088 \ln \frac{h_{\text{rms}}}{\theta}, \\
f_+(\Delta H_{\text{CF},+}(H_{\text{CF}}, R^{\text{turb}})) &= 6200 \Delta H_{\text{CF},+}(H_{\text{CF}}, R^{\text{turb}}) + 50000 \Delta H^2_{\text{CF},+}(H_{\text{CF}}, R^{\text{turb}}), \\
f_-(\Delta H_{\text{CF},-}(H_{\text{CF}}, R^{\text{turb}})) &= 75 \tanh \frac{\Delta H_{\text{CF},-}(H_{\text{CF}}, R^{\text{turb}})}{0.0125}, \\
\Delta H_{\text{CF},+}(H_{\text{CF}}, R^{\text{turb}}) &= \max(0.1066 - \Delta H_{\text{CF}}(H_{\text{CF}}, R^{\text{turb}}), 0), \\
\Delta H_{\text{CF},-}(H_{\text{CF}}, R^{\text{turb}}) &= \max(-(0.1066 - \Delta H_{\text{CF}}(H_{\text{CF}}, R^{\text{turb}})), 0), \\
\Delta H_{\text{CF}}(H_{\text{CF}}, R^{\text{turb}}) &= H_{\text{CF}} \left[1.0 + \min\left(R^{\text{turb}}, 0.4\right)\right]
\end{aligned} \tag{2.88}$$

Note that Langtry's CFT criterion includes the effect of distributed surface roughness. The root-mean-square (RMS) roughness height h_{rms} gets non-dimensionalized by the momentum thickness θ which represents the fact that the transition is the more upstream the higher the roughness is compared to the boundary layer thickness $\delta \sim \theta$.
The RMS roughness of the surface is defined as

$$h_{\text{rms}} = \sqrt{\frac{1}{|\Gamma|} \int_{\Gamma} h(\vec{x})^2 \mathrm{d}^2\vec{x}}, \tag{2.89}$$

where h is the deviation of the surface profile from the mean contour. In case the roughness is given by different parameters, these are defined, too. The *arithmetic mean roughness* is

$$h_{\text{ma}} = \frac{1}{|\Gamma|} \int_{\Gamma} |h(\vec{x})| \mathrm{d}^2\vec{x}. \tag{2.90}$$

If a sine-like roughness profile is assumed, it is $h_{\text{rms}} \approx 1.11\, h_{\text{ma}}$.[7] A third way is the *peak-to-peak-roughness* h_{p2p}, whose definition is dependent on the used standard. In [49] it was $h_{\text{rms}} \approx 0.37\, h_{\text{p2p}}$ for the painted NLF(2)-0415 infinite swept wing. In contrast, in [46] it was $h_{\text{rms}} \approx 0.15\, h_{\text{p2p}}$ for the painted *TU Braunschweig Sickle Wing*.
Unfortunately, the roughness is not known for many wind tunnel experiments. Langtry et al. [31] only had one test case (the swept NLF(2)-0415 infinite swept wing [49]) with three different known surface roughnesses h_{rms} for the calibration of the roughness function $f_{\text{roughness}}$.[8] If the surface roughness of the wind tunnel model is unknown, Langtry et al. [31] assumed a painted surface with the $h_{\text{rms}} = 3.3\,\mu\text{m}$ according to table 2.1.

Table 2.1: Root-mean-square roughnesses for different surface finishes for the NLF(2)-0415 infinite swept wing [49]

surface finish	RMS roughness h_{rms} in μm
painted	3.30
polished	0.50
highly polished	0.25

In Langtry's approach the influence of the roughness is a shift of the CFT momentum thickness Reynolds number $\text{Re}_{\theta\text{t,cf}}$. The shift is proportional to the logarithm of the RMS surface roughness

[7] That can be shown by insertiong of a sine function into the integrals of equations 2.89 and 2.90.

[8] Note that, in [49], the surface roughness $h_{\text{rms}} = 0.25\,\mu\text{m}$ for the highly polished surface finish is the measured value near the attachment line. In the midchord region the surface roughness is given as $h_{\text{rms}} = 0.10\,\mu\text{m}$, instead. This was not considered in the calibration of [31].

h_{rms}. The higher the roughness, the lower the CFT momentum thickness Reynolds number $\mathrm{Re}_{\theta \mathrm{t,CF}}$. This is independent of the other influences, i.e. the cross derivatives are zero:

$$\frac{\partial}{\partial H_{\mathrm{CF}}} \frac{\partial}{\partial h_{\mathrm{rms}}} f_{\mathrm{criterion,Langtry}}(H_{\mathrm{CF}}, \frac{h_{\mathrm{rms}}}{\theta}, R^{\mathrm{turb}}) = 0 \tag{2.91}$$

and

$$\frac{\partial}{\partial R^{\mathrm{turb}}} \frac{\partial}{\partial h_{\mathrm{rms}}} f_{\mathrm{criterion,Langtry}}(H_{\mathrm{CF}}, \frac{h_{\mathrm{rms}}}{\theta}, R^{\mathrm{turb}}) = 0. \tag{2.92}$$

This is contrary to the observations described in section 2.4.2 about the influences on CFT, but it is probably the strongest but reasonable simplification in order to take into account the surface roughness in the model in any way.
The calibration of equation 2.87 took into account the following test cases [31]:

- inclined 6:1 prolate spheroid Kreplin et al. [26]
- NLF(2)-0415 infinite swept wing by Dagenhart and Saric [11]/by Radeztsky et al. [49]
- Further NLF(2)-0415 infinite swept configurations, for which the transition location $\vec{x}_{\mathrm{t}}$ was computed by the e^N-method

Furthermore, the Langtry CFT criterion depends on the local viscosity ratio $R^{\mathrm{turb}}(\vec{x}_{\Omega})\, \forall \vec{x}_{\Omega} \in \Omega$. This does not mean that the viscosity ratio R^{turb} of the laminar boundary layer would be relevant to the transition, but is needed to prevent an additional transition delay due to the local evaluation of transition criterion [31].
In a paper by Venkatachari et al. [71] equation 2.87 has been improved to represent the experiments better. This was done because the Reynolds numbers in the paper by Radeztsky et al. [49] for the wind tunnel experiments of Dagenhart and Saric [11] appear to be offsetted to the left by $\Delta \mathrm{Re} = 0.2\,\mathrm{mio.}$ compared to the original data of Dagenhart and Saric [11]. This is probably a mistake by Radeztsky et al. [49], but the data was taken by Langtry et al. [31] for their calibration nevertheless. The second variant of Venkatachari et al. [71] is for installed configurations (in wind tunnel experiments)

$$\begin{aligned} &f_{\mathrm{criterion,Langtry}}\left(H_{\mathrm{CF}}, \frac{h_{\mathrm{rms}}}{\theta}, R^{\mathrm{turb}}\right) \\ &= f_{\mathrm{roughness}}\left(\frac{h_{\mathrm{rms}}}{\theta}\right) + 294.87 + f_{+}(\Delta H_{\mathrm{CF},+}) - f_{-}(\Delta H_{\mathrm{CF},-}) \end{aligned} \tag{2.93}$$

with

$$f_{\mathrm{roughness}}\left(\frac{h_{\mathrm{rms}}}{\theta}\right) = -31.176 \ln \frac{h_{\mathrm{rms}}}{\theta}. \tag{2.94}$$

The terms $f_{+}(\Delta H_{\mathrm{CF},+})$ and $f_{-}(\Delta H_{\mathrm{CF},-})$ are unchanged to the original formulation. The CFT momentum thickness Reynolds number $\mathrm{Re}_{\theta \mathrm{t,CF}}$ is lower for the equations of the installed configuration than for the ones for the first variant of the transition criterion which is given by Venkatachari et al. [71] for the free-air configurations. The difference in the CFT momentum thickness Reynolds number $\mathrm{Re}_{\theta \mathrm{t,CF}}$ is approximately 25, which is very small, as can be seen later in the discussion of the results for the recalibration. The calibration for the installed case is more trustworthy, as it is a fit for data coming from a test case that had a large chord length relative to the wind tunnel test section size (test case of the *NLF(2)-0415* airfoil). From now on, whenever it is referred to Langtry's criterion, the modified version of Venkatachari at al. [71] is addressed.
In appendix D.4 it is described how the CFT momentum thickness Reynolds number $\mathrm{Re}_{\theta \mathrm{t,CF}}$ is approximated locally.

3 Numerical Methods

In this chapter the numerical methods for the solution of the partial differential equations are given. First the partial differential equation problem is given in a well-posed manner, i.e. together with the boundary and initial conditions used. Then the spatial discretization is derived. Even if steady state problem are solved, a pseudo-time integration is applied. Therefore there is also a section about the (pseudo-) temporal discretization. In the end the influence of the numerical solution procedure on the results of the models is summarized.

3.1 Statement of the Numerical Problem

The system of nine non-linear convection-diffusion partial differential equations has to be solved for the unknowns, the conservative variables

$$\underbrace{\rho, \rho u_i, \rho e_\mathrm{t},\ i=\{1,2,3\}}_{\text{mean flow equations (RANS)}}, \qquad \underbrace{\rho k, \rho\omega}_{\text{turbulence model equations (SST)}} \quad , \quad \underbrace{\rho\gamma, \rho\tilde{\mathrm{Re}}_{\theta\mathrm{t}}}_{\text{transition equations } (\gamma\text{-}\tilde{\mathrm{Re}}_{\theta\mathrm{t}})} \quad . \tag{3.1}$$

The equations are 2.43, 2.62, and 2.71.[1] They are convection-diffusion equations, in other words they have the form of equation 2.36, which is repeated here:

$$\partial_t \phi(t,\vec{x}) + \partial_j \underbrace{\left(u_j \phi\right)(t,\vec{x})}_{\text{convective flux } \mathbf{F}_\mathrm{c}} = \partial_j \underbrace{d_{\phi,j}\,(t,\vec{x})}_{\text{viscous flux } \mathbf{F}_\mathrm{v}} + s_\phi(t,\vec{x}). \tag{3.2}$$

Again, ϕ is a general placeholder for some flow variables. In the following, its dependence on the time and position $(t,\vec{x}_\Omega)$ is dropped for brevity.
The flux Jacobians together with their eigendecompositions is introduced, which is exemplarily for the convective fluxes

$$\mathrm{A_c}(\boldsymbol{\phi}) = \frac{\partial \mathbf{F}_\mathrm{c}}{\partial \boldsymbol{\phi}}(\boldsymbol{\phi}) = \mathbf{T}\,\mathrm{diag}(\boldsymbol{\lambda}_\mathrm{c})\,\mathbf{T}^{-1}\,(\boldsymbol{\phi}) \tag{3.3}$$

with the matrix of the eigenvectors $\mathbf{T}$ and the vector of the eigenvalues $\boldsymbol{\lambda}_\mathrm{c}$.
Commonly, the initial condition is the freestream state

$$\phi(t=0,\vec{x}_\Omega) = \phi_\infty \ \forall (t,\vec{x}_\Omega) \in [0,T]\times\Omega. \tag{3.4}$$

Often, the solution of a previous simulation was used for the initializiation, instead. Note that in this work only steady computations are done, so the initial condition does not have any influence onto the solution of the equation system. But the numerical solution quality may be influenced by the initial condition, as a numerical pseudo-time integration is applied.
In this work the following types of boundaries are needed:

[1] Note that in the fluid dynamics solver *TAU* the variables are nondimensionalized through division by some reference quantites, for example the freestream values and/or a the chord length c. By doing so, it is achieved that the values for the nondimensional variables have approximately the same order of magnitude, which increases the accuracy of the computation as the numbers are processed only with a finite number of digits.

Farfield boundaries for freestream boundaries Γ_{FF} serve as the in-/outflow of the domain Ω:

$$\begin{aligned} &\nabla(\cdot)(\vec{x}) = \mathbf{0}, \;\; \boldsymbol{\Delta r}_{\mathrm{entering}}(\vec{x}) = 0, \\ &(\rho, \vec{u}, p, k, \omega, \gamma, \tilde{\mathrm{Re}}_{\theta \mathrm{t}})(\vec{x}) = (\rho, \vec{u}, p, k, \omega, \gamma, \tilde{\mathrm{Re}}_{\theta \mathrm{t}})_\infty, \;\; \forall \vec{x} \in \Gamma_{\mathrm{FF}} \end{aligned} \tag{3.5}$$

$\boldsymbol{\Delta r}_{\mathrm{entering}}$ is the vector of the charateristic variable pertubations of the characteristics of the convective fluxes that are pointing into the domain Ω. The condition is achieved by computing the eigendecomposition of the convective flux Jacobian at the boundary, setting the corresponding entries of the vector of the eigenvalues $\boldsymbol{\lambda}_{\mathrm{c}}$ in equation 3.3 to zero, and transforming back. The freestream state of the primitive variables is

$$\begin{pmatrix} \rho_\infty \\ \vec{u_\infty} \\ p_\infty \\ k_\infty \\ \omega_\infty \\ \gamma_\infty \\ \tilde{\mathrm{Re}}_{\theta \mathrm{t}, \infty} \end{pmatrix} = \begin{pmatrix} \rho_\infty \\ \vec{u_\infty} \\ p_\infty \\ \frac{3}{2}(\mathrm{Tu}_\infty \, u_\infty)^2 \\ \frac{\rho_\infty k_\infty}{R_\infty^{\mathrm{turb}} \mu(T_\infty)} \\ 1.0, \\ f_{\mathrm{criterion}, \gamma\text{-}\tilde{\mathrm{Re}}_{\theta \mathrm{t}}}(\mathrm{Tu}_\infty, \lambda_2 = 0) \end{pmatrix} \tag{3.6}$$

with the freestream density ρ_∞, velocity $\vec{u}_\infty$, pressure p_∞, temperature T_∞, turbulence intensity Tu_∞, and viscosity ratio R_∞^{turb}. These values are specified by the user.

Symmetry boundaries Γ_{sym} are present when only a part of a flow is calculated, that contains symmetry planes:

$$\partial_n(\cdot)(\vec{x}) = 0, \;\; u_n(\vec{x}) = 0 \; \forall \vec{x} \in \Gamma_{\mathrm{symm}} \tag{3.7}$$

In addition, to conserve the momentum $\rho\vec{u}$ and total energy e_{t} at the symmetry plane during the time integration, the pressure at the wall is increased appropriately to compensate the momentum and kinetic energy losses due to the substraction of the wall normal component of the velocity u_n in each timestep [12].

Adiabatic no-slip walls Γ are used for body surfaces:

$$\begin{pmatrix} \vec{u} \\ k \\ \omega \end{pmatrix}(\vec{x}) = \begin{pmatrix} \vec{0} \\ 0 \\ \frac{60.0 \mu(\vec{x})}{\beta^{(\omega)} \rho(\vec{x}) \, d_1(\vec{x})^2} \end{pmatrix}, \;\; \partial_n \begin{pmatrix} T \\ \gamma \\ \tilde{\mathrm{Re}}_{\theta \mathrm{t}} \end{pmatrix}(\vec{x}) = \begin{pmatrix} 0 \\ 0 \\ 0 \end{pmatrix} \;\; \forall \vec{x} \in \Gamma \tag{3.8}$$

The model constant $\beta^{(\omega)}$ of the k-ω-Menter-SST-model is used for the boundary condition of the specific turbulent dissipation rate ω, which has a value dependend on the distance of the first grid point above the wall d_1. This is needed because theoretically the value should be set to infinity [12].

Adiabatic free-slip walls Γ_{inv} are applied for wind tunnel walls:

$$\begin{aligned} &\text{same conditions as for adiabatic no-slip walls } \Gamma \text{ (except for } \vec{u}), \\ &\vec{u} \cdot \vec{n}(\vec{x}) = 0 \; \forall \vec{x} \in \Gamma_{\mathrm{inv}} \end{aligned} \tag{3.9}$$

Equation 3.9 is applied for wind tunnel walls because the boundary layer on it is irrelevant in most experiments. In addition, the wind tunnel walls are often shaped diverging such that the

flow between the wind tunnel wall boundary layers can be taken as the flow domain Ω with a streamwise constant cross-section:

3.2 Spatial Discretization

The spatial discretization of the equations 3.2 is done by the *finite volume method*. Its advantages are that unstructured grids can be used, non-smooth and even discontinuous solutions are possible, and the convective term is discretized without numerical dissipation.
First, the equations 3.2 are rewritten into the form

$$\partial_t \int_{\omega_c} \phi \, \mathrm{d}^3\vec{x} + \int_{\partial\omega_c} (\phi \, u_j) n_{\mathrm{c},j} \, \mathrm{d}^2\vec{x} = \int_{\partial\omega_c} d_{\phi,j} n_{\mathrm{c},j} \, \mathrm{d}^2\vec{x} + \int_{\omega_c} s_\phi \, \mathrm{d}^3\vec{x}, \; c = 1, \ldots, N_c \tag{3.10}$$

which is the more general *Reynolds transport theorem*. $\omega_c \subseteq \Omega$ is a control volume/grid cell/element (index $(\cdot)_c$ specifies the element) that has the outward pointing unit normal vector $\vec{n}_c$. The elements are an admissible decomposition of $\Omega = \bigcup_{c=1}^{N_c} \omega_c$, i.e. a grid/mesh of the flow domain. In *TAU*, the *dual-mesh*/vertex-centered approach is used, which means that from the user-given mesh a so-called dual-mesh is computed, whose cells have their midpoints at the nodes of the original mesh.
The boundary of the control volume is written as the union of its $N_{c,f}$ parts $\gamma_{c,f}$ (index f stands for the face). The faces are assumed to be planar. Then, an integral over the boundary $\partial\omega_c$ of the control volume can be written as

$$\int_{\partial\omega_c} \phi \, \mathrm{d}^2\vec{x} = \sum_{f=1}^{N_{c,f}} \int_{\gamma_{c,f}} \phi \, \mathrm{d}^2\vec{x}, \; \forall c \in \{1, \ldots, N_c\}. \tag{3.11}$$

The midpoint rule of numerical integration is used, which is for example for the set ω_c

$$\int_{\omega_c} \phi(\vec{x}) \, \mathrm{d}^3\vec{x} \approx \phi_c \, |\omega_c|, \; \forall c \in \{1, \ldots, N_c\}. \tag{3.12}$$

ϕ_c is the value at the centroid of the cell ω_c. It follows

$$\partial_t \phi(\vec{x}_{\bar{\omega}_c}) = s_{\phi,c} - \frac{1}{|\omega_c|} \sum_{f=1}^{N_{c,f}} (\phi \, u_j - d_{\phi,j})_{c,f} \, n_{c,j} \, |\gamma_{c,f}|, \; \forall c \in \{1, \ldots, N_c\}. \tag{3.13}$$

In equation 3.13 the link between the element centroid ϕ_c and the element face midpoint values $\phi_{c,f}$, which is called *solution reconstruction*, is missing, which couples the N_c equations. For the mean flow equations, the *central scheme* with the average of fluxes is used, which states (ϕ is a placeholder for a flux)

$$\phi_{c,f} \approx \frac{1}{2} [\phi_\mathrm{L} + \phi_\mathrm{R}] + D_{\mathrm{L,R}}^{\text{art. diss.}}, \tag{3.14}$$

where the indices L and R indicate the midpoint values of the two (left and right) elements that share the face $\gamma_{c,f} = \partial\omega_\mathrm{L} \cap \partial\omega_\mathrm{R}$. The central scheme has a consictency order of two on an optimal mesh (connection line between the cell midpoints of two adjacent cells is perpendicular to the shared cell face) [6]. An artificial dissipation term

$$D_{\mathrm{L,R}}^{\text{art. diss.}} = c_{\mathrm{L,R}}^{\text{art. diss.}} [\varepsilon_2 [\phi_\mathrm{R} - \phi_\mathrm{L}] - \varepsilon_4 [L(\phi_\mathrm{R}) - L(\phi_\mathrm{L})]] \tag{3.15}$$

is added, which introduces a small dissipation based on approximations of the second and forth order gradients of $\phi_{c,f}$. This is needed to make the numerical scheme stable, as otherwise a generation of two independend numerical solutions may occur by odd-even-decoupling [6]. The operator $L(\cdot)$ is similar to a numerical Laplace-operator. ε_2 and ε_4 are the second and forth order dissipation coefficients. They are dependend on two user-defined coefficients, which are set to $k_1 = \frac{1}{2}$ and $k_2 = \frac{1}{64}$ in this work [6]. The artificial dissipation coefficient $c_{\mathrm{L,R}}^{\mathrm{art.\ diss.}}$ is roughly equal to the maximum eigenvalue $\max \boldsymbol{\lambda}_{\mathrm{c}}$ of the convective flux Jacobian $\mathrm{A_c}(\boldsymbol{\phi})$ (*scalar dissipation*), such that in the equations of all the conservative variables the same artificial dissipation coefficient is active. Alternatively, it is different for each characteristic variable (*matrix dissipation*). Then the second and forth order gradient approximations, when tranformed into the charateristic variables, are scaled for each of them individually by the magnitude of the corresponding entry of the vector of eigenvalues $\boldsymbol{\lambda}_{\mathrm{c}}$ of the convective flux Jacobian $\mathrm{A_c}(\boldsymbol{\phi})$. The matrix dissipation introduces less dissipation than the scalar dissipation and is therefore more accurate [6] and used in this work whereever possible. Nevertheless, the numerical solution of some simulations diverges, if initialized with freestream conditions and using the matrix dissipation. In these cases it helps to use the scalar dissipation for a few thousand iterations, after which it is switched back to the matrix dissipation. The central scheme is used only for the mean flow equations, as the artificial dissipation was developed for these. For the turbulence and transition equations, the second-order *upwind-scheme of Roe* [50] is used, which states

$$\phi_{c,f} \approx \frac{1}{2}\left[\tilde{\phi}_{\mathrm{R},f} + \tilde{\phi}_{\mathrm{L},f} - \mathbf{A}_{\mathbf{c}}^{\mathrm{Roe}}(\tilde{\phi}_{\mathrm{R},f}, \tilde{\phi}_{\mathrm{L},f})\,(\tilde{\phi}_{\mathrm{R},f} - \tilde{\phi}_{\mathrm{L},f})\right],\ c = 1, \dots, N_c, \tag{3.16}$$

where $\tilde{\phi}_{\mathrm{R},f}$ and $\tilde{\phi}_{\mathrm{L},f}$ are approximations of the state at the face as computed from the element midpoint value and gradient of the left or right element, respectively:

$$\tilde{\phi}_{c,f} = \phi_c + \psi_c\, \nabla\phi_c \cdot (\vec{x}_{c,f} - \vec{x}_c),\ \forall f \in \{1, \dots, N_{c,f}\}\ \forall c \in \{1, \dots, N_c\} \tag{3.17}$$

The limiter ψ_c ensures stability of the solution at shocks, because the solution reconstruction 3.17 may lead to overshoots at very steep gradients of flow variables. The limiter is formulated in a way that the face value $\tilde{\phi}_{c,f}$ does not exceed both the average of the cell value ϕ_c and the maximum value of the cell midpoints of all neightbor cells of ω_c (the same holds with the minimum, that must not be subceeded).
The *Roe-matrix* $\mathbf{A}_{\mathbf{c}}^{\mathrm{Roe}}(\tilde{\phi}_{\mathrm{R},f}, \tilde{\phi}_{\mathrm{L},f}) = \mathbf{A_c}(\phi^{\mathrm{Roe}}(\tilde{\phi}_{\mathrm{R},f}, \tilde{\phi}_{\mathrm{L},f}))$ is the convective flux Jacobian $\mathbf{A_c}$ evaluated with the so-called *Roe-averaged variables* $\phi^{\mathrm{Roe}}(\tilde{\phi}_{\mathrm{R},f}, \tilde{\phi}_{\mathrm{L},f})$ instead of the unknown primitive ones $\phi_{c,f}$, for example

$$\rho^{\mathrm{Roe}}(\rho_{\mathrm{l}}, \rho_{\mathrm{r}}) = \sqrt{\rho_{\mathrm{l}}\rho_{\mathrm{r}}}. \tag{3.18}$$

In equations 3.13 for the diffusive flux $d_{\phi,j}$ and for the upwind solution reconstruction 3.17 gradients are needed in the cell midpoints. They are computed by the *Green-Gauss theorem* and the midpoint rule approximation as [6]

$$\nabla\phi_c = \frac{1}{|\omega_c|}\sum_{f=1}^{N_{c,f}} \phi_{c,f}\ \vec{n}_{c,f}\,|\gamma_{c,f}|,\ c = 1, \dots, N_c. \tag{3.19}$$

Dirichlet boundary conditions can be set directly in the central-scheme 3.14 or upwind-scheme 3.16 by overwriting the left/right state. Neumann boundary conditions can be set directly by overwriting the gradients in equation 3.19. For the farfield boundary, the convective fluxes are computed by

the Roe-upwind scheme with the Roe-averaged variables coming from the boundary-adjacent cell and the farfield-state $(\cdot)_\infty$ while setting the appropriate entries of the vector of eigenvalues to zero according to equation 3.5. [12]
Now the system 3.13, which is a system of ordinary differential equations in time t, can be solved numerically by any ordinary differential equation solver. It is written in a shorter form as

$$\frac{\mathrm{d}}{\mathrm{d}t}\boldsymbol{\phi}(t) = -\mathbf{R}_\Omega(\boldsymbol{\phi}(t)) \tag{3.20}$$

with the the *vector of the conservative variables* $\boldsymbol{\phi}$ and the *residual* of the spatial discretization $\mathbf{R}_\Omega$.

3.3 Temporal Discretization

In this work only steady state problems ($\partial_t(\cdot) = 0$) are solved and therefore no temporal discretization is needed. But in order to speed up the computation of the steady solution by certain acceleration techniques, the steady state problem is transformed into an unsteady one by introduction of the pseudo-time t^*:

$$\frac{\mathrm{d}}{\mathrm{d}t^*}\boldsymbol{\phi}(t^*) = -\mathbf{R}_\Omega(\boldsymbol{\phi}(t^*)) \stackrel{!}{=} \mathbf{0} \tag{3.21}$$

This ordinary differential equation is solved approximately by the second-order backward Euler method, whose iteration rule reads

$$\frac{\boldsymbol{\phi}^{n+1} - 4\boldsymbol{\phi}^n + \boldsymbol{\phi}^{n-1}}{2\Delta t^*} + \mathbf{R}_\Omega^{n+1} := \mathbf{R}_{t^*}^{n+1} \stackrel{!}{=} \mathbf{0}, \tag{3.22}$$

where the superscript $n+1$ stands for the next pseudo-timestep number and Δt^* is the pseudo-timestep size. $\boldsymbol{\phi}^n$ and $\boldsymbol{\phi}^{n-1}$ are known from the current and the previous pseudo-timestep. The implicit formulation allows unconditionally large pseudo-timesteps Δt^* at the price of higher computational effort. The needed change $\boldsymbol{\delta\phi}^n$ such that $\boldsymbol{\phi}^{n+1} = \boldsymbol{\phi}^n + \boldsymbol{\delta\phi}^n$ and $\mathbf{R}_{t^*}^{n+1} = \mathbf{0}$ is found by solving the system of linear equations (Newton-method)

$$\frac{\partial \mathbf{R}_{t^*}^n}{\partial \boldsymbol{\phi}^n}\,\boldsymbol{\delta\phi}^n = -\mathbf{R}_{t^*}^n \tag{3.23}$$

by the iterative *lower-upper symmetric Gauss-Seidel* method (LUSGS). Herefore, the *multigrid* technique is used, which helps to reduce large wavelength contributions to the residual (*defect*) $\mathbf{R}_{t^*}^n$: After some iterations n of the LUSGS solver the defect is restricted to a coarser grid $\mathbf{R}_{t^*\mathrm{coarser}}^n$. On it, the *defect equation*

$$\frac{\partial \mathbf{R}_{t^*}^n}{\partial \boldsymbol{\phi}_{\mathrm{coarser}}^n}\,\boldsymbol{\delta\delta\phi}_{\mathrm{coarser}}^n = -\mathbf{R}_{t^*\mathrm{coarser}}^n \tag{3.24}$$

is solved iteratively for some iterations before passing on the *defect of the defect equation* the next coarser grid and so on until the coarsest grid, on which the solution $\boldsymbol{\delta\delta\phi}_{\mathrm{coarsest}}^n$ is computed until convergence. It is then prolongated back to the finest grid by interpolation and added to the intermediate solution of the current pseudo-timestep. In this work, for the turbulence and transition equations *no* multigrid is used, which is known to increase the stability of the scheme [13]. In addition, in the first 100 to 256 pseudo-timesteps no multigrid at all is used, which increases the stability due to the large temporal derivatives in the beginning of the simulation. After these *startup singlegrid iterations*, the "4w"-multigrid scheme was used.
The pseudo-timestep size Δt^* is chosen for each cell (index c) individually (local time-stepping) by

the *CFL-criterion* as

$$\Delta t_c^* = \mathrm{CFL} \min \left\{ \frac{1}{\tilde{\lambda}_{\mathrm{c,max}}(\vec{x}_{\omega_c})}, \frac{K_\mathrm{v} \left|\omega_c\right|}{\tilde{\lambda}_\mathrm{v}(\vec{x}_{\omega_c})} \right\} \tag{3.25}$$

with the scaled approximated maximum eigenvalue $\tilde{\lambda}_{\mathrm{c,max}}$ of the convective flux Jacobian. It is similar to the surface integral of the sum of the velocity and the speed of sound over the boundary of the control volume ω_c. The scale factor is $K_\mathrm{v} = 0.25$ and $\tilde{\lambda}_\mathrm{v}$ is the approximated maximum eigenvalue of the viscous flux Jacobian (which is similar to the "propagation speed" of the diffusion of the conserved quantities). The CFL number is user-chosen.
To additionally accellarate convergence, residual smoothing is used: The change in the vector of unknowns $\boldsymbol{\delta\phi}^n$ is spatially smoothed before addition to the old field $\boldsymbol{\phi}^n$.
Many simulations in this work have a low Mach number $\mathrm{Ma}_\infty < 0.3$ (essentially incompressible flow). The interesting physical phenomena happen significantly slower than the speed of sound a, or, in other words, the difference between the maximum and the minimum eigenvalue of the convective flux Jacobian $\mathrm{A_c}$ becomes large, which reduces the accuracy of the pseudo-time-integration (equation 3.21). Therefore, a preconditioning of equation 3.21 is used for the mean flow equations, in which a preconditioner matrix $\mathbf{P}(\boldsymbol{\phi})$ is multiplied only to the right-hand-side of equation 3.21. This is allowed because the pseudo-transient term on the left-hand-side has no physical meaning and will be zero for the converged steady-state solution anyway. The task of the preconditioner matrix $\mathbf{P}(\boldsymbol{\phi})$ is to scale the eigenvalues of the convective flux Jacobian to be of the same order of magnitude and much smaller than the largest unpreconditioned eigenvalue before, which increases the convective timestep size according to equation 3.25. Hereby, the artificial dissipation $D_{\mathrm{L,R}}^{\mathrm{art.\ diss.}}$ of the central scheme (equation 3.14) is scaled by the inverse of the preconditioning matrix $\mathbf{P}(\boldsymbol{\phi})$ in order to let it be unaffected by the preconditioning, as the scheme shall be as less dissipative as possible. The preconditioner used in this work is

$$\mathbf{P}(\boldsymbol{\phi}) = \begin{pmatrix} 1+\zeta_1 & \zeta_2 u_1 & \zeta_2 u_2 & \zeta_2 u_3 & -\zeta_2 \\ \zeta_1 u_1 & 1+\zeta_2 u_1^2 & \zeta_2 u_1 u_2 & \zeta_2 u_1 u_3 & -\zeta_2 u_1 \\ \zeta_1 u_2 & \zeta_2 u_1 u_2 & 1+\zeta_2 u_2^2 & \zeta_2 u_2 u_3 & -\zeta_2 u_2 \\ \zeta_1 u_2 & \zeta_2 u_1 u_2 & \zeta_2 u_2 u_3 & 1+\zeta_2 u_3^2 & -\zeta_2 u_3 \\ \frac{a^2 \zeta_0 \zeta_1}{\tilde{\gamma}-1} & \zeta_0 \zeta_3 u_1 & \zeta_0 \zeta_3 u_2 & \zeta_0 \zeta_3 u_3 & 1-\zeta_0 \zeta_3 \end{pmatrix} \tag{3.26}$$

with the abbreviations ζ_0, to ζ_3, which are terms involving the local velocity u, the local Mach number Ma, and the user-chosen *spatial cutoff-value* $K_{\mathrm{spatial}} = 1.0$, which is the recommended value for a Mach number-independent numerical pseudo-time-integration [12]. The matrix of equation 3.23 (the Jacobian of the residual with respect to the unknowns) is also preconditioned. The amount of predcondition in that equation is controlled by the user-chosen *general cutoff-value*, which is chosen as $K_{\mathrm{general}} = 1.0, \ldots, 2.0$ depending on the test case. In constrast to the spatial cutoff-value K_{spatial}, the general cutoff-value K_{general} does not influence the accuracy of the numerical solution of ordinary differential equation 3.21 but only the convergence of the iterative solution of the linear system 3.23 solved for the implicit timestepping.

3.4 Requirements for an Accurate Numerical Solution

For simulations based on transition criteria it is important that the variables appearing in the equations of the transition criteria (pressure gradient parameter λ_2, turbulence intensity Tu, momentum thickness Reynolds number Re_θ, shape factor H_{12}, crosswise displacement thickness

Reynolds number $\mathrm{Re}_{\delta 2}$, helicity Reynolds number $\mathrm{Re}_{\mathrm{He}}$) are computed accurately. This breaks down to the accurate computation of the boundary layer velocity profiles $u(\vec{x}_\Omega) \forall \vec{x}_\Omega \in \mathcal{B}$.
An accurate spatial discretization needs an appropriate grid/mesh resolution. The creation of the grids was not part of this work, but they were reused from old works where it was proven that the grids are good enough by grid convergence studies. A grid is good enough, if the relevant result parameters (for example the integral boundary layer properties or the transition location) do not change notably with an uniform refinement of the grid. Such grids usually yield a fine resolution of the boundary layer $\mathcal{B}$ in wall normal direction (at least approximately 80 points) and the entire boundary layer $\mathcal{B}$ is covered in structured grid in case of a hybrid mesh. The first node above the surface Γ should be at a non-dimensional wall normal coordinate of $y^* < 1$, such that at least three nodes are located in the viscous sublayer of the boundary layer $\mathcal{B}$. These rules for a good mesh are only valid if a second order spatial discretization is used (as in this work with the central scheme and the second-order Roe scheme), which is common for the finite volume method on unstructed grids.
In addition, it is required to get a good convergence of the iterative numerical solution of equation 3.21. As different available grids are tried out for the present work it can be stated that the solver converges best with a structured O-grid for the boundary layer. A simulation is seen as converged if on the one hand the computed lift coefficients c_L and drag coefficients c_D change relatively by less than 10^{-5} in the last few thousand pseudo timesteps. Especially the drag coefficient c_D must have converged, as this implies that the transition location converged. On the other hand the residuals $\mathbf{R}(\boldsymbol{\phi})$ of the equations shall have dropped enough. The latter is determined by the number of orders of magnitude the spatial RMS (RMS) of the residuals $\mathbf{R}(\boldsymbol{\phi}(t^*))$ dropped relative to the initial value of $\mathbf{R}(\boldsymbol{\phi}(t^* = 0))$. The residual of the ρk-equation is always the one dropping the least. In the first few hundred iterations it increases strongly. This is due to the increase of the turbulent kinetic energy k in the boundary layer $\mathcal{B}$ which did not exist in the initial condition equation 3.4. To take the computation as converged, the RMS ρk-residual must have dropped from its maximum by more than three orders of magnitude. For two-dimensional simulations usually a drop by more than five orders of magnitude is possible.
In general, the results of numerical computations must be verified and validated before they are trustworthy [22]. In the *verification* it is checked that the solver yields the results that are expected from the implemented model, independent of the accuracy of this model. The *TAU* solver was already extensively verified [30]. When new correlations are implemented for this thesis, it is assumed that no additional verification is necessary. In the *validation* it is checked whether the solver yields results that match corresponding measurements. The major way to validate the simulations in this work is the comparison of the computed pressure coefficient c_p^{CFD} distributions with the measured ones c_p^{exp}, which are commonly given in the papers of the measurements. If no pressure coefficient c_p^{exp} distribution was measured in the experiments, the measured lift coefficient c_L^{exp} may be given in order to check the correct lift L computation.

4 Definition of Calibration Test Cases

In this chapter the test cases are presented that serve as a basis of the assessment and calibration work. It prepares for chapter 5 about the assessment of the CFT criteria.
The rules for the selection of configurations within the test cases that probably feature CFT are explained. The proceeding is described for the case that in the literature about the experiments no full information about the reference conditions of the wind tunnel is given. General rules for the determination of the simulation domain Ω are given. Afterwards, for each test case the experimental and the numerical setups are described. For most of the test cases the measured and simulated pressure coefficient c_p distributions are compared in order to verify that the angle of attack α is set appropriately and in order to validate the mean flow results.

4.1 Identification of Appropriate Test Cases

4.1.1 Selection of Test Cases

The following test cases are taken into account as reference for the recalibration work:
Two-dimensional:

- ONERA D infinite swept wing by Manie et al. [36]
- NLF(2)-0415 infinite swept wing by Dagenhart and Saric [11]/Radeztsky et al. [49]
- NACA 64_2A015 infinite swept wing by Boltz et al. [7]
- HQ26N/14.82 infinite swept wing by Seitz [61]
- infinite swep cylinder by Poll [47]

Three-dimensional:

- TELFONA Pathfinder wing by Streit et al. [67]
- Inclined 6:1 prolate spheroid by Kreplin et al. [26]
- TU Braunschweig Sickle wing by Petzold and Radespiel [46]

It is good to have as many test cases with reliably measured transition locations as possible, in order to make the most general transition criterion formulation possible. In addition, the scatter of correlations of the boundary layer parameters over different test cases can be evaluated. This scatter is present because of uncertainties of the measurements, the differences in the setups of the measurements and the simulation (for example slightly different reference conditions or test-section and wing geometry), and the assumptions made in order to allow a formulation of the CFT criterion (see section 2.5.5).
For each test case the sets of reference conditions, sweep angles Λ and angles of attack α were selected that have a high probability of featuring CFT. The following positive indications are applied to identify a CFT case:

- The authors of the measurements explictely identify the case as featuring CFT.
- The transition visualization images show a zig-zag-shaped transition front. This likely correspond to stationary crossflow vortices.
- Computations with the e^N method done by researchers show a dominating crossflow instability amplification factor N^{CF} at the transition line in comparison to the Tollmien-Schlichting instability amplification factor N^{TS}.

- The measured transition location $\vec{x}_\mathrm{t}$ changes strongly with the sweep angle Λ (if a variation of the sweep angle Λ was carried out).

The following negative indications are applied to identify cases that shall not be taken into account for the recalibration work:

- The pressure gradient at the transition location is adverse, what makes TST likely.
- After performing a simulation, the skin friction coefficient c_f is negative at the transition location, which is a sign for separation-induced transition.
- When trying to simulate the case as a steady state problem, no convergence could be achieved due to a laminar separation bubble or a turbulent flow separation somewhere on the wall Γ.

4.1.2 Identification of the Wind Tunnel Test Conditions

The freestream state must be set for the farfield boundary condition. For the mean flow this needs exactly three parameters, from which at least one contains information about the velocity u. Often, the freestream Reynolds number Re_∞, Mach number Ma_∞ and static temperature T_∞ are set together with the freestream direction. For many test cases, the problem arises that only less than three reference state variables are given in the papers. Then the freestream static temperature is assumed to be $T_{\infty,\mathrm{assumption}} = 300\,\mathrm{K}$. By that, it is assumed to have a closed-loop wind tunnel without cooling or an open wind tunnel with relatively warm environment air. According to equation 2.10, only the Reynolds number Re_∞ and the Mach number Ma_∞ are important for the aerodynamic problem, which justifies the assumption of a value for the freestream temperature T_∞. If the freestream turbulence intensity is not given, $\mathrm{Tu}_{\infty,\mathrm{assumption}} = 0.1\%$ is assumed, which is a medium-low value. This is justified by the fact that at such low turbulence intensity Tu_∞ the stationary crossflow instabilities should be dominant over the travelling. As reasoned in section 2.4 about transition theory, for aircraft flows the stationary crossflow instability is relevant due to the extremely low freestream turbulence intensity Tu_∞. Beyond the decision between stationary and travelling crossflow instabilities the turbulence intensity Tu_∞ is assumed to be irrelevant for the CFT location. This is why a value for Tu_∞ is assumed rather than letting the corresponding cases out completely.
The freestream viscosity ratio R_∞^turb is usually not measured. Therefore, the recommended value of $R_{\infty,\mathrm{assumption}}^\mathrm{turb} = 1.2$ is set [13]. According to the recommandation of [65] this corresponds to a freestream Reynolds number of $\mathrm{Re}_\infty = 6 \cdot 10^6$.
If no surface roughness data for the wind tunnel model is available, a painted surface is assumed, which corresponds to a RMS surface roughness height of $h_\mathrm{rms} = 3.3\,\mu\mathrm{m}$ [31].

4.1.3 Specification of the Simulation Domain

The flow domain Ω is chosen as small as possible to save computational effort, but as large/complex as necessary to correctly model the aerodynamics.
The test cases were simulated with *two-dimensional* setups whereever possible. This means that perpendicular to the grid the spatial derivatives of all variables are assumed as zero. The grid then contains only the airfoil which is a cross section of the imaginary infinite rectangular wing normal to the leading edge, and the upper and lower wind tunnel walls. In the experiments, the wing has a finite aspect ratio and there are wind tunnel walls that interact with the flow (if not shaped according to the streamlines by end-liners). Therefore, it must be proven that at least in the midsection of the real wing the spanwise derivatives of the flow variables are negligible small. The

longer the wing, i.e. the higher the aspect ratio, the better the assumption in the inner sections.
Even further simplification is possible in certain cases by *omitting the upper and lower wind tunnel walls* (called *free-air condition*). This approach has the advantage that for different angles of attack in the experiment no separate grids are needed with airfoils rotated relative to the upper and lower wind tunnel walls. Of course, it must be ensured that the pressure coefficient c_p distribution is still valid with respect to the experiments. For that, the angle of attack α has to be corrected. In wind tunnels wings at a given angle of attack α perform generally worse than in free air, because the streamwise-straight upper and lower wind tunnel walls force the streamlines far away from the wing to be directed closer to the freestream-direction (potential effect). In order to get a similar pressure coefficient c_p distribution in a wind tunnel as in free air, the angle of attack α in the wind tunnel has to be larger than in free air. The angle of attack α correction for the free-air configurations is found by trial and error.
Furthermore, because the surface roughness is not taken into account in the computations of the RANS equations with the SST model, it is assumed that the surface under the turbulent boundary layer $\mathcal{B}$ is entirely hydraulically smooth. As the focus of this work is on the laminar boundary layer, the influence of that is expected to be low. In contrast, in the laminar boundary layer the surface roughness has an important effect on the CFT (see section 2.4). But this is effect is modeled by adapting the CFT criteria rather than modifying the corresponding boundary of the simulation domain.

4.2 Description of the Test Cases

4.2.1 ONERA D Infinite Swept Wing

Experimental Setup

The airfoil normal to the leading edge is the ONERA D [36]. It is a symmetric low-speed airfoil with a relatively large leading edge radius and a "peaky" nature towards the trailing edge [36].
The wing of the experiments [36] was a rectangular variable sweep wing of normal chord length $c_n = 0.3\,\mathrm{m}$ and unswept aspect ratio of 2.7. It had a tip extension appended to it, in order to reduce the invoking of three-dimensional flow.
The wind tunnels of the experiments were called "S1Ca" (pressure-measurement) and "S2Ch" (transition location measurement). Both were of type "Eiffel", which means they were unpressurized, open and the blower it located downstream of the test section. This has the consequence that the test section freestream flow had the ambient pressure form outside the wind tunnel (resting air) as total pressure $p_{0,\infty} = 1\,\mathrm{atm}$. The test section was circular with a diameter of $D_{\mathrm{WT}} = 10c_n$.
The pressure measurements were done for the sweep angles $\Lambda/^\circ \in \{0, 15, 35, 45, 55\}$ and normal freestream velocity $u_{n,\infty} = 20\,\frac{\mathrm{m}}{\mathrm{s}}$. Other reference conditions are not given in [36]. It is assumed that the missing freestream conditions are the same as for the transition measurements with the freestream normal velocity $u_{n,\infty} = 20\,\frac{\mathrm{m}}{\mathrm{s}}$. For the transition measurements the freestream normal velocity $u_{n,\infty}/\frac{\mathrm{m}}{\mathrm{s}} \in \{20, 30, 40, 50, 70\}$ and Reynolds number based on the normal chord length and the normal velocity $\mathrm{Re}_\infty^{c_n,u_n}/10^6 \in \{0.4, 0.6, 0.8, 1.0, 1.5\}$ are given. That the latter is based on the normal velocity $u_{n,\infty}$ is not reported explicitely in [36], but assumed here based on the fact that the ratio $\frac{\mathrm{Re}_\infty^{c_n,u_n}}{u_{n,\infty}}$ stayed constant for the varied sweep angle $\Lambda/^\circ \in \{0, 30, 40, 50, 60\}$ (see figure 5 of [36]).
The freestream turbulence intensity is given as $\mathrm{Tu}_\infty = 0.3\%$, which is relatively high in the context of aircraft flow [55]. Therefore, travelling crossflow instabilities may be the cause of the CFT rather

than stationary ones.
The transition was detected on the *lower* wing side by visualization of the sublimation of a thin layer of paradichlorobenzene crystals.

Numerical Setup

The computations are performed for the same freestream conditions as the experiments, except the freestream *static* pressure which is set to $p_\infty = 1\,\text{atm}$ instead of setting the *total* pressure to $p_{0,\infty} = 1\,\text{atm}$. This is a fault, that cannot be fixed due to limited time, but its influence is assumed to be low because of the low Mach number Ma_∞. Missing conditions for the freestream temperature T_∞ and viscosity ratio R^{turb} are supplemented according to section 4.1.2.
As for some of the cases the Mach number $\text{Ma} < 0.3$, for all test cases low-Mach preconditioning is applied.
The simulation is performed two-dimensional. No wind tunnel walls are included. The farfield is a circle of radius $50\,c_n$. The grid is hybrid with a structured O-grid around the airfoil embedded in an unstructured mesh of triangles (see figure 4.1). The mesh properties are listed in table 4.1. For

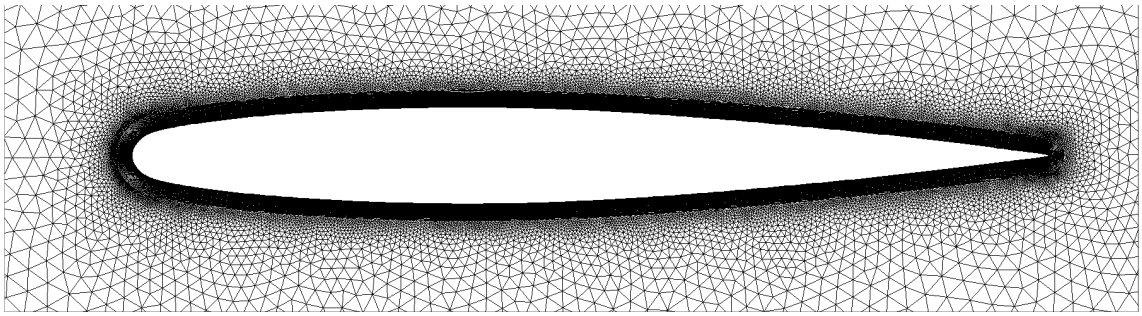

Figure 4.1: ONERA D test case: View of the grid around the airfoil

Table 4.1: ONERA D test case: Mesh properties

Mesh property	Value
Total number of nodes N_c	160518
Number of surface nodes chordwise (upper or lower surface)	256
Number of wall normal structured layers	128
Minimum number of nodes in laminar boundary layer at $\vec{x}_{\text{t,exp}}$	≈ 84
Maximum first node non-dimensional wall normal distance y_1^+	≈ 0.32

the farfield boundary Γ_{FF} the farfield boundary condition and for the wing surface Γ the no-slip wall boundary condition is used according to section 3.1.
For the majority of the configurations a laminar separation bubble occurs on the upper wing side, what lets the numerical solution diverge in case of free transition simulations. In order to improve the convergence, a "hack" is applied in the *TAU* code: The effective intermittency above the upper surface of the wing is manually set to $\gamma_{\text{eff}} = 1$ inside box that is slightly larger than the maximum boundary layer thickness $\max_{\vec{x}_\Gamma \in \Gamma} \delta(\vec{x}_\Gamma)$. Thus the boundary layer $\mathcal{B}$ on the upper wing side is turbulent and no separation bubble occurs.

Correction of the Angle of Attack α and Validation of the Mean Flow Results

The normal angle of attack $\alpha_{n,\mathrm{exp}} = 6°$ is constant in the experiments. The normal angle of attack in all simulations is set to $\alpha_{n,\mathrm{CFD}} = 5.2°$ in order to get the best pressure coefficient c_p distribution according to the measured one. In figure 4.2 an exemplary pressure coefficient c_p distribution (sweep angle $\Lambda = 55°$, Reynolds number $\mathrm{Re}_\infty^{c_n,u_n} = 0.8 \cdot 10^6$) is shown in form of the pressure coefficient of the corresponding unswept wing $c_{p,\Lambda=0}$ (equation 2.27), which allows the comparison of the curves of multiple sweep angles Λ. The agreement on the lower surface is very good and on the upper

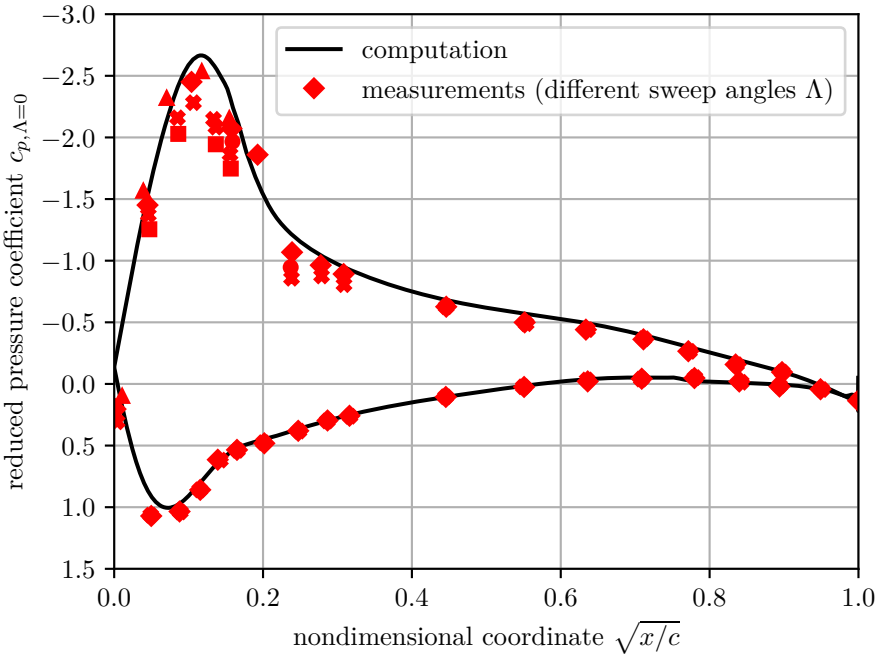

Figure 4.2: ONERA D test case: Comparison of the measured and computed pressure coefficient c_p distributions, given as the pressure coefficient of the corresponding unswept wing $c_{p,\Lambda=0}$

surface good. A close agreement on the lower side is more important as the transition is detected there.

Identification of Configurations with Crossflow Instability Dominated Transition

In [36] 14 transition location measurements are presented. Eight of these were identified by the authors of [36] as featuring separation-induced transition. This was confirmed in the present work by means of simulations. Additionally to the experimental transition locations $x_{\mathrm{t,exp}}$, transition locations predicted by the e^N-method x_{t,e^N} with a critical crossflow instability amplification factor of $N_{\mathrm{crit}}^{\mathrm{CF}} = 4.0$ are given via personal communication by Dr.-Ing. Normann Krimmelbein. These agree well with the the measured transition locations $x_{\mathrm{t,exp}}$, but provide more data points. From this data, for each normal velocity u_n four to six configurations with equidistantly changing sweep angle Λ were selected. The selected CFT test cases from both the experiments and the personal communicated data are summarized in appendix C, table C.1.

4.2.2 NLF(2)-0415 Infinite Swept Wing

Experimental Setup

The NASA NLF(2)-0415 airfoil of the experiments [11, 49] is a natural laminar flow airfoil [64, 63]. That means that its shape was designed to delay the TST, i.e. reduce the amplification factor N^{TS} of Tollmien-Schlichting instabilities. Thus, the pressure gradient $\partial_{\mathrm{sw}} p < 0$ is favorable up to about 71% chord for the design freestream conditions with an angle of attack $\alpha \in [-4°, 0°]$ on the upper surface. In addition, attachment line instability is avoided by a small leading edge radius. Görtler instabilities are not present, as no concave regions of the upper surface exist. At negative angles of attack α, the negative pressure gradient $\partial_{\mathrm{sw}} p$ region and the boundary layer thickness δ on the upper surface are large, what favors crossflow. Therefore the transition experiments were performed for an angle of attack of $\alpha = -4°$. At that condition the swept wing is a very good crossflow generator and thus CFT is probable. The experimental transition lines $\mathcal{T}_{\mathrm{exp}}$ show a saw-tooth-pattern [11], what indicates stationary CFT.
The experiments [11, 49] were performed in the *Arizona State University Unsteady Wind Tunnel*, a closed-loop wind tunnel with a square test section of side length 1.37 m. End-liners for the wind tunnel side walls were inserted because of the relatively large freestreamwise chord length of $c_{\mathrm{sw}} = 1.83\,\mathrm{m}$ of the wing model. The upper and lower wind tunnel walls are kept planar in order to allow visual inspections.
The reference conditions are given in terms of the freestream Reynolds number based on the streamwise velocity and the streamwise chord $\mathrm{Re}_{\infty}^{c_{\mathrm{sw}},u_{\mathrm{sw}}}$. It is not stated explicitely in [11, 49] that the *streamwise* velocity is used for it, but can be assumed based on a description in [54] about the wind tunnel in general. The freestream turbulence intensity is $\mathrm{Tu}_{\infty,\mathrm{sw}} \in [0.069\%, 0.095\%]$ in streamwise and $\mathrm{Tu}_{\infty,\mathrm{traverse}} \in [0.018\%, 0.040\%]$ in traverse direction [54].
The experimental transition line $\mathcal{T}_{\mathrm{exp}}$ was detected on the *upper* wing side by means of Naphthalene-trichlorotrifluoroethane spray, which sublimes faster in regions of high shear and thus visualizes the transition. The transition location $\vec{x}_{\mathrm{t}}$ detected by that method is not a single value per case but rather an interval due to the spanwise variation of the transition line. The authors provide also an representative value for that interval, which is more or less the average. Furthermore, hot-film and hot-wire measurements of the velocity fluctuations were used to measure the intermittency $\gamma(\vec{x}_{\Omega})$ inside the boundary layer $\vec{x}_{\Omega} \in \mathcal{B}$. The streamwise location x_{sw} at which the turbulent fluctuations suddenly increase is taken as the transition location x_{t}.

Numerical Setup

The computations are performed for the same freestream conditions as the experiments. The freestream static temperature $T_{\infty} = 303.15\,\mathrm{K}$ and freestream static pressure $p_{\infty} = 1\,\mathrm{atm} = 101325\,\mathrm{Pa}$ are assumption. In appendix C of the paper [11] (an analysis of the measurement error) representative values for the freestream static temperature T_{∞} and freestream static pressure p_{∞} are given, which do not differ much from the assumed values. As in the present work isotropic turbulent fluctuations are presupposed, the streamwise and traverse turbulence intensities are combined as

$$\mathrm{Tu}_{\infty}(u_{\infty}) = \frac{\sqrt{u'^2_{\mathrm{sw}} + u'^2_{\mathrm{traverse}}}(u_{\infty})}{u_{\infty}}, \tag{4.1}$$

based on the assumption that the flcutation components are in-phase. If the freestream velocity u_{∞} differ from the values given in table 1 of [54], linear interpolation is applied.
Due to the low freestream Mach number $\mathrm{Ma}_{\infty} < 0.3$, preconditioning is used.

The computation is performed two-dimensional, as the experimental setup is designed to image an inifinite swept wing flow. As the normal chord is large relative to the distance between the upper and lower wind tunnel walls (see figure 4.3), they are taken into account as free-slip walls. The

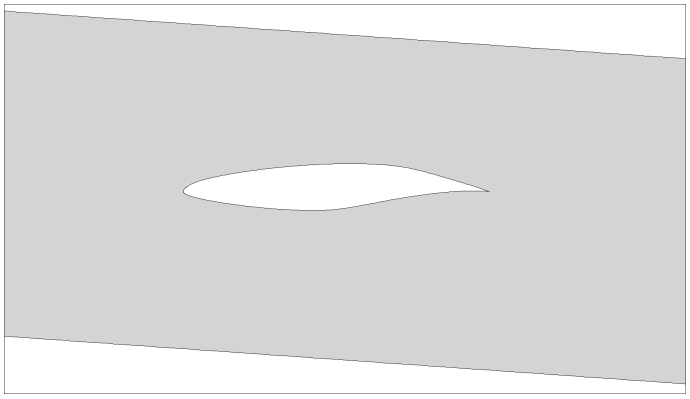

Figure 4.3: NLF(2)-0415 test case: View of the airfoil together with the upper and lower wind tunnel walls

walls are prolongated both up- and dowstream by 50 normal chord lengths c_n. The mesh is hybrid and the structured part around the airfoil is again an O-grid (see. figure 4.4). The mesh properties

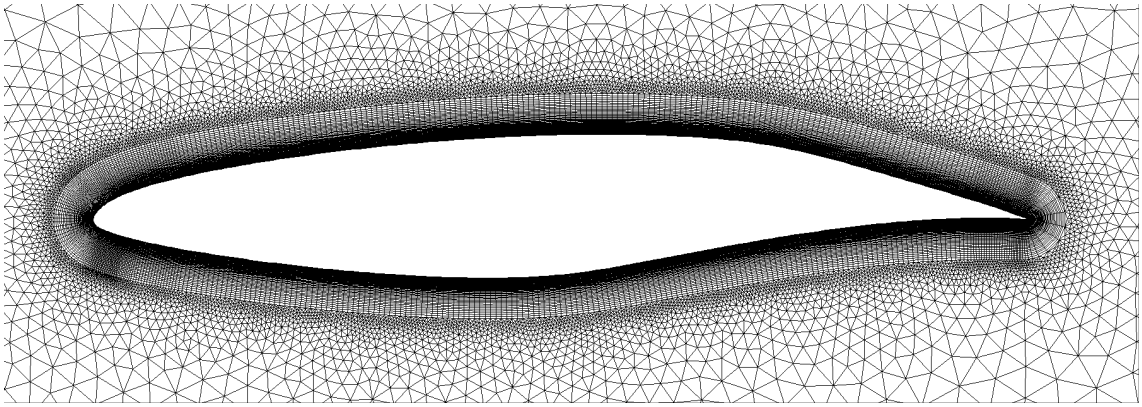

Figure 4.4: NLF(2)-0415 test case: View of the grid around the airfoil

are listed in table 4.2.

Table 4.2: NLF(2)-0415 test case: Mesh properties

Mesh property	Value
Total number of nodes N_c	424913
Number of surface nodes chordwise (upper surface)	256
Number of wall normal structured layers	256
Minimum number of nodes in laminar boundary layer at $\vec{x}_{\mathrm{t,exp}}$	≈ 76
Maximum first node non-dimensional wall normal distance y_1^+	≈ 0.50

Validation of the Mean Flow Results

The pressure coefficient c_p was measured near both wind tunnel side walls, i.e. at the upstream end (*inboard station*) and downstream end (*outboard station*) of the wing. The two distributions differ

slightly, which indicates the presence of a three-dimensional flow in the test section, challenging the infinite swept wing flow assumption. The measurements were only done for the upper side of the wing, as the transition location is determined there. The comparison of the measured and simulated pressure coefficient c_p distributions is presented exemplarily for the freestream Reynolds number $\mathrm{Re}_\infty^{c_{\mathrm{sw}},u_{\mathrm{sw}}} = 3.725 \cdot 10^6$ in figure 4.5. The agreement is very good, if upstream of $x/c \approx 0.3$

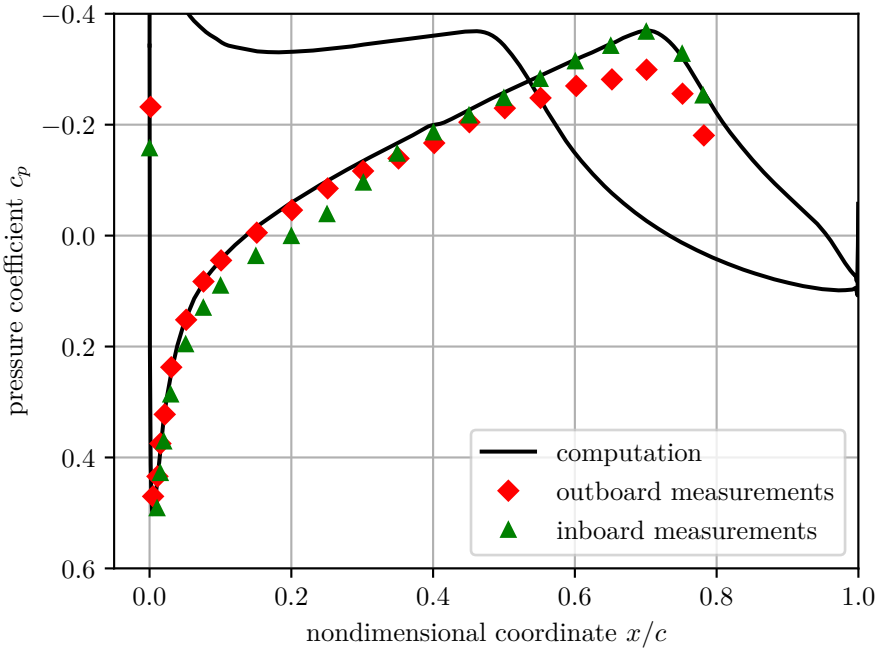

Figure 4.5: NLF(2)-0415 test case: Comparison of measured and computed pressure coefficient c_p distributions for the Reynolds number $\mathrm{Re}_\infty^{c_{\mathrm{sw}},u_{\mathrm{sw}}} = 3.725 \cdot 10^6$

the outboard and downstream the inboard station pressure coefficient c_p distribution is taken as reference.

Identification of Configurations with Crossflow Instability Dominated Transition

In [11] six detected transition locations x_{t} by the Naphthalene and two by hot-wire measurements are given. All of them are considered for the analysis of this thesis. Furthermore, from the eight hot-film measurements given in [11] one representative point is deduced by averaging. From the measurements of [49] all configurations are considered.
Additionally to the experimental transition locations $x_{\mathrm{t,exp}}$, transition locations predicted by the e^N-method with a critical amplification factor for crossflow instabilities of $N_{\mathrm{crit}}^{\mathrm{CF}} = 2.3 - \ln \frac{h_{\mathrm{rms}}}{\delta_1}$ are given via personal communication by Dr.-Ing. Normann Krimmelbein. These locations agree very well with the experimental transition locations $x_{\mathrm{t,exp}}$ and allow an interpolation between the relatively few data points of the measurements of [11, 49].
The list of CFT configurations used as reference for the present analysis is given in table C.2 in appendix C.

4.2.3 NACA 64_2A015 Infinite Swept Wing

Experimental Setup

The airfoil normal to the leading edge is a *NACA 64_2A015*. It is symmetric and has a maximum relative thickness of 15% at $\frac{x}{c} = 0.35$.
The wing model is rectangular with a chord length normal to the leading edge of $c_n = 4\,\text{ft}$. The unswept aspect ratio is 2.5. If swept with an adjustable angle, extensions are attached to the wing tip, as it is seeked to simulate infinite swept wing conditions. The surface roughness h_{rms} of the wing was not measured, but can be inferred. The wing was sprayed with several layers of flat black lacquer and hand rubbed with 600-grid sandpaper afterwards [7]. According to [60] about a completely different experiment, such a treatment results into a RMS surface roughness of $h_{\text{rms}} \approx 0.73\,\mu\text{m}$ (without high-pass filter for the roughness profile). However, it is well-known that the resulting surface roughness h_{rms} is strongly affected by the applied pressure and feed velocity, so the value assumption is highly uncertain.
The measurements [7] were done in the closed-loop *Ames 12-Foot Low-Turbulence Pressure Tunnel*. The cross section of the test section is circular with a diameter of $D_{\text{WT}} = 3c_n$. In the streamwise direction the walls of the test section are straight. Based on the assumption of planar sound waves, Boltz et al. [8] provide a formula for computing the freestream turbulence intensity Tu_∞ based on the sound pressure level L_p. The latter was measured for different freestream Mach numbers Ma_∞ and total pressures $p_{0,\infty}$ [8].
The pressure coefficient c_p was measured for sweep angles $\Lambda/^\circ \in \{0, 10, 20, 30, 40, 50\}$, streamwise angles of attack $\alpha_{\text{sw}}/^\circ \in [-3.0, 3.0]$ in steps of 0.5°, freestream Mach number $\text{Ma}_\infty = 0.27$, and freestream static pressure $p_\infty = 1\,\text{atm}$.
Very many transition measurements were carried out by means of microphones located in the model on both sides of the wing. The configurations feature the same sweep angles Λ and angles of attack α_{sw} as the pressure measurements. In addition, a few transition measurements were performed for the streamwise angles of attack $\alpha_{\text{sw}} \in \{3.5, 4.0\}$. For the transition measurements the freestream Reynolds number $\text{Re}_\infty^{c_{\text{sw}},u_{\text{sw}}}/10^6 \in [2.12, 39.9]$ based on the streamwise chord length c_{sw} and streamwise velocity u_∞ is given. Furthermore the total pressure $p_{0,\infty}/\text{psia} \in [43, 46] \cup [70, 75]$ is reported. The transition locations are provided for the *upper* wing side.

Numerical Setup

The computations are performed for the same freestream conditions as the experiments. The freestream static temperature is assumed as $T_\infty = 303.15\,\text{K}$. Note that for the transition measurements, to calculate the freestream Mach number Ma_∞ from the freestream Reynolds number $\text{Re}_\infty^{c_{\text{sw}},u_{\text{sw}}}$, temperature T_∞, and total pressure $p_{0,\infty}$ analytically is impossible, so it is solved numerically. The freestream turbulence intensity Tu_∞ given in [8] can be well correlated with the freestream Mach number Ma_∞ by [27]

$$\text{Tu}_\infty = \exp(4.58\,\text{Ma}_\infty - 9.14). \tag{4.2}$$

As for the majority of the cases the Mach number Ma is low, for all test cases low-Mach preconditioning is applied. The simulation is performed two-dimensional without wind tunnel walls. The farfield is a circle of radius $50\,c_n$. The grid is hybrid, that is, an O-grid around the airfoil embedded in an unstructured mesh of triangles (see figure 4.6). The mesh properties are listed in table 4.3.

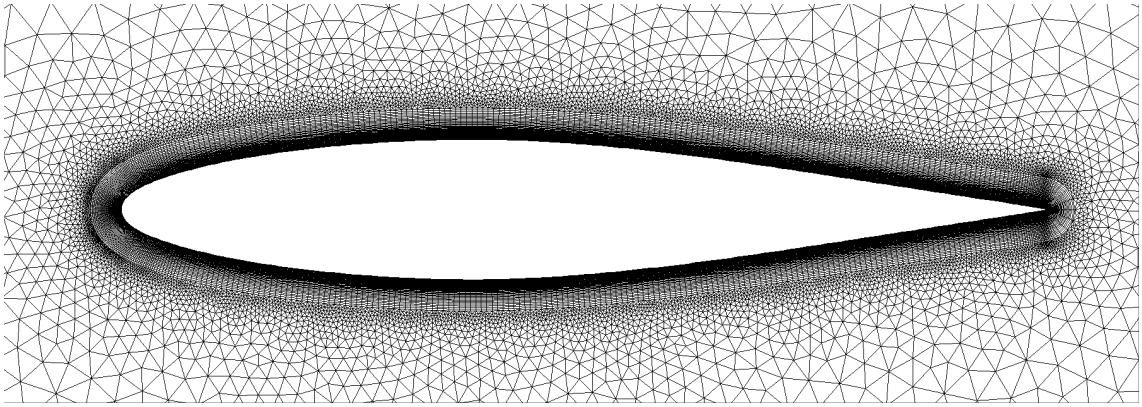

Figure 4.6: NACA 64_2A015 test case: View of the grid around the airfoil

Table 4.3: NACA 64_2A015 test case: Mesh properties

Mesh property	Value
Total number of nodes N_c	147716
Number of surface nodes chordwise (upper or lower surface)	256
Number of wall normal structured layers	128
Minimum number of nodes in laminar boundary layer at $\vec{x}_{\mathrm{t,exp}}$	≈ 69
Maximum first node non-dimensional wall normal distance y_1^+	≈ 0.88

Correction of the Angle of Attack α_{sw} and Validation of the Mean Flow Results

The correction of the normal angle of attack α_n in the simulations has to be dependent on the angle of attack α_{sw}. This can intuitively be understood because at zero angle of attack α_{sw} the correction has to be zero, as the airfoil is symmetric. In addition it turns out that the correction has to be dependent on the sweep angle Λ. By trial and error a correlation for the needed angle of attack α can be found, for which all pressure coefficient c_p distributions are reached the best. The correlation was already found by Krimmelbein [27]:

$$\alpha_n^{\mathrm{CFD}} \approx \left(\frac{0.0091\Lambda}{^\circ} + 0.69\right) \alpha_{\mathrm{sw,exp}} \tag{4.3}$$

Hereby, $\alpha_{\mathrm{sw,exp}}$ is the streamwise angle of attack of the experiment.
Boltz et al. [7] measured the pressure coefficient c_p distribution in sections normal to the leading edge at 45% and 80% span of the wing. As the measured distributions differ, there is apparently a three-dimensional flow present. In figure 4.7 an exemplary plot of the pressure coefficient c_p distributions is given. The agreement between the measurements and the simulation is very good.

Identification of Configurations with Crossflow Instability Dominated Transition

The authors [7] present the transition measurements partly in terms of the Reynolds number

$$\mathrm{Re_t} = \frac{u_\infty\, x_\mathrm{t}}{\nu_\infty}. \tag{4.4}$$

The data is provided in different plotting styles. Not every plot contains all tested configurations, and many but not all configurations are presented multiple times in different plots. In order to collect all configurations and check their consistency, the plots of the papers are recreated, but without letting certain points out like the Boltz et al. [7] did (see figure 4.8 for examples). As

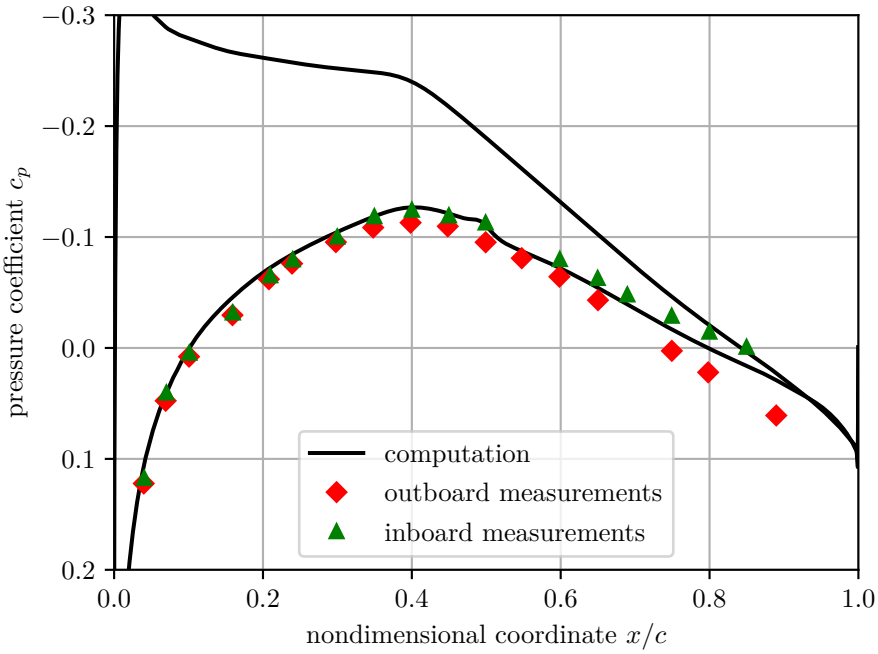

Figure 4.7: NACA 64_2015 test case: Comparison of the measured and computed pressure coefficient c_p distributions. Sweep angle $\Lambda = 50°$, streamwise angle of attack $\alpha = -2.5°$, Reynolds number $\mathrm{Re}_\infty^{c_{\mathrm{sw}},u_{\mathrm{sw}}} = 4.01 \cdot 10^6$, Mach number $\mathrm{Ma} = 0.0320$

there are many points, it is no problem to choose only relatively few of them, for which it is almost certain that they feature CFT. This is done in the following manner:

- If for identical flow cases multiple transition Reynolds numbers Re_t are existing, they are averaged. For certain points, like $(\Lambda, \alpha) = (50°, 1.5°)$ in figure 4.8a, the Reynolds numbers Re_t given by the different plots differ significantly, by more than $3 \cdot 10^6$. This is probably a plotting fault by Boltz et al. [7].
- In figure 4.8b it can be seen that the data points are scattered partly strongly ("zig-zag"-curves). Therefore, for each sweep angle Λ and angle of attack α_{sw} individually the points $\mathrm{Re}_\mathrm{t}(\mathrm{Re}_\infty^{c_{\mathrm{sw}},u_{\mathrm{sw}}})$ were smoothened by a *zig-zag-remover* in the double-logarithmic domain. Herefore, the midpoints of the linear pieces between the given points are connected by a surrogate curve and afterwards the given points are projected onto the surrogate curve perpendicularly.
- The transition location x_t is ambiguous for certain flow cases (see figure 4.8b): If the curves become (almost) vertical, there are different transition locations x_t for the same sweep angle Λ, angle of attack α_{sw} and (almost) same freestream Reynolds number $\mathrm{Re}_\infty^{c_{\mathrm{sw}},u_{\mathrm{sw}}}$. This violates the basic assumption that there are no unknown influences on the CFT. Thus, those data points are rejected completely.
- If, for a given transition location x_t, the freestream Reynolds number $\mathrm{Re}_\infty^{c_{\mathrm{sw}},u_{\mathrm{sw}}}$ does not change significantly with the angle of attack α_{sw}, as in figure 4.8a for $\Lambda = 50°$, the corresponding points are also rejected. It is assumed that the measurements are distorted. This is because for most of the curves in the plots of the type of 4.8a, there is no such plateau visible.
- In figure 4.8a it can be seen that for large sweep angles Λ, the curves have maxima. It is stated in [7] that the points to the left of the maxima are considered as featuring CFT. Thus, in this work, the points are taken into account if the slope in the plots of the type of figure 4.8a is (positively) large enough.

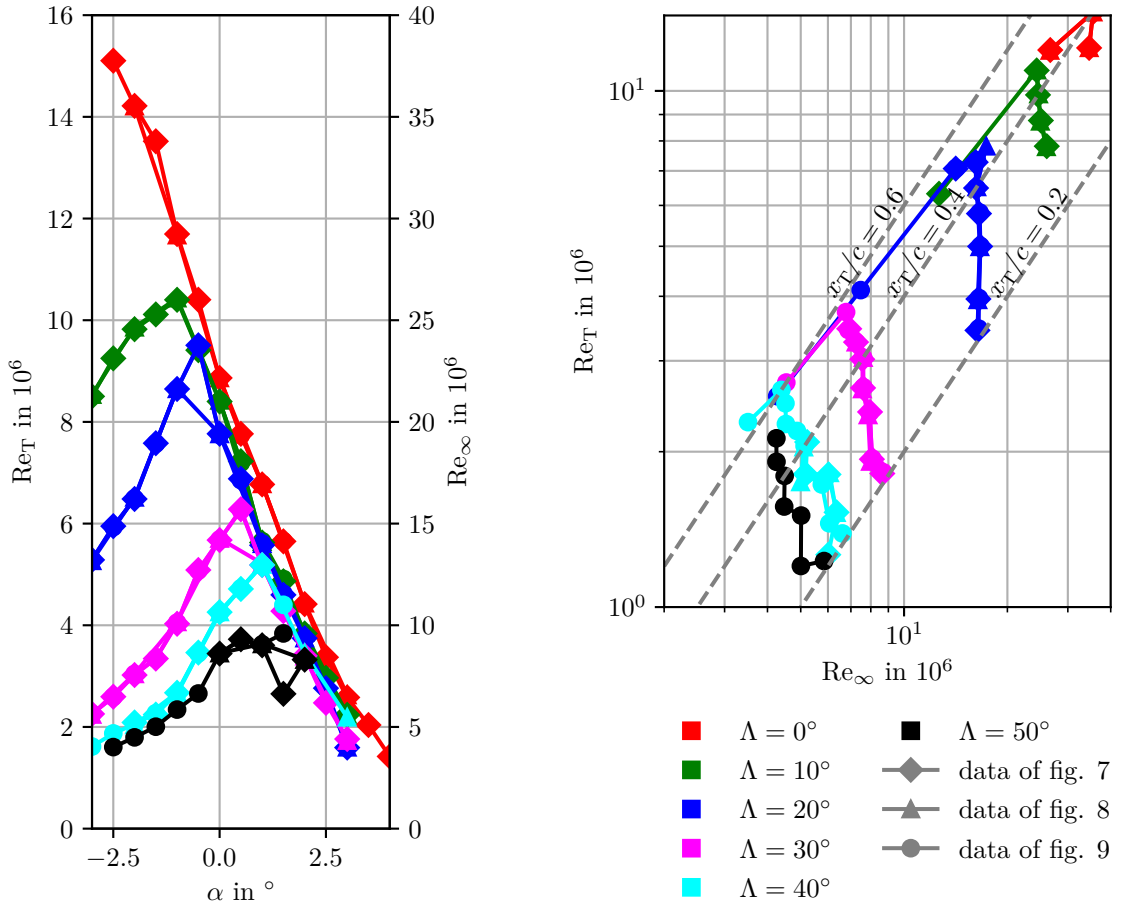

(a) Recreation of figure no. 7 of Boltz et al. [7] for transition location $x_t/c = 0.4$

(b) Recreation of figure no. 9 of Boltz et al. [7] for streamwise angle of attack $\alpha_{sw,exp} = -2.0°$

Figure 4.8: NACA 64_2015 test case: Recreation of the plots of Boltz et al. [7]

- If in the $\mathrm{Re}_t(\mathrm{Re}_\infty^{c_{sw},u_{sw}})$-plot 4.8b too few points of a curve are left after applying the rules from above, they are also let out.

The data points chosen according to these rules are plotted in figure 4.9 (exemplarily). The whole list of the 110 selected configurations is given in table C.3 in appendix C. In the selection, the angle of attack is $\alpha_{sw}/° \in \{-3.0, -2.5, -2.0, -1.5, -1.0, -0.5, 0.0\}$, the sweep angle is $\Lambda/° \in \{30, 40, 50\}$, and the freestream Reynolds number ranges in $\mathrm{Re}_\infty^{c_{sw},u_{sw}}/10^6 \in [3.34, 11.3]$.

4.2.4 HQ26N/14.82 Infinite Swept Wing

Experimental Setup

The HQ26N/14.82 airfoil of the experiments [61] was developed for a tailless sailplane with low pitching moments [66]. The shape is very characteristic: The upper surface is curved with a approximately constant curvature radius between the leading edge and the middle. Downstream of that, it is mostly concave. In contrast, the lower surface is almost flat. It is known that certain curvature terms must be included if the e^N-method is used for transition prediction, as otherwise the on the upper side the transition is predicted too upstream by the e^N-method [66]. This makes the airfoil interesting for the calibration of transition models.

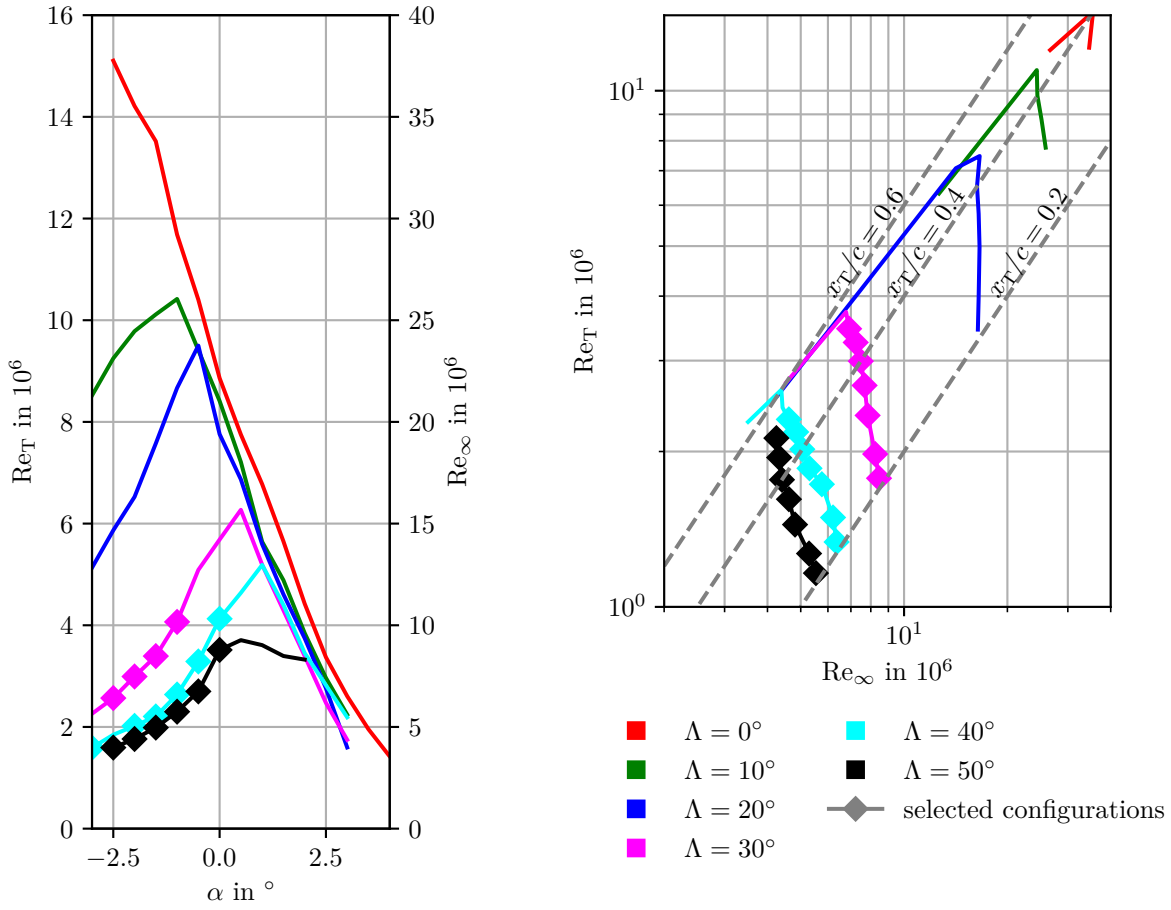

(a) Selected configurations for transition location $x_t/c = 0.4$

(b) Selected configurations for streamwise angle of attack $\alpha_{sw,exp} = -2.0°$

Figure 4.9: NACA 64_2015 test case: Recreation of the plots of Boltz et al. [7] (points considered for this thesis are marked)

The wing chord length normal to the leading edge is $c_n = 0.65\,\mathrm{m}$. The wing has an unswept aspect ratio of 3.0. When swept, root and tip extensions are applied to the ends of the wing, such that the wing covers the whole test section. The wind tunnel of the experiments [61] is the *Niedergeschwindigkeitskanal Braunschweig (NWB)*. The test section has a diameter of $D_{WT} = 4.3c_n$. For each configuration, the pressure and transition were measured simultaneously. The configurations are given by the freestream Reynolds number $\mathrm{Re}_\infty^{c_{sw},u_{sw}}/10^6 \in [1.82, 4.48]$ based on the streamwise chord c and streamwise velocity u_∞. The freestream Mach number is in the range $\mathrm{Ma} \in [0.11, 0.24]$. The streamwise angle of attack varies in the range $\alpha_{sw}/° \in [-2.01, 8.59]$. The sweep angle is $\Lambda/° \in \{30, 45\}$.

The pressure coefficient c_p was measured approximately in the middle of the wing on both sides. An infrared camera was used to detect the transition line $\mathcal{T}$ by means of the temperature $T(\vec{x}_\Gamma)\,\forall \vec{x}_\Gamma \in \Gamma$ difference between the laminar and the turbulent boundary layer $\mathcal{B}$ due to the different heat exchange coefficient with the model surface. Per measured configuration, Seitz [61] gives the minimum, maximum and a representative value (the integral average) due to the spanwise variation of the transition location $\vec{x}_t$. He notes that the more flat the pressure distribution and the smaller the freestream Reynolds number $\mathrm{Re}_\infty^{c_{sw},u_{sw}}$ is, the larger is the range between the minimum

and maximum transition coordinate. Transition locations x_t are given either for the upper or the lower wing side.

Numerical Setup

The computations are performed for the same freestream conditions as the experiments, except for the freestream static temperature T_∞ and turbulence intensity Tu_∞, which are assumed according to subsection 4.1.2.
Due to the low Mach number $\mathrm{Ma}_\infty < 0.3$, preconditioning is used.
The computations are done two-dimensional, as the wind tunnel test simulates infinite swept wing flow. In addition, the upper and lower wind tunnel walls are neglected, as the test section is large relatively to the normal chord c_n of the wing. A circular farfield of radius $50c_n$ around the airfoil is used. The grid is presented in figure 4.10. The mesh properties are listed in table 4.4.

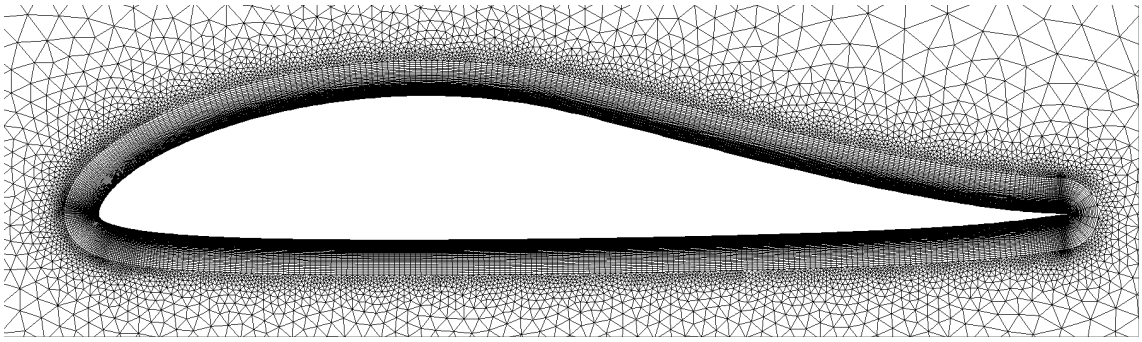

Figure 4.10: HQ26N/14.82 test case: View of the grid around the airfoil

Table 4.4: HQ26N/14.82 test case: Mesh properties

Mesh property	Value
Total number of nodes N_c	146632
Number of surface nodes chordwise (upper or lower surface)	256
Number of wall normal structured layers	128
Minimum number of nodes in laminar boundary layer at $\vec{x}_{t,\mathrm{exp}}$	≈ 76
Maximum first node non-dimensional wall normal distance y_1^+	≈ 0.38

Correction of the Angle of Attack α and Validation of the Mean Flow Results

The correction of the angle of attack α is different for all configurations, but almost linear with the experimental angle of attack α_{exp}. The values for the streamwise angle of attack used are given in table C.4 in appendix C. The comparison of the pressure coefficient c_p distributions is depicted in figure 4.11 for two configurations for the upper and the lower wing side. The agreement is very good on both sides of the wing.

Identification of Configurations with Crossflow Instability Dominated Transition

In the report of Seitz [61] 20 configurations with CFT are given together with the corresponding transition coordinates x_t. Four of them for the upper side and one for the lower side are removed as the corresponding simulations do not converge due to laminar separation bubbles. The list of the selected configurations is given in appendix C, table C.4.

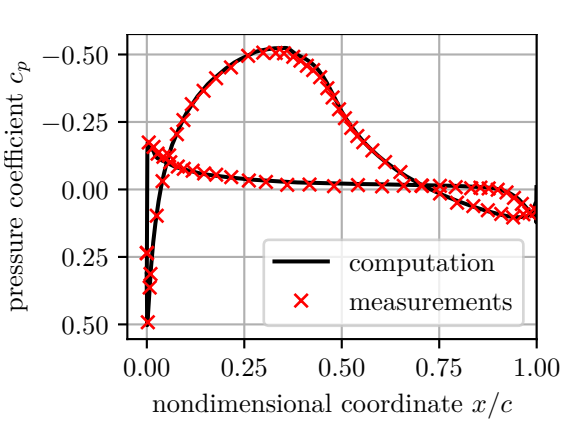

(a) upper side, sweep angle $\Lambda = 45°$, angle of attack $\alpha = -2.01°$, Reynods number $\mathrm{Re}_\infty^{c_{\mathrm{sw}},u_{\mathrm{sw}}} = 2.98 \cdot 10^6$, Mach number $\mathrm{Ma} = 0.15$

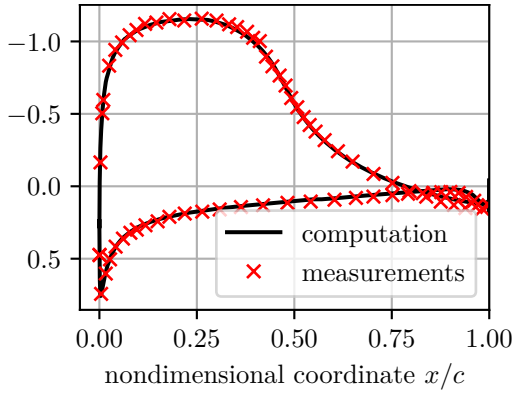

(b) lower side, sweep angle $\Lambda = 30°$, angle of attack $\alpha = 5.56°$, Reynods number $\mathrm{Re}_\infty^{c_{\mathrm{sw}},u_{\mathrm{sw}}} = 3.60 \cdot 10^6$, Mach number $\mathrm{Ma} = 0.24$

Figure 4.11: HQ26N/14.82 test case: Comparison of the measured and computed pressure coefficient c_p distributions

4.2.5 Infinite Swept Cylinder

Experimental Setup

The model of the experiments [47] is a cylinder with an afterbody to avoid turbulent separation at the leeward side. The chord length of the whole body normal to the leading edge is $c_n = 0.457\,\mathrm{m}$. The unswept aspect ratio of the body is 5.34.

The experiments were done in the College of Aeronautics 2.4 m times 1.8 m closed-loop low-speed wind tunnel [47].

The pressure p measurements were carried out for the Reynolds number $\mathrm{Re}_\infty^{c_n,u_{\mathrm{sw}}} = 1.6 \cdot 10^6$ based on the normal chord length c_n and the streamwise freestream velocity u_∞. The sweep angle was $\Lambda/\circ \in \{55, 63, 71\}$. The angle of attack was $\alpha = 0°$. The transition measurements were done for the Reynolds numbers $\mathrm{Re}_\infty^{c_n,u_{\mathrm{sw}}}/10^6 \in [0.89, 1.68]$ and sweep angles $\Lambda/° \in [53.0, 70.7]$. The angle of attack was again $\alpha = 0°$. The freestream temperature is given as $T_\infty \in [15°\mathrm{C}, 35°\mathrm{C}]$. The freestream turbulence intensity is $\mathrm{Tu}_\infty \approx 0.16\%$. [47]

The transition was detected by means of a modified Pitot tube that allows to measure the dynamic pressure $q(\vec{x}_\Omega)\,\forall \vec{x}_\Omega \in \Omega$ inside the boundary layer $\mathcal{B}$. For a given point $\vec{x}_\Omega$, the freestream Reynolds number $\mathrm{Re}_\infty^{c_n,u_{\mathrm{sw}}}$ is adapted until the measured dynamic pressure $q(\vec{x}_\Omega)$ changes in a characteristic manner, which indicates transition at the chosen point [47]. The conditions for both the onset and completion of the transition were detected.

Numerical Setup

The computations are performed for the same configurations as described above for the experiments, except the turbulence intensity, which is set to $\mathrm{Tu}_\infty = 0.10\%$. This is a fault, coming from the fact that the correct paper was not available from the beginning of the work on the thesis. The influence is expected to be low, as no TST is analyzed. The freestream temperature is averaged to $T_\infty = 30°\mathrm{C}$. The ambient static pressure is assumed as $p_\infty = 1\,\mathrm{atm}$.

As the freestream Mach number is $\mathrm{Ma} < 0.3$, low-Mach preconditioning is applied.

The simulation is performed two-dimensional. No wind tunnel walls are included. No correction of the angle of attack is applied, as the model operates at zero angle of attack $\alpha = 0°$. The farfield is a

circle of radius $50\,c_n$. The grid is hybrid, an O-grid around the airfoil embedded in an unstructured mesh of triangles (see. figure 4.12). It can be seen that the complete cross section is simulated. It

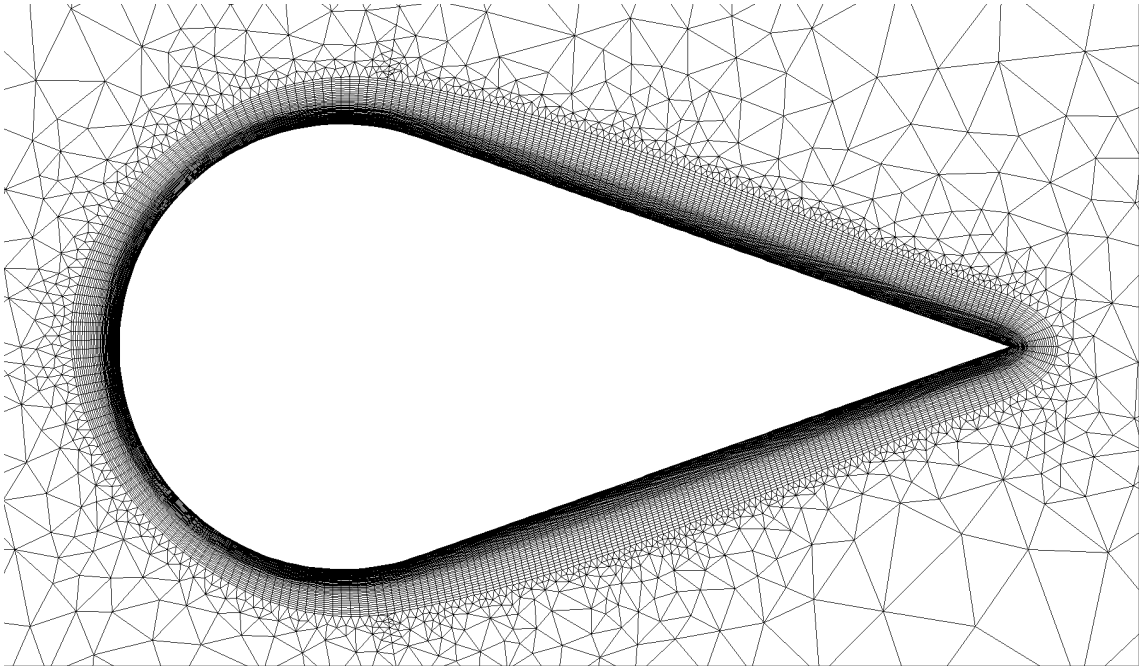

Figure 4.12: Swept cylinder test case: View of the grid around the cross section

would have been possible to only compute half of the model, as the flow has a symmetry plane. However, this would have needed a new grid, and no grids should be created for this thesis.
The mesh properties are listed in table 4.5.

Table 4.5: Swept cylinder test case: Mesh properties

Mesh property	Value
Total number of nodes N_c	60624
Number of surface nodes chordwise (upper or lower surface)	200
Number of wall normal structured layers	84
Minimum number of nodes in laminar boundary layer at $\vec{x}_{\mathrm{t,exp}}$	≈ 39
Maximum first node non-dimensional wall normal distance y_1^+	≈ 0.09

Validation of the Mean Flow Results

The configurations of the pressure measurements are computed with a fully turbulent boundary layer, as no transition locations are delivered. Attention has to be payed to different definitions of the chordwise coordinate: Poll [47] deliver all data in "streamwise coordinates" $\left(\frac{x}{c}\right)_{\mathrm{Poll}}$. The relationship to the standard definition $\left(\frac{x}{c}\right)_{\mathrm{thesis}}$ of this thesis is (personal communication by Dr.-Ing. Normann Krimmelbein)

$$\left(\frac{x}{c}\right)_{\mathrm{thesis}} = \frac{1}{4} - \frac{1}{4}\cos_{\mathrm{rad}}\left[4\left(\frac{x}{c}\right)_{\mathrm{Poll}}\right]. \tag{4.5}$$

A comparison of the pressure coefficient c_p distributions is given in figure 4.13 for a chosen configuration. The agreement is very good, much better than in the paper of Stock and Seitz [66]. Note that in the paper of Stock and Seitz [66] the label of the horizontal axis of figure 16 is wrong (at least for the points of the experimental data): it should be $\left(\frac{x}{c}\right)_{\mathrm{Poll}}$ and is the same as in figure 6

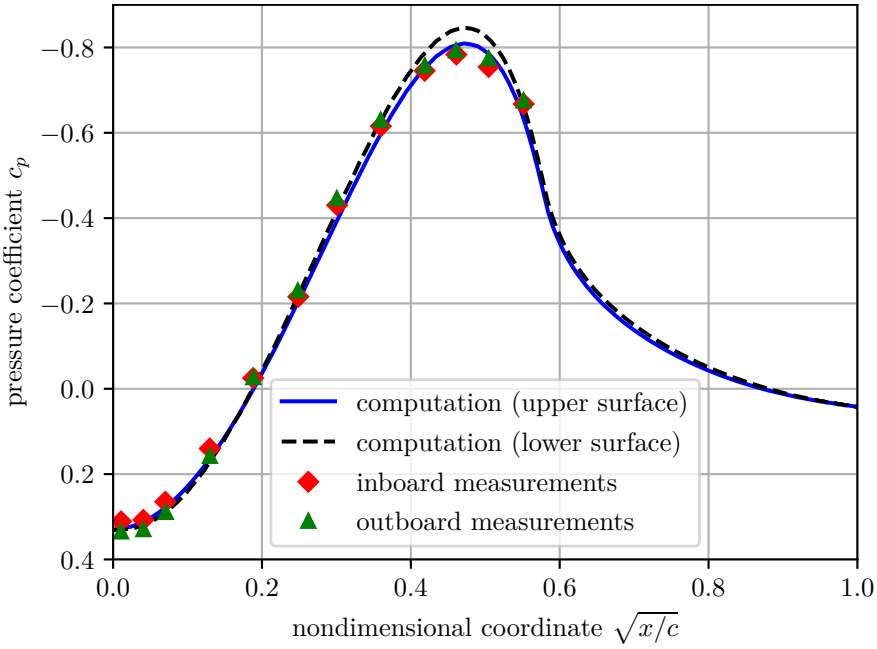

Figure 4.13: Swept cylinder test case: Comparison of the measured and computed pressure coefficient c_p distributions (sweep angle $\Lambda = 55°$, Reynolds number $\mathrm{Re}_\infty^{c_n,u_{sw}} = 1.6 \cdot 10^6$, Mach number $\mathrm{Ma} = 0.147$)

of the original paper by Poll [47]. This could be the mistake source of [66]. However, the pressure distributions differ for the upper and lower surface of the cylinder, even though the angle of attack is $\alpha = 0°$. This is caused by the asymmetrical mesh (see figure 4.12).

Identification of Configurations with Crossflow Instability Dominated Transition

Poll [47] gives both the "onset" and "completion" of transition for a large range of Reynolds numbers and $\mathrm{Re}_\infty^{c_n,u_{sw}}$ sweep angles. As in [66], the *onset* locations are used for the analysis here. In [47] it is indicated that the measured transition locations $\vec{x}_t$ are for pure CFT. This is supported by the fact that all transition locations are upstream of the maximum thickness of the cross-section of the model ($25\%c_n$), as there a favorable pressure gradient is present, which makes TST unlikely. In addition, in the experiments it is ensured that there is no attachment line instability induced transition.

Only the configurations that are given in [66] are considered, as at the beginning of the present work the original paper [47] about the experiments was not available. From the 98 configurations, only 14 could successfully be simulated, as turbulent separations appeared often. The list of the selected test case configurations is given in table C.6 (appendix C).

4.2.6 TELFONA Pathfinder Wing

Experimental Setup

The TELFONA Pathfinder wing-body configuration model of the experiments [44, 45, 68, 67] consists of a simple fuselage with an attached wing. It was developed as part of the European Research Project *Testing for Laminar Flow On New Aircraft (TELFONA)*. The wing has an aspect ratio of 7.05, a taper ratio of 0.778, a full span of $b = 1.7\,\mathrm{m}$ and an aerodynamic mean chord length of $\bar{c} = 0.24125\,\mathrm{m}$. The leading edge sweep angle is $\Lambda_{LE} = 18°$. The airfoil is the *DLR LV5*, see

figure 4.14. It was derived from an ATTAS laminar glove section [44]. The design driver for the

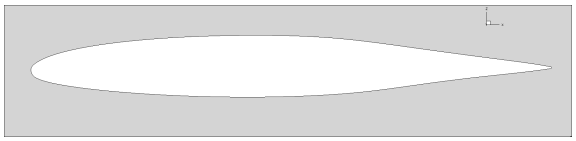

Figure 4.14: TELFONA Pathfinder wing test case: View of the airfoil normal to the leading edge

airfoil was the delay of natural transition at high freestream Reynolds numbers Re_∞ and transonic freestream Mach numbers Ma_∞. In addition, spanwise edge parallel isobars are reached by an appropriate shape of the wing [45]. Thus, the TELFONA Pathfinder wing-body configuration is well-suited for the calibration of transition models parameters by means of measurements [44].
The model surfaces are polished, and the RMS surface roughness is given as $h_{\mathrm{rms}} = 0.1\,\mu\mathrm{m}$.
The tests were conducted in the *European Transonic Wind Tunnel (ETW)* [44, 45, 68, 67]. The wind tunnel allows the use of high freestream Reynolds numbers Re_∞ at low freestream temperatures T_∞ and high freestream pressure p_∞. This is achieved by a closed-loop design and a continuous injection of liquid nitrogen.
The test cases are given in form of the freestream Reynolds number $\mathrm{Re}_\infty^{\bar{c},u_{\mathrm{sw}}}$ based on the aerodynamic mean chord length $\bar{c}$ and streamwise velocity u_∞, together with the freestream Mach number Ma_∞ and total temperature $T_{0,\infty}$ (which sometimes is misleadingly called "temperature", e.g. in [68] for the total temperature $T_{0,\infty} = 175\,\mathrm{K}$ the corresponding static temperature is $T_\infty \approx 156\,\mathrm{K}$).
The angle of attack α is not given, but the lift coefficient c_L. A value for the freestream turbulence intensity $\mathrm{Tu}_\infty = 0.20\%$ is given in [45]. Nevertheless, based on discussions with the authors of [44], it was found that $\mathrm{Tu}_\infty = 0.1\%$ is more accurate (personal communication of Dr. Daniela François).
The transition line $\mathcal{T}_{\mathrm{exp}}$ was detected by means of a cryogenic temperature-sensitive paint. This re-emits light, if excited with light of specific wavelengths. It serves as a measure of the surface temperature $T(\vec{x}_\Gamma)\,\forall \vec{x}_\Gamma \in \Gamma$, which is lower for the turbulent boundary layer due to the higher heat exchange with the surface Γ. To further increase the difference between the laminar and turbulent boundary layer surface temperature T, a thermal inequilibrium is invoked by quickly changing the freestream temperature T_∞ by approximately 10 K in multiple steps. After each step images are taken with CCD cameras. The transition was measured on the upper and lower side, approximately in the middle of the wing at spanwise coordinate $0.33b$.
Note that the authors of the experiments defined the transition location $\vec{x}_{\mathrm{t,exp}}$ as the most downstream point of the detected transition line $\mathcal{T}_{\mathrm{exp}}$.

Numerical Setup

The computations are performed for the same freestream conditions as the experiments. The angle of attack α is adapted automatically to match the measured lift coefficient c_L. To do so, the fixed transition line $\mathcal{T}_{\mathrm{CFD}}$ is set according to the experiments $\mathcal{T}_{\mathrm{CFD}} = \mathcal{T}_{\mathrm{exp}}$.
The simulation is done three-dimensional, as the geometry is three-dimensional, but without any wind tunnel walls. The farfield is spherical and has a radius of about $70\bar{c}$.
The grid is hybrid, with the boundary layer $\mathcal{B}$ completely covered by the structured grid. An image of the grid is provided in figure 4.15. The mesh properties are listed in table 4.6. According to the best practice rules for mesh properties given in section 3.4, the wall normal resolution is too low.
For many simulations a shock-induced separation of the turbulent boundary layer on the upper side of the wing leads to a bad convergence of the numerical solution. But nevertheless, as the

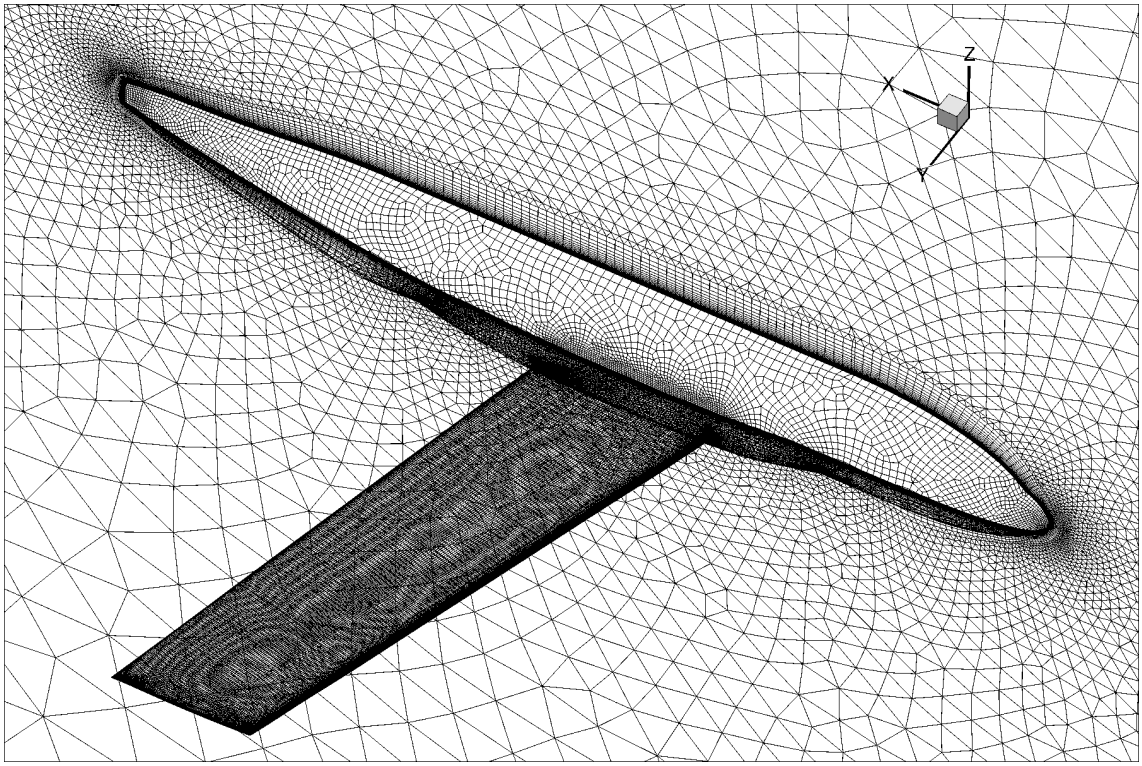

Figure 4.15: TELFONA Pathfinder wing test case: View of the grid around the wing-body configuration

Table 4.6: TELFONA Pathfinder wing test case: Mesh properties

Mesh property	Value
Total number of nodes N_c	4253789
Number of surface nodes chordwise (upper surface)	≈ 110
Number of surface nodes spanwise (upper surface)	≈ 165
Number of wall normal structured layers	42
Minimum number of nodes in laminar boundary layer at $\vec{x}_{\mathrm{t,exp}}$	≈ 29
Maximum first node non-dimensional wall normal distance y_1^+	≈ 1.41 (at $\vec{x}_{\mathrm{t}}$: 0.97)

high residuals are located solely inside the separation, the laminar boundary layer is taken as well-converged. To improve the overall convergence, scalar instead of matrix artificial dissipation is used.

Validation of the Mean Flow Results

In figure 4.16 an exemplarily comparison of the pressure coefficient c_p distributions of the measurements and the simulation is shown for Reynolds number $\mathrm{Re}_\infty^{\bar{c},u_{\mathrm{sw}}} = 20 \cdot 10^6$, lift coefficient $c_L = 0.401$, lower wing side. The agreement between the measurements and the simulation is very good.

Identification of Configurations with Crossflow Instability Dominated Transition

The CFT configurations are collected from the papers [44, 45, 68, 67]. In addition, in [59] transition locations predicted by the e^N-method are given. In all sources, the authors identify CFT configurations as such.

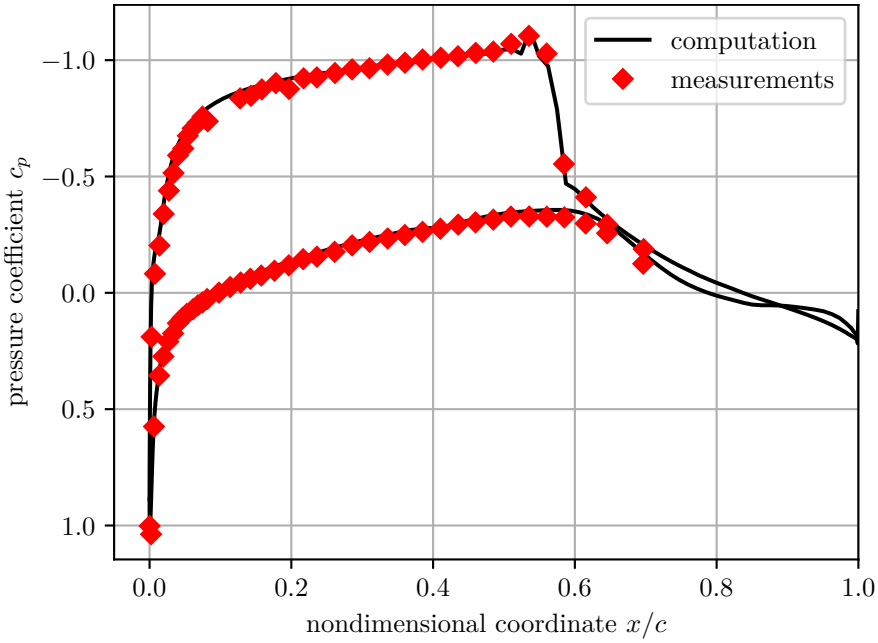

Figure 4.16: TELFONA Pathfinder wing test case: Comparison of the measured and computed pressure coefficient c_p distributions for Reynolds number $\mathrm{Re}_\infty^{\bar{c},u_{\mathrm{sw}}} = 20{\cdot}10^6$, lift coefficient $c_L = 0.401$, lower wing side

The list of the selected configurations (together with the found angles of attack α_{CFD}) is given in table C.5 (appendix C).

4.2.7 Inclined 6:1 Prolate Spheroid

Experimental Setup

The spheroid of the experiments [26] is an ellipse rotated around its larger half axis (ellipsoid). It can be seen as a strongly simplified aircraft fuselage or a generic missile. When exposed to oblique flow, crossflow develops inside the boundary layer $\mathcal{B}$. In contrast to flows over long or infinite swept wings, the flow around the spheroid is three-dimensional, in the sense that the boundary layer edge streamlines are strongly curved in stream- and crosswise direction and are non-parallel. Both TST and CFT are observed. The length of the spheroid is $c = 2.4\,\mathrm{m}$ and it has a diameter of $\frac{c}{6}$.
The surface roughness of the model is unknown. But, as it was made of glass-fiber reinforced resin and looks glossy on a photographs of the model [26], it is assumed to be painted. The hot films of the transition measurements, which have a heigth of 5 μm [26], disturb the flow, but the experimentators indicate that "Extreme care was taken to mount the hot films on the model surface in order to avoid a boundary layer transition due to artificial roughness" [38]. In addition, the hot films were distributed on the spheroid surface in a manner that disturbances by the upstream probes should not influence the measurements. In order to be consistent with previous research on transition modeling [31], a surface roughness of $h_{\mathrm{rms}} = 3.3\,\mu\mathrm{m}$ is assumed.
The flow was measured in the DFVLR (DLR) low-speed wind tunnel Göttingen [26]. The test section is a large open room (cross sectional area 3.5 m times 4.5 m).
The free transition experiments were carried out for a varying angle of attack $\alpha/^\circ \in \{5, 10, 15, 20, 24, 30\}$, a varying freestream velocity $u_\infty \in \{10, 20, 30, 45, 60\}$ and a varying freestream Reynolds number $\mathrm{Re}_\infty^{c_{\mathrm{sw}},u_{\mathrm{sw}}}/10^6 \in \{1.5, 3.0, 4.5, 6.4, 6.5, 10.0\}$ based on the spheroid length c and the streamwise freestream velocity u_∞. The temperature is known to be constant [1], but no value

is given. The freestream turbulence intensity $\mathrm{Tu}_\infty \in [0.1\%, 0.3\%]$ is given by [26]. It is said that the freestream Reynolds number $\mathrm{Re}_\infty^{c_{\mathrm{sw}},u_{\mathrm{sw}}}$ is influencing the turbulence intensity [26].
The transition was detected by measuring the wall shear stress $\tau_{\mathrm{w}}(\vec{x}_\Gamma), \vec{x}_\Gamma \in \Gamma$ with twelve flush mounted surface hot film probes [26]. The probing of the surface was relatively coarse, and the skin friction coefficient c_f has much uncertainty [28]. For the analysis of this thesis, the experimental transition lines $\mathcal{T}_{\mathrm{exp}}$ are taken at certain isolines of the skin friction coefficient c_{f} according to [28].

Numerical Setup

The computations are performed for the same freestream Reynolds numbers $\mathrm{Re}_\infty^{c_{\mathrm{sw}},u_{\mathrm{sw}}}$ as the experiments, except for the turbulence intensity Tu_∞, which is set to the average $\mathrm{Tu}_\infty = 0.15\%$ of the experiments. A better approach would be to correlate the turbulence intensity linearly with the freestream Reynolds number $\mathrm{Re}_\infty^{c_{\mathrm{sw}},u_{\mathrm{sw}}}$, but this is not done due to limited time left for the present work. In addition, the freestream Mach number is set according to [28] as $\mathrm{Ma}_\infty = 0.13$. The freestream static temperature is assumed as $T_\infty = 300\,\mathrm{K}$.
Due to the low freestream Mach number $\mathrm{Ma}_\infty < 0.3$, preconditioning is used. The computation is performed without wind tunnel walls, as the test section is large. No correction of the angle of attack α is needed, because the spheroid does not generate much lift L, so the potential interaction with the wind tunnel walls is low. The farfield Γ_{FF} is a sphere of radius $100c$. Only a half of the flow is modeled, as it is symmetrical. The grid around the spheroid is shown in figure 4.17. The

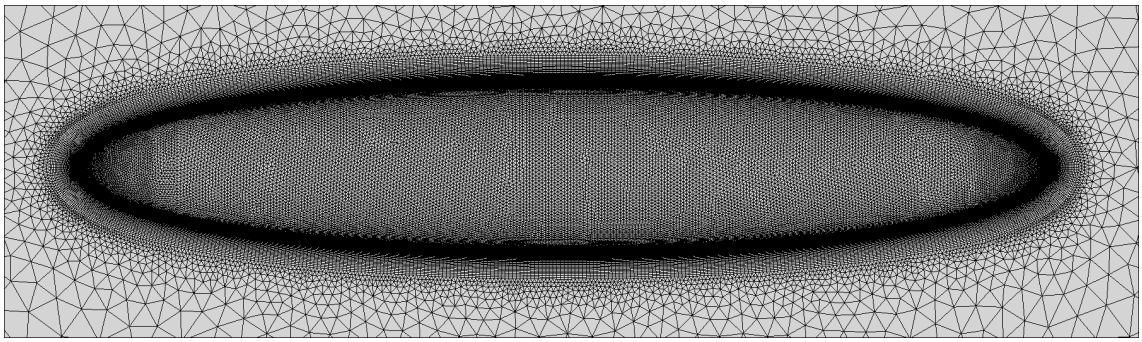

Figure 4.17: Prolate spheroid test case: View of the grid around the spheroid

mesh properties are listed in table 4.7. For some configurations the free transition simulations lead

Table 4.7: Prolate spheroid test case: Mesh properties

Mesh property	Value
Total number of nodes N_c	2846519
Number of surface nodes	20026
Number of wall normal structured layers	128
Minimum number of nodes in laminar boundary layer at $\vec{x}_{\mathrm{t,exp}}$	≈ 60
Maximum first node non-dimensional wall normal distance y_1^+	≈ 0.44

to a completely laminar boundary layer on the lower part of the surface of the prolate spheroid. That invokes laminar separations, letting the numerical solution diverge. In order to stabilize the computation, the "hack" as for the ONERA D numerical setup is applied: For $\frac{x}{c} > 0.935$[1] the effective intermittency is set to $\gamma_{\mathrm{eff}} = 1$ in order to set the boundary layer to turbulent.

[1] That is the location of the most downstream hot-film probe applied in the experiments [26].

Identification of Configurations and Locations with Crossflow Instability Dominated Transition

Only the configurations of [28] are taken for time reasons. Surface points on the experimental transition line $\mathcal{T}_{\text{exp}}$ are selected for the anaylsis for which CFT is probable. The points cannot be on the symmetry plane $\varphi \in \{0°, 180°\}$ of the spheroid, as the velocity normal to the symmetry plane is zero (no crossflow u_{cw}). The locations are chosen such that they are equally distributed over the transition line $\mathcal{T}_{\text{exp}}$ for azimuth angles φ smaller than the azimuth angle φ of the most upstream transition location $\vec{x}_{\text{t}}$.
In addition, the transition lines $\mathcal{T}_{e^N}$ as computed by the e^N-method are considered. These are given in [28], together with the amplification factor distributions for both Tollmien-Schlichting N^{TS} and crossflow instabilities N^{CF} in the laminar boundary $\mathcal{B}_{\text{lam}}$. The locations for the analysis are chosen as points on the computed transition line $\mathcal{T}_{e^N}$ at which the Tollmien-Schlichting instability amplification is $N^{\text{TS}} < 1.0$. Thus, mixed mode transition locations are sidelined.
The points $\vec{x}_{\text{t}} \in \mathcal{T}_{\text{exp}}$ taken into account are defined by the chordwise non-dimensional coordinate $\frac{x}{c}$ and the azimuth angle φ. They are given in figure 4.18. It can be seen that the e^N-transition lines

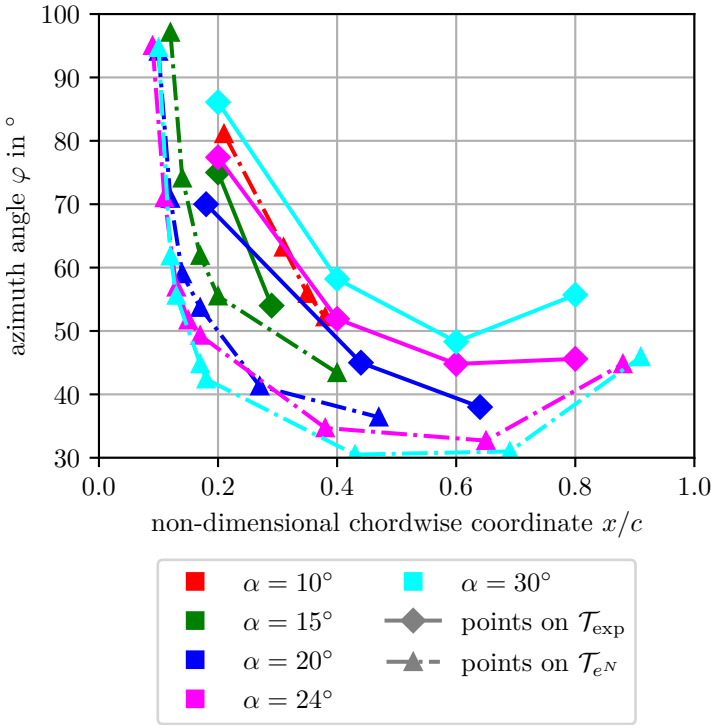

Figure 4.18: Prolate spheroid test case: Evaluation points for CFT

$\mathcal{T}_{e^N}$ are generally more upstream than the experimental ones $\mathcal{T}_{\text{exp}}$. That deviation is described in [28], but could not be resolved. However, in order to assess the differences of the laminar boundary layer at the two transition lines, both the experimental $\mathcal{T}_{\text{exp}}$ and the e^N-transition line $\mathcal{T}_{e^N}$ are used in the analysis.

4.2.8 TU Braunschweig Sickle Wing

Experimental Setup

The *KR01* airfoil was used for the wing of the experiments [46]. It is designed such that on its upper side crossflow vortices are strongly amplified, while Tollmien-Schlichting waves are dampened,

and on the lower side a mix of both crossflow and Tollmien-Schlichting vortices/waves is present. The wing has a distinct shape of a three times abruptly changing sweep angles $\Lambda \in \{30°, 45°, 55°\}$, whereby the streamwise chord length $c = 0.8\,\mathrm{m}$ is constant along the span. The corresponding three sections/swept segments have a span of 0.3 m each. By the spanwise varying sweep angle Λ, different CFT conditions are present per configuration. The wing was not connected to a fuselage, but mounted to the lower wind tunnel wall directly. The model surface roughness is given as $h_{\mathrm{rms}} = 1.47\,\mu\mathrm{m}$.

The wind tunnel of the analysed experiments is the closed-loop *Modell-Unterschallkanal Braunschweig (MUB)*. The test section has a cross section of 1.3 m × 1.3 m.

The measurements were performed for varying angles of attack $\alpha/° \in \{-2.6, 1.2\}$ and Reynolds numbers $\mathrm{Re}_\infty^{c,u_{\mathrm{sw}}}/10^6 \in \{1.75, 2.25, 2.75\}$ based on the streamwise chord length c and the freestream velocity u_∞. The freestream turbulence intensity was $\mathrm{Tu}_\infty \approx 0.17\%$, which is relatively high. It is noted that the configuration angle of attack $\alpha = -2.6°$ and freestream Reynolds number $\mathrm{Re}_\infty^{c,u_{\mathrm{sw}}} = 2.75 \cdot 10^6$ was also used in a similar experiment in another wind tunnel [29]. There, additional information about the configuration is given. It is assumed that this additional information for the corresponding configuration can be taken over for the experiments of [46]. The freestream Mach number was $\mathrm{Ma} = 0.156$ and freestream static temperature was $T_\infty = 22.62\,\mathrm{C°}$.

The pressure and transition measurements were done simultaneously and are reported only for the configurations with the freestream Reynolds number $\mathrm{Re}_\infty^{c,u_{\mathrm{sw}}} = 2.75 \cdot 10^6$ and angle of attack $\alpha \in \{-2.6, 1.2\}$. The transition was detected by measuring the surface temperature of the wing with an infrared camera. In addition, the surface was heated from the inner by a carbon fiber heating layer. This increases the visible difference between the laminar and turbulent boundary layer due to the different wall heat exchange.

Numerical Setup

Only the configuration with angle of attack $\alpha = -2.6°$ and freestream Reynolds number $\mathrm{Re}_\infty^{c,u_{\mathrm{sw}}} = 2.75 \cdot 10^6$ is computed, as for it both transition measurements and a grid for the simulation were available.

The simulation is performed with wind tunnel walls, as the wing is relatively large compared to the test section size. For the simulation domain Ω, the length of the test section is 10 m. The structured grid around the wing is a C-grid, which is embedded in an unstructed grid of the wind tunnel test section.

An overall view of the mesh is given in figure 4.19. The airfoil and the grid around it are shown in figure 4.20. The mesh properties are listed in table 4.8. Due to the low freestream Mach number

Table 4.8: TU Braunschweig Sickle Wing test case: Mesh properties

Mesh property	Value
Total number of nodes N_c	14809654
Number of surface nodes chordwise (upper surface)	≈ 200
Number of surface nodes spanwise (upper surface)	≈ 180
Number of wall normal structured layers	≈ 120
Minimum number of nodes in laminar boundary layer at $\vec{x}_{\mathrm{t,exp}}$	≈ 90
Maximum first node non-dimensional wall normal distance y_1^+	≈ 0.88

$\mathrm{Ma}_\infty < 0.3$, the simulation is done with low-Mach preconditioning (with a general cut-off value of $K_{\mathrm{general}} = 1.5$). In order to get a converging numerical solution, for the first few thousand

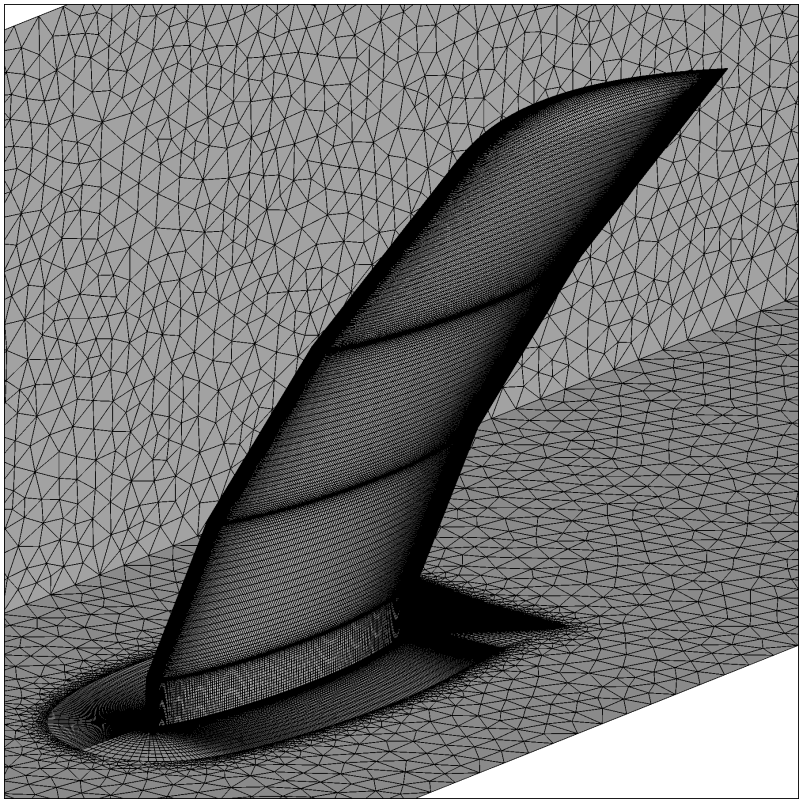

Figure 4.19: TU Braunschweig Sickle Wing test case: Overall view of the grid

pseudo timesteps scalar artificial dissipation must be used. This is due to the large pseudo temporal derivatives at the beginning of the simulation. Afterwards, it is switched to matrix dissipation for higher numerical accuracy.

Validation of the Mean Flow Results

In figure 4.21 the pressure coefficient c_p distributions of the measurements and the simulation are compared. The agreement is very good. The small variations of the pressure coefficient c_p for the upper curves is due to small laminar separation bubbles at the upper surface right before the fixed transition.

Identification of Locations with Crossflow Instability Dominated Transition

Points $\vec{x}_\mathrm{t}$ on the measured transition line $\mathcal{T}_\mathrm{exp}$ were selected for which it is very probable that in the experiments CFT happened at them. For that, newer results for the transition line $\mathcal{T}$ measurements by Kruse et al. from another wind tunnel with same reference conditions, except a lower freestream turbulence intensity Tu_∞, were considered [29]. As the turbulence intensity Tu_∞ is lower, the Tollmien-Schlichting transition is more delayed. As a result of that, the part of the transition line $\mathcal{T}$ of the MUB experiment, that is clearly crossflow instability dominated, can be identified better. The points are chosen in the region of stationary crossflow, which is at the spanwise coordinates where the transition line $\mathcal{T}$ (of the more recent experiment) is saw-tooth-shaped. Only the upper surface of the wing can be considered, as the lower side features TST. The chosen points $\vec{x}_\mathrm{t}$ are depicted in figure 4.22.

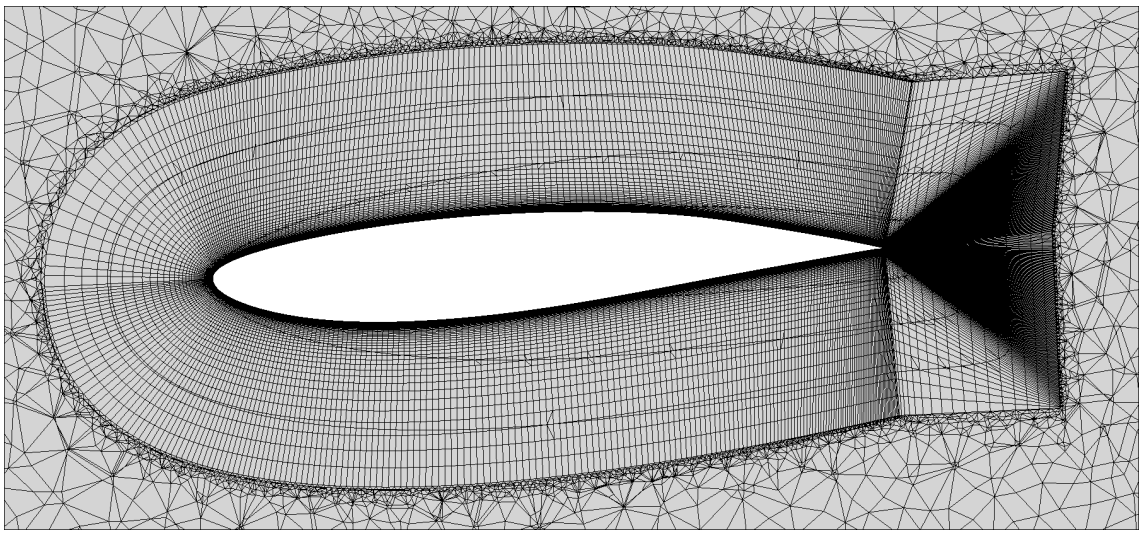

Figure 4.20: TU Braunschweig Sickle Wing test case: View of the grid around the airfoil

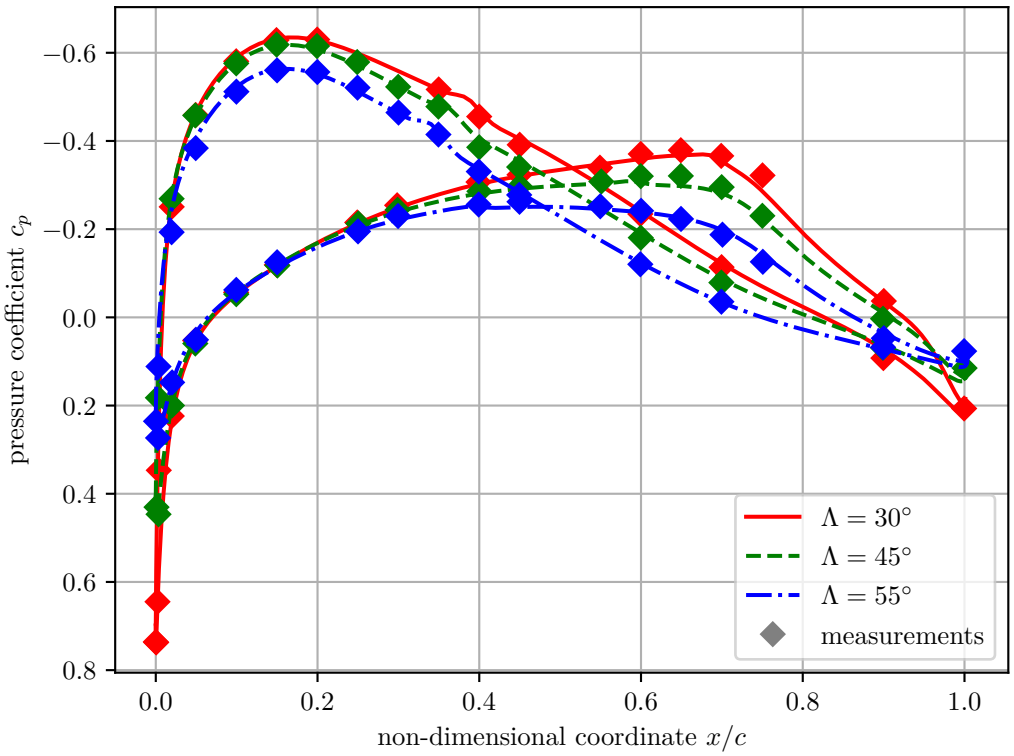

Figure 4.21: TU Braunschweig Sickle Wing test case: Comparison of the measured and computed pressure coefficient c_p distributions

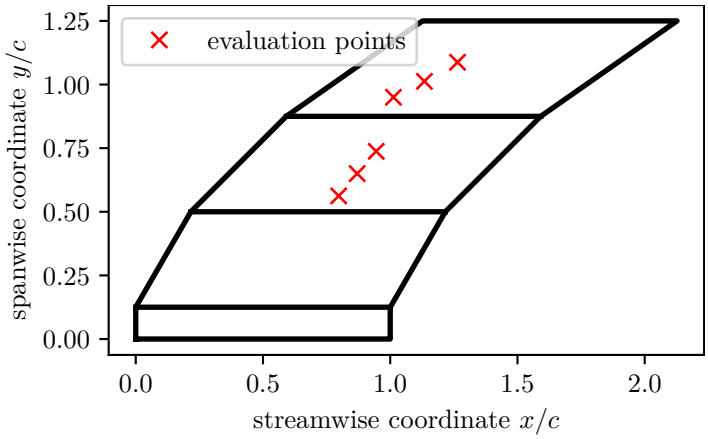

Figure 4.22: TU Braunschweig Sickle Wing test case: Depiction of the analyzed transition locations $\vec{x}_\mathrm{t}$ on the upper surface

5 Assessment of Transition Criteria by Simulations with fixed Transition

In this chapter the assessment of transition criteria for crossflow instability dominated transition is presented. The C1 [3], helicity [19] and Langtry's criterion [31] are analyzed. The approach for the assessment and recalibration is given in detail. The fixed transition analyses for each test case indivually are described. Afterwards, the results for all test cases simultaneously are used to judge the criteria regarding their universality. For both the C1 and Langtry's criteria improved formulations are proposed. The one of the C1 criterion is applied to the relevant test cases and results for the free transition prediction are presented and interpreted.

5.1 Approach

In order to verify or reformulate the CFT criteria, a set of N_m data points (data point index $m = 1, \dots, N_m$) is collected by assessing the laminar boundary layer properties at points $\vec{x}_\Gamma \in \mathcal{T}_{\text{exp}}$ on the reference transition line $\mathcal{T}$ (from experiments or the e^N-method). Then,

$$\underbrace{\text{Re}_{\delta 2,m}(\vec{x}_\Gamma)}_{\frac{u_e \delta_2}{\nu_e}(\vec{x}_\Gamma)} = f_{\text{criterion, C1}}(H_{12,m}(\vec{x}_\Gamma)) \tag{5.1}$$

for the C1 criterion,

$$\max_{y_n \in [0,\delta(\vec{x}_\Gamma)]} \underbrace{\text{Re}_{\text{He},m}(\vec{x}_\Gamma)}_{\frac{y_n^2}{\nu_\mathcal{B}(\vec{x}_\Gamma,y_n)} \frac{\text{He}_\mathcal{B}(\vec{x}_\Gamma,y_n)}{u_\mathcal{B}(\vec{x}_\Gamma,y_n)}} = f_{\text{criterion,He}}(H_{12,m}(\vec{x}_\Gamma)) \tag{5.2}$$

for the helicity criterion, and

$$\begin{aligned} \underbrace{\text{Re}_{\theta,m}(\vec{x}_\Gamma)}_{\frac{\theta\, u_e}{\nu_e(\vec{x}_\Gamma)}} &= \max_{y_n \in [0,\delta(\vec{x}_\Gamma)]} f_{\text{criterion,Langtry}} \left(\text{H}_{\text{CF},m,\mathcal{B}}(\vec{x}_\Gamma, y_n), \frac{h_{\text{rms}}}{\theta_m(\vec{x}_\Gamma)}, R^{\text{turb}}_{m,\mathcal{B}}(\vec{x}_\Gamma, y_n) \right) \\ &\approx f_{\text{criterion,Langtry}} \left(\max_{y_n \in [0,\delta(\vec{x}_\Gamma)]} \text{H}_{\text{CF},m,\mathcal{B}}(\vec{x}_\Gamma, y_n), \frac{h_{\text{rms}}}{\theta_m(\vec{x}_\Gamma)}, R^{\text{turb}}_{m,\mathcal{B}}(\vec{x}_\Gamma, \underset{y_n \in [0,\delta(\vec{x}_\Gamma)]}{\text{argmax}} \text{H}_{\text{CF},\mathcal{B}}(\vec{x}_\Gamma, y_n)) \right) \end{aligned} \tag{5.3}$$

for Langtry's criterion. In the underbraces it is denoted how exactly the parameters are computed from the local variables in the boundary layer $\mathcal{B}$ and the integral boundary layer parameters.
In the vicinity of the transition from the laminar to the turbulent boundary layer state the boundary layer parameters change quickly. As the transition criteria are relevant inside the *laminar* boundary layer, only the variables from the laminar boundary layer upstream of the transition location can be assessed for the recalibration of the transition criteria. This streamwise offset is overcome by performing *fixed transition simulations* with a transition set approximately 10%c (chord c) *downstream* $\vec{x}_{\text{t,ref}} + 0.1c\,\vec{e}_{\text{sw}}$ of the reference (experimental of by e^N-method) transition location $\vec{x}_{\text{t,ref}}$. Then, at the reference transition location $\vec{x}_{\text{t,ref}}$ the laminar boundary layer parameters can be well-evaluated and are assumed to be inaffected by the upstream effects of the transition happening

a little downstream. The approach is accompanied by the assumption that in the simulation the *laminar* boundary layer properties at the reference transition line $\mathcal{T}_{\text{ref}}$ do not change with a downstream shift of the fixed transition line $\mathcal{T}_{\text{fixed}}$. If no reference transition location is known, for example for the opposite wing side, the boundary layer is set to completely turbulent. In addition, no sustaining turbulence is applied according to equation 2.47 because the implementation in the *TAU* solver does not work for fixed transition simulations. As the turbulence intensity $\text{Tu}(\vec{x}_\Omega)\,\forall\vec{x}_\Omega \in \Omega$ is not directly important for the laminar boundary layer velocity profile $u(\vec{x}_\Omega)\,\forall\vec{x}_\Omega \in \mathcal{B}_{\text{lam}}$, it is assumed that freestream turbulence decay does not influence the results of the assessment of the CFT criteria.
The data points of equations 5.1, 5.2 and 5.3 will be plotted in so-called *transition criterion plots*. The plots will be discussed in the following ways:

- If such are available, the results of other authors for the same test cases are compared to the new results of the present work.
- The scatter of the points is quantified by means of the *determination coefficient*

$$R^2(\phi) = \frac{\sum_{m=1}^{N_m} (\hat{\phi}_m - \bar{\phi})^2}{\sum_{m=1}^{N_m} (\phi_m - \bar{\phi})^2}, \tag{5.4}$$

  which, for a given set of points $\{\phi_m\}_{m=1,\dots,N_m}$, its mean $\bar{\phi}$, and the regression value $\hat{\phi}_m$, calculates how well the points are represented by a regression curve. It is $0 \leq R^2 \leq 1$ and the larger the determination coefficient R^2, the less scatter of the data is present. Only in this context of quantifying the data scatter of a single test case, the regression curve is assumed to be a least-squared-error-fitted parabola. The corresponding determination coefficient R^2 is called *parabolic determination coefficient*. Note that a high determination coefficient R^2 does not mean that the transition criterion is "good". Instead, it means that the configurations behave similarly with respect to the flow features. In addition, the determination coefficient R^2 only considers the scatter in terms of the Reynolds number ("vertical scatter"), not the scatter in terms of the shorted distance of a point to the regression curve. Thus, a low determination coefficient R^2 can only be seen as an indication for a highly scattered correlation.
- The curve of the reference formulations of the CFT criteria is plotted, i.e. equation 2.79 for the C1 criterion, equation 2.82 for the helicity criterion and equation 2.93 for Langtry's criterion (the improved version by Venkatachari [71]). For the latter a constant non-dimensionalized surface roughness $\frac{h_{\text{rms}}}{\theta} = 0.004$ is chosen arbitrarily, which corresonds to a polished surface for certain test cases [31]. If the non-dimensionalized surface roughnesses of the individual configurations are different (which is always the case, as the momentum thickness θ differ), the CFT momentum thickness Reynolds number Re_θ is calculated back to the one of a non-dimensional surface roughness of $\frac{h_{\text{rms}}}{\theta} = 0.004$ as

$$\text{Re}_{\theta,0.004} = \text{Re}_{\theta,h_{\text{rms}}} - f_{\text{roughness}}\left(\frac{h_{\text{rms}}}{\theta}\right) + f_{\text{roughness}}\left(0.004\right). \tag{5.5}$$

  This allows a direct comparison of the data points to the reference curve. If no surface roughness is known for the experiment, a painted surface (RMS roughness $h_{\text{rms}} = 3.3\,\mu\text{m}$) is assumed according to [31]. Note that the reference curve is plotted for a viscosity ratio $R^{\text{turb}} = 0$, as the boundary layer is laminar.
- The sensitivitiy of the transition prediction is judged by means of "errorbars". These do not

stand for any error, but are used to assess the change of the boundary layer parameters, when moving upstream by $5\%c$ (chord length c) from the experimental transition line $\mathcal{T}_{\mathrm{exp}}$. The shift is done only upstream, as downstream the nearby happening transition due to the fixed transition simulation may distort the laminar boundary layer velocity profile $u(\vec{x}_\Omega)\,\forall\vec{x}_\Omega \in \Omega$. It is assumed that the general behaviour $5\%c$ downstream is the same as $5\%c$ upstream, so additional errorbars for the downstreamwise shift would not yield new information, anyway. One can think of fictitious errorbars which are appended to the points for the downstream shift. The length of the horizontal errorbars is proportional to the change of the argument of the transition criterion. The length of the vertical errorbars is proportional to the change of the *difference* $\Delta\mathrm{Re}_\phi = \mathrm{Re}_{\phi\mathrm{t}} - \mathrm{Re}_\phi$ between the transition Reynolds number $\mathrm{Re}_{\phi\mathrm{t}}$ (placeholder ϕ) coming from the evaluation of the transition criterion and the local computed Reynolds number Re_ϕ.[1] To be precise:

$$\text{vertical errorbar length} = \Delta\mathrm{Re}_\phi(\vec{x}_\Gamma - 5\%c\,\vec{e}_{\mathrm{sw}}) - \Delta\mathrm{Re}_\phi(\vec{x}_\Gamma)\ \forall\vec{x}_\Gamma \in \mathcal{T} \tag{5.6}$$

The Reynolds numbers may change, if the model itself and/or the numerical solution of the model are inaccurate. If the errorbars are long, the *criterion-predicted transition location*

$$\vec{x}_{\mathrm{t,criterion}}(\vec{x}_\Gamma) = \underset{\vec{\tilde{x}}_\Gamma \in \mathcal{S}_{\mathcal{E}\to\Gamma}(\vec{x}_\Gamma)}{\arg} \left(\Delta\mathrm{Re}_\phi(\vec{\tilde{x}}_\Gamma) = 0\right)\ \forall\vec{x}_\Gamma \in \Gamma. \tag{5.7}$$

is *insensitive* to a change in $\mathrm{Re}_{\theta\mathrm{t}}(\vec{x}_{\mathrm{t,criterion}})$ or $\mathrm{Re}_\theta(\vec{x}_{\mathrm{t,criterion}})$, which is good.[2] If data points deviate strongly from the theoretical curve given by the criterion, possible reasons for that are discussed. A point is considered as deviating strongly from the reference curve if the reference curve is not intersecting the *vertical* errorbar of the respective point.

Since many simulations are analyzed in this work (≈ 1000), Python classes are written for this thesis that allow an efficient postprocessing: The *TAU results* class describes a general TAU simulation. It has attributes and methods that can be used to automatically detect the convergence of the computation. In addition, routines for reading out the boundary layer variables along chosen surface curves/cross sections from the *TAU* solution files and saving them as *NumPy* arrays are implemented. Note that due to a bug in the PyTecplot library of Tecplot Inc., the variables in the boundary layer $\mathcal{B}$ are read out only by means of a *nearest neighbor* (NN) algorithm, rather than a linear interpolation between the grid points of the actual grid. The probe points are distributed on an equidistant grid of points between the wall Γ and the boundary layer edge $\mathcal{E}$. As the grid from the CFD simulations is very fine in wall normal direction, the influence is expected to be low. However, a grid convergence study for the probe points is performed for the NLF(2)-0415 test case. It is found that the number of points in wall normal direction should be at least 16.
A subclass of *TAU results*, called *crossflow test case*, adds attributes to it that uniquely describes a test case, i.e. reference conditions, chord length c and so on. In addition, methods are added for the computation of the variables needed for the analysis, for example Reynolds numbers defined on the surface Γ or in the whole boundary layer $\mathcal{B}$. Plotting methods are added, that allow the easy plot of chordwise distributions, for example of the pressure coefficient c_p.
Another class, called *parameter variation*, holds a list of *test case* objects as an attribute. It can

[1] See appendix E.

[2] It is highlighted that the length of the vertical errorbar is *not* the streamwise change of the computed Reynolds number Re_ϕ. It was decided to use equation 5.6 for the vertical errorbars because the sensitivity of the criterion-predicted transition location $\vec{x}_{\mathrm{t,criterion}}$ on a change of the Reynolds numbers can be seen more easily.

be used to automatically create several types of plots, for example transition criterion plots, or automatically create tables of the sets of reference conditions for clear CFT cases, that are taken into account for the analysis.

5.2 Results for Individual Test Cases

The results are sorted by the analyzed wings/bodies. For each of them, the transition criterion plots are presented and discussed for the C1, the helicity and Langtry's criterion for CFT.

5.2.1 ONERA D Infinite Swept Wing

C1 Criterion

The CFT criterion plot for the C1 criterion is given in figure 5.1. As can be seen, the new data points are in general higher and closer to the curve of the transition criterion. In the paper of Arnal et al. [3] there is also a point with a very high shape factor $H_{12} > 2.6$. Unfortunately, the corresponding case configuration is unknown, so it is impossible to find out why this point cannot be reproduced. Probably the corresponding configuration is one that did not converge due to a laminar separation bubble.
For each point, the criterion curve of the CFT criterion roughly intersects the vertical error bars. This means that the error in the transition criterion regression in term of the transition location is less than/about 5%c and therefore, the deviation from the criterion curve can be indentified as being relatively small.
The determination coefficient for a parabola fit is $R^2_{\text{ONERA D, C1}} = 0.857$.

Helicity Criterion

The CFT criterion plot for the helicity criterion is given in figure 5.2. The comparison with the points of the original calibration [19] shows that the new points have higher shape factors H_{12} and lower helicity Reynolds numbers Re_{He}. This could be due to the improved numerical setup.
The points are not so close to the criterion curve as the original points. Under consideration of the error bars the error in the transition location is less than 5%c for about half of the configurations. The parabolic determination coefficient for the helicity criterion data is $R^2_{\text{ONERA D, helicity}} = 0.546$, which is the lowest of the three criteria assessed. This is due to the two outliers for $(\Lambda, \text{Re}_\infty^{c_n,u_n}) = (50°, 10^6)$ and $(55°, 0.8 \cdot 10^6)$ (e^N-transition locations). These points are also notable in the transition criterion plot of the C1 criterion, but with less deviation from the other points. This indicates that the individual configurations for this test case do not behave similary with respect to the helicity criterion, but rather with respect to the C1 criterion.

Langtry's Criterion

The CFT criterion plot for Langtry's criterion is given in figure 5.3. This time, the error bars show that the points are farther distant to the criterion curve than for the other criteria. This means that for most of the configurations the predicted transition location would by wrong by more than 5%c. But the data is the least scattered from the three criteria, as the parabolic determination coefficient is $R^2_{\text{ONERA D, Langtry}} = 0.944$.

5.2.2 NLF(2)-0415 Infinite Swept Wing

C1 Criterion

The CFT criterion plot for the C1 criterion is given in figure 5.4. As can be seen, the lower the roughness h_{rms}, the higher the crosswise displacement thickness Reynolds number $\mathrm{Re}_{\delta 2}$ for a given shape factor H_{12}, which corresponds to a downstream shift of the transition location $\vec{x}_{\mathrm{t}}$. If for each of the different roughnesses h_{rms} separately regression curves were drawn, the parabolic determination coefficient $R^2 > 0.96$ would be very high. In addition, the regression curves would intersect the vertical errorbars. Thus, the scattering is very little and the points can be correlated strongly.
Apparently for low shape factors H_{12} the curve of the C1 criterion gives too low values. When coming from the right-hand side (from positive shape factors H_{12}), the abolute value of the slope of the curve should increase rather than decrease in order to follow the data points.
Attention is called on the fact that the horizontal errobars are pointing to the right. This means that the shape factor H_{12} is decreasing at the transition location $\vec{x}_{\mathrm{t}}$.

Helicity Criterion

The CFT criterion plot for the helicity criterion is given in figure 5.5. The comparison of the respective points for the highest roughness to the ones of the original calibration by Grabe et al. [19] shows a very good agreement. As the new data points are more, it is more obvious that the slope of a regression curve have to be slightly steeper.
The determination coefficients for the roughnesses $h_{\mathrm{rms}} = (0.25,\, 0.50,\, 3.30)\,\mu\mathrm{m}$ are $R^2 = (0.82, 0.97, 0.94)$, which is very high, except for the lowest roughness h_{rms}. The errorbars support the observation that the helicity criterion is well suited to predict the transition for the NLF(2)-0415 configurations with the highest roughness.

Langtry's Criterion

The CFT criterion plot for Langtry's criterion is given in figure 5.6. The points for the different surface roughnesses h_{rms} have almost the same momentum thickness Reynolds number Re_{θ}. This shows that the idea of the Langtry's criterion to take into account the different roughnesses h_{rms} (and of plotting them for $\frac{h}{\theta} = 0.004$) works well. In addition, the points have approximately the same non-dimensional crossflow strength H_{CF}. Thus they collapse to almost a single point at $(H_{\mathrm{CF}}, \mathrm{Re}_{\theta}) \approx (0.10, 645)$. This is why the parabolic determination coefficient $R^2 = 0.62$ (for all roughnesses h_{rms} together) is not close to 1. On the one hand, the collapsing point reveals itself as being significant, which indicates that the regression curve should cover it. On the other hand, this yield less information about how the transition criterion curve should be shaped for other non-dimensional crossflow strengths than $H_{\mathrm{CF}} \approx 0.10$.
The points are far distanced to the curve of the criterion, in absolute values by $\Delta\mathrm{Re}_{\theta} \approx 145$, and also relative to the lengths of errorbars. The errorbars in general are very short compared to the other test cases (see for example figure 5.3 for the *ONERA D* airfoil). This is because the streamwise slopes of the transition momentum thickness Reynolds number $\partial_{\mathrm{sw}}\mathrm{Re}_{\theta \mathrm{t}}$ and computed momentum thickness Reynolds number $\partial_{\mathrm{sw}}\mathrm{Re}_{\theta}$ are very similar at the measured transition location $\vec{x}_{\mathrm{t,exp}}$. This is a second reason for the necessity that the curve of the transition criterion should cover the point cluster $(H_{\mathrm{CF}}, \mathrm{Re}_{\theta}) \approx (0.10, 645)$.

5.2.3 NACA 64_2A015 Infinite Swept Wing

C1 Criterion

The CFT criterion plot for the C1 criterion is given in figure 5.7.
It can be seen that the more positive the angle of attack α, the larger the shape factor H_{12} at the measured transition location $\vec{x}_\mathrm{t}$. In addition, the higher the sweep angle Λ, the higher the crosswise displacement thickness Reynolds number $\mathrm{Re}_{\delta 2}$ at the transition location. This is expected, as the crosswise displacement thickness Reynolds number $\mathrm{Re}_{\delta 2}$ contains the crosswise displacement thickness δ_2, which is increasing with the sweep angle Λ, because the crossflow becomes larger.
The new points and the points from the original calibration of Arnal et al. [3] are located similarly, albeit the new points are concentrated in a region where only a few points from Arnal et al. [3] exist.
Many points are close to the curve of the transition criterion, measured by the errorbar lengths, but many others are not, especially for high shape factors H_{12}. This is why the parabolic determination coefficient is only $R^2 = 0.46$.

Helicity Criterion

The CFT criterion plot for the helicity criterion is given in figure 5.8. The qualitative results are the same as for the C1 criterion. The parabolic determination coefficient is $R^2 = 0.33$, which is rather low.

Langtry's Criterion

The CFT criterion plot for Langtry's criterion is given in figure 5.9. The points cover a wide range of non-dimensional crossflow strengths H_CF. It can be seen that the higher the angle of attack α, the higher the momentum thickness Reynolds number Re_θ at the experimental transition location $\vec{x}_{\mathrm{t,exp}}$. With increasing sweep angle Λ the non-dimensional crossflow strength H_cf gets larger, which is expected. In addition, the momentum thickness Reynolds number Re_θ at the transition location $\vec{x}_\mathrm{t}$ gets smaller.
The scatter of the data is little, as the curve of the transition criterion intersects the vertical errorbars, when the errorbars are "copied" and appended to the points for a fictitious downstreamwise shift. The points can be very well correlated by a parabola, as the corresponding determination coefficient is $R^2 = 0.97$. So the formulation of the Langtry's criterion seems to take into account parameters meaningful to CFT.

5.2.4 HQ26N/14.82 Infinite Swept Wing

C1 Criterion

The CFT criterion plot for the C1 criterion is given in figure 5.10. It is visible that the points for the curved upper wing side yield higher displacement thickness Reynolds numbers $\mathrm{Re}_{\delta 2}$ than the points for the flat lower wing side. This matches the observation for the e^N-method without curvature terms, as the transition would be predicted too upstream on the upper side, if the same criterion as for the lower wing side was applied. Furthermore, the points on the upper wing side feature similar crosswise displacement thickness Reynolds numbers $\mathrm{Re}_{\delta 2} \approx 140$ at the experimental transition location $\vec{x}_{\mathrm{t,exp}}$. At the transition locations $\vec{x}_{\mathrm{t,exp}}$ on the lower wing side the points also have almost the same displacement thickness Reynolds number $\mathrm{Re}_{\delta 2} \approx 115$. In general, the point deviates

strongly from the curve of the transition criterion (measured by the errorbar lengths). Only for the angles of attack $\alpha = -2.01°$ and $\alpha = 6.59°$ the criterion curve intersects the vertical errorbars. The parabolic determination coefficient $R^2 = 0.04$[3] for the points on both sides of the wing together is very low. If only the points on the lower wing side are considered, the determination coefficient $R^2 = 0.08$ is not much higher. The values are vey low due to the large variation of the shape factor H_{12} of the data points.
Concludingly, for the HQ26N/14.82 test case the correlation $\mathrm{Re}_{\delta 2}(H_{12})$ seems to be not meaningful for the CFT.

Helicity Criterion

The CFT criterion plot for the helicity criterion is given in figure 5.11. The same result as for the C1 criterion is true. The parabolic determination coefficient $R^2 < 0.03$ is very low (for the points of both sides together and also if only the data for the lower surface is considered).

Langtry's Criterion

The CFT criterion plot for Langtry's criterion is given in figure 5.12. The results are suprisingly good, when compared to the C1 criterion and the helicity criterion. It seems that Langtry's criterion uses variables for the transition criterion that are more meaningful. There is no big difference between the points of the upper and the lower wing side. In addition, the parabolic determination coefficient $R^2 = 0.92$ is very high. So the scatter for the formulation of a transition criterion is low with respect to the value of the momentum thickness Reynolds number Re_θ. But, when the relatively small lengths of the errorbars are taken into account, it can be seen that, for the majority of the points, the scatter is large with respect to the transition location sensitivity. This means that the original transition criterion will predict wrong transition locations by more than $5\%c$.

5.2.5 Infinite Swept Cylinder

C1 Criterion

The CFT criterion plot for the C1 criterion is given in figure 5.13. First, the data is compared to the points for the swept cylinder in the paper of Arnal et al. [3]. The agreement is good, albeit less points for high shape factors $H_{12} > 2.4$ are present in the new set of points.
The scatter of the new data is very low (parabolic determination coefficient $R^2 = 0.94$).
The errorbars are long compared to other ones of the other test cases analyzed, which is good, as the predicted transition location $\vec{x}_{\mathrm{criterion}}$ is insensitive to a change of the Reynolds number. But in the this thesis the sensitivity is measured in terms of $\left(\frac{x}{c}\right)_{\mathrm{thesis}}$, where x is the chordwise coordinate. As the non-dimensional transition locations $\frac{x}{c} \approx 0.1$ are very small, it is no longer approximatedly physically meaningful to look only onto the chordwise coordinate. It would be better (but is not done here) to look onto the streamwise coordinate $\frac{s}{c} = \left(\frac{x}{c}\right)_{\mathrm{Poll}}$ (as Poll did [47], see equation 4.5).
Interestingly, the swept cylinder flow does not follow the trend at low shape factors H_{12} as observed for the NLF(2)-0415 infinite swept wing and TELFONA Pathfinder wing. The swept cylinder has the transition more upstream (at lower crosswise displacement thickness Reynolds numbers $\mathrm{Re}_{\delta 2}$), similar to the 6:1 prolate spheroid (section 4.2.7). This could be explained by the streamline curvature instability, which causes an early transition. In the overview paper of Saric et al. [55] it is said "These flows are referred to as *swept cylinder flows* to distinguish them from both swept

[3] At these low values the determination coefficient is generally not meaningful anymore.

wing and attachment line flows." (emphasized by the author of the thesis). This indeed indicates that the swept cylinder test case features another type of natural transition than CFT.

Helicity Criterion

The CFT criterion plot for the helicity criterion is given in figure 5.14. The qualitative results and interpretation are the same as for the C1 criterion. The criterion curve does not represent the points very well, but is still good with regard to the long errorbars of the points. The parabolic determination coefficient $R^2 = 0.94$ is again very high.

Langtry's Criterion

The CFT criterion plot for Langtry's criterion is given in figure 5.15. The points do more or less collapse around $(H_{\mathrm{CF}}, \mathrm{Re}_\theta) \approx (0.188, 355.0)$, which means that this point is very characteristic for the *swept cylinder* flow and should be covered by the Langtry's criterion. On the other side, it does not provide much information needed for a formulation of a criterion regression curve for a larger range of non-dimensional crossflow strengths H_{CF}.
For Langtry's criterion the swept cylinder points behave different than the data points for the NLF(2)-0415 swept wing and TELFONA Pathfinder wing (the argument of the CFT criterion is different). This is a contrast to the other two CFT criteria assessed. A possible conclusion from that: the Langtry's criterion is capable of capturing streamline-curvature-instability-triggered transition.
The parabolic determination coefficient is $R^2 = 0.20$, which is a low value. This is because the range of non-dimensional crossflow strengths H_{CF} of the points is low.

5.2.6 TELFONA Pathfinder Wing

C1 Criterion

The CFT criterion plot for the C1 criterion is given in figure 5.16. The point distributions are showing different trends for the upper and lower wing side as well as with and without the use of the transition location by the e^N-method or the experiment. There is no tendency of the point locations with the lift coefficient c_L. It can be seen that the points for the lower wing side behave similarly than the ones for the NLF(2)-0415 infinite swept wing: the points tend to show larger crosswise displacement thickness Reynolds numbers $\mathrm{Re}_{\delta 2}$ than the criterion curve for low shape factors H_{12}. The e^N-point for the lower wing side can be correlated more or less well with the experimental points for the lower wing surface.
The upper wing side points also feature higher crosswise displacement thickness Reynolds numbers $\mathrm{Re}_{\delta 2}$ at the transition location than the curve of the criterion. The errorbars are short compared to the deviation from the reference curve.
Attention is called on the fact that the horizontal errobars are pointing to the right. This means that the shape factor is decreasing at the transition location $\vec{x}_{\mathrm{t}}$.
The parabolic determination coefficient for the points on the lower wing side is $R^2 = 0.82$, which is high and indicates a strong relation between the points.

Helicity Criterion

The CFT criterion plot for the helicity criterion is given in figure 5.17. The qualitative results are the same as for the C1 approach. The parabolic determination coefficient for the lower wing side

points is $R^2 = 0.65$. If all points are taken into account, the parabolic determination coefficient is $R^2 = 0.53$.

Langtry's Criterion

The CFT criterion plot for Langtry's criterion is given in figure 5.18. For this criterion, the points for the upper and lower wing side visually correspond to each other. Nevertheless, the parabolic determination coefficient for the points of both wing sides together is only $R^2 = 0.66$, which is because the quality of the regression is only evaluated in terms of the crosswise displacement thickness Reynolds number $\mathrm{Re}_{\delta 2}$ (vertical direction).
The points deviate from the reference curve, as (most of) the points are distanced far from the curve relative to the errorbar lengths. So a recalibration of the curve is helpful.

5.2.7 Inclined 6:1 Prolate Spheroid

Note that for this test geometry the properties are evaluated along the wall-projected boundary layer edge streamlines $\mathcal{S}_{\mathcal{E}\to\Gamma}(\vec{x}_\mathrm{t})$ through the selected points $\vec{x}_\mathrm{t} \in \mathcal{T}_\mathrm{exp}$ on the transition line $\mathcal{T}_\mathrm{exp}$. For the highest angle of attack, these virtual streamlines are depicted in figure 5.19 (flow coming from the lower left-hand side). As can be seen, on the upper side a flow detachment is happening.

C1 Criterion

The CFT criterion plot for the C1 criterion is given in figure 5.20. It is notable that no errorbars were plotted. This is because of their high lengths, in particular with increasing angle of attack α, which makes the plot less clear. The long errorbars are explained by the fact that the properties of the boundary layer $\mathcal{B}$ are evaluated along the wall-projected boundary layer edge streamlines $\mathcal{S}_{\mathcal{E}\to\Gamma}$. The upstream shift by "5%c" is large compared to the $\mathcal{S}_{\mathcal{E}\to\Gamma}$-wise distance between the attachment line on the lower symmetry line and the flow detachment near the upper symmetry line, what decreases with increasing angle of attack α.
It is remarkable that the points for the measured transition line $\mathcal{T}_\mathrm{exp}$ (parabolic determination coefficient $R^2 = 0.90$) are more or less following the criterion curve. But not so the points for the e^N-transition line $\mathcal{T}_{e^N}$ (parabolic determination coefficient only $R^2 = 0.37$), which exhibit a slightly decreasing crosswise displacement thickness Reynolds number Re_{delta2} for decreasing shape factor H_{12}. This is because the e^N-transition lines $\mathcal{T}_{e^N}$ is generally more upstream, where the crosswise displacement thickness δ_2 is smaller (as the boundary layer is thinner).
So, judging based on the C1 criterion, the experimental transition line $\mathcal{T}_\mathrm{exp}$ is the "correct" one. On the other hand, the local C1 approach, i.e. the local approximation of the crosswise displacement thickness Reynolds number $\mathrm{Re}_{\delta 2}$ and the shape factor H_{12}, is based on the FSC boundary layer solutions (see appendix D.2). This is why the local C1 approach will fail to predict the transition line $\mathcal{T}$ for the spheroid, regardless of how "good" the transition criterion is.
In addition, it is interesting that the trend of the points is in agreement with the criterion curve, even if the shape factors H_{12} for these cases are low. This is contrary to the results for the NLF(2)-0415 airfoil and the TELFONA Pathfinder wing. These two cases are long/infinite swept wing flows. The curvature of the surface is significantly lower than for the spheroid, which is more similar to the swept cylinder. This may explain the generally different behaviour for low shape factors H_{12}: For strongly curved surfaces (as for the spheroid and the swept cylinder), the streamline curvature instability may cause early transition. This is not the same effect as for the upper side of the

HQ26N/14.82 wing: Here it is found that the inclusion of curvature terms into the linear stability analysis/e^N-method shifts the transition downstream, as the concave curvature acts stabilizing [66].

Helicity Criterion

The CFT criterion plot for the helicity criterion is given in figure 5.21. Reference points are available from the paper of Grabe et al. [19]. The new points for the experimental transition line $\mathcal{T}_{\text{exp}}$ behave similarly (high parabolic determination coefficient $R^2 = 0.81$), except that they are offsetted to lower helicity Renolds-numbers Re_{He} by about $\Delta\text{Re}_{\text{He}} \approx 25$. This may be due to an improved numerical setup.
Albeit the offset, the criterion curve follows the new points well, in contrast to the points for the predicted transition line $\mathcal{T}_{e^N}$. This implies again that the "true" transition line is the experimental one $\mathcal{T}_{\text{exp}}$ rather then the one predicted by the e^N-method $\mathcal{T}_{e^N}$ (for which the parabolic determination coefficient $R^2 = 0.50$ is rather low, anyway).
Beside this information, the same observations and interpretations as for the C1 criterion hold.

Langtry's Criterion

The CFT criterion plot for Langtry's criterion is given in figure 5.22. It can be seen that the points are relatively close to each other. The points for the experimental transition line $\mathcal{T}_{\text{exp}}$ yield only slightly higher momentum thickness Reynolds numbers Re_θ than for the line $\mathcal{T}_{e^N}$ from the linear stability analysis.
In addition, the trend of the points is predicted well by the criterion curve, which even covers the "kink" of the point distribution (which is only evident if the points from both the experimental $\mathcal{T}_{\text{exp}}$ and the computed transition line $\mathcal{T}_{e^N}$ are taken into account).
The parabolic determination coefficient is only $R^2 = 0.54$, which is medium good. Thus, scatter of the data is present.

5.2.8 Sickle Wing

C1 Criterion

The CFT criterion plot for the C1 criterion is given in figure 5.23. It can be seen the the points for section C (outmost swept section) has very good agreement with the curve, which intersects the vertical errorbars. Thus, the error of the predicted transition location $\vec{x}_{\text{t,criterion}}$ due to the regression is smaller than $5\%c$. In contrast, the points for section B (middle swept segment) are far distanced to the curve. That is because the absolute value of the crosswise displacement thickness δ_2 is actually larger in section B than in section C.
The definition of parabolic determination coefficients R^2 for the two sections individually does not make sense because there are only three points to which a parabola can be fitted exactly.

Helicity Criterion

The CFT criterion plot for the helicity criterion is given in figure 5.24. The qualitative results are the same as for the C1 criterion.

Langtry's Criterion

The CFT criterion plot for Langtry's criterion is given in figure 5.25. The points for section B seem to collapse. This is not the case for the points of section C. Nevertheless, a correlation that takes

into account the points from both section B and C is better possible than for the C1 or the helicity criterion. The parabolic determination coefficient for all points together is $R^2 = 0.56$.
In general the errorbars are very short. This is bad because this means that Langtry's approach is incapable of predicting the correct transition location $\vec{x}_\mathrm{t}$ for this test case.

5.3 Synopsis of the Test Cases

In this section the criteria are assessed by means of comparisons among the several test campaigns. Abnormalities among the individual configurations of a given test case with regard to the transition criterion plots were explained in section 5.2. This is why, in the following plots, the different configurations of the individual data points of a test case are not distinguished by different colors/markers anymore.

5.3.1 C1 Criterion

The C1 criterion plot is given in figure 5.26. The CFT is mostly important on wing-like objects, which is why the transition criterion is reformulated for low shape factors $H_{12} < 2.43$ in order to follow better the points for the TELFONA Pathfinder wing and the NLF(2)-0415 swept wing, rather than the points of the swept cylinder and the spheroid. For higher shape factors $H_{12} \geq 2.43$ the original formulation is kept, as no significant improvements can be proposed. The improved criterion function reads

$$f_{\text{criterion, C1}}(H_{12}(\vec{x}_\Gamma)) = \begin{cases} (4.107H_{12} - 4.550H_{12}^2 + 1.660H_{12}^3 - 0.1987H_{12}^4) \cdot 10^5 & \text{if } H_{12}(\vec{x}_\Gamma) \leq 2.43 \\ \frac{300}{\pi}\arctan\frac{0.106}{(H_{12}(\vec{x}_\Gamma)-2.3)^{2.052}} & \text{otherwise} \end{cases} \quad \forall \vec{x}_\Gamma \in \Gamma. \tag{5.8}$$

The equation is found by computing a polynomial of appropriate degree by means of chosen values and derivatives (similar to a hermite interpolation). From the NLF(2)-0415 data the points of the highest surface roughness are used, in order to be consistent with the default assumption of a painted surface with a RMS roughness of $h_\mathrm{rms} = 3.3\,\mu\mathrm{m}$.
The function is continuously differentiable (smooth) at $H_{12} = 2.43$. It is assumed, that the physics behind the model behave continuously differentiable in all variables. But in the solver the derivative $\frac{\partial \mathrm{Re}_{\delta 2\mathrm{t}}}{\partial H_{12}}$ is not needed, anyway.
In addition, the function is limited from above by $\mathrm{Re}_{\delta 2\mathrm{t,max}} = 200$, as no extensive extrapolation shall be done and no data points for lower shape factors H_{12} are available. No extensive extrapolation shall be done because this could lead to unphysical laminar separations in simulations with low shape factors H_{12}, likely causing the numerical solution to diverge.
The following test cases are not covered by the improved C1 criterion:

- Inclined 6:1 prolate spheroid test case for the experimental transition line $\mathcal{T}_\mathrm{exp}$ and infinite swept cylinder test case for low shape factors H_{12}: This is maybe another instability mechanism (streamline curvature instability)
- Inclined 6:1 prolate spheroid test case for the e^N-transition line $\mathcal{T}_{e^N}$: the transition lines $\mathcal{T}_{e^N}$ based on the e^N-method are assumed to be wrong
- TELFONA Pathfinder wing test case, upper wing side: The crosswise displacement thickness Reynolds number Re_δ is very high for moderately high shape factors H_{12}. This can be explained by a too coarse mesh (see table 4.6)

- Sickle Wing test case, middle swept segment: The crossflow is stronger than in the outer segment, but the shape factors H_{12} are larger, too
- HQ26N/14.82 test case, lower wing side: The lower wing side is very flat, which influences the CFT in a unknown manner

It must be note that the local C1 approach is known to be rather inaccurate for low shape factors H_{12} (figure 2 of [19]).

5.3.2 Helicity Criterion

The plot of the helicity criterion is shown in figure 5.27. No improved criterion curve is drawn into it. There is too much difference among the several test cases. For example, the *NACA 64$_2$A015* points are higher than expected based on the points of the ONERA D infinite swept wing, NLF(2)-0415 infinite swept wing, and TELFONA Pathfinder wing. In contrast, the prolate spheroid points (for the experimental transition line $\mathcal{T}_{\mathrm{exp}}$) are lower than expected. The local helicity approach is derived from the local C1 approach [19]. The derivation contains certain neglections. Maybe these approximations let the helicity criterion perform worse than the C1 criterion.

5.3.3 Langtry's Criterion

Langtry's criterion plot is presented in figure 5.28. When judging based on the differences between the different test campaigns, the parameters chosen by Langtry et al. [31] to formulate the CFT criterion work surprisingly well, compared to the C1 and the helicity criterion. In particular the TELFONA Pathfinder wing (except for the upper surface), NACA 64$_2$A015 infinite swept wing, HQ26N/14.82 infinite swept wing, ONERA D infinite swept wing and prolate spheroid (experimental transition line $\mathcal{T}_{\mathrm{exp}}$) test cases behave consistently with respect to the parameters of Langtry's criterion.
However, some points for the Sickle Wing test case (both sections B and C) are too high with respect to the criterion curve. With similar values of the non-dimensional crossflow strength H_{CF} and momentum thickness Reynolds number Re_θ, that is also true for the clustering point $(H_{\mathrm{CF}}, \mathrm{Re}_\theta) \approx (0.10, 645)$ of the NLF(2)-0415 test case. That clustering point is highly significant, as many configurations with very short errorbars are contained in it.[4]
It can be seen in figure 5.28 that the points of the prolate spheroid and the infinite swept cylinder, as well as the NLF(2)-0415 infinite swept wing and TELFONA Pathfinder wing test cases are covered by a single correlation. This in contrast to the C1 and the helicity criterion. The following competing explanations for that are offered:

- The hypothesis that the prolate spheroid and the infinite swept cylinder test cases feature another type of transition than CFT is wrong. In this case the reason for the deviation of the prolate spheroid and the infinite swept cylinder points from the C1 criterion curve must be explained differently than with streamline curvature instability dominated transition.
- The transition on the prolate spheroid and the infinite swept cylinder is indeed streamline curvature instability dominated. In terms of the variables relevant for the Langtry criterion the streamline curvature instability and the crossflow instability dominated transition are smoothly merging into each other at high non-dimensional crossflow strength $H_{\mathrm{CF}} > 0.125$. This is where the curve of the criterion becomes approximately horizontal, whereby it has a parabolic shape for lower non-dimensional crossflow strength $H_{\mathrm{CF}} \leq 0.125$.

[4] In addition some points for prolate spheroid are also in the region $(H_{\mathrm{CF}}, \mathrm{Re}_\theta) \approx (0.10, 600)$, but the points correspond to the transition line computed by the e^N method, so they are disregarded.

- That a single correlation works for the prolate spheroid, the infinite swept cylinder, the NLF(2)-0415 infinite swept wing and TELFONA Pathfinder wing test cases has not directly anything to do with CFT, but must be explained by other properties the test cases have in common. This hypothesis is supported by the fact that the vertical errorbars were generally rather short for Langtry's criterion, which means that the correlation is approximately fulfilled for large parts of the wing surface Γ.[5]

An improved formulation for Langtry's criterion is proposed, for which in particular some points of the ONERA D test case are disregarded:

$$f_{\text{criterion,Langtry}}\left(H_{\text{CF}}, \frac{h_{\text{rms}}}{\theta} = 0.004, R^{\text{turb}} = 0\right) = -276.1\ln(H_{\text{CF}} - 0.03312) - 179.1. \tag{5.9}$$

The curve for the new correlation equation 5.10 is also plotted in figure 5.28. In order to use equation 5.10 for other non-dimensional roughnesses $\frac{h_{\text{rms}}}{\theta} \neq 0.004$, equation 5.5 must be applied backwards. In addition, in order to include the viscosity ratio $R^{\text{turb}} > 0$ in a similar manner as in [31], H_{CF} may be replaced by $\Delta H_{\text{CF}}(H_{\text{CF}}, R^{\text{turb}})$ (equation 2.88). The resulting formulation is

$$\begin{aligned} f_{\text{criterion,Langtry}}\left(H_{\text{CF}}, \frac{h_{\text{rms}}}{\theta}, R^{\text{turb}}\right) = &-276.1\ln(\Delta H_{\text{CF}}(H_{\text{CF}}, R^{\text{turb}}) - 0.03312) - 179.1 \\ &- f_{\text{roughness}}\left(0.004\right) + f_{\text{roughness}}\left(\frac{h_{\text{rms}}}{\theta}\right). \end{aligned} \tag{5.10}$$

5.4 Application of the Adapted C1 Criterion for Free Transition Prediction

In the *TAU* solver the original C1 criterion is replaced by equation 5.8. In order to check the improvements of the free transition prediction, the γ-$\tilde{\text{Re}}_{\theta\text{t}}$ model with crossflow extension based on the local C1 approach is applied to the test cases that feature shape factors $H_{12} < 2.43$ at the reference transition location $\vec{x}_{\text{t}}$.[6] It is expected that the computed transition location $\vec{x}_{\text{t,cf}}$ moves downstream, as the the transition Reynolds number $\text{Re}_{\delta 2\text{t}}$ is increased.

5.4.1 NLF(2)-0415 Infinite Swept Wing

The skin friction transition location resulting from the simulation with the adapted C1 criterion is almost equal to the one computed with the original C1 criterion. This is because the transition criterion is triggered at the critical location $\vec{x}_{\text{c}}$ rather than at the actual transition location $\vec{x}_{\text{t}}$. For the NLF(2)-0415 test case the shape factor H_{12} is decreasing over the majority of the wing. Therefore, equation 5.8 gets evaluated for shape factors $H_{12} > 2.43$. For such high shape factors H_{12} the C1 criterion is unmodified. This is also presented in figure 5.29. The plot is similar to figure 5.26. But the integral boundary layer parameters are evaluated at the *location of onset of*

[5] An extreme example for short vertical errorbars could be seen in a transition criterion plot for a correlation of the crosswise displacement thickness Reynolds number $\text{Re}_{\delta 2}(\vec{x}_{\text{t}})$ to the helicity Reynolds number $\text{Re}_{\text{He}}(\vec{x}_{\text{t}})$ at the transition location $\vec{x}_{\text{t}}$ (figure F.5 in appendix F). This correlation would have very little scatter. But as $\text{Re}_{\delta 2}(\vec{x}_{\Gamma})/\max_{y_n \in [0,\delta(\vec{x}_{\Gamma})]} \text{Re}_{\text{He},\mathcal{B}}(\vec{x}_{\Gamma}, y_n) \approx$ const. on the *whole* surface Γ [19] that correlation would be fulfilled everywhere on the surface Γ and therefore not be useful to predict CFT. Note that the fact that the correlation on the transition line $\mathcal{T}$ "works well" for all test cases simultaneously has nothing to do with CFT.

[6] Recomputations of the remaining test cases did not show any difference, as the shape factor is $H_{12} > 2.43$ at the intermittency production onset location $\vec{x}_{P(\gamma)}$.

the intermittency production

$$\vec{x}_{P(\gamma)}(\vec{x}_\Gamma) = \underset{\vec{\tilde{x}}}{\operatorname{argmin}} \left\{ \vec{\tilde{x}}_\Gamma \in \mathcal{S}_{\mathcal{E}\to\Gamma}(\vec{x}_\Gamma), \exists y_n \in [0, \delta(\vec{\tilde{x}}_\Gamma)], \gamma_{\mathcal{B}}(\vec{\tilde{x}}_\Gamma, y_n) > 0.1 : \frac{\vec{u}_\mathrm{e}}{u_\mathrm{e}}(\vec{\tilde{x}}_\Gamma) \cdot \vec{\tilde{x}}_\Gamma \right\} \in \Gamma. \tag{5.11}$$

It is the most upstream wall point along the wall-projected boundary layer edge streamline $\mathcal{S}_{\mathcal{E}\to\Gamma}(\vec{x}_\Gamma)$, where the intermittency $\gamma_{\mathcal{B}}(\vec{x}_\Gamma, y_n)$ somewhere along the wall normal $y_n \in [0, \delta(\vec{\tilde{x}}_\Gamma)]$ increases above 0.1. $\vec{x}_{P(\gamma)}$ is computed from the results generated by simulations using the adapted C1 criterion. It is visible that the points of the NLF(2)-0415 test case moved to the right in comparison to figure 5.4. Note that the equivalent effect is taken into account with regard to the transition Reynolds number $\mathrm{Re}_{\delta 2\mathrm{t}}$: It gets multiplied by the critical-to-transition ratio C in order to account for the streamwise change.
For future work it is proposed to introduce another critical-to-transition ratio C_arg, that gets multiplied to the argument H_{12} of the C1 criterion:

$$F_{\mathrm{onset,cw},1} = \frac{\mathrm{Re}^*_{\delta 2}}{C\, f_{\mathrm{criterion,C1}}(C_\mathrm{arg}\, H^*_{12}(\vec{x}_\Omega))} \tag{5.12}$$

By doing so, the streamwise change of the argument of the transition criterion between the intermittency production onset location $\vec{x}_{P(\gamma)}$ and the transition location according to the skin friction coefficient $\vec{x}_{\mathrm{t},c_\mathrm{f}}$ can be taken into account for the evaluation of the transition criterion. The critical-to-transition ratio C_arg would have to be calibrated, similar to the critical-to-transition ratio C for the Reynolds number. The general idea holds true not only for the C1 criterion, but for all transition transport models that use transition criteria in conjunction with convection/diffusion transport of intermittency γ.

5.4.2 TELFONA Pathfinder Wing

For test configurations for the upper wing surface the computed transition location $\vec{x}_{\mathrm{t},c_\mathrm{f}}$ moves somewhat downstream for the adapted C1 criterion compared to the original C1 criterion. But the computed transition location $\vec{x}_{\mathrm{t},c_\mathrm{f}}$ is still far upstream of the experimental transition location $\vec{x}_{\mathrm{t,exp}}$. That there is no significant change of the computed transition location $\vec{x}_{\mathrm{t},c_\mathrm{f}}$ is explained by the fact that in the transition criterion plot figure 5.26 the curves for both the original and the adapted C1 criterion deviate strongly from the data points for the upper wing surface.
In contrast, the configurations for the lower surface do not show a visible change of computed transition location $\vec{x}_{\mathrm{t},c_\mathrm{f}}$ with the switch from the original to the adapted C1 criterion. The reason for that is the same as for the NLF(2)-0415 test case: At the location of intermittency production onset $\vec{x}_{P(\gamma)}$ the argument of the C1 criterion is $H_{12} > 2.43$ (see figure 5.30).
Another aspect is that the growing intermittency γ has a distorting effect on the laminar boundary layer velocity profile $u(\vec{x}_\Omega) \forall \vec{x}_\Omega \in \Omega$. This effect is stronger for regions close to the transition line $\mathcal{T}_\mathrm{CFD}$. It is remarkable that for the TELFONA Pathfinder wing test case the *length of the intermittency development region*

$$l_\gamma(\vec{x}_\Gamma) = [\vec{x}_{\mathrm{t},c_\mathrm{f}}(\vec{x}_\Gamma) - \vec{x}_{P(\gamma)}(\vec{x}_\Gamma)] \cdot \vec{e}_\mathrm{sw}(\vec{x}_\Gamma) \tag{5.13}$$

is very small. Therefore evaluating the transition criterion at the intermittency production onset location $\vec{x}_{P(\gamma)}$ is even more erroneous. This could also be solved by introducing a critical-to-transition ratio C_arg for the argument of the transition criterion.

The test case shows another issue of the model: The streamwise slopes of the local crosswise displacement thickness Reynolds number $\mathrm{Re}_{\delta 2}$ and the transition crosswise displacement thickness Reynolds number $\mathrm{Re}_{\delta 2\mathrm{t}}$ are very similar for the adapted C1 criterion in the vicinity of the criterion-predicted transition location $\vec{x}_{\mathrm{t,criterion}}$. If the data points in the transition criterion plot 5.16 were plotted with the errorbars corresponding to the *adapted* C1 criterion, they would be very short. This indicates a very high sensitivity to changes of the Reynolds numbers.

5.4.3 Inclined 6:1 Prolate Spheroid

In figure 5.31 the distribution of the skin friction coefficient c_f is plotted examplarily for the angle of attack $\alpha = 30°$ for the simulation with the adapted C1 criterion. The transition line is not visibly changed by switching the C1 criterion from the original to the adapted one (not shown). This is because in the vicinity of the predicted transition line $\mathcal{T}_\mathrm{CFD}$ the shape factor is $H_{12} > 2.43$ for all angles of attack α, what contradicts the finding from the fixed transition analysis (section 5.2.7). This indicates that the C1 criterion does not get used correctly in the local approximation framework of the LCTM. Indeed, it is well-known that the transition prediction based on the local C1 approach fails to correctly predict the transition line for the spheroid [19]. This is because the FSC equations yield only for wing-like geometries a good approximation of the boundary layer velocity profile $u_\mathcal{B}(\vec{x}_\Gamma, \cdot)\, \forall \vec{x}_\Gamma \in \Gamma$ [18]. Therefore, a comparison of the measured and the predicted transition lines is not presented.

5.4.4 Infinite Swept Cylinder

For all configurations a separation-induced transition is detected by both the original and the adapted C1 criterion. This is again because the intermittency production is beginning at $\vec{x}_{P^{(\gamma)}}$, upstream of the skin friction transition location $\vec{x}_{\mathrm{t,cf}}$, and the diffusion towards the wall is happening relatively slowly. Thus, the crossflow transition does not take place before the separation-induced transition takes place. The latter occurs due to the adverse pressure gradient downstream of the maximum thickness location of the cross section. In this case, the streamwise transition criterion (equation 2.57) of the original γ-$\tilde{\mathrm{R}}\mathrm{e}_{\theta\mathrm{t}}$ model lets the intermittency production $P^{(\gamma)}$ increase very quickly through equation 2.66.
The reason for the long intermittency development region l_γ due to the CFT term in equation 2.73 is a destruction of the intermittency γ in the boundary layer. This can be seen in figure 5.32. At the location of onset of the intermittency production $\vec{x}_{P^{(\gamma)}}$ the intermittency increases above $\gamma \approx 0.6$. Then it decreases to almost the minimum value of the distribution due to the destruction of intermittency $D^{(\gamma)}$. The intermittency destruction $D^{(\gamma)}$ was calibrated for the γ-$\tilde{\mathrm{R}}\mathrm{e}_{\theta\mathrm{t}}$ model without CFT extension. For the swept cylinder test case the intermittency destruction $D^{(\gamma)}$ seems to incorrectly counteract the intermittency production $P^{(\gamma)}$. Thus, a recalibration of the intermittency destruction $D^{(\gamma)}$ by appropriate CFT test cases is proposed for future work.
However, figure 5.32 shows a difference for the intermittency production onset location $\vec{x}_{P^{(\gamma)}}$ between the original (subfigure 5.32a) and the adapted C1 criterion (subfigure 5.32b). For the adapted C1 criterion, the intermittency production $P^{(\gamma)}$ starts more downstream, which corresponds to the increased transition Reynolds number $\mathrm{Re}_{\delta 2\mathrm{t}}$ for low shape factors $H_{12} < 2.43$. This verifies the implementation of the adapted C1 criterion.

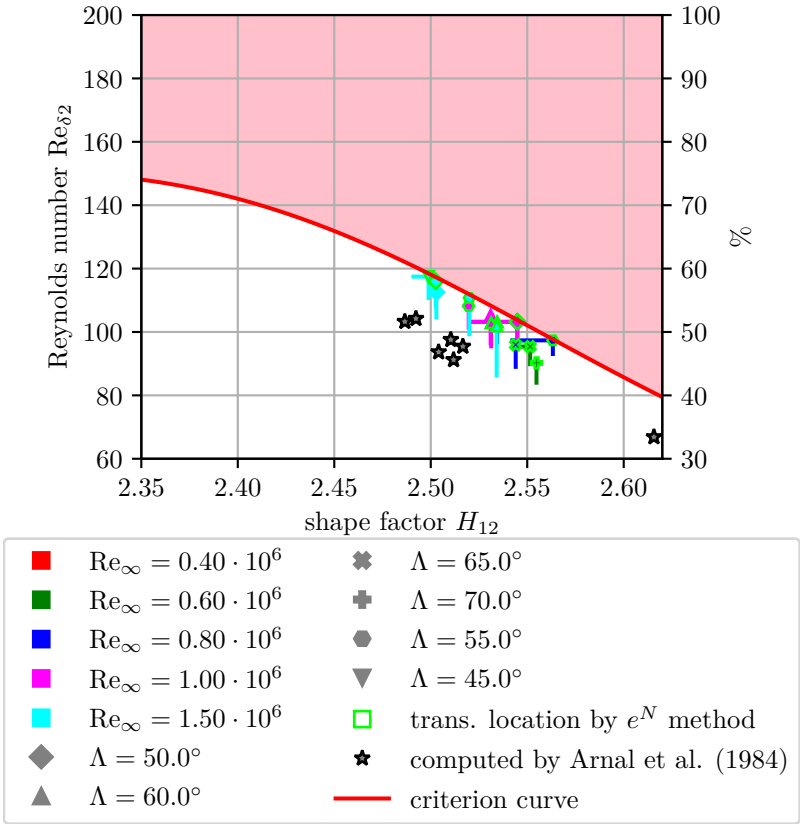

Figure 5.1: ONERA D test case: CFT criterion plot for the C1 criterion

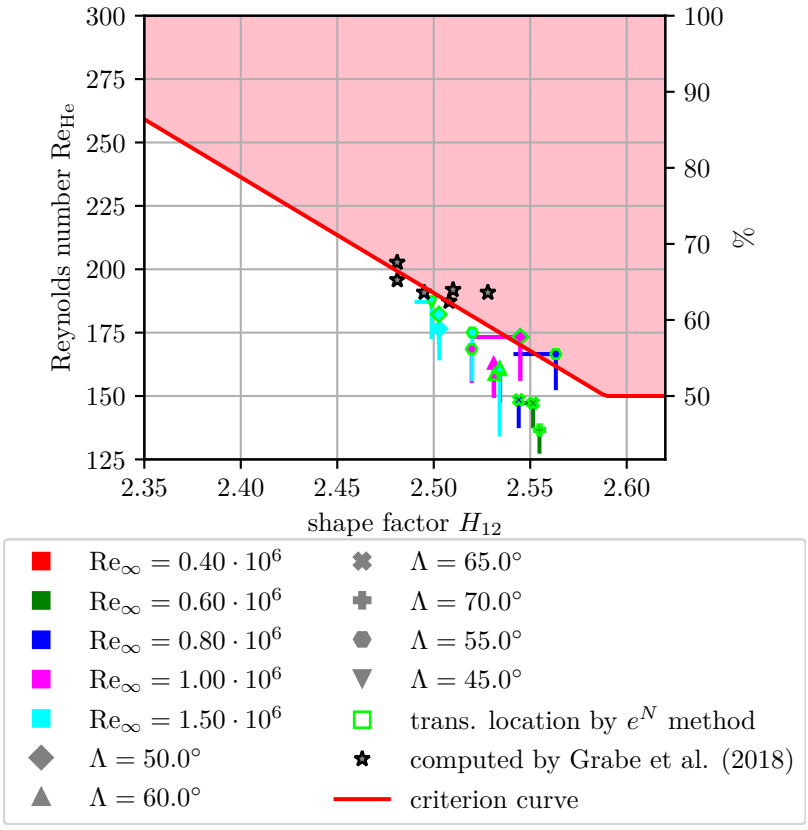

Figure 5.2: ONERA D test case: CFT criterion plot for the helicity criterion

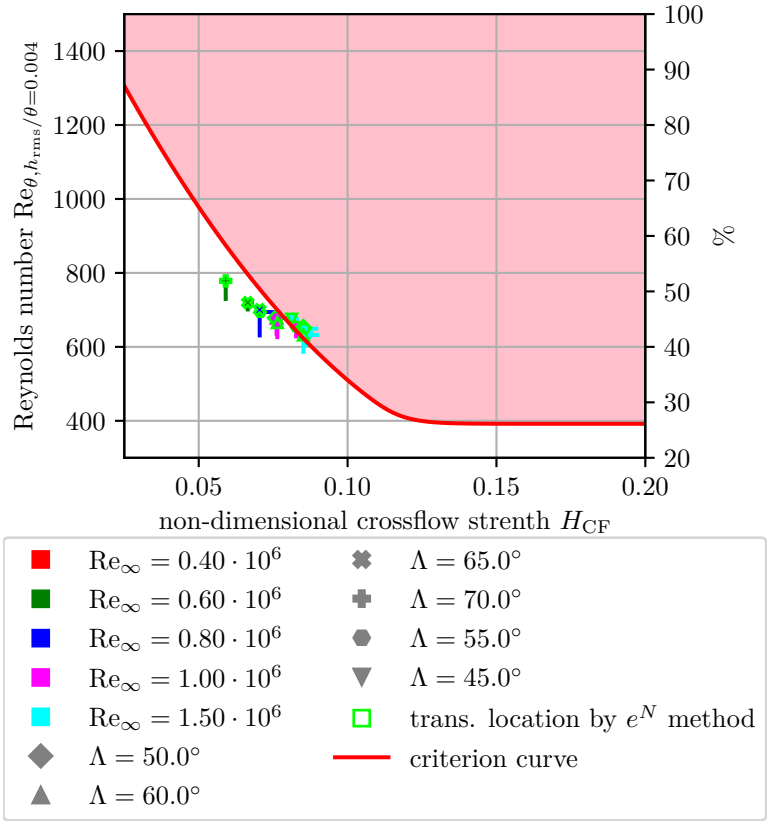

Figure 5.3: ONERA D test case: CFT criterion plot for the Langtry's criterion

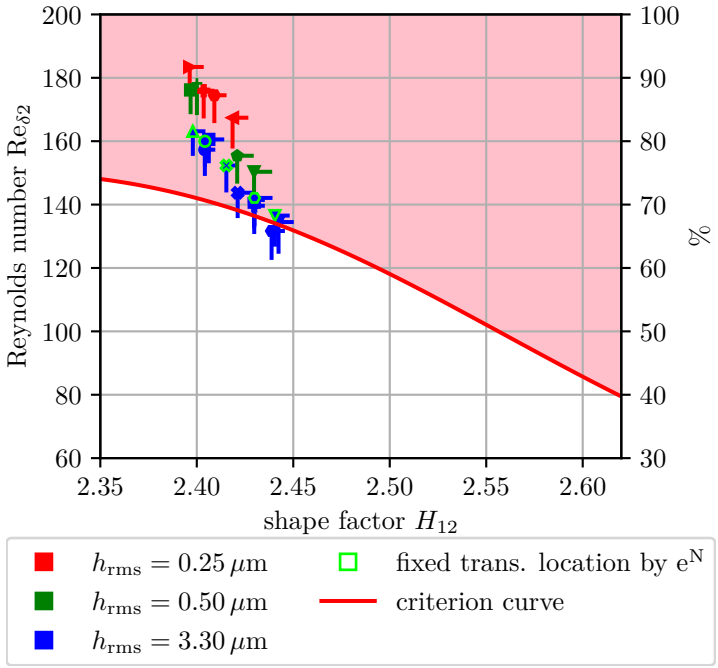

Figure 5.4: NLF(2)-0415 test case: CFT criterion plot for the C1 criterion

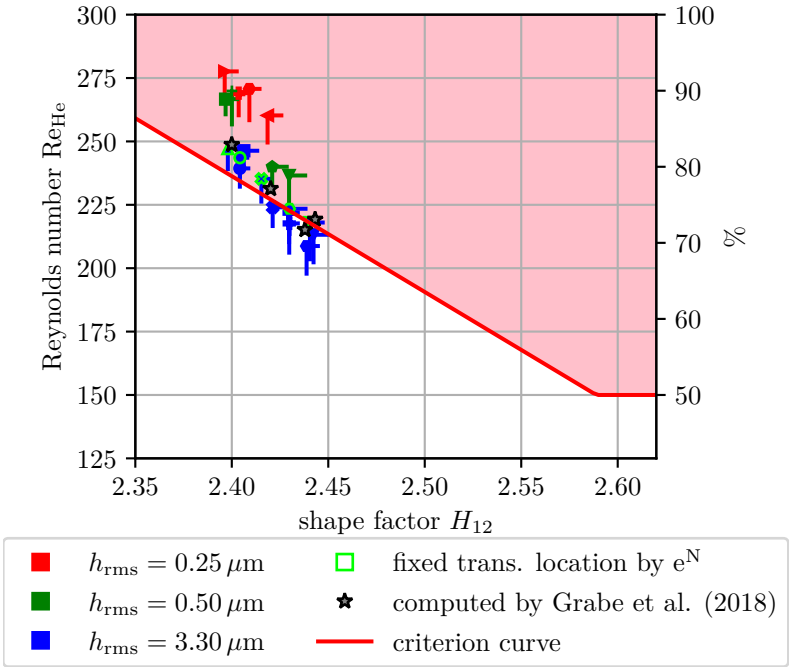

Figure 5.5: NLF(2)-0415 test case: CFT criterion plot for the helicity criterion

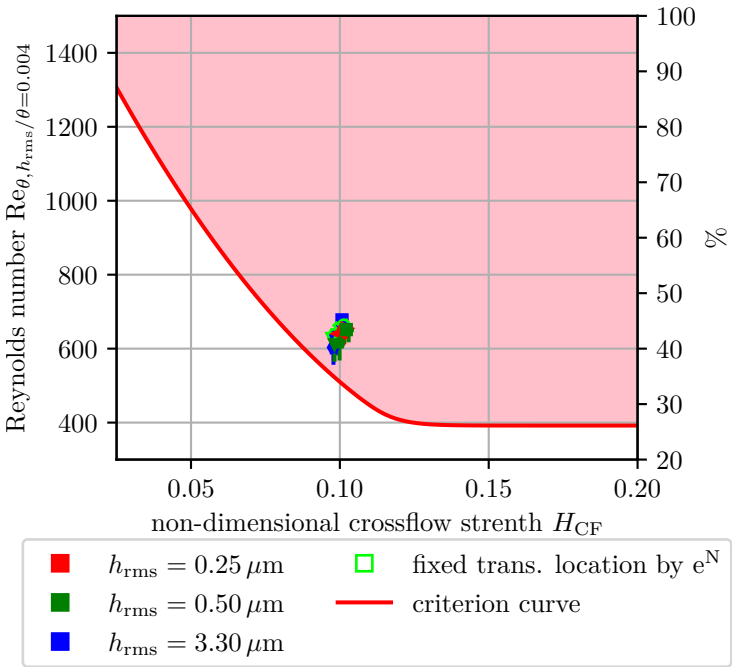

Figure 5.6: NLF(2)-0415 test case: CFT criterion plot for Langtry's criterion

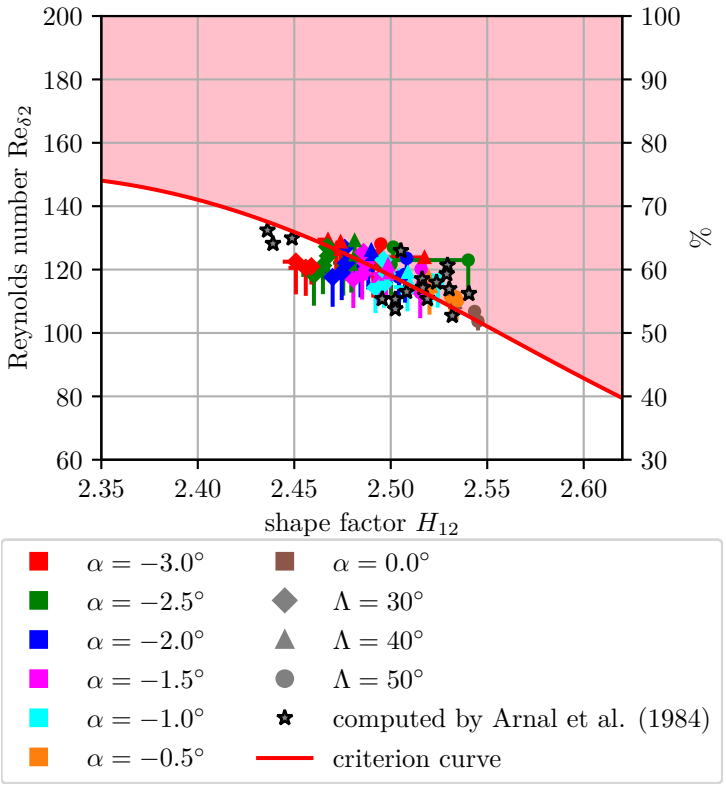

Figure 5.7: NACA 64_2A015 test case: CFT criterion plot for the C1 criterion

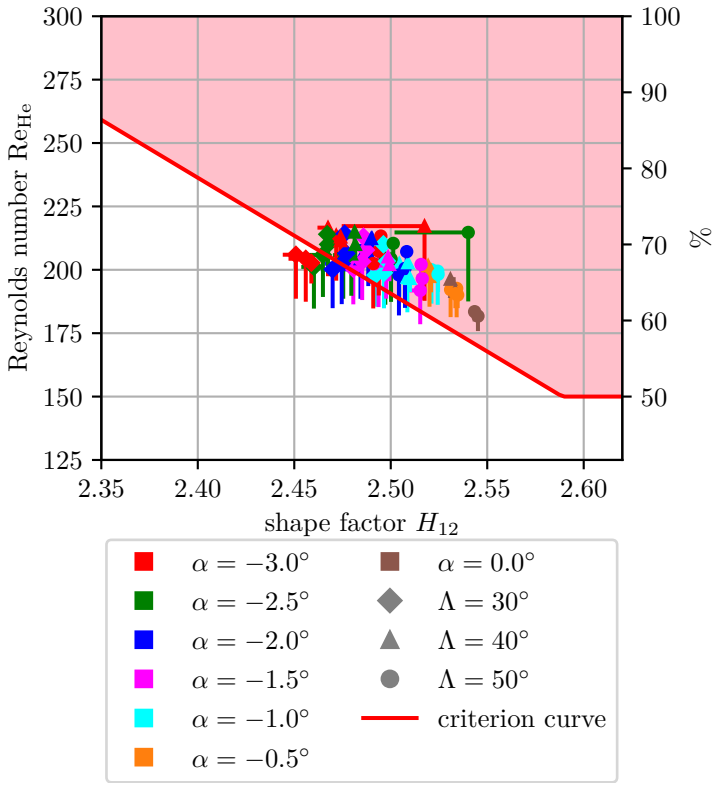

Figure 5.8: NACA 64_2A015 test case: CFT criterion plot for the helicity criterion

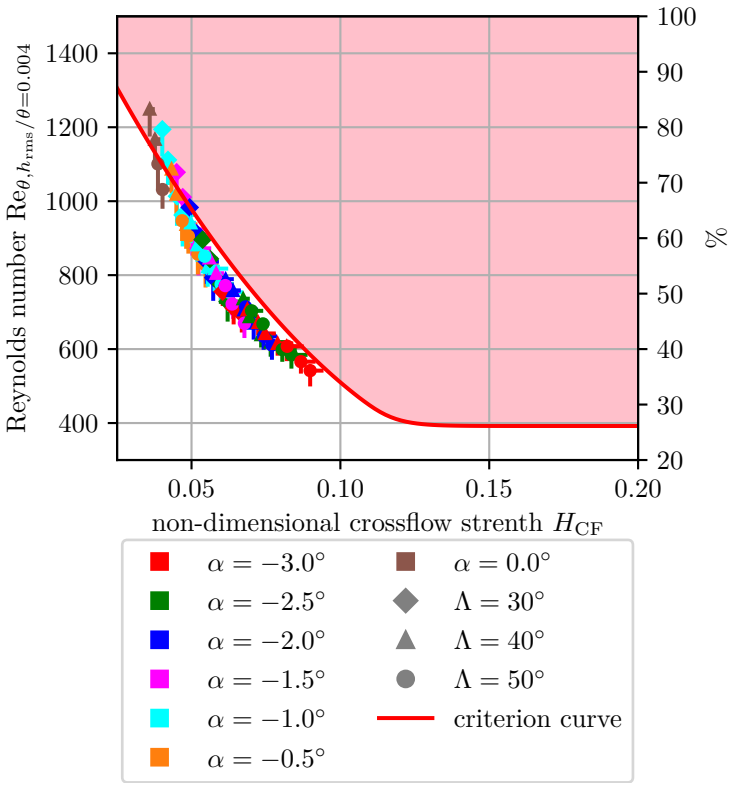

Figure 5.9: NACA 64_2A015 test case: CFT criterion plot for Langtry's criterion

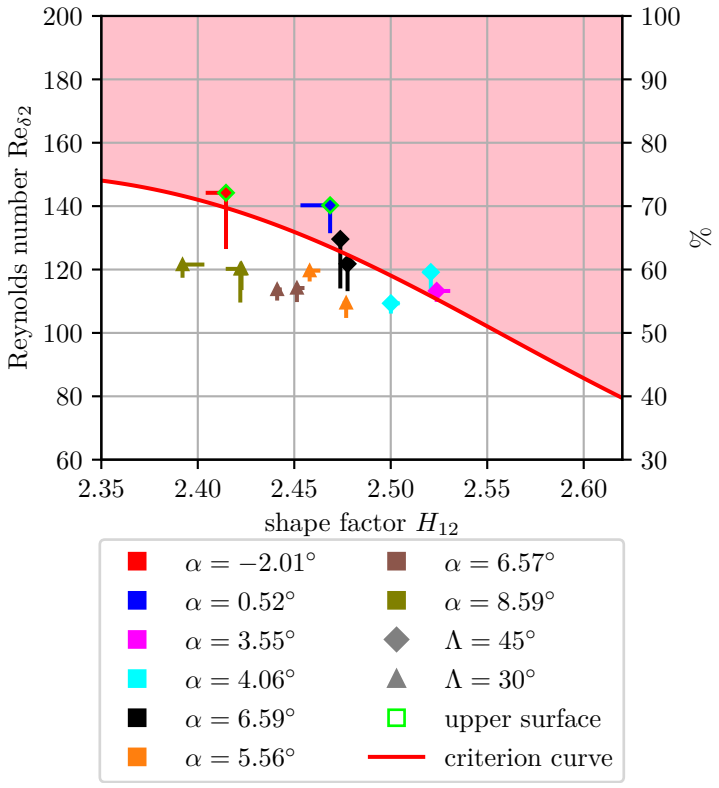

Figure 5.10: HQ26N/14.82 Test case: CFT criterion plot for the C1 criterion

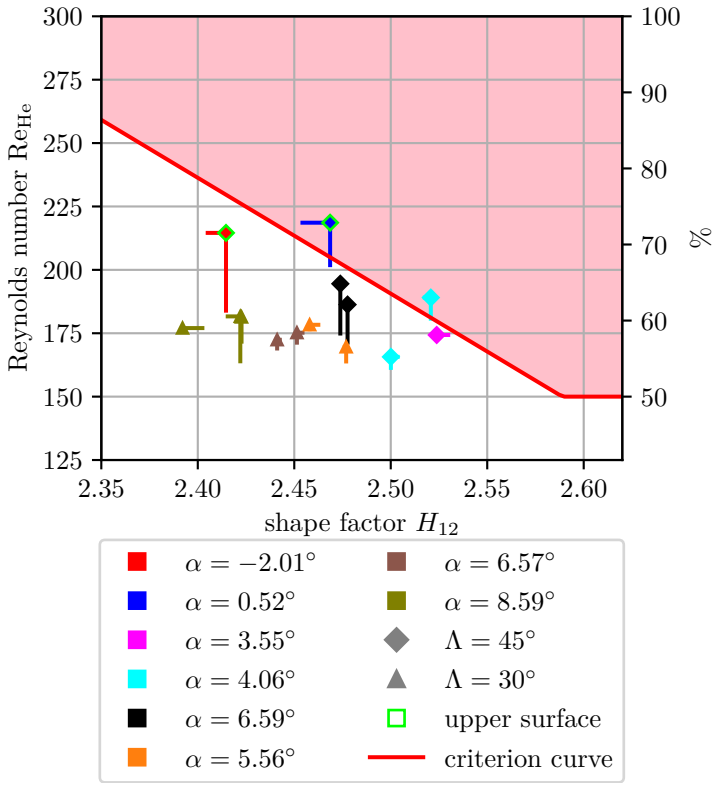

Figure 5.11: HQ26N/14.82 Test case: CFT criterion plot for the helicity criterion

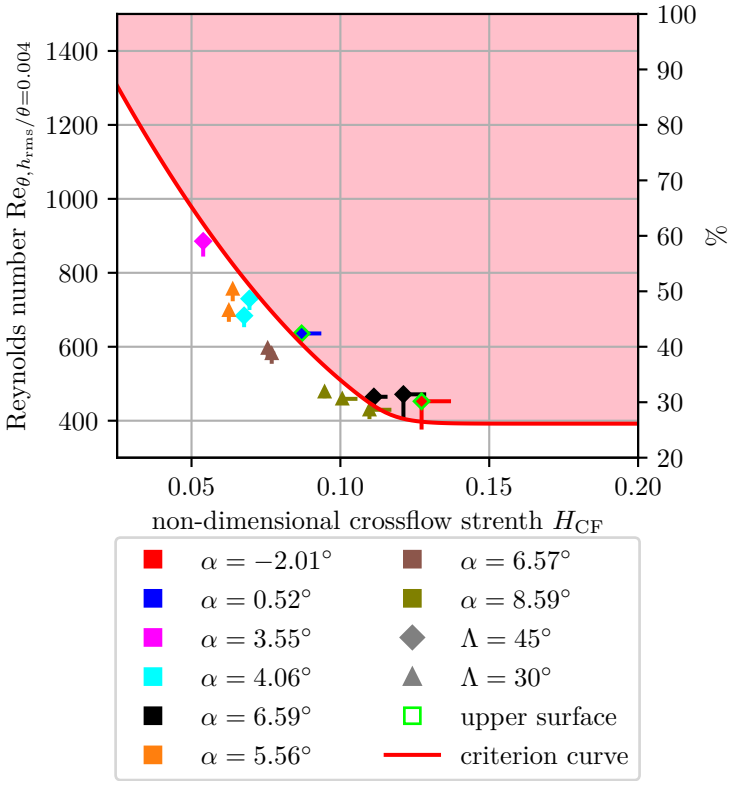

Figure 5.12: HQ26N/14.82 Test case: CFT criterion plot Langtry's criterion

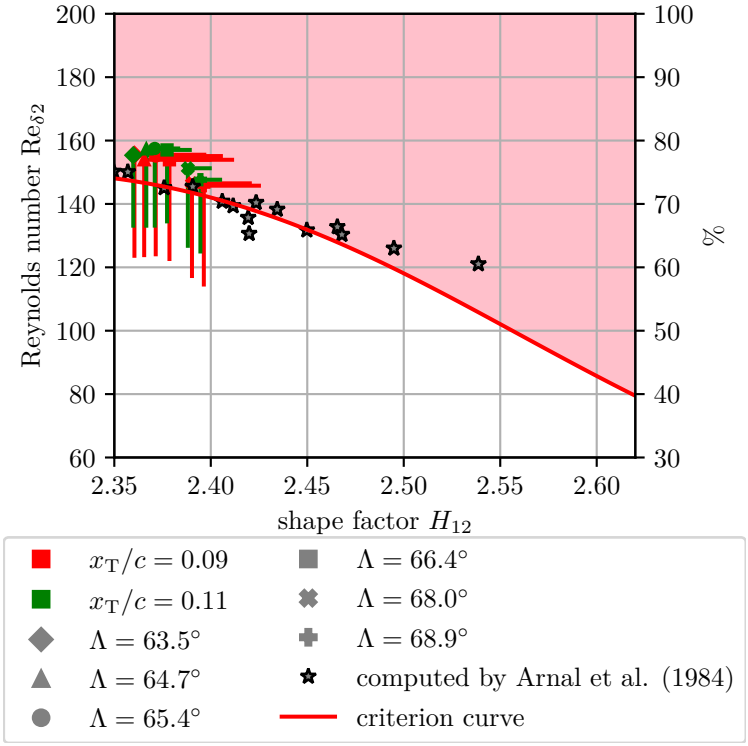

Figure 5.13: Swept cylinder test case: CFT criterion plot for the C1 criterion

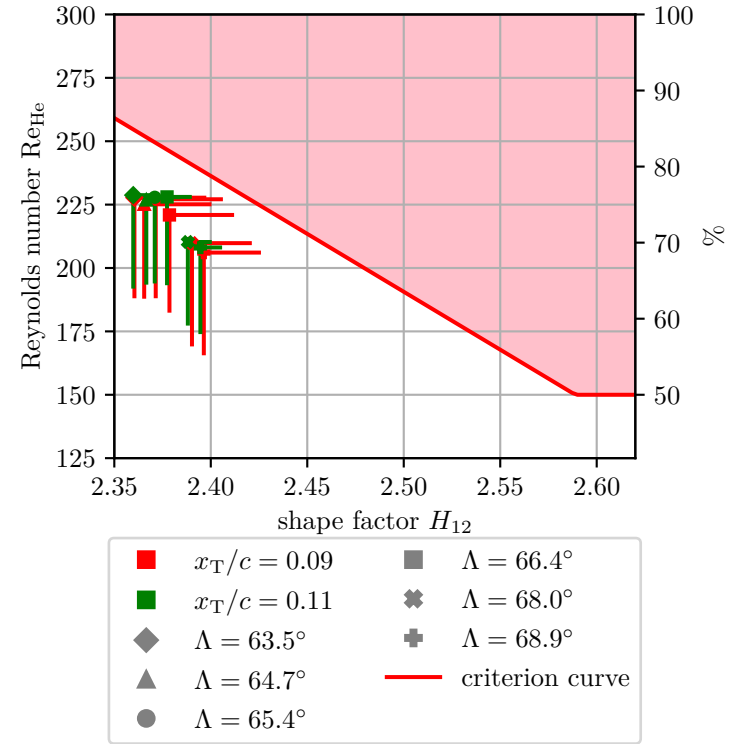

Figure 5.14: Swept cylinder test case: CFT criterion plot for the helicity criterion

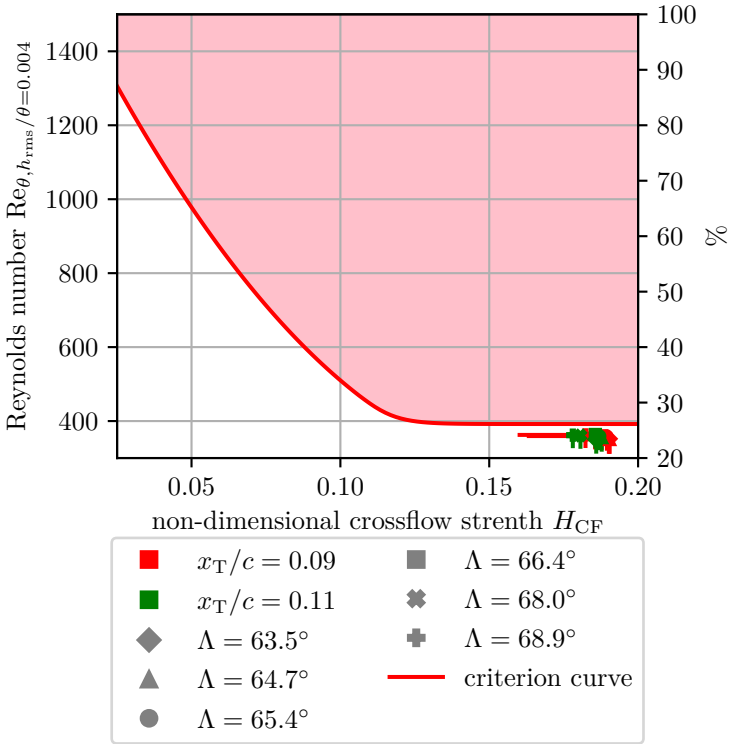

Figure 5.15: Swept cylinder test case: CFT criterion plot for Langtry's criterion

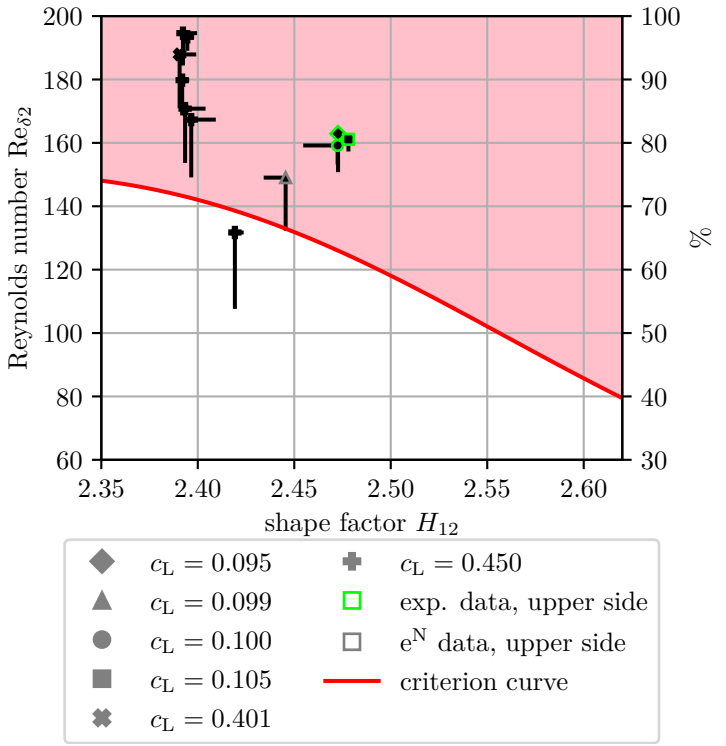

Figure 5.16: TELFONA Pathfinder test case: CFT criterion plot for the C1 criterion

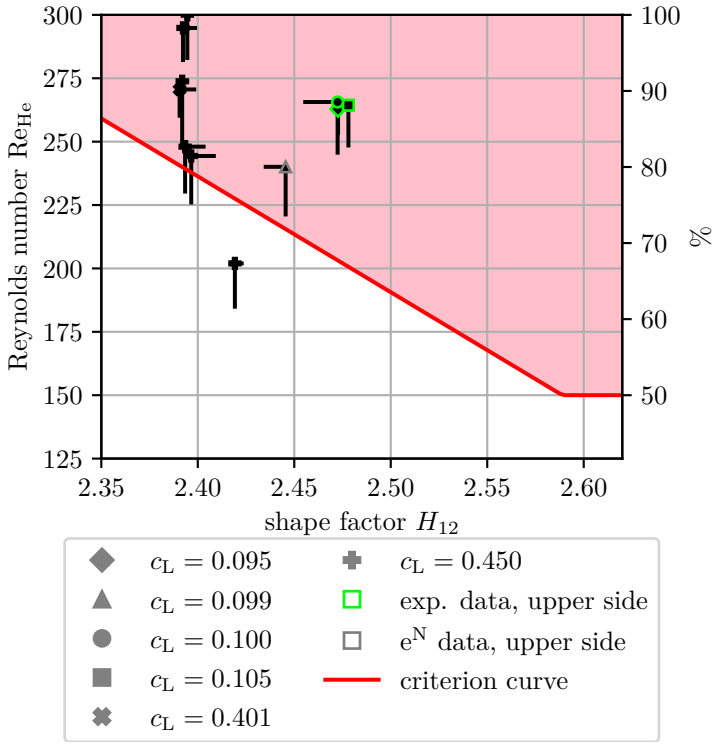

Figure 5.17: TELFONA Pathfinder test case: CFT criterion plot for the helicity criterion

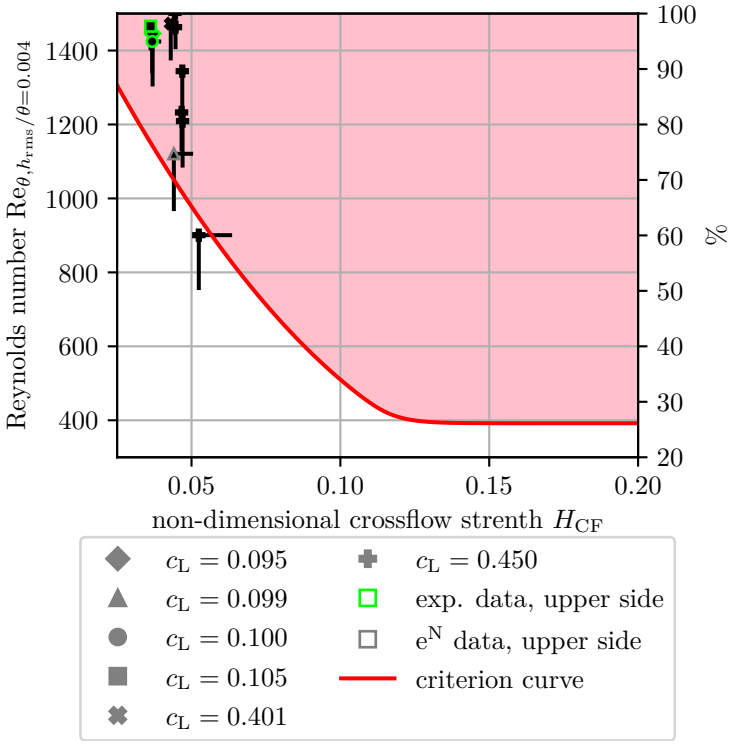

Figure 5.18: TELFONA Pathfinder test case: CFT criterion plot for Langtry's criterion

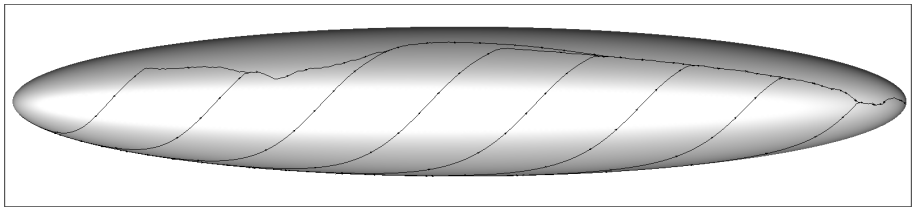

Figure 5.19: Prolate spheroid test case: Some wall-projected boundary layer edge streamlines $\mathcal{S}_{\mathcal{E}\to\Gamma}$ at the angle of attack $\alpha = 30°$

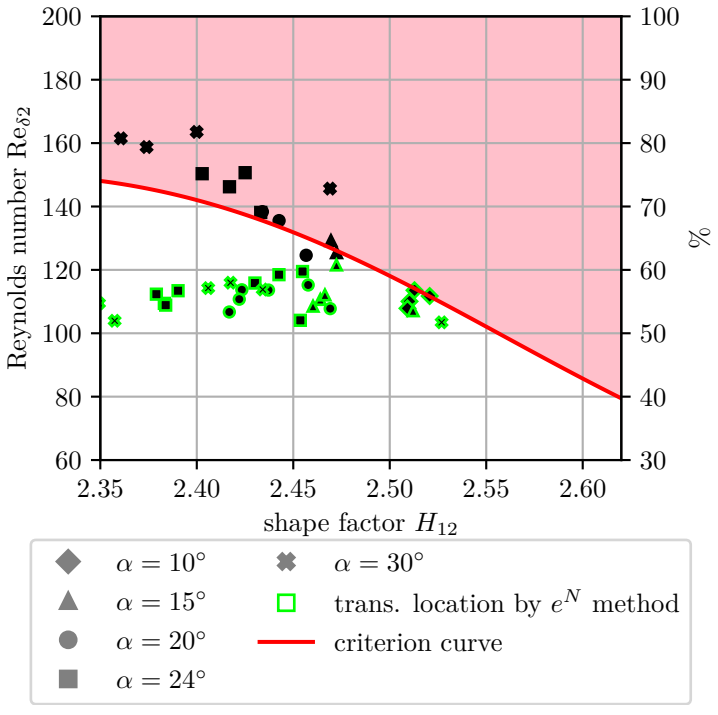

Figure 5.20: Prolate spheroid test case: CFT criterion plot for the C1 criterion

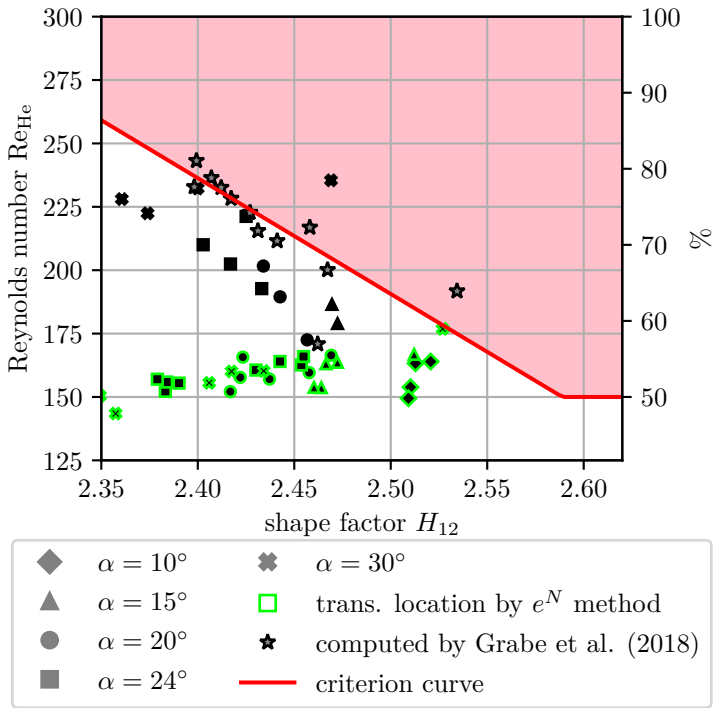

Figure 5.21: Prolate spheroid test case: CFT criterion plot for the helicity criterion

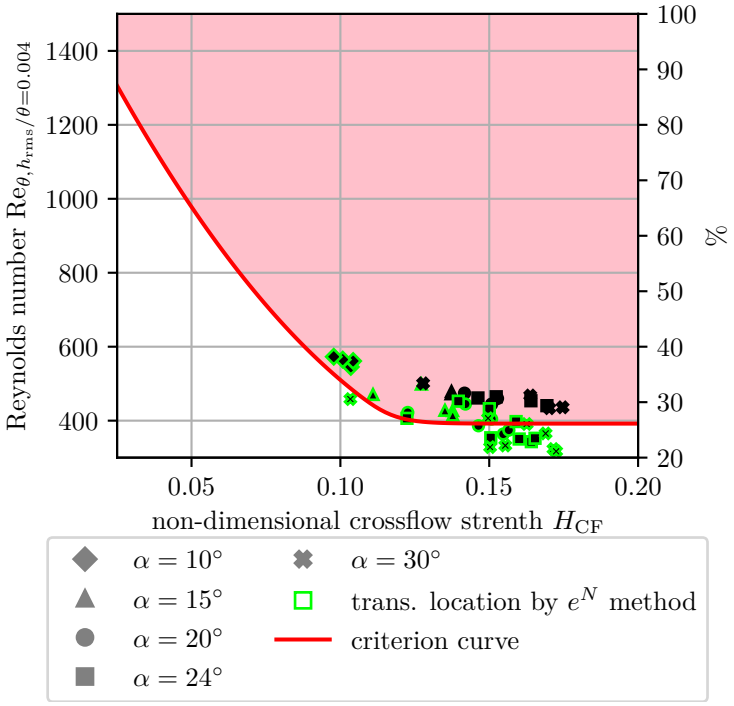

Figure 5.22: Prolate spheroid test case: CFT criterion plot for Langtry's criterion

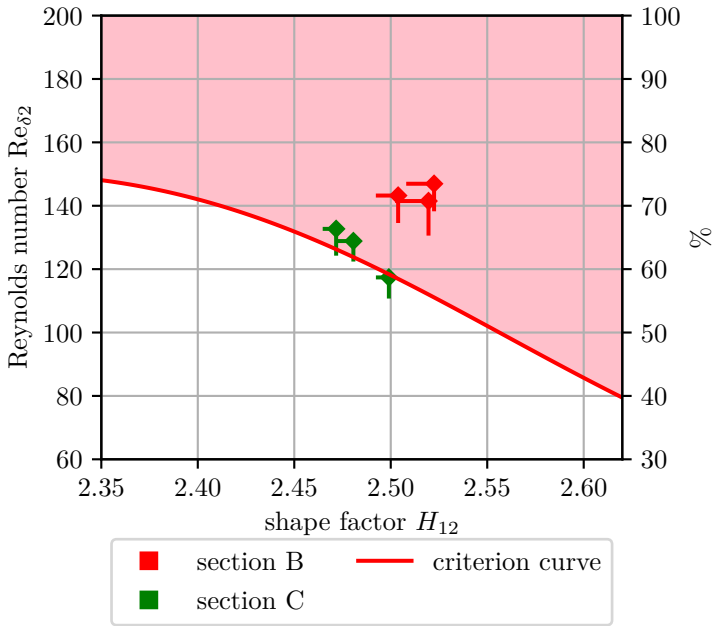

Figure 5.23: Sickle Wing test case: CFT criterion plot for the C1 criterion

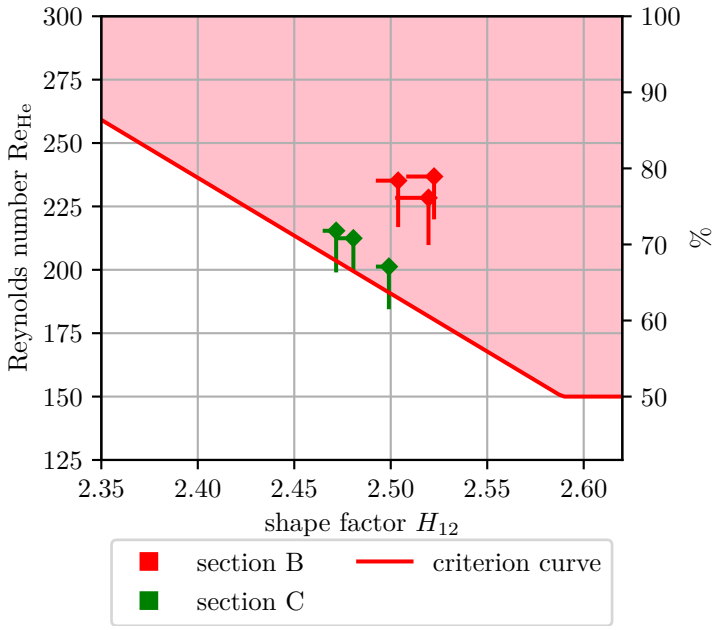

Figure 5.24: Sickle Wing test case: CFT criterion plot for the helicity criterion

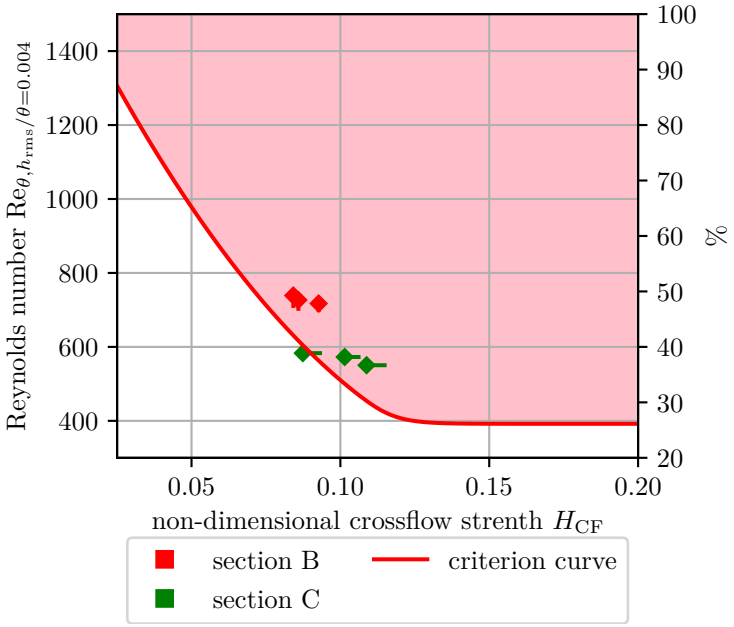

Figure 5.25: Sickle Wing test case: CFT criterion plot for Langtry's criterion

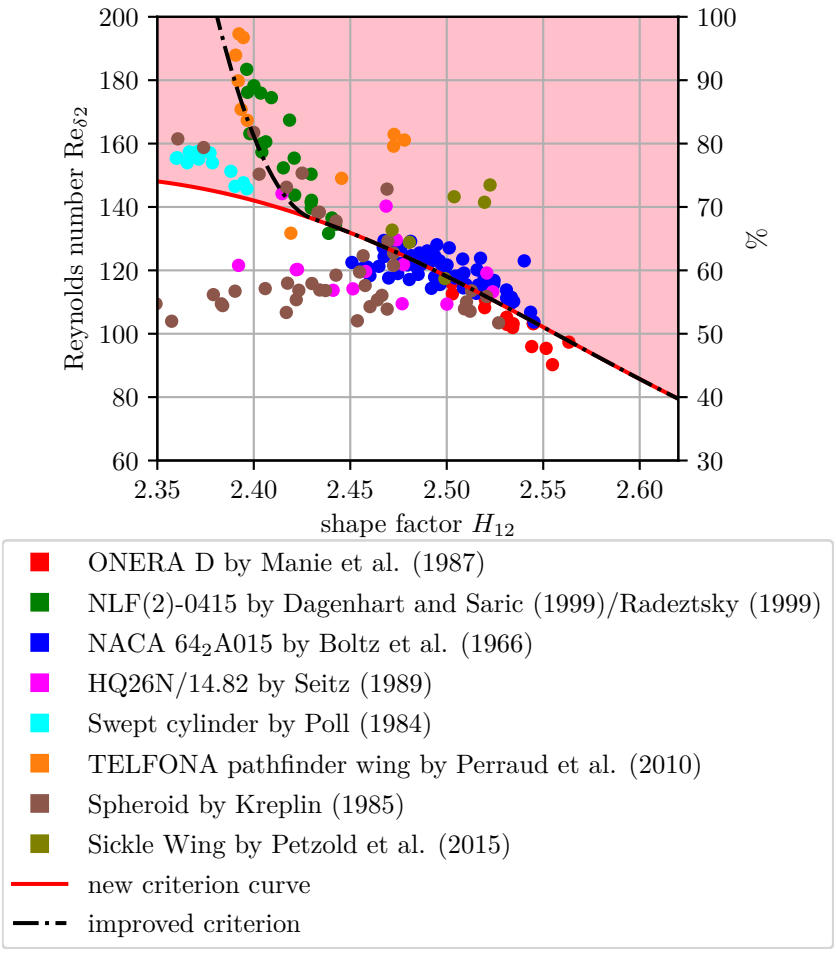

Figure 5.26: C1 criterion plot for all test cases combined

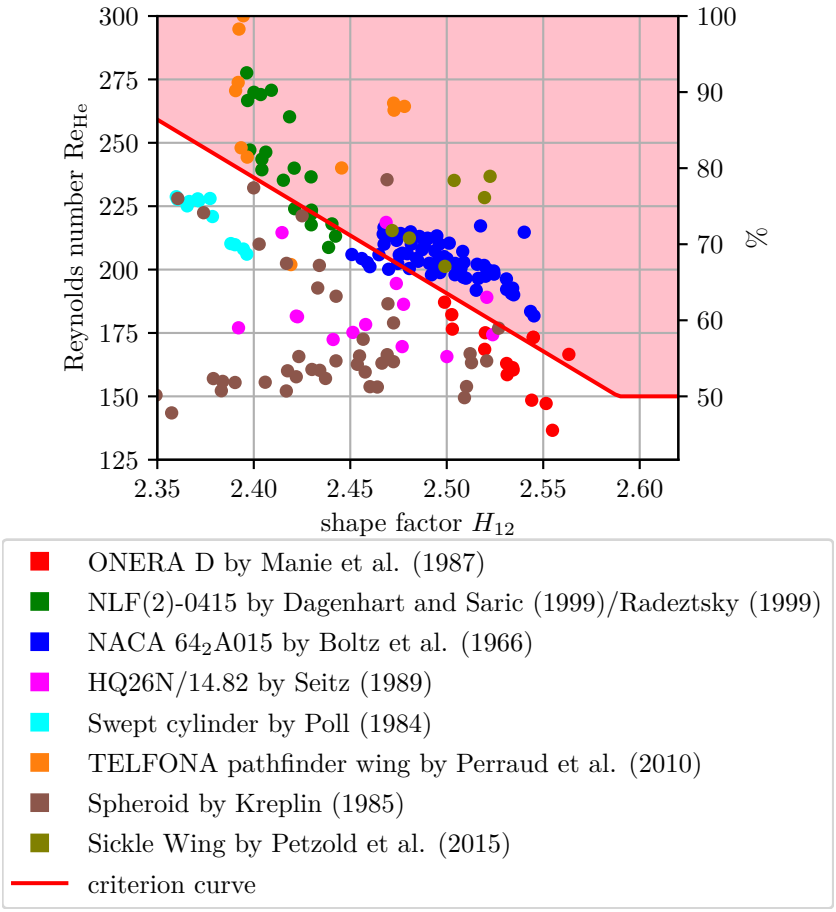

Figure 5.27: Helicity criterion plot for all test cases combined

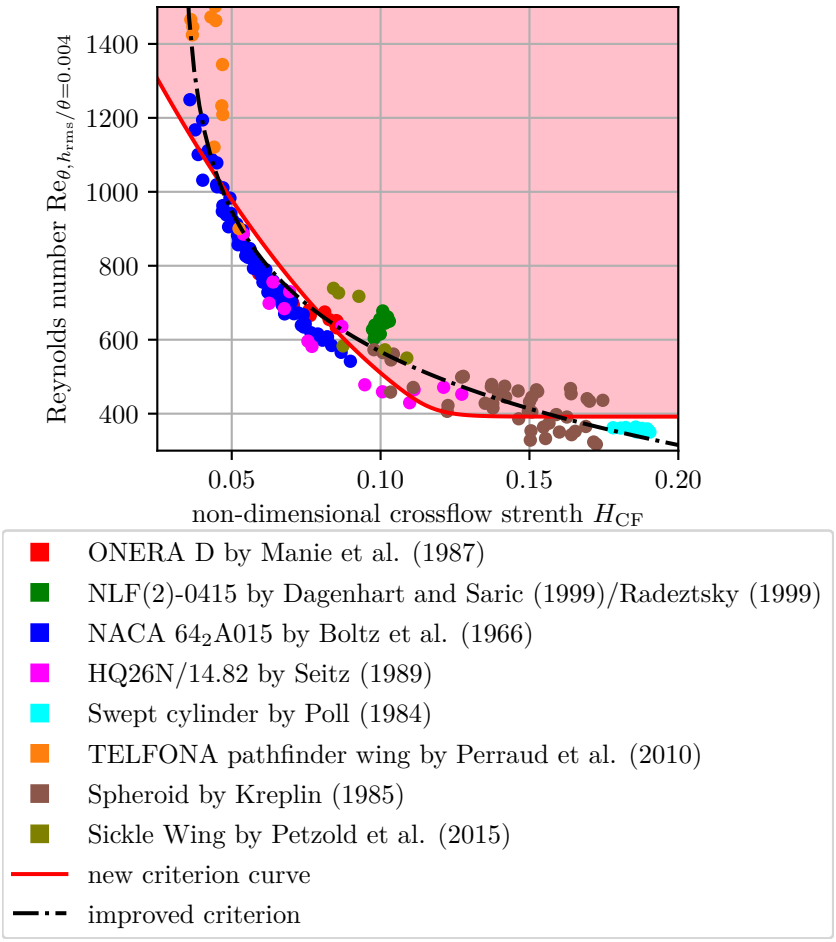

Figure 5.28: Langtry's criterion plot for all test cases combined

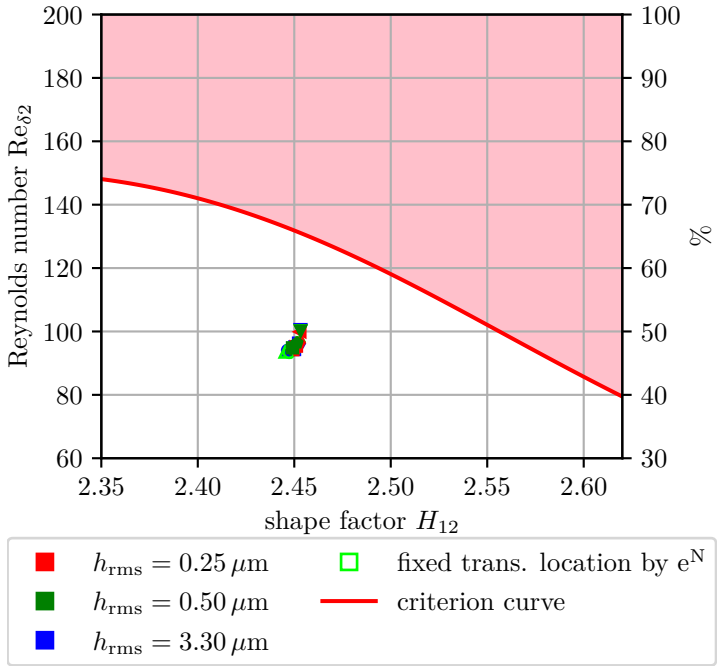

Figure 5.29: NLF(2)-0415 test case: Integral boundary layer parameters at the location of intermittency production onset $\vec{x}_{P(\gamma)}$

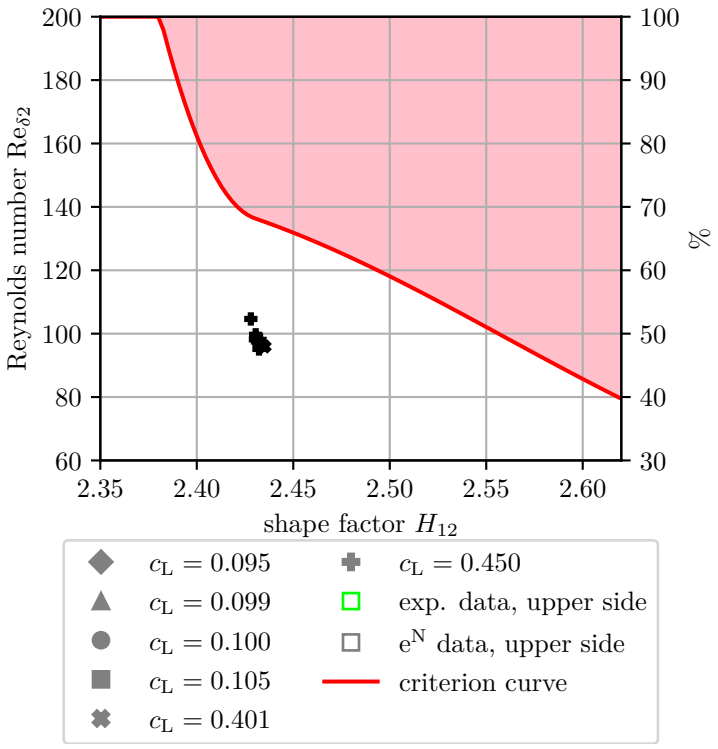

Figure 5.30: TELFONA Pathfinder wing test case: Integral boundary layer parameters at the location of intermittency production onset $\vec{x}_{P(\gamma)}$

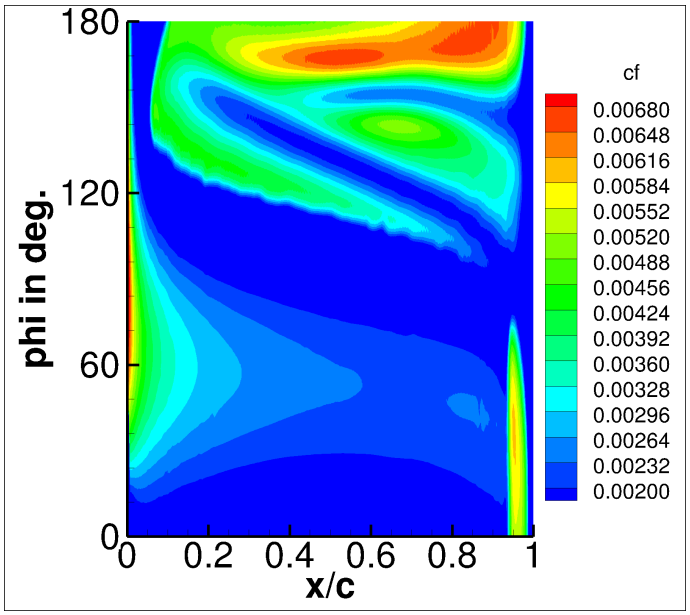

Figure 5.31: Prolate spheroid test case: Simulated skin friction coefficient c_f distribution at angle of attack $\alpha = 30°$, simulated with the adapted C1 criterion

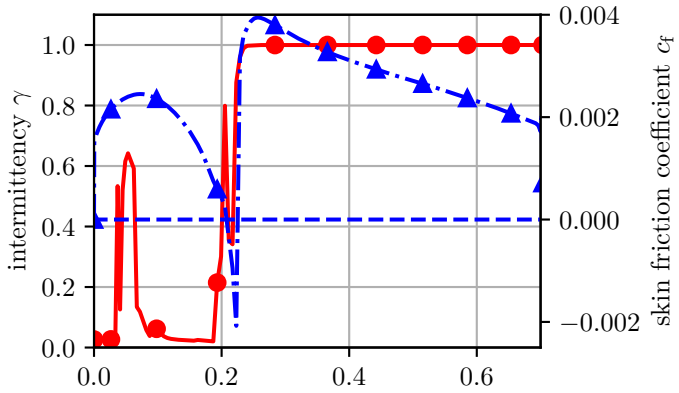

(a) Original C1 criterion

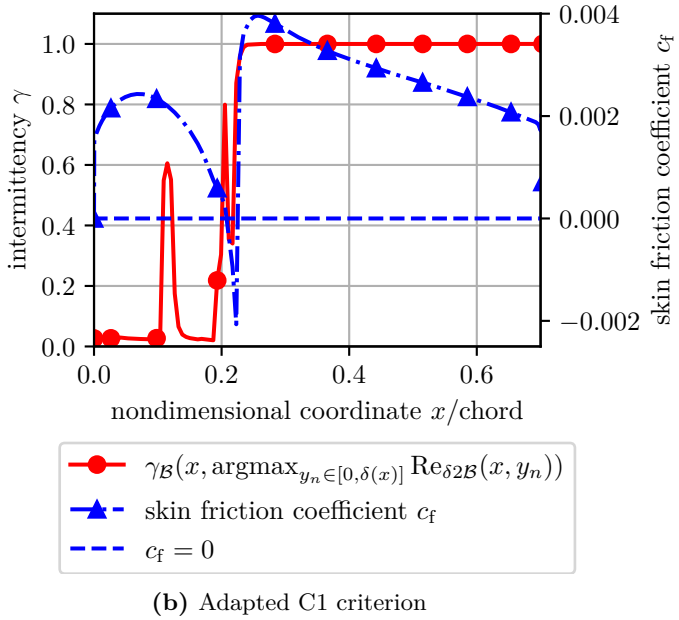

(b) Adapted C1 criterion

Figure 5.32: Swept cylinder test case: Computed streamwise distribution of the skin friction coefficient c_f and the intermittency γ at the wall normal position of the maximum crosswise displacement thickness Reynolds number Re_{delta2}.

6 Recalibration of the Critical-to-Transition Ratio for the local C1 Approach

In this chapter the recalibration of the critical-to-transition ratio C is described. First the approach for the derivation of an optimal critical-to-transition ratio C by means of fixed and free transition simulations is described. Then it is shown how the optimal critical-to-transition ratio C can be correlated to a Reynolds number characterizing the test configurations. A new C-correlation is derived. It applied for the NLF(2)-0415 test case in order to assess the differences in the computed transition location and in order to see how well the computed transition location coindice with the theoretical transition locations given by the evaluation of the criterion with the parameters from the fixed transition simulations.

6.1 Recalibration Approach

The *optimal critical-to-transition ratio* is computed as

$$C_{\text{opt}} = \frac{\text{Re}_{\delta 2}}{\text{Re}_{\delta 2\text{t}}}(\vec{x}_{\Gamma} = \vec{x}_{\text{t,criterion}} - l_{\gamma}\vec{e}_{\text{sw}}). \tag{6.1}$$

It is the ratio of the crosswise displacement thickness Reynolds number $\text{Re}_{\delta 2}$ to the transition crosswise displacement thickness Reynolds number $\text{Re}_{\delta 2\text{t}}$, evaluated at a specific point. That point is the optimal location of intermittency production onset $\vec{x}_{P^{(\gamma)},\text{opt}}$. If the intermittency production $P^{(\gamma)}$ is triggered at this location, the transition location according to the skin friction distribution $\vec{x}_{\text{t},c_{\text{f}}}$ will be approximately at the transition location predicted by the criterion $\vec{x}_{\text{t,criterion}}$. $\vec{x}_{P^{(\gamma)},\text{opt}}$ is computed by subtracting the length of the intermittency development region l_{γ} from the criterion-predicted transition location $\vec{x}_{\text{t,criterion}}$. The length of the intermittency development region l_{γ} is found by free transition simulations as the streamwise distance between the actual intermittency production onset location $\vec{x}_{P^{(\gamma)}}$ and the computed transition location $\vec{x}_{\text{t},c_{\text{f}}}$. The criterion-predicted transition location $\vec{x}_{\text{t,criterion}}$ if found by fixed transition simulations as the location ($\vec{x}_{\Gamma}$) in the laminar boundary layer $\mathcal{B}_{\text{lam}}$ at which the Reynolds number ratio is $\frac{\text{Re}_{\delta 2}}{\text{Re}_{\delta 2\text{t}}}(\vec{x}_{\Gamma}) = 1$.[1] Equation 6.1 implies the assumption that a change of the critical-to-transition ratio C leads to a streamwise shift of the intermittency development region without changing the length l_{γ} of the intermittency development region. However, as the computed transition location $\vec{x}_{\text{t},c_{\text{f}}}$ changes due to the different critical-to-transition ratio C, it moves to regions of different boundary layer parameters, and the length of the intermittency development region l_{γ} may change. Therefore, the recalibration must be repeated iteratively, in order to get a convergence of the optimal critical-to-transition ratio C. The process is depicted in figure 6.1. Due to limited time for the present work, only one iteration of the process is carried out. The optimal critical-to-transition ratio C will be calculated for all test cases. Afterwards a correlation of these values is formulated in terms of a locally available Reynolds number. This Reynolds number is called *argument of the C-correlation*. Multiple arguments of the C-correlation are tried out until a sufficiently simple regression curve for the points C(argument) with sufficiently low scatter can be found. The regression curve is taken as sufficiently simple, if it

[1] Note that *no* experimental transition location $\vec{x}_{\text{t,exp}}$ is involved into the recalibration of the critical-to-transition ratio C.

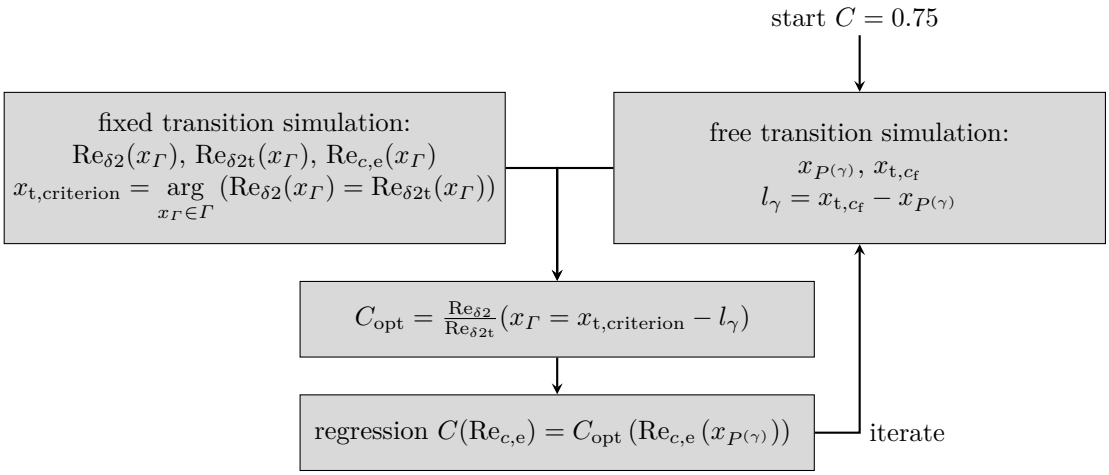

Figure 6.1: Flow chart of the recalibration approach for the critical-to-transition ratio C

has no inflection points. The scatter is taken as sufficiently low, if the determination coefficient is $R^2 > 0.5$. In addition it is demanded that the argument of the C correlation is available locally. Thus, the correlation is adaptive to different flows.
The new C-correlation will then replace the constant $C = 0.75$ of the original local C1 approach [19]. The new C-correlation is implemented into the *TAU* code. The test cases are recomputed with the adapted C1 criterion and the C-correlation. The effect of the new calibration is judged by comparison of the computed transition locations $\vec{x}_{\mathrm{t},,c_\mathrm{f}}$ to the experimental transition locations $\vec{x}_{\mathrm{t,exp}}$. Due to limited time for the work, only preliminary results can be shown.

6.2 Derivation of a New Correlation

The resulting values for the optimal critical-to-transition ratio are in the range of $C \in [0.48, 0.98]$. Note that some test configurations are excluded from the analysis, for example the ones for the swept cylinder and some for the HQ26N/14.82. This is done because the C1 approach fails to predict CFT. In section 5.4.4 this is described exemplarily for the swept cylinder test case.
A correlation of the optimal critical-to-transition ratio C with the momentum thickness Reynolds number Re_θ at the location of the optimal γ-production onset $\vec{x}_{P^{(\gamma)}}$ can be found.[2] It is presented in figure 6.2. The correlation (regression curve in figure 6.2) shoud not be used for the LCTM due to a problem arising from the fact that the assumption of equation 2.60 is violated, i.e. the streamwise distribution of the computed crosswise displacement thickness Reynolds number $\mathrm{Re}_{\delta 2}(\vec{x}_\Gamma)$ has multiple intersections with the critical crosswise displacement thickness Reynolds number

$$C(\mathrm{Re}_\theta(\vec{x}_\Gamma))\,\mathrm{Re}_{\delta 2\mathrm{t}}(\vec{x}_\Gamma) \tag{6.2}$$

on the laminar surface Γ_{lam}. This can be seen in figure 6.3a. It shows both the streamwise distributions of the Reynolds number $\mathrm{Re}_{\delta 2}(\vec{x}_\Gamma)$ and $\mathrm{Re}_{\delta 2\mathrm{t}}(\vec{x}_\Gamma)$ for a NLF(2)-0415 infinite swept wing configuration, *computed by a fixed transition simulation.* In addition, the curve of the critical Reynolds number $C\,\mathrm{Re}_{\delta 2\mathrm{t}}$ is drawn into the plot in with the new C-correlation $C(\vec{x}_\Gamma) = C(\mathrm{Re}_\theta(\vec{x}_\Gamma))$. Furthermore, coming from a free transition simulation with $C = 0.75$ of the same configuration, the

[2]The momentum thickness Reynolds number Re_θ can be approximated locally as Re^*_θ in the same manner as in equation D.5.

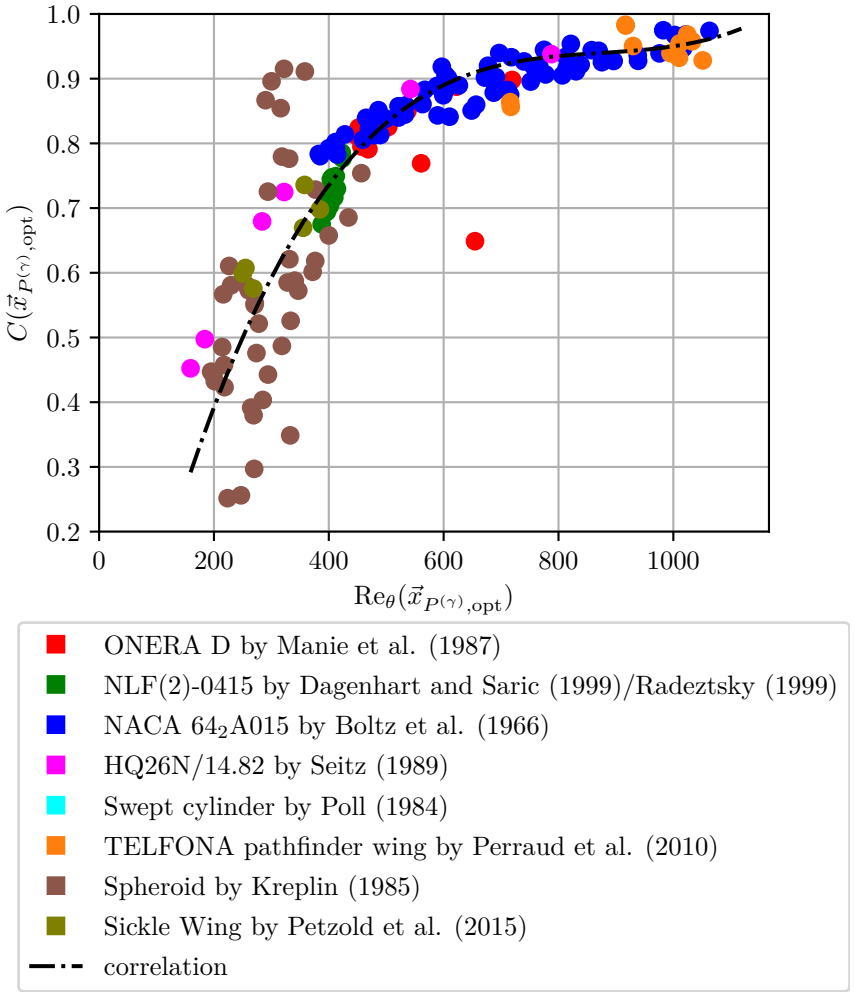

Figure 6.2: Optimal critical-to-transition ratio C for the local C1 approach for all test cases combined with the momentum thickness Reynolds number Re_θ is the argument

location of the onset of intermittency production $\vec{x}_{P^{(\gamma)}}$ and the transition location $\vec{x}_{\mathrm{c},c_\mathrm{f}}$, *computed by a free transition simulation*, are drawn as vertical lines.[3] Starting from the leading edge the critical Reynolds number $C(\mathrm{Re}_\theta)\,\mathrm{Re}_{\delta 2\mathrm{t}}$ is very low, which would trigger the production of intermittency γ far too upstream. It is a necessary that the transition crosswise displacement thickness Reynolds number $\mathrm{Re}_{\delta 2\mathrm{t}}$ is larger in the region where the boundary layer is expected to be laminar. Thus, the momentum thickness Renolds number Re_θ is not well-suited for the new C-correlation
An alternative correlation can be formulated in terms of the *Reynolds number based on the streamwise chord and the boundary layer edge state*

$$\mathrm{Re}_{c,\mathrm{e}}(\vec{x}_\Gamma) = \frac{u_\mathrm{e}(\vec{x}_\Gamma)\, c_\mathrm{sw}}{\nu_\mathrm{e}(\vec{x}_\Gamma)} \;\forall \vec{x}_\Gamma \in \Gamma. \tag{6.3}$$

The correlation is plotted in figure 6.4. It can be seen that the points of the prolate spheroid test case are disregarded for the calibration. This is done because it is known that the local C1 approach will fail the correct transition prediction due the use of the FSC equations [19].

[3] The fact that the intersection of the vertical line for the computed transition location $\vec{x}_{\mathrm{t},c_\mathrm{f}}$ is intersecting the point of intersection of the computed crosswise displacement thickness Reynolds number $\mathrm{Re}_{\delta 2}$ with the transition crosswise displacement thickness Reynolds number $\mathrm{Re}_{\delta 2\mathrm{t}}$ is a coincidence. Put differently, it is $\vec{x}_{\mathrm{t},c_\mathrm{f}} = \vec{x}_{\mathrm{t,criterion}}$, which is desired. It shows that the constant value $C = 0.75$ was well suited for this particular configuration.

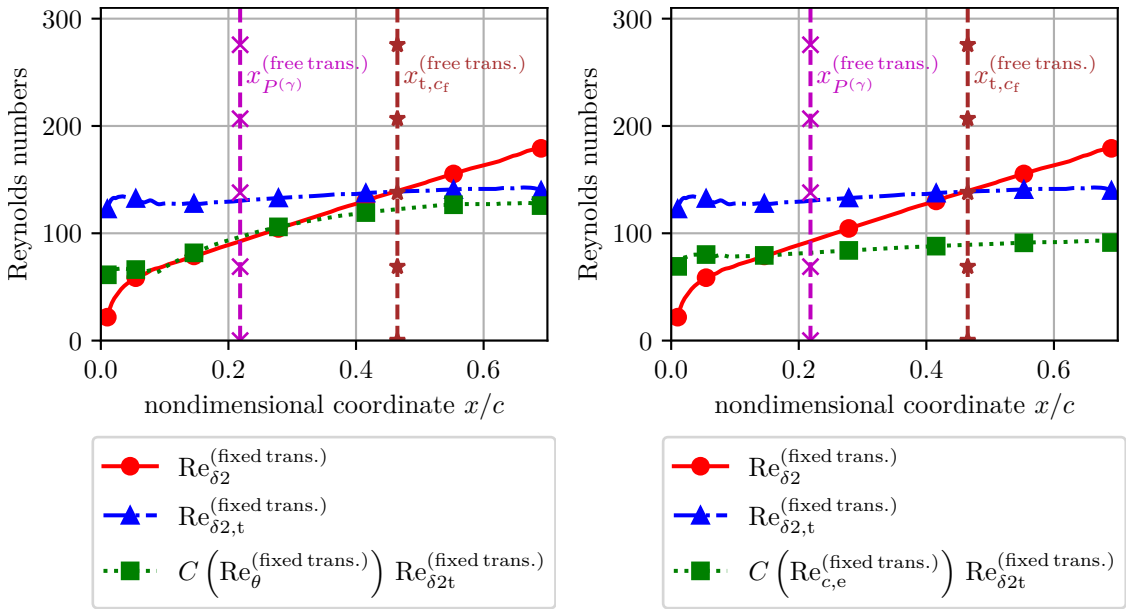

(a) $C = f(\text{Re}_\theta)$ **(b)** $C = f(\text{Re}_{c,\text{e}})$

Figure 6.3: Plot of the chordwise distributions of crosswise displacement thickness Reynolds numbers $\text{Re}_{\delta 2}$ for the adapted C1 criterion, together with characteristic locations marked by vertical lines (Test case configuratoin: NLF(2)-0415 infinite swept wing with $\text{Re}_\infty^{c_\text{sw},u_\text{sw}} = 2.486 \cdot 10^6$)

The equation for the regression curve reads

$$C(\,\text{Re}_{c,\text{e}}(\vec{x}_\Omega)\,) = \begin{cases} 3.559 \cdot 10^{-1} + 1.831 \cdot 10^{-7}\text{Re}_{c,\text{e}} \\ \quad - 2.028 \cdot 10^{-14}\text{Re}_{c,\text{e}}^2 + 7.359 \cdot 10^{-22}\text{Re}_{c,\text{e}}^3 & \text{if } \text{Re}_{c,\text{e}} \leq 8 \cdot 10^6, \\ 0.9 & \text{otherwise} \end{cases}. \tag{6.4}$$

The function is limited from below by 0.5 in order to prevent that CFT is detected too upstream. In addition, not much data is available for such low values of the optimal critical-to-transition ratio C.

For a local approximation of $\text{Re}_{c,\text{e}}$ as $\text{Re}_{c,\text{e}}^*$, the boundary layer edge velocity $u_\text{e}(\vec{x}_\Gamma)\,\forall \vec{x}_\Gamma \in \Gamma$ is computed by equation 2.15 with the assumption of wall normal constant pressure p:

$$u_{\text{e},\mathcal{B}}^*(\vec{x}_\Gamma, y_n) \approx \sqrt{u_\infty^2 + \frac{2\tilde{\gamma}}{\tilde{\gamma}-1}\left[1 - \left(\frac{p_\mathcal{B}(\vec{x}_\Gamma, y_n)}{p_\infty}\right)^{1-\frac{1}{\tilde{\gamma}}}\right]\frac{p_\infty}{\rho_\infty}} \;\forall (\vec{x}_\Gamma, y_n) \in \Gamma \times [0, \delta(\vec{x}_\Gamma)]. \tag{6.5}$$

This is justified by the fact that also for the local C1 approach this approximation is used (see appendix D.2). In addition the boundary layer edge kinematic viscosity $\nu_\text{e}(\vec{x}_\Gamma)\,\forall \vec{x}_\Gamma \in \Gamma$ is replaced by the local kinematic viscosity $\nu(\vec{x}_\Omega)\,\forall \vec{x}_\Omega \in \Omega$. This is justified by the fact that

$$\partial_n \nu(\vec{x}_\Omega) = \frac{\rho\,\partial_n \mu - \mu\,\partial_n \rho}{\rho^2}(\vec{x}_\Omega) \approx 0 \;\forall \vec{x}_\Omega \in \mathcal{B} \tag{6.6}$$

because

$$\partial_n \mu(\vec{x}_\Omega) = \partial_T \mu(T)\;\partial_n T(\vec{x}_\Omega) \approx 0 \;\forall \vec{x}_\Omega \in \mathcal{B} \tag{6.7}$$

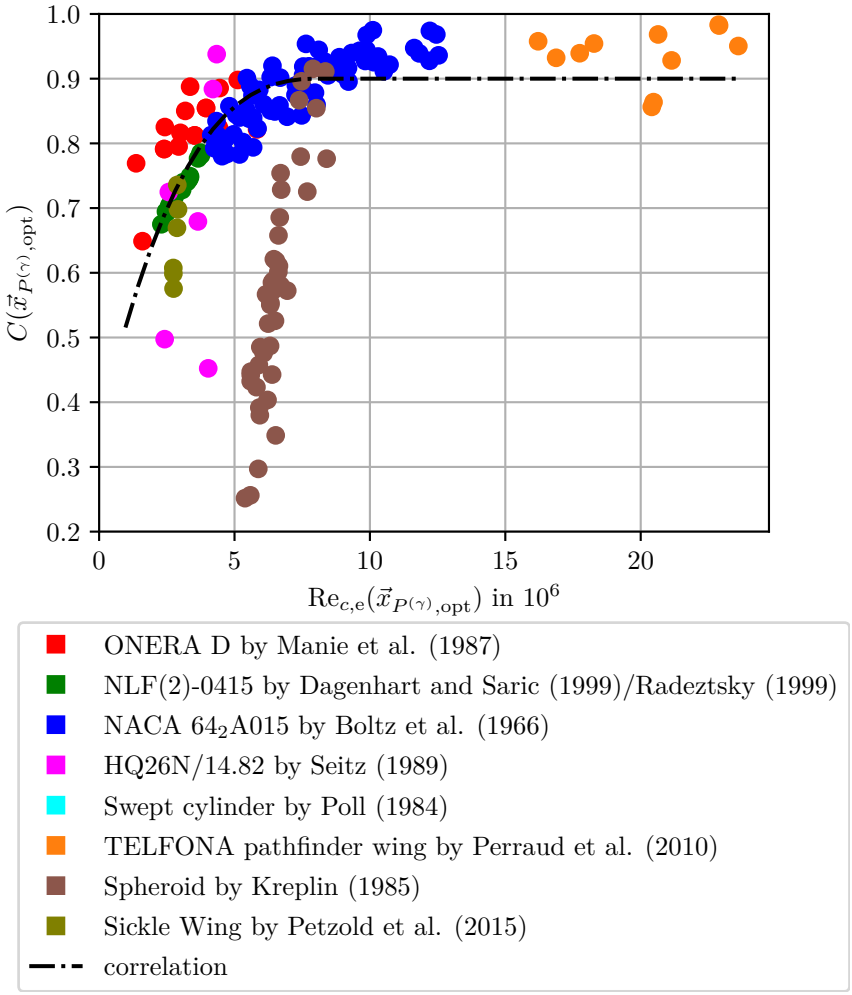

Figure 6.4: Optimal critical-to-transition ratio C for the local C1 approach, with the Reynolds number $\mathrm{Re}_{c,\mathrm{e}}$ based on the streamwise chord and the boundary layer edge state as argument

and

$$\partial_n \rho(\vec{x}_\Omega) = \frac{1}{R}\frac{T\partial_n p - p\,\partial_n T}{T^2}(\vec{x}_\Omega) \approx 0 \;\forall \vec{x}_\Omega \in \mathcal{B}, \tag{6.8}$$

since $\partial_n T(\vec{x}_\Gamma) = 0 \;\forall \vec{x}_\Gamma \in \Gamma$ (adiabatic boundary condition, see equation 3.8). Therefore, it is $\partial_n T(\vec{x}_\Omega) \approx 0 \,\forall \vec{x}_\Omega \in \mathcal{B}$. In addition, it is $\partial_n p(\vec{x}_\Omega) \approx 0 \;\forall \vec{x}_\Omega \in \mathcal{B}$ (see section 2.1.2 about boundary layer theory).

The Reynolds number $\mathrm{Re}_{c,\mathrm{e}}$ changes much less along the surface in comparison to the momentum thickness Reynolds number Re_θ. The problem of a too low critical Reynolds number $C\,\mathrm{Re}_{\delta 2\mathrm{t}}$ in the laminar boundary layer $\mathcal{B}$ is solved, as can be seen in subfigure 6.3b.

6.3 Application of the New Correlation for Free Transition Prediction

If the value $C(\mathrm{Re}_{c,\mathrm{e}})$ is higher than the original value of 0.75, the intermittency production onset location $\vec{x}_{P^{(\gamma)}}$ is expected to move downstream and reversed. This is presented exemplarily for the

NLF(2)-0415 test case in figure 6.5 (preliminary results).[4] It shows the computed transition locations

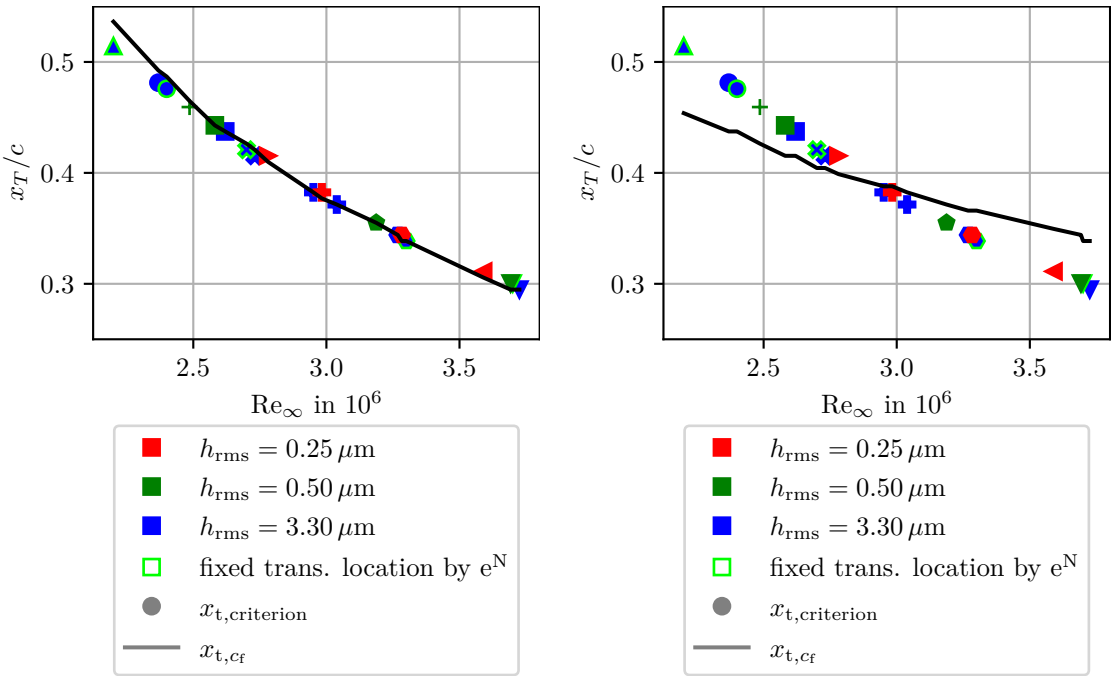

(a) Original $C = 0.75$ **(b)** Recalibrated $C = C(\mathrm{Re}_{c,\mathrm{e}})$

Figure 6.5: NLF(2)-0415 test case: Computed transition locations $\vec{x}_{\mathrm{t},c_\mathrm{f}}$ in comparison to the transition locations given by the adapted C1 criterion $\vec{x}_{\mathrm{t,criterion}}$ for different C-correlation calibrations. Note that the C1 criterion does not take into account the surface roughness, which is why the points for the different roughnesses collapse to a single curve.

$\vec{x}_{\mathrm{t},c_\mathrm{f}}$ for the simulations with both the original and the recalibrated critical-to-transition ratio C, as well as the criterion-predicted transition locations $\vec{x}_{\mathrm{t,criterion}}$, coming from the fixed transition analysis. It is expected that $\vec{x}_{\mathrm{t},c_\mathrm{f}} = \vec{x}_{\mathrm{t,criterion}}$. For freestream Reynolds numbers $\mathrm{Re}_\infty^{c_\mathrm{sw},u_\mathrm{sw}} < 3 \cdot 10^6$ the computed transition location $\vec{x}_{\mathrm{t},c_\mathrm{f}}$ is shifted upstream due to the new C-correlation. This is expected, because the corresponding optimal critical-to-transition ratios C yield values below 0.75. The reversed fact is true for higher freestream Reynolds numbers $\mathrm{Re}_\infty^{c_\mathrm{sw},u_\mathrm{sw}} > 3 \cdot 10^6$. Obviously, the agreement between the computed transition locations $\vec{x}_{\mathrm{t},c_\mathrm{f}}$ and the ones given by the transition criterion $\vec{x}_{\mathrm{t,criterion}}$ is *worsened* by the new C-correlation. This is because the assumption that the length of the intermittency development region l_γ stays constant when changing the critical-to-transition ratio C, is wrong. One has to perform multiple iterations of the procedure, thus repeatedly derive the C-correlation by means of the results for the C-correlation of the previous iteration until convergence of it. In figure 6.6 the dependency of the optimal critical-to-transition ratio C on the momentum thickness Reynolds number Re_θ after the first loop iteration is shown for several test cases. It can be seen that points for the NLF(2)-0415 test case all have approximately the same optimal critical-to-transition ratio. This corresponds to very good agreement between the computed transition locations $\vec{x}_{\mathrm{t},c_\mathrm{f}}$ and the criterion-predicted transition locations $\vec{x}_{\mathrm{t,criterion}}$ when using the original $C = 0.75$ (see subfigure 6.5a).

For future work it is proposed to test the C-correlation equation 6.4 for further test cases. In addition, multiple iterations of determining the optimal critical-to-transition ratio must be performed according to figure 6.1.

[4] No other test cases are tried out due to time reasons.

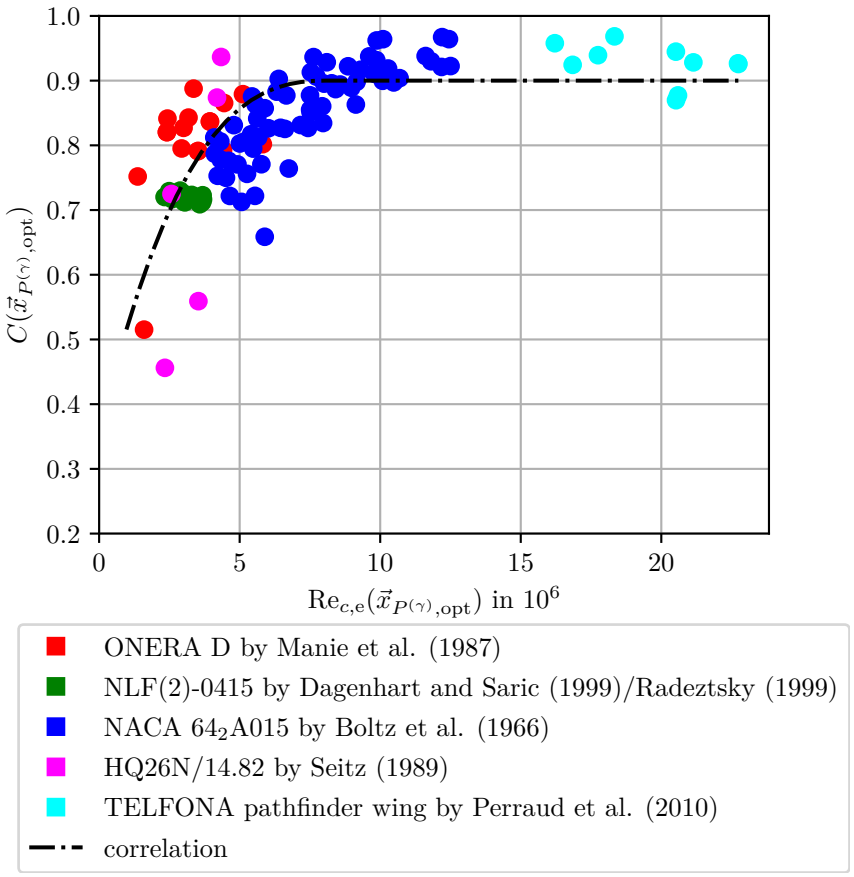

Figure 6.6: Optimal critical-to-transition ratio C after one iteration of recalibration. The drawn regression curve is given by equation 6.4.

7 Conclusion

7.1 Summary

In this thesis, different transition criteria for crossflow instability dominated transition (CFT) in swept wing flows were assessed by using the results of wind tunnel experiments reported in literature. In addition, it was tried to made sure that the transition criterion is applied appropriately within the frame of the *transition transport model with crossflow extension*. This was done by recalibration of a specific model constant in a locally Reynolds number-dependent manner.

For that, in the first part of this thesis the fundamentals of aerodynamics, turbulence and laminar-turbulent transition, alongside with the used modeling approaches for it, were explained. In particular, the γ-$\tilde{\mathrm{R}}\mathrm{e}_{\theta \mathrm{t}}$ transition transport model was given together with three different ways of extending it to CFT modeling. These three ways are associated to the different CFT criteria, which were analyzed in this work: the C1 criterion of Arnal et al. [3], the helicity criterion of Grabe et al. [19] and Langtry's criterion of Langtry et al. [31].

After that, the methods used for the *numerical solution* of the partial differential equations of the model were given. Possible impacts of the numerical solution approaches on the results were identified, for example the consistency order of the spatial and temporal discretization, numerical dissipation and diffusion and convergence of the pseudo-time integration.

Afterwards, the test cases to be used for the analysis were described. The general rules for the selection of CFT configurations within the test cases were based on positive and negative indications for whether a configuration is featuring CFT. If reference conditions were missing in the literature sources about the experiments, assumptions were made, usually for the freestream static temperature T_∞ or/and turbulence intensity Tu_∞. Then all test cases used in this work were presented in form of both the experimental setups from the literature sources and the numerical setups of the present work. The computed pressure coefficient c_p distributions were compared to the measured ones, in the majority of the cases with very good agreement. The concretely selected CFT configurations were given, with the lists in appendix C.

It followed the assessment/recalibration of the CFT criteria. It was described in detail how the analysis is done. The transition criterion plots for the individual test campaigns were discussed. Afterwards, the transition criterion plots for the three CFT criteria filled in with the data points of all test campaigns simultaneously was presented and interpreted:

The C1 criterion showed a "branching" for low shape factors H_{12}: The flow over the NLF(2)-0415 infinite swept wing and the TELFONA Pathfinder wing feature higher crosswise displacement thickness Reynolds numbers $\mathrm{Re}_{\delta 2}$ at the transition locations than the flow over the prolate spheroid and the infinite swept cylinder. Maybe another transition mechanism, the streamline curvature instability, has an effect for the latter two. As the application of the transition transport model will be mostly on the simulation of the flow around wing-like geometries, a recalibration is proposed, given in equation 5.8.

The helicity criterion performs worse than the C1 criterion, which is ascertained by the fact that the scatter in the transition criterion plot among the different CFT test campaigns is larger. It was not possible to find a better correlation for the helicity criterion.

The Langtry's criterion showed significantly less scatter in the transition criterion plot, which means that the different test campaigns behave very similarly with respect to the variables relevant for

the Langtry's criterion. Therefore, an implementation of the Langtry's approach for CFT modeling into the *TAU* solver is *recommended*, especially as it includes the effect of surface roughness. But it must be kept in mind that the Langtry-approach may have a larger sensitivity of the predicted transition location $\vec{x}_{\mathrm{t}}$ with errors in the computations of the momentum thickness Reynolds number Re_{θ} of the boundary layer, as was shown for some test campaigns.
The adapted C1 criterion was implemented into the *TAU* code. When the improved C1 criterion was applied in simulations of test cases for which it was expected to see a difference in the predicted transition line, almost no improved results could be achieved in comparison to the transition prediction with the original C1 criterion. The following explanations for that were proposed:

- Generally, the intermittency production $P^{(\gamma)}$ must be activated upstream of the transition location in order to let the intermittency γ be transported downstream and towards the wall. Where the intermittency γ at the wall is large, the skin friction coefficient c_{f} increases, depicting the computed transition location $\vec{x}_{\mathrm{t},c_{\mathrm{f}}}$. But at the intermittency production onset location $\vec{x}_{P^{(\gamma)}}$ the *argument* $H_{12}(\vec{x}_{P^{(\gamma)}})$ of the transition criterion is different than at the transition location $\vec{x}_{\mathrm{t},c_{\mathrm{f}}}$, thus giving a different transition crosswise displacement thickness Reynolds number $\mathrm{Re}_{\delta 2\mathrm{t}}(\vec{x}_{P^{(\gamma)}})$ than $\mathrm{Re}_{\delta 2\mathrm{t}}(\vec{x}_{\mathrm{t},c_{\mathrm{f}}})$. This "levers out" the performed calibration of the transition criterion, which used the argument $H_{12}(\vec{x}_{\mathrm{t,exp}})$ at the experimental transition location $\vec{x}_{\mathrm{t,exp}}$.
- In order to have a laminar boundary layer $\mathcal{B}$ unaffected by the transition happening downstream, the transition criteria were calibrated by means of evaluating laminar boundary layer parameters with a fixed transition $10\%c$ (chord length c) downstream of the reference transition location. But in free transition simulations the transition may happen less downstream of the intermittency production onset location $\vec{x}_{P^{(\gamma)}}$ than $10\%c$. In addition, in free transition simulation the intermittency γ distribution has a wedge-like form, what lets the transition occur more distributed in chordwise direction than in the fixed transition simulation. Thus, the boundary layer velocity profile $\vec{u}(\vec{x}_{\Omega})\,\forall\vec{x}_{\Omega} \in \mathcal{B}$ gets distorted by the nearby happening transition and the transition criterion is triggered differently than assumed during the calibration.
- For low shape factors H_{12}, the transition prediction by the adapted C1 criterion is very sensitive to a change in the crosswise displacement thickness Reynolds number $\mathrm{Re}_{\delta 2}$. Thus a slight change in the Reynolds number, for example due the facts described in the other bullet points of this list, results in a large change of the transition location $\vec{x}_{\mathrm{t},c_{\mathrm{f}}}$. Therefore the transition prediction gives wrong locations.
- The destruction term $D^{(\gamma)}$ of the γ-$\tilde{\mathrm{Re}}_{\theta\mathrm{t}}$ model might undesirably reduce the CFT-invoked growth of the intermittency γ in the boundary layer $\mathcal{B}$. Thus, no free CFT can be computed for all of the selected configurations of the infinite swept cylinder test case with both the original and the adapted C1 criterion, but only separation-induced transition. The destruction term $D^{(\gamma)}$ was calibrated in the original formulation [32] for streamwise transition mechanisms only and might therefore be unsuitable for crossflow instability dominated configurations.

Finally, a recalibration of the critical-to-transition ratio C for the local C1 approach was carried out. This was done by finding the optimal critical-to-transition ratio C for all test case configurations by combining the results of fixed and free transition simulations with the γ-$\tilde{\mathrm{Re}}_{\theta\mathrm{t}}$ model with CFT extension by the local C1 approach. It was observed that the optimal critical-to-transition ratio is $C > 0.75$ for the majority of the configurations, what is higher than the original constant value of $C = 0.75$ [19]. In the next step a correlation of it with the Reynolds number $\mathrm{Re}_{c,\mathrm{e}}$ based on

the streamwise chord length c_{sw} and the boundary layer edge state is found (equation 6.4). It was described how this Reynolds number can be approximated locally. The regression curve of the new C-correlation was implemented into the *TAU* code and preliminary results of it were shown for the NLF(2)-0415 infinite swept wing test case. The transition prediction was worsened with respect to the transition locations $\vec{x}_{\mathrm{t,criterion}}$ given by the criterion for most of the configurations. A possible explanation for that is the regression error, i.e. the original value of $C = 0.75$ was very well suited for this test case, but a correlation valid for mutliple test cases must be found, which necessarily deviates from some of the data points coming from the configurations.

7.2 Outlook

The negative influence of the numerical solution process onto the model results should be quantified and reduced. For example the mesh independency of the spatial discretization could be determined by redoing the simulations and postprocessing procedures with finer meshes. There are indication signs that the mesh is not good enough for some of the test cases, for example with regard to the number of points in wall normal direction inside the boundary layer. In addition, this can improve the convergence of the iterative numerical solution of the model equations for the flow variables. In particular for the TELFONA Pathfinder wing test case, the matrix artificial dissipation scheme could be used instead of the scalar one, in order to increase the accuracy of the numerical solution. Analogously, the temporal discretization (numerical pseudo-time integration) can be improved. A study of the dependency of the flow solution on the CFL number should be carried out. In this work the CFL numbers for the simulations of the individual test campaigns are chosen more or less arbitrarily, such that a sufficiently good convergence could be achieved. For example, it was found out that the CFL number should not be smaller than 3, in order to get an accurate solution of the crosswise velocity profile of the boundary layer (personal communication by Dr.-Ing. Normann Krimmelbein). This is violated in most of the test cases of this thesis.
In addition, the postprocessing strategy with the use of *Python* can be improved: The read of the flow variables inside the boundary layer $\mathcal{B}$ out of the *TAU* solution files was done based on the *nearest neighbor* algorithm instead of linear interpolation on a equally spaced grid of points distributed between the wall Γ and boundary layer edge $\mathcal{E}$. This inaccuracy introduced into the analysis should be avoided, by solving a bug of the read-out routines of the *PyTecplot* Python module. The influence of the nearest neighbor algorithm onto the analysis was tested only for the NLF(2)-0415 infinite swept wing test case, for which it was low. If the mesh for other test cases, for example the TELFONA Pathfinder wing, has less points inside the boundary layer in wall normal direction, the introduced error due to the nearest neighbor algorithm might be larger.
Another error source was that for some of the test cases the reference conditions could have been wrong (for example for the freestream temperature T_∞ or the freestream turbulence intensity Tu_∞). In addition, for the NLF(2)-0415 swept wing flow contradictory information on the freestream Reynolds number is given in different papers about the experiments [11, 49]. It remains unclear, which values are true.
More validation of the mean flow results could be carried out by comparing measured and computed boundary layer velocity profiles $u(\vec{x}_\Omega)\,\forall \vec{x}_\Omega \in \mathcal{B}$.
The general accuracy of the usage of the CFT criterion in the transition transport model can be improved by adressing the aspects listed in section 7.1 as result of the application of the adapted C1 criterion:

- To counteract the streamwise change of the argument of the transition criterion, another critical-to-transition ratio C_{arg} for the *argument* of the transition criterion could be introduced according to equation 5.12. C_{arg} would have to be calibrated in a similar manner as C for the transition Reynolds number.
- The fixed transition location for the calibration of the transition criteria should be adapted in order to make the the destruction $D^{(k)}$ of total energy e_{t} and the corresponding production $P^{(k)}$ of turbulent kinetic energy k in the fixed transition simulation more comparable to the free transition simulation. Instead of being relatively far downstream of the experimental transition location $\vec{x}_{\mathrm{t,exp}}$, the fixed transition should happen nearer to the measured transition location. In addition, it should occur at the different streamwise coordinates for the streamlines inside the boundary layer $\mathcal{B}$. By that the convection/diffusion transport of intermittency from approximately the middle of the boundary layer towards the wall and the boundary layer edge $\mathcal{E}$, happening in free transition computations, is simulated. Then the laminar boundary layer parameters at the approximate location of intermittency production onset $\vec{x}_{P^{(\gamma)}}$ could be assessed and used to recalibrate a transition criterion.
- An idea that could be examined is to invert the transition criterion, for example write it as $H_{12}(\mathrm{Re}_{\delta 2})$ instead of $\mathrm{Re}_{\delta 2}(H_{12})$. A mixture of both is possible, for example $H_{12}(\mathrm{Re}_{\delta 2})$ is used as transition criterion in regions of low shape factors H_{12} and $\mathrm{Re}_{\delta 2}(H_{12})$ otherwise. For the inverted transition criterion, high sensitivities of the transition prediction to Reynolds number changes might become low sensitivities to shape factor changes. Of course, the usage of the transition criterion in the transition model would have to be adapted (mainly the $F_{\mathrm{onset,cw,1}}$-function, see equation 2.75).
- It must be prevented that the destruction term $D^{(\gamma)}$ becomes active, if the intermittency production $P^{(\gamma)}$ is driven by the CFT term (right hand side underbrace term in equation 2.73). This could be achieved for example by scaling the destruction term $D^{(\gamma)}$ by the ratio of the streamwise and crosswise $F_{\mathrm{onset},1}$-funtions, i.e.

$$\tilde{D}^{(\gamma)} = D^{(\gamma)} \frac{F_{\mathrm{onset},1}}{F_{\mathrm{onset,cw},1}}. \tag{7.1}$$

Apart from that, investigation on the following topics could be performed:
The C1 criterion and the helicity criterion could be extended to include the roughness influence in a similar manner as Lantry's criterion. Unfortunately, the only experiment that can be used well for a corresponding calibration is the NLF(2)-0415 infinite swept wing test case [49], what is a small data base. There are a few test campaigns reported in literature that include information on the surface roughness, but no other experiments explicitely systematically analyze the influence of distributed roughness onto CFT. As the roughness influence onto CFT is industrially relevant, to design and carry out an appropriate new wind tunnel experiment would be helpful.
Apart from the test cases analyzed in this thesis, the flows of further test campaigns could be analyzed (see appendix B). This would enlarge the data base for the calibration.
Furthermore, other CFT criteria could be analyzed by following similar approaches as in this thesis, for example the *Kohama criterion* [25] (with improvements by Watanabe et al. [73]) or the *Modyfied Crossflow Reynolds number criterion* by Medida and Baeder [37]. Furhtermore, there is a criterion derived from the original C1 criterion [3], called *Menter Tc1* criterion [40] (recalibrated by Rubino [51]).

A Deutsche Zusammenfassung

Die Hauptaufgabe der laminar-turbulenten Transitionsmodellierung für Grenzschichten ist die Vorhersage der Transitionslinie auf festen Oberflächen, um die Oberflächenreibung möglichst genau vorherzusagen. Eine korrekte Vorhersage der Oberflächenreibung ist wichtig für die Gestaltung der Oberflächengeometrie neuer Flugzeuge, vor allem für den Flügel. Eine Methode der Transitionsvorhersage ist die lokale korrelations-basierte Transitionsmodellierung, die stark auf der Nutzung von *Transitionskriterien* beruht. Es gibt unterschiedliche Transitionskriterien für unterschiedliche Transitionsmechanismen. In dieser Arbeit werden drei Transitionskriterien für *Transition durch Querströmungsinstabilitäten* (CFT) untersucht: Das C1-Kriterium von Arnal et al. (1984), das Helizitätskriterium von Grabe et al. (2018) und das Kriterium von Langtry et al. (2015). Sie werden bewertet in Bezug auf ihre Genauigkeit, beurteilt anhand von Simulationen verschiedener Windkanal-Experimente aus der Literatur. In den Simulationen wird die Transition entweder manuell gesetzt (festgehaltene Transition) oder mit den γ-$\tilde{\mathrm{Re}}_{\theta \mathrm{t}}$-Transitionstransportmodell mit CFT-Erweiterung unter Nutzung des C1-Kriteriums (freie Transition).
Die Analyse ist durch folgende Fakten motivier: Für bestimmte Testfälle liefert die Transitionsvorhersage auf Basis des C1- und des Helizitätskriteriums ungenauere Ergebnisse als für andere Testfälle. Außerdem ist die Transitionsvorhersage, die Langtry's Kriterium nutzt, noch nicht im genutzten Fluiddynamiklöser *TAU* implementiert. Jedoch kann die Genauigkeit von Langtry's Kriterium in Bezug auf Transitionsvorhersage mithilfe von Simulationen mit festgehaltener Transition trotzdem evaluiert werden. Die Analyse zeigt, ob die Implentierung des Ansatzes von Langtry et al. (2015) den Aufwand wert wäre.
Dies sind die Ergebnisse für das C1-Kriterium: Für Formfaktoren $H_{12} > 2.43$ kann die Reynolds-Zahl $\mathrm{Re}_{\delta 2}$ basierend auf der quergerichteten Verdrängungsdicke an der experimentellen Transitionlage für viele Testfälle gut mit dem Formfaktor korreliert werden. Für kleinere Formfaktoren ist die ursprüngliche Korrelationsgleichung gut geeignet für die Umströmung eines gestreckten Ellipsoids und eines unendlichen gepfeilten Zylinders gut geeignet, nicht jedoch für die Umströmung von flügelartigen Geometrien. Daher wird für kleine Formfaktoren eine Neuformulierung des C1 Kriteriums vorgeschlagen, die in den Fluiddynamiklöser implementiert wird. Es wird präsentiert, dass Berechnungen mit dem γ-$\tilde{\mathrm{Re}}_{\theta \mathrm{t}}$-Transitionsmodell mit CFT-Erweiterung basierend auf dem geänderten C1-Kriterium im Vergleich zu den Berechnungen auf Basis des ursprünglichen C1-Kriteriums fast keine Verbesserungen der Transitionslinien ergeben. Erklärungen für diese Tatsache werden vorgeschlagen, die allgemeine Defizite des Transitionsvorhersagemodells aufzeigen.
Die für das Helizitäts-Kriterium relevante Helizitäts-Reynolds-Zahl $\mathrm{Re}_{\mathrm{He}}$ kann über mehrere Testfälle hinweg nicht gut mit dem Formfaktor H_{12} an der experimentellen Transitionlage korreliert werden. Es geschlussfolgert, dass die Parameter für das Helizitäts-Kriterium weniger geeignet für die CFT-Vorhersage sind als die des C1- und Langtrys Kriterium.
Die Reynolds-Zahl Re_{θ} basierend auf der Impulsverlustdicke für Langtry's Kriterium kann sehr gut mit der dimensionslosen Querströmungsintensität H_{cf} an der gemessenen Transitionslage korreliert werden. Da die ursprüngliche Gleichung für Langtrys Kriterium die Testfälle nicht optimal trifft, wird eine verbesserte Formulierung vorgeschlagen. Die Implementierung von Langtrys Ansatz im Fluiddynamiklöser *TAU* wird empfohlen. Jedoch ist die Empfindlichkeit der Vorhersage der Transitionslinie gegen ungenau berechnete Verdrängungsdicken-Reynolds-Zahlen hoch, da die

Transitions-Verdrängungsdicken-Reynolds-Zahlen $\mathrm{Re}_{\theta \mathrm{t}}$ einen ähnliche Steigung entlang der Stromlinie haben wie die berechnete Verdrängungsdicken-Reynolds-Zahlen Re_{θ}.
Generell werden im Rahmen des γ-$\tilde{\mathrm{Re}}_{\theta \mathrm{t}}$-Transitionsmodells mit CFT-Erweiterung die Parameter der CFT-Kriterien lokal approximiert. Für den lokalen C1-Ansatz wird die Genauigkeit dieser Approximation durch die Rekalibrierung eines bestimmten Modellparameters, genannt *kritisch-zu-transitionelles Verhältnis* C. In der Formulierung von Grabe et al. (2018) is es eine Konstante, aber in der vorliegenden Arbeit wird eine Abhängigkeit des optimalen Werts von der Reynolds-Zahl basierend auf der Sehnenlänge der Oberflächengeometrie und dem Grenzschichtrandzustand gefunden. Die neue C-Korrelation wird im Fluiddynamiklöser implementiert. Vorläufige Ergebenisse für einen Testfall werden gezeigt und diskutiert. Es werden nächste Schritte zur Weiterführung der Arbeit vorgeschlagen.

B List of Test Cases for Crossflow Instability Dominated Transition

This chapter contains lists of test cases for crossflow instability dominated transition.

Test cases analyzed in this work (in parantheses: sources for additional measurement data/configurations, which were not taken into account in this thesis):

- ONERA D airfoil by Manie et al. [36] (Arnal et al. [4, 5])
- NLF(2)-0415 airfoil by Dagenhart and Saric [11]/Radetzki et al. [49] (Agarwal et al. [2])
- NACA 64_2A015 airfoil by Boltz et al. [7]
- HQ26N/14.82 airfoil by Seitz [61]
- Swept cylinder by Poll [47] (Kohama et al. [24])
- TELFONA Pathfinder wing by Perraud et al. [44, 45]/Streit et al. [68, 67]
- 6:1 prolate spheroid by Kreplin et al. [26]
- TU Braunschweig Sickle Wing by Petzold and Radespiel [46] (Muñoz et al. [42])

Other test cases (incomplete list):

- DLR F4 wing body configuration by Fey et al. [17]
- NASA Common Reasearch Model with Natural Laminar Flow by Lynde et al. [35]
- DTP-A swept wing by Arnal et al. [5]
- DTP-B swept wing by Vermeersch et al. [72]
- Generic swept wing by Lemarechal et al. [34]
- NACA0012 swept wing by Tokugawa et al. [69]
- ONERA M6 wing by Schmitt et al. [57]
- ASU(67)-0315 infinite swept wing by Downs et al. [14]
- Airbus AERAST wing by Saeed et al. [52]
- AVF generic high-lift model by Seraudie et al. [62]
- Swept flat plate with pressure bodies by Saric et al. [53]/Mueller et al. [41]

C Lists of the Selected Test Case Configurations

This chapter contains lists of the selected configurations for the test cases analyzed in this thesis.

Table C.1: ONERA D test case: List of the selected CFT configurations of the experiments by Manie et al. [36], augmented by e^N-method results by Dr.-Ing. Normann Krimmelbein. The normal angle of attack of the experiments is $\alpha_n = 6°$. The transition is detected at the lower wing side.

type	Reynolds number $\mathrm{Re}_\infty^{c_n,u_n}/10^6$	sweep angle Λ in °	Mach number Ma_∞	reference transition location $\frac{x_{\mathrm{t,ref}}}{c}$
e^N	0.6	65.0	0.2034	0.38
e^N	0.6	70.0	0.2513	0.29
e^N	0.8	55.0	0.1998	0.47
e^N	0.8	60.0	0.2292	0.35
e^N	0.8	65.0	0.2712	0.26
e^N	1.0	50.0	0.2229	0.45
e^N	1.0	55.0	0.2498	0.34
e^N	1.0	60.0	0.2865	0.26
e^N	1.5	45.0	0.2836	0.37
e^N	1.5	50.0	0.3120	0.28
e^N	1.5	55.0	0.3497	0.21
e^N	1.5	60.0	0.4011	0.15
exp.	1.0	50.0	0.2229	0.45
exp.	1.0	60.0	0.2865	0.27
exp.	1.5	50.0	0.3120	0.26

Table C.3: NACA 64_2A015 test case: List of the selected CFT cases of the experiments by Boltz et. al. [7]. The transition measurements are for the upper wing side.

sweep angle Λ in °	Angle of attack α in °	Reynolds-number $\mathrm{Re}_\infty^{c_{\mathrm{sw}},u_{\mathrm{sw}}}/10^6$	Mach-number Ma_∞	reference transition location $\frac{x_{\mathrm{t,ref}}}{c}$
30.0	-3.0	5.954	0.06415	0.30
30.0	-3.0	6.636	0.07155	0.24
30.0	-3.0	7.234	0.07805	0.21
30.0	-2.5	6.719	0.07246	0.35
30.0	-2.5	7.055	0.07610	0.30
30.0	-2.5	7.478	0.08071	0.24
30.0	-2.5	7.587	0.08190	0.21
30.0	-2.0	7.712	0.05095	0.35
30.0	-2.0	7.864	0.05196	0.30
30.0	-2.0	8.286	0.05476	0.24
30.0	-2.0	8.523	0.05633	0.21
30.0	-1.5	8.856	0.05854	0.35

Continued on next page

Table C.3: NACA 64_2A015 test case: List of the selected CFT cases of the experiments by Boltz et. al. [7]. The transition measurements are for the upper wing side.

sweep angle Λ in °	Angle of attack α in °	Reynolds-number $\mathrm{Re}_{\infty}^{c_{\mathrm{sw}},u_{\mathrm{sw}}}/10^6$	Mach-number Ma_{∞}	reference transition location $\frac{x_{\mathrm{t,ref}}}{c}$
30.0	-1.5	9.178	0.06068	0.30
30.0	-1.5	9.587	0.06340	0.24
30.0	-1.5	9.781	0.06469	0.21
30.0	-1.0	10.350	0.06849	0.35
30.0	-1.0	10.560	0.06987	0.30
30.0	-1.0	10.950	0.07246	0.24
30.0	-1.0	11.270	0.07463	0.21
40.0	-3.0	4.000	0.03805	0.40
40.0	-3.0	4.246	0.04039	0.35
40.0	-3.0	4.564	0.04343	0.30
40.0	-3.0	5.212	0.04962	0.24
40.0	-3.0	5.765	0.05490	0.21
40.0	-2.5	4.849	0.04615	0.35
40.0	-2.5	4.997	0.04757	0.30
40.0	-2.5	5.385	0.05128	0.24
40.0	-2.5	5.750	0.05476	0.21
40.0	-2.0	5.332	0.05076	0.35
40.0	-2.0	5.782	0.05506	0.30
40.0	-2.0	6.243	0.05948	0.24
40.0	-2.0	6.413	0.06110	0.21
40.0	-1.5	5.862	0.03422	0.35
40.0	-1.5	6.218	0.03631	0.30
40.0	-1.5	6.830	0.03988	0.24
40.0	-1.5	7.138	0.04169	0.21
40.0	-1.0	6.902	0.04031	0.35
40.0	-1.0	7.110	0.04152	0.30
40.0	-1.0	7.666	0.04478	0.24
40.0	-1.0	8.568	0.05007	0.21
40.0	-0.5	8.719	0.05095	0.35
40.0	-0.5	8.973	0.05244	0.30
40.0	-0.5	9.407	0.05499	0.24
40.0	0.0	10.930	0.06396	0.35
40.0	0.0	11.170	0.06538	0.30
50.0	-3.0	4.268	0.03406	0.30
50.0	-3.0	4.598	0.03670	0.24
50.0	-3.0	4.794	0.03827	0.21
50.0	-2.5	4.240	0.03384	0.35
50.0	-2.5	4.933	0.03938	0.24
50.0	-2.5	5.325	0.04251	0.21

Continued on next page

Table C.3: NACA 64_2A015 test case: List of the selected CFT cases of the experiments by Boltz et. al. [7]. The transition measurements are for the upper wing side.

sweep angle Λ in °	Angle of attack α in °	Reynolds-number $\mathrm{Re}_{\infty}^{c_{\mathrm{sw}},u_{\mathrm{sw}}}/10^6$	Mach-number Ma_{∞}	reference transition location $\frac{x_{\mathrm{t,ref}}}{c}$
50.0	-2.0	4.644	0.03707	0.35
50.0	-2.0	5.310	0.04240	0.24
50.0	-2.0	5.588	0.04462	0.21
50.0	-1.5	5.189	0.04143	0.35
50.0	-1.5	5.326	0.04253	0.30
50.0	-1.5	5.671	0.04529	0.24
50.0	-1.0	6.026	0.04813	0.35
50.0	-1.0	7.181	0.05740	0.24
50.0	-1.0	7.673	0.06135	0.21
50.0	-0.5	7.103	0.05677	0.35
50.0	-0.5	7.570	0.06052	0.30
50.0	-0.5	8.337	0.06669	0.24
50.0	-0.5	8.789	0.07033	0.21
50.0	0.0	9.098	0.04459	0.35
50.0	0.0	9.321	0.04569	0.30

Table C.2: NLF(2)-0415 test case: List of the selected CFT configurations of the experiments by Dagenhart and Saric [11]/Radeztsky et al. [49], augmented by e^N-method results by Dr.-Ing. Normann Krimmelbein. The sweep angle is $\Lambda = 45°$. The angle of attack is $\alpha = -4°$. The transition is detected at the upper wing side.

RMS roughness h_{rms} in μm	Reynolds number $\mathrm{Re}_\infty^{c_{\mathrm{sw}},u_{\mathrm{sw}}}/10^6$	Mach number Ma_∞	reference transition location $\frac{x_{\mathrm{t,ref}}}{c}$
0.25	2.781	0.06961	0.65
0.25	2.983	0.07467	0.58
0.25	3.283	0.08216	0.53
0.25	3.589	0.08982	0.46
0.50	2.486	0.06221	0.68
0.50	2.581	0.06460	0.65
0.50	3.187	0.07977	0.45
0.50	3.692	0.09241	0.37
3.30	2.200	0.05506	0.65
3.30	2.369	0.05929	0.58
3.30	2.400	0.06007	0.59
3.30	2.620	0.06557	0.56
3.30	2.700	0.06757	0.50
3.30	2.731	0.06835	0.45
3.30	2.951	0.07386	0.40
3.30	3.039	0.07607	0.40
3.30	3.268	0.08178	0.33
3.30	3.300	0.08259	0.37
3.30	3.700	0.09260	0.31
3.30	3.725	0.09324	0.30

Table C.4: HQ26N/14.82 test case: List of the selected CFT configurations of the experiments by Seitz et al. [61]. Note that for the simulations the normal angle of attack $\alpha_{n,\mathrm{CFD}}$ must to be used rather than the streamwise angle of attack $\alpha_{\mathrm{sw,CFD}}$.

side	sw. ang. Λ in °	exp. ang. of att. $\alpha_{\mathrm{sw,exp}}$ in °	CFD ang. of att. $\alpha_{\mathrm{sw,CFD}}$ in °	Reynolds $\mathrm{Re}_\infty^{c_{\mathrm{sw}},u_{\mathrm{sw}}}/10^6$	Mach Ma_∞	trans. $\frac{x_{\mathrm{t,ref}}}{c}$
lower	30	5.56	5.12	3.60	0.24	0.45
lower	30	5.56	5.30	2.96	0.19	0.65
lower	30	6.57	6.40	2.96	0.19	0.43
lower	30	6.57	6.48	2.43	0.16	0.55
lower	30	8.59	8.50	2.97	0.19	0.32
lower	30	8.59	8.50	3.60	0.23	0.24
lower	30	8.59	9.56	1.82	0.11	0.57
lower	45	3.55	3.20	4.47	0.23	0.50
lower	45	4.06	3.92	2.29	0.15	0.65
lower	45	4.06	3.92	4.47	0.23	0.36
lower	45	6.59	6.66	2.99	0.15	0.28
lower	45	6.59	6.66	4.45	0.23	0.19
upper	45	-2.01	-2.18	4.46	0.23	0.17
upper	45	0.52	0.32	4.48	0.23	0.27

Table C.5: TELFONA Pathfinder wing test case: List of the selected CFT configurations of the experiments by Perraud et al. [44], augmented by e^N data by [59]

type	wing side	lift coefficient c_L (exp.)	Reynolds number $\mathrm{Re}_\infty^{\bar{c},u_{\mathrm{sw}}}/10^6$	angle of attack α (CFD) in °	reference transition location $\frac{x_{\mathrm{t,ref}}}{c}$
e^N	upper	0.099	20.00	0.30	0.15
exp.	lower	0.401	20.00	3.08	0.30
exp.	lower	0.450	15.30	3.62	0.40
exp.	lower	0.450	16.00	3.61	0.40
exp.	lower	0.450	16.90	3.58	0.30
exp.	lower	0.450	17.40	3.56	0.25
exp.	lower	0.450	19.75	3.54	0.21
exp.	lower	0.450	23.00	3.50	0.10
exp.	upper	0.095	18.10	0.24	0.28
exp.	upper	0.100	20.00	0.30	0.25
exp.	upper	0.105	18.00	0.31	0.30

Table C.6: Swept cylinder test case: List of the selected CFT configurations of the experiments by Poll [47]. The angle of attack is $\alpha = 0°$.

sweep angle Λ in °	Reynolds-number $\mathrm{Re}_\infty^{c_n,u_{\mathrm{sw}}}/10^6$	Mach-number Ma_∞	reference transition location $\frac{x_{\mathrm{t,ref}}}{c}$
63.5	3.43	0.141	0.107
63.5	3.76	0.154	0.090
64.7	3.56	0.140	0.107
64.7	3.73	0.147	0.090
65.4	3.66	0.140	0.107
65.4	3.94	0.151	0.090
66.4	3.78	0.140	0.107
66.4	4.01	0.148	0.090
68.0	3.81	0.131	0.107
68.0	4.07	0.140	0.090
68.9	3.87	0.128	0.107
68.9	4.18	0.138	0.090

D Local Approximations of integral Boundary Layer Parameters

D.1 The Local Approach of Langtry and Menter

In order to implement the transition criterion of Langtry and Menter [32] in the γ-$\tilde{\mathrm{Re}}_{\theta \mathrm{t}}$ transition transport model, the momentum thickness Reynolds number Re_θ and the transition momentum thickness Reynolds number $\mathrm{Re}_{\theta \mathrm{t}}$ need to be computed locally. This is done according to [32]. First, define the *local approximated momentum thickness* θ_{t}^* by

$$\theta_{\mathrm{t}}^*(\vec{x}_\Omega) = \underset{\theta_{\mathrm{t}}^* \in \mathbb{R}^+}{\arg} \left(\frac{u\,\theta_{\mathrm{t}}^*}{\nu}(\vec{x}_\Omega) = f_{\text{criterion},\gamma\text{-}\tilde{\mathrm{Re}}_{\theta \mathrm{t}}} \left(\mathrm{Tu}(\vec{x}_\Omega), \frac{\theta_{\mathrm{t}}^{*2}}{\nu} \partial_{\mathrm{sw}}\, u(\vec{x}_\Omega) \right) \right), \ \forall \vec{x} \in \Omega, \tag{D.1}$$

which is the transition criterion equation 2.57 with *local evaluation* (locally in $\vec{x}_\Omega$) of the variables, except of the momentum thickness θ_{t}, for which the equation is solved numerically. The Reynolds number based on that momentum thickness is the *local approximated transition momentum thickness Reynolds number*

$$\mathrm{Re}_{\theta \mathrm{t}}^*(\vec{x}_\Omega) = \frac{u\,\theta_{\mathrm{t}}^*}{\nu}(\vec{x}_\Omega), \ \forall \vec{x} \in \Omega. \tag{D.2}$$

The next step is to introduce the vorticity Reynolds number

$$\mathrm{Re}_{\mathrm{v},\mathcal{B}}(\vec{x}_\Gamma, y_n) = \frac{y_n^2 S_{\mathcal{B}}(\vec{x}_\Gamma, y_n)}{\nu_{\mathcal{B}}(\vec{x}_\Gamma, y_n)} \ \forall (\vec{x}_\Gamma, y_n) \in \Gamma \times \mathbb{R}^+, \tag{D.3}$$

which is not based on the vorticity $\vec{\omega}$, but on the strain rate $S = \|\underline{\underline{S}}\|$. By the analytical solutions of Pohlhausen [21] and Schlichting [56] for two-dimensional laminar boundary layers without pressure gradients it holds

$$\max_{y_n \in [0, \delta(\vec{x}_\Gamma)]} \mathrm{Re}_{\mathrm{v},\mathcal{B}}(\vec{x}_\Gamma, y_n) \approx 2.192\, \mathrm{Re}_\theta(\vec{x}_\Gamma) \ \forall \vec{x}_\Gamma \in \Gamma \tag{D.4}$$

or, equivalently,

$$\mathrm{Re}_\theta(\vec{x}_\Gamma) \geq \mathrm{Re}_{\theta,\mathcal{B}}^*(\vec{x}_\Gamma, y_n) := \frac{\mathrm{Re}_{\mathrm{v},\mathcal{B}}(\vec{x}_\Gamma, y_n)}{2.192} \ \forall (\vec{x}_\Gamma, y_n) \in \Gamma \times [0, \delta(\vec{x}_\Gamma)]. \tag{D.5}$$

The *transition momentum thickness Reynolds number* is

$$\mathrm{Re}_{\theta \mathrm{t}}(\vec{x}_\Gamma) = f_{\text{criterion},\gamma\text{-}\tilde{\mathrm{Re}}_{\theta \mathrm{t}}}(\mathrm{Tu}_{\mathrm{e}}(\vec{x}_\Gamma), \lambda_2(\vec{x}_\Gamma)). \tag{D.6}$$

The ratio of the momentum thickness Reynolds number Re_θ to the transition momentum thickness Reynolds number $\mathrm{Re}_{\theta \mathrm{t}}$ inside the laminar boundary layer is written as

$$\frac{\mathrm{Re}_\theta}{\mathrm{Re}_{\theta \mathrm{t}}}(\vec{x}_\Gamma) < 1, \ \forall \vec{x}_\Gamma \in \Gamma_{\mathrm{lam}}. \tag{D.7}$$

By insertion of equation D.5 into equation D.7 one gets

$$\frac{\mathrm{Re}_{\theta,\mathcal{B}}^*(\vec{x}_\Gamma, y_n)}{\mathrm{Re}_{\theta \mathrm{t}}(\vec{x}_\Gamma)} \leq 1, \ \forall (\vec{x}_\Gamma, y_n) \in \Gamma_{\mathrm{lam}} \times [0, \delta(\vec{x}_\Gamma)]. \tag{D.8}$$

Now extend equation D.8 from the surface Γ to whole domain Ω by local evaluation of the variables:

$$\frac{\mathrm{Re}_\theta^*}{\mathrm{Re}_{\theta\mathrm{t}}^*}(\vec{x}_\Omega) \leq 1,\ \forall \vec{x}_\Omega \in \mathcal{B}_{\mathrm{lam}}. \tag{D.9}$$

The justification for the validity extension from the surface Γ to whole domain Ω by local evaluation is that the transition will not be triggered anyway at the locations where the equations were not valid before the extension.

D.2 Local C1 Approach

According to [19], the *local approximated transition displacement thickness Reynolds number* $\mathrm{Re}_{\delta 2\mathrm{t}}^*$ is found as follows:
Equation D.4 is rearranged by cancelling the kinematic viscosity ν [1]

$$\theta(\vec{x}_\Gamma) = \frac{\max\limits_{y_n \in [0,\delta(\vec{x}_\Gamma)]} \left(y_n^2 S_{\mathcal{B}}(\vec{x}_\Gamma, y_n)\right)}{2.192\, u_{\mathrm{e}}(\vec{x}_\Gamma)}\ \forall \vec{x}_\Gamma \in \mathcal{T}. \tag{D.10}$$

In it, the boundary layer edge velocity is replaced by means of the compressible Bernoulli equation under assumption of a wall normal-constant pressure p (equation 6.5).
Then, equation D.10 can be extended to whole Ω by local evaluation of the variables and drop of the max-operator. The result is called the *local approximated momentum thickness for the C1 criterion* $\theta^{*\mathrm{C1}}$.
Plugging the local approximated momentum thickness for the C1 criterion $\theta^{*\mathrm{C1}}$ into the formula of the pressure gradient parameter gives the *local approximated pressure parameter for the C1 criterion* $\lambda_2^{*\mathrm{C1}}$. As stated in section 2.1.2 about the boundary layer theory, there is a relation of the pressure gradient parameter λ_2 to the shape factor H_{12}. The concrete equation for that depends on the boundary layer velocity profile $\vec{u}(\vec{x})\,\forall \vec{x} \in \mathcal{B}$. There is an analytical solution for the three-dimensional laminar boundary layer of Falkner-Skan [16] and Cooke [10], abbreviated as the *FSC* boundary layer. It can be used as an approximate description of the boundary layer on infinite swept wings and yawed cylinders [19]. By the FSC equations the link between the pressure gradient parameter λ_2 and the shape factor $H_{12}^{\mathrm{FSC}}(\lambda_2)$ for the three-dimensional boundary layer is found [19]. Hence, the *local approximated transition displacement thickness Reynolds number* can be calculated as

$$\mathrm{Re}_{\delta 2\mathrm{t}}^*(\vec{x}_\Omega) = f_{\mathrm{criterion,\ C1}}\left(H_{12}^{\mathrm{FSC}}\left(\lambda_2^{*\mathrm{C1}}(\vec{x}_\Omega)\right)\right)\ \forall \vec{x}_\Omega \in \Omega. \tag{D.11}$$

Next, the crosswise displacement thickness Reynolds number must be determined locally as $\mathrm{Re}_{\delta 2}^*$: Writing down a trivial identity for the displacement thickness Reynolds number as

$$\mathrm{Re}_{\delta 2}(\vec{x}_\Gamma) = \frac{\sin\vartheta \max\limits_{y_n \in [0,\delta(\vec{x}_\Gamma)]} \mathrm{Re}_{\mathrm{v},\mathcal{B}}(\vec{x}_\Gamma, y_n)}{\frac{\sin\vartheta \max\limits_{y_n \in [0,\delta(\vec{x}_\Gamma)]} \mathrm{Re}_{\mathrm{v},\mathcal{B}}(\vec{x}_\Gamma, y_n)}{\mathrm{Re}_{\delta 2}(\vec{x}_\Gamma)}}\ \forall \vec{x}_\Gamma \in \Gamma. \tag{D.12}$$

The variable ϑ is the local sweep angle of the wing [19].
By computing the FSC equations for various sweep angles ϑ and Hartree parameters (a dimensionless parameter for the pressure chordwise gradient [18]), Grabe et al. [19] found a correlation $f_{\mathrm{corr,C1}}$

[1] It is assumed that $\nu_{\mathcal{B}}(\vec{x}_\Gamma, y_n) \approx \nu_{\mathrm{e}}(\vec{x}_\Gamma)\,\forall (\vec{x}_\Gamma, y_n) \in \Gamma \times [0, \delta(\vec{x}_\Gamma)]$.

(given in [19]) that fulfills

$$\frac{\sin\vartheta \max\limits_{y_n\in[0,\delta(\vec{x}_\Gamma)]} \mathrm{Re}_{\mathrm{v},\mathcal{B}}(\vec{x}_\Gamma, y_n)}{\mathrm{Re}_{\delta 2}(\vec{x}_\Gamma)} = f_{\mathrm{corr,C1}}(H_{12}(\vec{x}_\Gamma), \vartheta)\ \forall \vec{x}_\Gamma \in \Gamma. \tag{D.13}$$

The sweep angle ϑ of the wing is the angle between the chord-direction and the boundary layer edge velocity $\vec{u}_\mathrm{e}$. If the chord direction is approximated as the unit vector of the pressure gradient projection onto the wall (thus assuming a zero span-wise pressure gradient) and if the boundary layer edge velocity $\vec{u}_\mathrm{e}$ is replaced by the local velocity (same reasoning for that as before), the *local approximated sweep angle* ϑ^* is known. Then the denominator in equation D.12 can be expressed by equation D.13 with locally approximated quantities. In addition, the max-operator is dropped, with the same reasoning as before, to extend the equation to whole Ω by local evaluation of the variables. The result is the *local approximated crosswise-displacement thickness Reynolds number*

$$\mathrm{Re}^*_{\delta 2} = \frac{\sin\vartheta^* \mathrm{Re}_\mathrm{v}}{f_{\mathrm{corr,C1}}(H^{*\mathrm{C1}}_{12}, \vartheta^*)}(\vec{x}_\Omega)\ \forall \vec{x}_\Omega \in \Omega. \tag{D.14}$$

D.3 Local Helicity Approach

This is how the local approximation of the transition helicity Reynolds number $\mathrm{Re}_{\mathrm{He,t}}$ is found:
Compute a *local approximated pressure gradient parameter*

$$\lambda_2^{*\mathrm{He}}(\vec{x}_\Omega) = \frac{l^2}{\nu}(\vec{x}_\Omega)\, \partial_{\mathrm{sw}} u_\mathrm{e}(\vec{x}_\Omega) \tag{D.15}$$

by using a locally available length scale l that was calibrated by simulations over swept wings such that at the wall normal coordinate of the maximum helicity Reynolds number $y_n = \underset{y_n\in[0,\delta(\vec{x}_\Gamma)]}{\mathrm{argmax}}\ \mathrm{Re}_{\mathrm{He},\mathcal{B}}(\vec{x}_\Gamma, y_n)$ it is equal to the momentum thickness $\theta(\vec{x}_\Gamma)$ at the corresponding surface location $\vec{x}_\Gamma$ [19]:

$$l_\mathcal{B}(\vec{x}_\Gamma, y_n) = \frac{1}{C_{\mathrm{He,max}}}\frac{2}{15} y_n\ \forall (\vec{x}_\Gamma, y_n) \in \Gamma \times [0, \delta(\vec{x}_\Gamma)] \tag{D.16}$$

with $C_{\mathrm{He,max}} = 0.6944$ [19]. The boundary layer edge velocity in equation D.15 is again computed by equation 6.5.
Pluging in the local approximated pressure gradient parameter $\lambda_2^{*\mathrm{He}}$ into the the *correlation of Cliquet* [9]:

$$H_{12}^{\mathrm{Cliquet}}(\lambda_2) = 4.02923 - \sqrt{-8838.4\lambda_2^4 + 1105.1\lambda_2^3 - 67.962\lambda_2^2 + 17.574\lambda_2 + 2.0593} \tag{D.17}$$

Then the *local approximated transition helicity Reynolds number* can be computed as

$$\mathrm{Re}^*_{\mathrm{He,t}}(\vec{x}_\Omega) = f_{\mathrm{criterion,He}}\left(H_{12}^{\mathrm{Cliquet}}\left(\lambda_2^{*\mathrm{He}}(\vec{x}_\Omega)\right)\right)\ \forall \vec{x}_\Omega \in \Omega. \tag{D.18}$$

D.4 Langtry's Approach

The CFT momentum thickness Reynolds number $\mathrm{Re}_{\theta\mathrm{t}}$ is found in a similar manner as for the local approach of Langtry and Menter [31].

In each point $\vec{x} \in \Omega$ solve

$$\frac{\theta^{*\text{Langtry}}(\vec{x}_\Omega)\frac{u(\vec{x}_\Omega)}{0.82}}{\nu(\vec{x}_\Omega)} = f_{\text{criterion,Langtry}}\left(H_{\text{CF}}(\vec{x}_\Omega), \frac{h_{\text{rms}}}{\theta^{*\text{Langtry}}(\vec{x}_\Omega)}, R^{\text{turb}}(\vec{x}_\Omega)\right) \ \vec{x}_\Omega \in \Omega \tag{D.19}$$

numerically for the *local approximated transition momentum thickness for the Langtry-approach* $\theta^{*\text{Langtry}}$, thus extending the transition criterion equation 2.86 from the surface Γ to the whole domain Ω. The 0.82 in the denominator is for taking approximately into account the difference in the velocity u at the boundary layer edge $\mathcal{E}$ and the wall normal coordinate where the vorticity Reynolds number is maximum.
Plugging the local approximated transition momentum thickness for the Langtry-approach $\theta^{*\text{Langtry}}$ into the formula for the momentum thickness Reynolds number gives the *local approximated CFT momentum thickness Reynolds number*

$$\text{Re}^*_{\theta\text{t,cf}}(\vec{x}_\Omega) = \frac{u\,\theta^{*\text{Langtry}}}{\nu}(\vec{x}_\Omega) \ \forall \vec{x} \in \Omega. \tag{D.20}$$

The local approximated momentum thickness Reynolds number is again given by equation D.5.

E Sensitivity of the Transition Prediction to Inaccurate Reynolds Numbers

This section explains in more detail what is meant by the *sensitivity of the criterion-predicted transition location to a change of the Reynolds numbers*. In addition it is linked to the length of the vertical errorbars that are used in chapter 5 in the transition criterion plots.
For a briefer explanation the location on the surface along a wall projected boundary layer edge streamline $\mathcal{S}_{\mathcal{E}\to\Gamma}$ is denoted by a scalar x in this section. In addition, the computed Reynolds number Re_ϕ is one computed by the integral and local boundary layer parameters. The transition Reynolds number $\mathrm{Re}_{\phi\mathrm{t}}$ is the criterion function $f_{\mathrm{criterion}}$ evaluated with the integral and local boundary layer parameters. The *criterion-predicted transition location* is

$$x_{\mathrm{t,criterion}} = \underset{x}{\arg}(\underbrace{(\mathrm{Re}_{\phi\mathrm{t}} - \mathrm{Re}_\phi)}_{\Delta Re}(x) = 0), \tag{E.1}$$

i.e. the location where the Reynolds number difference $\Delta\mathrm{Re}$ is zero. The Reynolds number difference $\Delta\mathrm{Re}(x_{\mathrm{t,criterion}})$ can be approximated by an abridged Taylor expansion around some point x_0:

$$\begin{aligned} &\Delta\mathrm{Re}(x_{\mathrm{t,criterion}}) \approx \Delta\mathrm{Re}(x_0) + (\partial_x\Delta\mathrm{Re}(x_0))(x_{\mathrm{t,criterion}} - x_0) \overset{!}{=} 0 \\ \iff\ & x_{\mathrm{t,criterion}} = x_0 - \frac{\Delta\mathrm{Re}}{\partial_x\Delta\mathrm{Re}}(x_0) \end{aligned} \tag{E.2}$$

The Reynolds number difference $\Delta\mathrm{Re}$ is written as the *true value* $\Delta\mathrm{Re}_{\mathrm{true}}$ plus an *approximation error* ε, which comes from violated model assumptions or numerical errors:

$$\Delta\mathrm{Re}(x) = \Delta\mathrm{Re}_{\mathrm{true}}(x) + \varepsilon \tag{E.3}$$

The *sensitivity of the transition prediction* is defined as the absolute value of the derivative of the criterion-predicted transition location $x_{\mathrm{t,criterion}}$ with respect to the approximation error ε:[1]

$$\left|\frac{\partial x_{\mathrm{t,criterion}}}{\partial\varepsilon}\right|(x_0) = \frac{1}{|\partial_x\Delta\mathrm{Re}(x_0)|} \tag{E.4}$$

Concludingly, a large slope of the Reynolds number difference $\partial_x\Delta\mathrm{Re}$ is connected to a low sensitivity of the transition prediction.
If the points x_0, $x_{\mathrm{t,criterion}}$ and the experimental transition location $x_{\mathrm{t,exp}}$ are close to each other, it is

$$\left|\frac{\partial x_{\mathrm{t,criterion}}}{\partial\varepsilon}\right|(x_0) \approx \left|\frac{\partial x_{\mathrm{t,criterion}}}{\partial\varepsilon}\right|(x_{\mathrm{t,criterion}}) \approx \left|\frac{\partial x_{\mathrm{t,criterion}}}{\partial\varepsilon}\right|(x_{\mathrm{t,exp}}). \tag{E.5}$$

From that it follows

$$\begin{aligned} &\text{vertical errorbar length} = \Delta\mathrm{Re}(x_{\mathrm{t,exp}} - 5\%c) - \Delta\mathrm{Re}(x_{\mathrm{t,exp}}) \\ &\approx \partial_x\Delta\mathrm{Re}(x_{\mathrm{t,exp}}) \cdot 5\%c = \left|\frac{\partial x_{\mathrm{t,criterion}}}{\partial\varepsilon}\right|^{-1}(x_{\mathrm{t,criterion}}) \cdot 5\%c. \end{aligned} \tag{E.6}$$

[1] Note that $\partial_x\Delta\mathrm{Re}(x) = \partial_x\Delta\mathrm{Re}_{\mathrm{true}}(x)$

Hence, the longer the vertical errorbars, the less sensitive the transition prediction or modeling or numerical errors (inverse proportionality).

F Alternative Correlations for Crossflow Instability Dominated Transition

In the C1, helicity and Langtry's criteria different integral boundary layer parameters or wall normal maxima of local variables at the transition line $\mathcal{T}$ are correlated against each other. In this chapter, the transition criterion plots for all remaining combinations of the parameters are given (figures F.1 to F.7).

Note that the relatively good correlation of the wall normal maximum helicity Reynolds number $\max_{y_n \in [0,\delta(\vec{x}_\mathrm{t})]} \mathrm{Re}_{\mathrm{He},\mathcal{B}}(\vec{x}_\mathrm{t}, y_n)$ with the crosswise displacement thickness Reynolds number $\mathrm{Re}_{\delta 2}(\vec{x}_\mathrm{t})$ is due to the derivation of $\mathrm{Re}_{\delta 2}$ from Re_He [19].

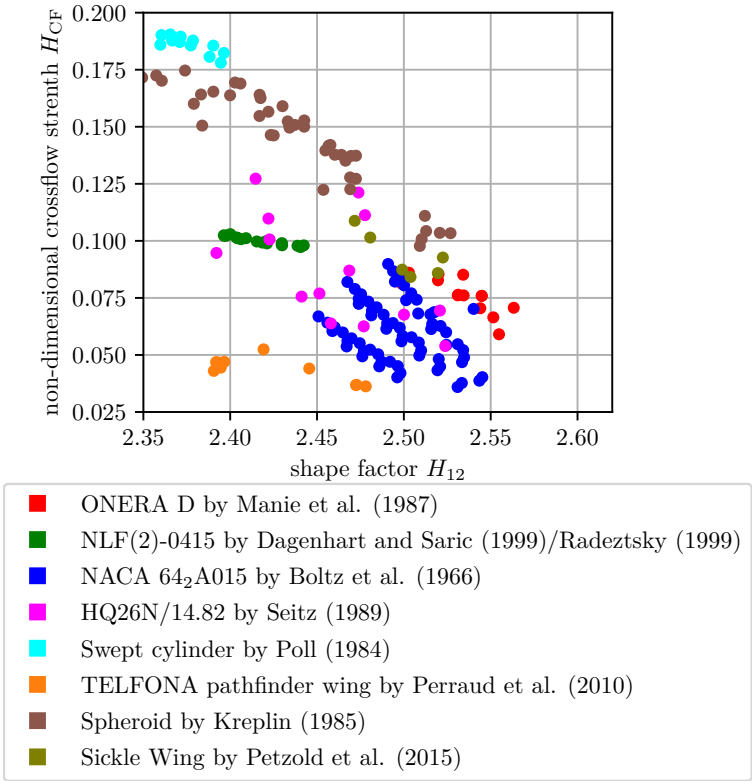

Figure F.1: Wall normal maximum Non-dimensional crossflow strenght $\max_{y_n \in [0,\delta(\vec{x}_\mathrm{t})]} H_{\mathrm{CF},\mathcal{B}}(\vec{x}_\mathrm{t}, y_n)$ vs. shape factor $H_{12}(\vec{x}_\mathrm{t})$

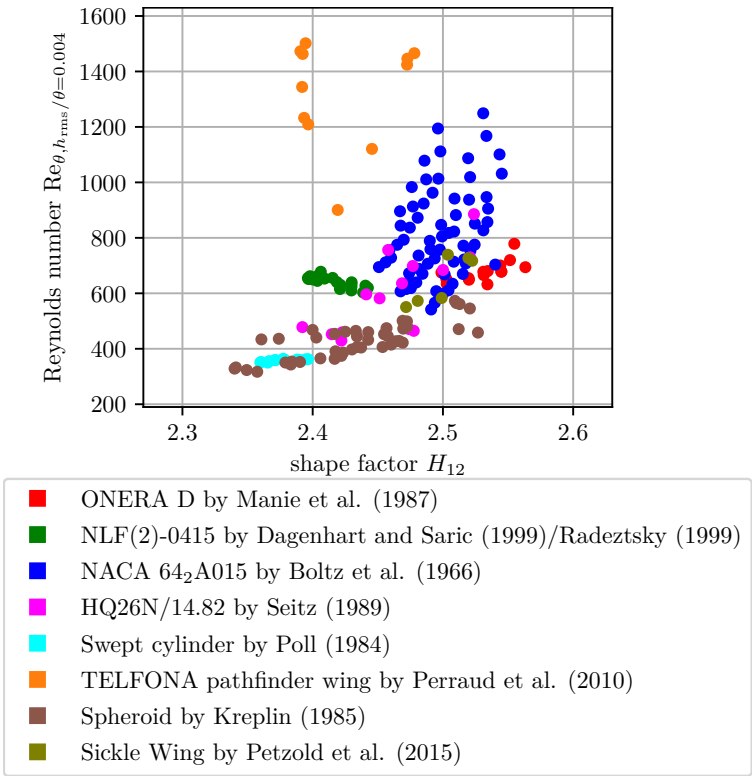

Figure F.2: Momentum thickness Reynolds number $\mathrm{Re}_\theta(\vec{x}_\mathrm{t})$ vs. shape factor $H_{12}(\vec{x}_\mathrm{t})$

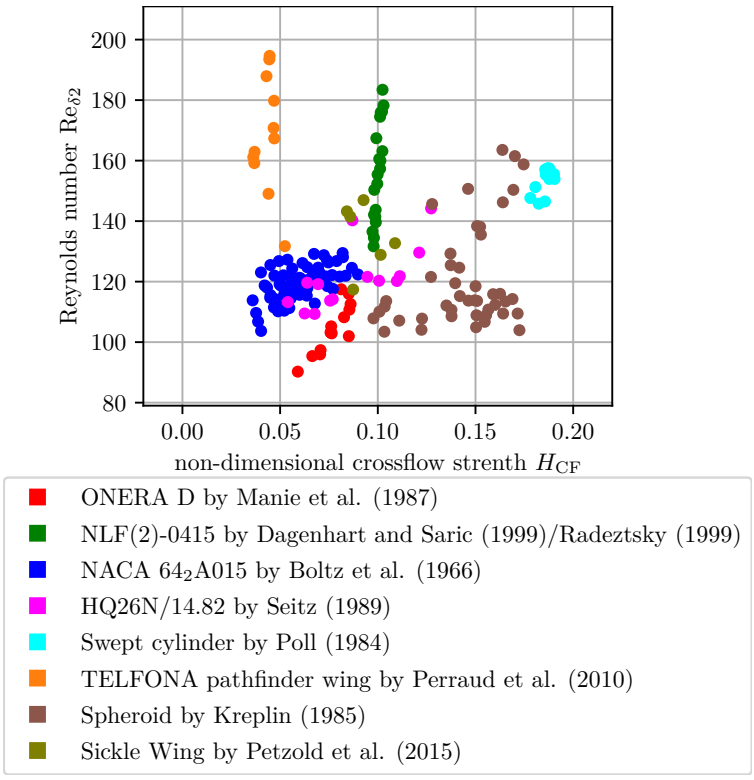

Figure F.3: Crosswise displacement thickness Reynolds number $\mathrm{Re}_{\delta 2}(\vec{x}_\mathrm{t})$ vs. wall normal maximum Non-dimensional crossflow strenght $\max_{y_n \in [0,\delta(\vec{x}_\mathrm{t})]} H_{\mathrm{CF},\mathcal{B}}(\vec{x}_\mathrm{t}, y_n)$

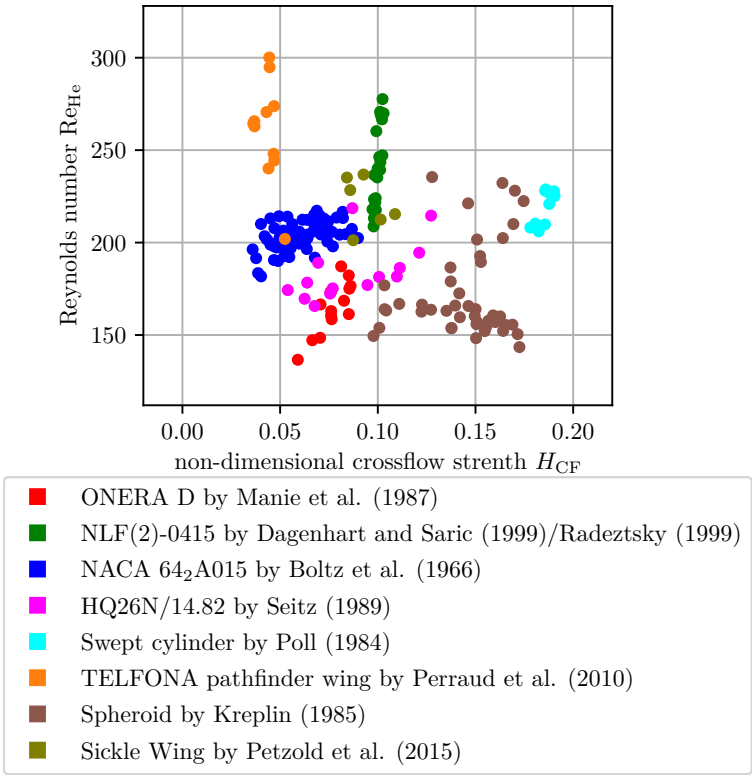

Figure F.4: Wall normal maximum helicity Reynolds number $\max_{y_n \in [0,\delta(\vec{x}_\mathrm{t})]} \mathrm{Re}_{\mathrm{He},\mathcal{B}}(\vec{x}_\mathrm{t}, y_n)$ vs. wall normal maximum Non-dimensional crossflow strenght $\max_{y_n \in [0,\delta(\vec{x}_\mathrm{t})]} H_{\mathrm{CF},\mathcal{B}}(\vec{x}_\mathrm{t}, y_n)$

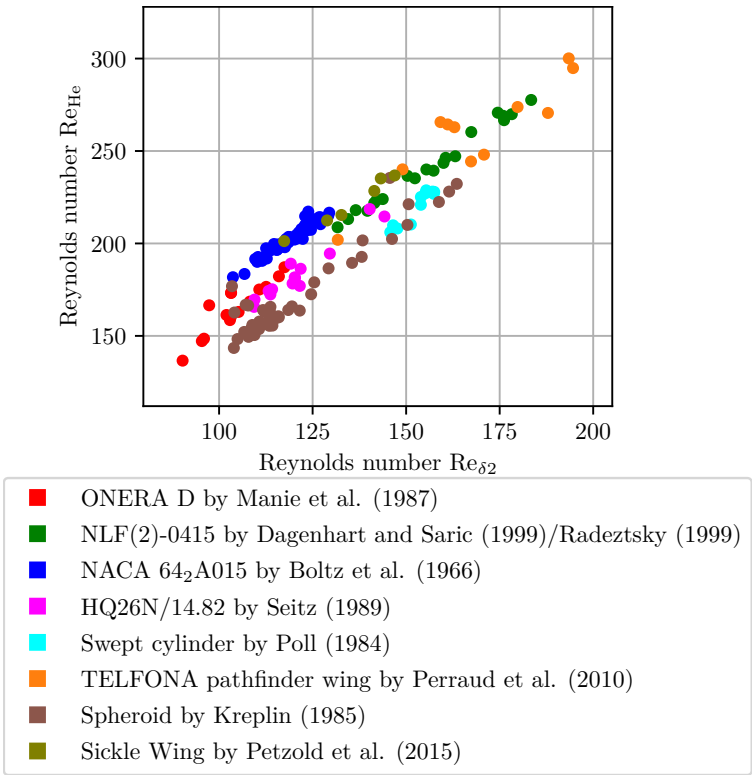

Figure F.5: Wall normal maximum helicity Reynolds number $\max_{y_n \in [0,\delta(\vec{x}_\mathrm{t})]} \mathrm{Re}_{\mathrm{He},\mathcal{B}}(\vec{x}_\mathrm{t}, y_n)$ vs. crosswise displacement thickness Reynolds number $\mathrm{Re}_{\delta 2}(\vec{x}_\mathrm{t})$

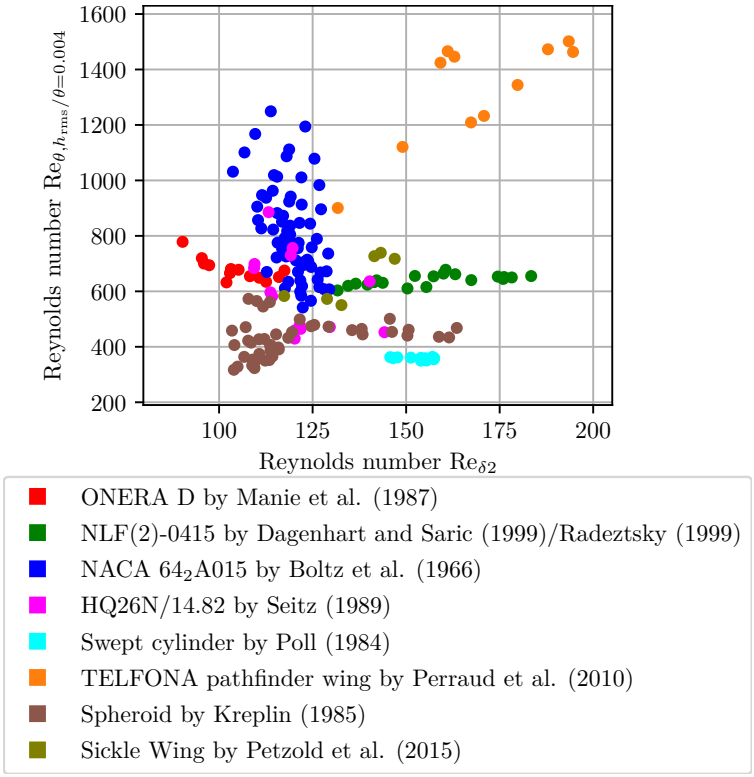

Figure F.6: Momentum thickness Reynolds number $\mathrm{Re}_\theta(\vec{x}_\mathrm{t})$ vs. crosswise displacement thickness Reynolds number $\mathrm{Re}_{\delta 2}(\vec{x}_\mathrm{t})$

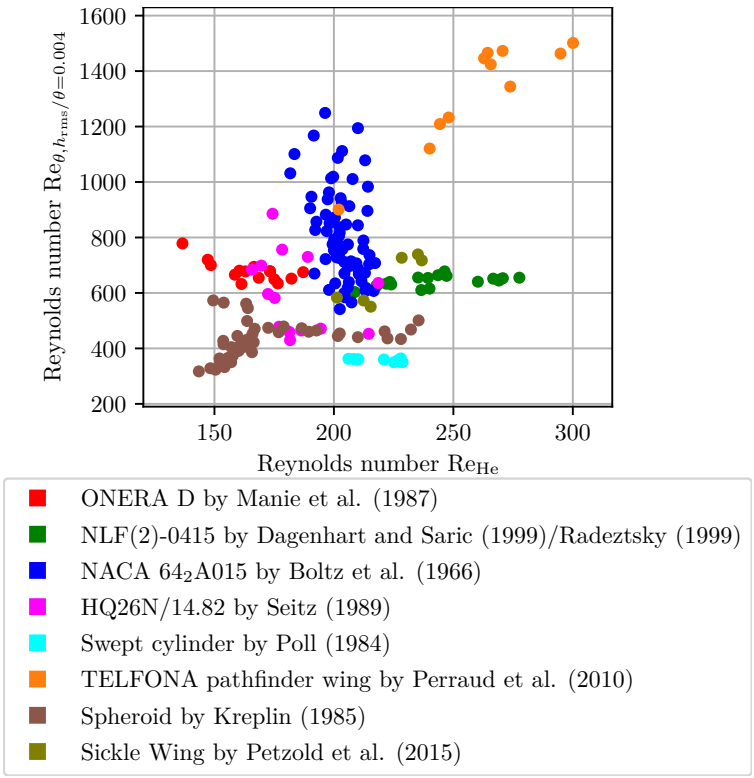

Figure F.7: Momentum thickness Reynolds number $\mathrm{Re}_\theta(\vec{x}_\mathrm{t})$ vs. wall normal maximum helicity Reynolds number $\max_{y_n \in [0,\delta(\vec{x}_\mathrm{t})]} \mathrm{Re}_{\mathrm{He},\mathcal{B}}(\vec{x}_\mathrm{t}, y_n)$

G Mathematical Conventions for this Thesis

When reading, one may be surprised by the quantity of mathematical expressions. It is helpful to have mathematical notations of otherwise verbally expressed statements. If the equations/terms are hard to read, a verbal explanation is always added in the text. In addition it is seeked for a clear expression. Therefore, certain mathematical conventions are used, that are explained here.
In general, symbols are written in *italic* font (for example temperature T, velocity u). This is not the case for symbols that consist of multiple letters (for example turbulence intensity Tu). If an index is appended to a variable, that is itself a variable, the index is written in italic font, otherwise in normal font (for example Re_c is the local chord-Reynolds number based on the chord c, but Re_c is the critical Reynolds number). Sometimes indices are not appended as subscript, but as superscripts (for readability only). To distinguish them from exponents, they are enclosed in parentheses (for example intermittency-production $P^{(\gamma)}$).
The existential quantificators are $\forall$ ("for all") and $\exists$ ("it exists at least one"). These are often combined with $\in$ ("in"). For example $u = 0 \,\forall \vec{x}_\Gamma \in \Gamma$ means that the variable u is zero for all points on the surface Γ.
A set of points is denoted either by greek letters (for example Ω for the domain) or latin letters in calligraphic font (for example $\mathcal{T}$ for the transition line). In the thesis, to the vector $\vec{x}$ usually a Γ or an Ω is appended as an index. This does not have any meaning but is only done for readability, to distinguish surface points $\vec{x}_\Gamma \in \Gamma$ defined on the surface Γ from volume points $\vec{x}_\Omega \in \Omega$ defined in the domain Ω.
The boundary of a set is denoted by the operator ∂ (for example $\partial\Omega$ is the boundary of the domain Ω). Subsets of the boundary are usually denoted by a capital or small Γ.
Partial derivatives are notated by the ∂ operator, that always has an index. If the index is a number, it is the number of the basis vector of the euclidean space (for example $\partial_1 u$ is the partial derivative of u with respect to the first basis vector of the space). If the index is another variable, it is the derivative with respect to that variable (for example $\partial_t u$ is the derivative of u with respect to the time t). Higher order derivatives are written by appending an exponent to the ∂-sign (for example $\partial_t^2 u$ is the second derivative of u with respect to time t).
The argument for which an equation or inequality holds, can be gotten by the arg-operator. Underneath the operator the "search space" is given (for example $\arg\limits_{\vec{x}_\Omega \in \Omega} u(\vec{x}_\Omega) < 0$ is the set of points of the domain Ω, at which the variable u is smaller than zero). This can also be combined with the max or min operator, which yield the maximum/minimum value of a set (for example $\operatorname{argmax}\limits_{\vec{x}_\Omega \in \Omega} u(\vec{x}_\Omega) < 0$ is the point in the subset of the set Ω, at which the variable u is smaller than zero, at which it is maximum).
There is no difference between the use of parantheses ( ) or brackets [ ]. In contrast, curly braces { } are reserved for the definition of sets (for example: $\{1, 2, 3\}$ is the set of the numbers 1, 2, and 3).
Sometimes, the Einstein summation convention is used: Whenever an index is appearing twice in a product, the term is an abbreviation for the sum over it with the twice appearing index going form 1 to 3 (for example $\partial_i u_i$ is the divergence of the vector $\vec{u}$ with the components u_i with $i \in \{1, 2, 3\}$).

Bibliography

[1] AGARD: Special Course on Progress in Transition Modelling. In: *AGARD Advisory Report* 793 (1994)

[2] Agarwal, Naval K. ; Maddalon, Dal V. ; Mangalam, Siva M. ; Collier, Fayette S.: Crossflow vortex and transition measurements by use of multielement hot films. In: *AIAA Journal* 30 (1992), Nr. 9, S. 2212–2218. http://dx.doi.org/10.2514/3.11207. – DOI 10.2514/3.11207. – ISSN 0001–1452

[3] Arnal, D. ; Coustols, E. ; Juillen, J.: Etude expérimentale et théorique de la transition sur une aile en flèche infinie. In: *La Recherche Aérospatiale* 1984-4 (1984)

[4] Arnal, D. ; Habillah, M. ; Delcourt, V.: Synthèse sur les méthodes de calcul de la transition développées au DERAT. In: *ONERA Technical Report* (1980)

[5] Arnal, D. ; Piot, E. ; Archambaud, Jean-Pierre ; Casalis, G. ; Content, C. ; Dandois, J. ; Colamartino, S.: TRACMIR : TRAnsition Control by Micron-sized Roughness elements. In: *RF 2/12136 DMAE* (2007)

[6] Blazek, Jiri: *Computational Fluid Dynamics: Principles and Applications*. Oxford : Elsevier, 2007. http://dx.doi.org/10.1016/B978-0-08-099995-1.09988-7. http://dx.doi.org/10.1016/B978-0-08-099995-1.09988-7. – ISBN 978–0–08–099995–1

[7] Boltz, Frederick W. ; Allen, Clyde Q. ; Kenyon, George C.: The Boundary-layer Transition Characteristics of Two Bodies of Revolution, a Flat Plate, and an Unswept Wing in a Low-turbulence Wind Tunnel. (1960)

[8] Boltz, Frederick W. ; Kenyon, Geroge C. ; Allen, Clyde Q.: Effects of sweep angle on the boundary-layer stability characteristics of an untapered wing at low speeds. In: *NASA technical note* (1960)

[9] Cliquet, J. ; Houdeville, R. ; Arnal, D.: Application of Laminar-Turbulent Transition Criteria in Navier-Stokes Computations. In: *AIAA Journal* 46 (2008), Nr. 5, S. 1182–1190. http://dx.doi.org/10.2514/1.30215. – DOI 10.2514/1.30215. – ISSN 0001–1452

[10] Cooke, J. C.: The boundary layer of a class of infinite yawed cylinders. In: *Mathematical Proceedings of the Cambridge Philosophical Society* 46 (1950), Nr. 4, S. 645–648. http://dx.doi.org/10.1017/S0305004100026220. – DOI 10.1017/S0305004100026220. – ISSN 0305–0041

[11] Dagenhart, J. ; Saric., W.: Crossflow Stability and Transition Experiments in Swept-Wing Flow. In: *NASA/TP* (1999), Nr. 209344

[12] DLR: Technical Documentation of the DLR TAU-code Release 2018.1.0: DLR-Institute ofAerodynamic and Flow Technology at Goettingen and Braunschweig. (2018)

[13] DLR: TAU-Code User Guide Release 2019.1.0: DLR-Institute ofAerodynamic and Flow Technology at Goettingen and Braunschweig. (2019)

[14] Downs, Robert S. ; White, Edward B.: Free-stream turbulence and the development of cross-flow disturbances. In: *Journal of Fluid Mechanics* 735 (2013), S. 347–380. http://dx.doi.org/10.1017/jfm.2013.484. – DOI 10.1017/jfm.2013.484. – ISSN 0022–1120

[15] Eisfeld, Bernhard: Elemente der statistischen Turbulenzmodellierung. (2020)

[16] Falkner, V. M. ; Skan, S. W.: Some approximate solutions of the boundary-layer equations. In: *Rep. Memor. aero. Res. coun. Lond.* (1930), Nr. 30

[17] Fey, Uwe ; Egami, Yasuhiro ; Engler, Rolf: High Reynolds Number Transition Detection by Means of Temperature Sensitive Paint. In: *44th AIAA Aerospace Sciences Meeting and Exhibit*. Reston, Virigina : American Institute of Aeronautics and Astronautics, 2006. – ISBN 978–1–62410–039–0

[18] Grabe, Cornelia: Correlation-based Transition Transport Modeling in the DLR TAU-Code. (2013)

[19] Grabe, Cornelia ; Shengyang, Nie ; Krumbein, Andreas: Transport Modeling for the Prediction of Crossflow Transition. In: *AIAA Journal* 56 (2018), Nr. 8, S. 3167–3178. http://dx.doi.org/10.2514/1.J056200. – DOI 10.2514/1.J056200. – ISSN 0001–1452

[20] Hirschfelder, J. O. ; Curtiss, C. F. ; Bird, R. B.: *Molecular Theory Of Gases And Liquids*. New York, London, Sydney : John Wiley & Sons, Inc., 1954

[21] Holstein, H. ; Bohlen, T.: Ein einfaches Verfahren zur Berechnung laminare Grenzschichten, die dem Näherungsansatz nach K. Pohlhausen genügen. In: *Bericht S 10 der Lilienthal-Gesellschaft für Luftfahrtforschung* (1940), S. 5

[22] IEEE: *IEEE Standard for System and Software Verification and Validation*

[23] Kaushik, Mrinal: *Theoretical and Experimental Aerodynamics*. Singapore : Springer Singapore, 2019. http://dx.doi.org/10.1007/978-981-13-1678-4. http://dx.doi.org/10.1007/978-981-13-1678-4. – ISBN 978–981–13–1677–7

[24] Kohama, Y. ; Ukaku, M. ; Ohta, F.: Boundary-layer transition on a swept cylinder. Version: 1988. http://dx.doi.org/10.1016/B978-0-08-036232-8.50031-1. In: Shen Yuan (Hrsg.): *Frontiers of Fluid Mechanics*. Pergamon, 1988. – DOI 10.1016/B978–0–08–036232–8.50031–1. – ISBN 978–0–08–036232–8, 151–156

[25] Kohama, Yasuaki ; Davis, Sanford S.: A new parameter for predicting crossflow instability. In: *JSME International Journal* 36 (1993), Nr. 1

[26] Kreplin, H-P. ; Vollmers, H. ; Meier, H. U.: Wall shear stress measurements on an inclined prolate spheroid in the DFVLR 3M x 3M low speed wing tunnel, Göttingen: Internal Data Report. In: *DFVLR-IB 222-84 A 33* (1985)

[27] Krimmelbein, Normann: *Transition prediction method for three-dimensional flows using linear stability theory*. 2020

[28] Krimmelbein, Normann ; Krumbein, Andreas: Validation of transition modeling techniques for a simplified fuselage configuration. In: *Aerospace Science and Technology* 118 (2021), S. 107043. http://dx.doi.org/10.1016/j.ast.2021.107043. – DOI 10.1016/j.ast.2021.107043

[29] Kruse, Martin ; Munoz, Federico ; Radespiel, Rolf ; Grabe, Cornelia: Transition Prediction Results for Sickle Wing and NLF(1)-0416 Test Cases. In: *2018 AIAA Aerospace Sciences Meeting*. Reston, Virginia : American Institute of Aeronautics and Astronautics, 2018. – ISBN 978–1–62410–524–1

[30] Langer, Stefan ; Schwöppe, Axel ; Kroll, Norbert: The DLR Flow Solver TAU - Status and Recent Algorithmic Developments. In: *52nd Aerospace Sciences Meeting, 13.-17. Jan. 2014, National Harbor, Maryland, USA* (2014)

[31] Langtry, Robin ; Sengupta, Kaustav ; Yeh, David T. ; Dorgan, Andrew J.: Extending the Gamma-Rethetat Correlation based Transition Model for Crossflow Effects. In: *45th AIAA Fluid Dynamics Conference*. Reston, Virginia : American Institute of Aeronautics and Astronautics, 2015. – ISBN 978–1–62410–362–9

[32] Langtry, Robin B. ; Menter, Florian R.: Correlation-Based Transition Modeling for Unstructured Parallelized Computational Fluid Dynamics Codes. In: *AIAA Journal* 47 (2009), Nr. 12, S. 2894–2906. http://dx.doi.org/10.2514/1.42362. – DOI 10.2514/1.42362. – ISSN 0001–1452

[33] Le Duc, Anne ; Sesterhenn, Jörn ; Friedrich, Rainer: Instabilities in compressible attachment–line boundary layers. In: *Physics of Fluids* 18 (2006), Nr. 4, S. 044102. http://dx.doi.org/10.1063/1.2187450. – DOI 10.1063/1.2187450. – ISSN 1070–6631

[34] Lemarechal, Jonathan ; Costantini, Marco ; Klein, Christian ; Kloker, Markus J. ; Würz, Werner ; Kurz, Holger B. ; Streit, Thomas ; Schaber, Sven: Investigation of stationary-crossflow-instability induced transition with the temperature-sensitive paint method. In: *Experimental Thermal and Fluid Science* 109 (2019), S. 109848. http://dx.doi.org/10.1016/j.expthermflusci.2019.109848. – DOI 10.1016/j.expthermflusci.2019.109848. – ISSN 08941777

[35] Lynde, Michelle N. ; Campbell, Richard L. ; Viken, Sally A.: Additional Findings from the Common Research Model Natural Laminar Flow Wind Tunnel Test. In: *AIAA Aviation 2019 Forum*. Reston, Virginia : American Institute of Aeronautics and Astronautics, 2019. – ISBN 978–1–62410–589–0

[36] Manie, F. ; Rehbach, C. ; Schmitt, V.: Study of variable sweep wing in sub or transonic flow. In: *NASA technical translation* (1987)

[37] Medida, Shivaji ; Baeder, James: A New Crossflow Transition Onset Criterion for RANS Turbulence Models. Version: 2013. http://dx.doi.org/10.2514/6.2013-3081. In: *21st AIAA Computational Fluid Dynamics Conference*. 2013. – DOI 10.2514/6.2013–3081

[38] Meier, H. U. ; Kreplin, H-P.: Experimental Investigations of the Boundary Layer Transition and Separation on a Body of Revolution. In: *Z. Flugwiss. Weltraumforsch.* (1980), Nr. 4

[39] Menter, F. R.: Two-equation eddy-viscosity turbulence models for engineering applications. In: *AIAA Journal* 32 (1994), Nr. 8, S. 1598–1605. http://dx.doi.org/10.2514/3.12149. – DOI 10.2514/3.12149. – ISSN 0001–1452

[40] Menter, F. R. ; Smirnov, P.: Development of a RANS-based model for predicting crossflow transition. In: *Proceedings of the Contributions to the 19th STAB/DGLR Symposium* (2014)

[41] Mueller, B. ; Bippes, H.: Experimental study of instability modes in a three-dimensional boundary layer. In: *Fluid Dyn. Three-Dimens. Shear Flows Transit.* (1989), Nr. AGARD CP 438, S. 13.1–15

[42] Munoz, Federico: Experimental Data and Description of Test Cases for the Sickle Wing Transition Experiment. (2017)

[43] Oertel, Herbert ; Delfs, Jan: *Strömungsmechanische Instabilitäten*. Karlsruhe : Universitätsverlag, 2005. http://dx.doi.org/10.5445/KSP/1000003552. http://dx.doi.org/10.5445/KSP/1000003552. – ISBN 3937300805

[44] Perraud, Jean ; Archambaud, Jean-Pierre ; Schrauf, Géza ; Donelli, Raffaele ; Hanifi, Ardeshir ; Quest, Jurgen ; Streit, Thomas. ; Hein, Stefan ; Fey, Uwe ; Egami, Yasuhiro: Transonic High Reynolds Number Transition Experiments in the ETW Cryogenic Wind Tunnel. In: *American Institute of Aeronautics and Astronautics* (2010)

[45] Perraud, Jean ; El Din, Ithma S. ; Schrauf, Géza ; Hanifi, Ardeshir ; Donelli, Raffaele ; Hein, Stefan ; Fey, Uwe ; Egami, Yasuhiro ; Streit, Thomas.: High Reynolds number transition experiments in the ETW test facility with the pathfinder model. In: *V European Conference on Computational Fluid Dynamics. ECCOMAS CFD 2010 Lisbon, Portugal, 14–17 June 2010* (2010)

[46] Petzold, R. ; Radespiel, R.: Transition on a Wing with Spanwise Varying Crossflow and Linear Stability Analysis. In: *AIAA Journal* 53 (2015), Nr. 2, S. 321–335. http://dx.doi.org/10.2514/1.J053127. – DOI 10.2514/1.J053127. – ISSN 0001–1452

[47] Poll, D. I. A.: Some observations of the transition process on the windward face of a long yawed cylinder. In: *J. Fluid Mech.* 1985 (1984), Nr. 150, S. 329–356

[48] Prandtl, L.: Über Flüssigkeitsbewegung bei sehr kleiner Reibung. In: Krazer, A. (Hrsg.): *Verhandlungen des dritten internationalen Mathematiker-Kongresses*, 1904, S. 484–491

[49] Radeztsky, Ronald H. ; Reibert, Mark S. ; Saric, William S.: Effect of Isolated Micron-Sized Roughness on Transition in Swept-Wing Flows. In: *AIAA Journal* 37 (1999), Nr. 11, S. 1370–1377. http://dx.doi.org/10.2514/2.635. – DOI 10.2514/2.635. – ISSN 0001–1452

[50] Roe, P.L: Approximate Riemann solvers, parameter vectors, and difference schemes. In: *Journal of Computational Physics* 43 (1981), Nr. 2, S. 357–372. http://dx.doi.org/10.1016/0021-9991(81)90128-5. – DOI 10.1016/0021–9991(81)90128–5. – ISSN 00219991

[51] Rubino, Ginevra: *Laminar-to-Turbulence Transition Modeling of Incompressible Flows in a RANS Framework for 2D and 3D Configurations*, Unpublished, Diss., 2022. http://dx.doi.org/10.13140/RG.2.2.13761.68969. – DOI 10.13140/RG.2.2.13761.68969

[52] Saeed, T. I. ; Morrison, J. F. ; Mughal, M. S.: Roughness effects on swept-wing crossflow transition in moderate free-stream turbulence. In: *29th Congress of International Council of the Aeronautical Sciences, St. Petersburg, Sept. 2014* (2014)

[53] Saric, W. S. ; Yeates, L. G.: Generation of crossflow vortices in a three-dimensional flat-plate flow. In: *Laminar-Turbulent Transition*. Springer, 1985, S. 429–437

[54] SARIC, WILLIAM: The ASU Transition Research Facility. In: *28th Joint Propulsion Conference and Exhibit*. Reston, Virigina : American Institute of Aeronautics and Astronautics, 1992

[55] Saric, William S. ; Reed, Helen L. ; White, Edward B.: Stability and Transition of Three-Dimensional Boundary Layers. In: *Annual Review of Fluid Mechanics* 35 (2003), Nr. 1, S. 413–440. http://dx.doi.org/10.1146/annurev.fluid.35.101101.161045. – DOI 10.1146/annurev.fluid.35.101101.161045. – ISSN 0066–4189

[56] Schlichting, H. ; Gersten, K.: Grenzschicht-Theorie. (2006)

[57] Schmitt, V. ; Monneris, B. ; Dorey, G. ; Capelier, C.: Étude de la couche limite tridimensionnelle sur une aile en flèche. In: *ONERA, Rapport Technique* (1975), Nr. 14/1713

[58] Schobeiri, Meinhard T.: *Advanced Fluid Mechanics and Heat Transfer for Engineers and Scientists*. Cham : Springer International Publishing, 2022. http://dx.doi.org/10.1007/978-3-030-72925-7. http://dx.doi.org/10.1007/978-3-030-72925-7. – ISBN 978–3–030–72924–0

[59] Schrauf, Géza ; Schmidt, K.: Prediction of the Transition Behaviour of the TELFONA Pathfinder Wing: Deliverable 1.1-5. In: *AIRBUS Technical Report* (2006)

[60] Schultz, Michael: The Relationship Between Frictional Resistance and Roughness for Surfaces Smoothed by Sanding. In: *J. Fluids Eng.* (2002), Nr. Jun 2002, S. 492–499

[61] Seitz, Arne: Ermittlung des Querstromungs ¨ N Faktors zur Umschlagvorhersage im Niedergeschwindigkeitswindkanal Braunschweig (NWB). (1989), Nr. IB/129-89/26

[62] Seraudie, A. ; Perraud, J. ; Moens, F.: Transition measurement and analysis on a swept wing in a high lift configuration. In: *ICAS 2002 Congress* (2002)

[63] Somers, D. M.: Subsonic Natural-Laminar-Flow Airfoils. In: Barnwell, R. W. (Hrsg.) ; Hussaini, M. Y. (Hrsg.): *Natural Laminar Flow and Laminar Flow Control*. Springer, 1992, S. 143–176

[64] Somers, D. M. ; Horstmann, Karl H.: Design of a Medium-Speed, Natural-Laminar-Flow Airfoil for Commuter Aircraft Application. In: *DFVLR data report* (1985), Nr. IB 129-85/26

[65] Spalart, P. ; Rumsey, C. L.: Effective Inflow Conditions for Turbulence Models in Aerodynamic Calculations. In: *AIAA Journal* (2007), Nr. 45, S. 2544–2553. – ISSN 0001–1452

[66] Stock, Hand W. ; Seitz, Arne: Crossflow-Induced Transition Prediction Using Coupled Navier–Stokes and eN Method Computations. In: *AIAA Journal* (2004), Nr. 42, S. 1746–1754. – ISSN 0001–1452

[67] Streit, Thomas. ; Horstmann, Karl H. ; Schrauf, Géza ; Hein, Stefan ; Fey, Uwe ; Egami, Yasuhiro ; Perraud, Jean ; El Din, Ithma S. ; Cella, Ubaldo ; Querst, Jürgen: Complementary Numerical and Experimental Data Analysis of the ETW Telfona Pathfinder Wing Transition Tests. In: *49th AIAA Aerospace Sciences Meeting including the New Horizons Forum and Aerospace Exposition* 881 (2011)

[68] Streit, Thomas. ; Schrauf, Géza ; El Din, Ithma S. ; Cella, Ubaldo ; Fey, Uwe ; Egami, Yasuhiro: The Telfona Pathfinder model, a second look. In: *V European Conference on Computational Fluid Dynamics. ECCOMAS CFD 2010 Lisbon, Portugal, 14–17 June 2010* (2010)

[69] Tokugawa, N. ; Takagi, S. ; Ueda, Y. ; Ido, A.: Influence of the External Disturbances on Natural Boundary-Layer Transition in Rectangular Wing Flows. In: *Journal of Japan Society of Fluid Mechanics* 24 (2005), Nr. 6, S. 629–639

[70] Tsinober, Arkady: *The Essence of Turbulence as a Physical Phenomenon*. Cham : Springer International Publishing, 2019. http://dx.doi.org/10.1007/978-3-319-99531-1. http://dx.doi.org/10.1007/978-3-319-99531-1. – ISBN 978–3–319–99530–4

[71] Venkatachari, Balaji S. ; Paredes, Pedro ; Derlaga, Joseph M. ; Buning, Pieter G. ; Choudhari, Meelan M. ; Li, Fei ; Chang, Chau-Lyan: Assessment of Transition Modeling Capability in OVERFLOW with Emphasis on Swept-Wing Configurations. In: *AIAA Scitech 2020 Forum*. Reston, Virginia : American Institute of Aeronautics and Astronautics, 2020. – ISBN 978–1–62410–595–1

[72] Vermeersch, Olivier ; Arnal, Daniel ; El Din, Itham S.: Transition control by micron-sized roughness elements: stability analyses and wind tunnel experiments. In: *International Journal of Engineering Systems Modelling and Simulation* 5 (2013), Nr. 1-3, S. 84–98. http://dx.doi.org/10.1504/IJESMS.2013.052381. – DOI 10.1504/IJESMS.2013.052381

[73] Watanabe, Yuto ; Misaka, Takashi ; Obayashi, Shigeru ; Arima, Toshiyuki ; Yamagichi, Yoshihiro: Application of Crossflow Transition Criteria to Local Correlation-Based Transition Model. In: *47th AIAA Aerospace Sciences Meeting including The New Horizons Forum and Aerospace Exposition*. Reston, Virigina : American Institute of Aeronautics and Astronautics, 2009. – ISBN 978–1–60086–973–0